

Imaging  
Cerebral  
Physiology  
Meeting  
2023

## ABSTRACT & PROGRAM BOOK



UMC Utrecht

**November 29<sup>th</sup> – December 1<sup>st</sup>, 2003**

**University Medical Centre Utrecht**

On-site Organization

Alex A. Bhogal (Chair)

Wouter Schellekens

Organizing Committee

Lena Vaclavu

Stefano Moia

Mario Gilberto Baez-Yanez

Manus Donahue

Claudine Gauthier

Hanzhang Lu

**Partners**





# Program

Imaging Cerebral Physiology

Network

Meeting, 5<sup>th</sup> Edition

Day 1 – November 29<sup>th</sup>

Time		Length (minutes)		
08:30-9:15		45		Arrival, registration, coffee & tea
			Speaker	Title
09:15-09:20		5	Alex Bhogal Assistant Professor	Welcome
09:20-10:00		40	Jaco Zwanenburg Associate Professor	Seismology of the Brain
10:00-13:00				Session 1a - Methods
	10:00-10:20	20	Joe Fisher	Model-free cerebral perfusion metrics calculated directly from a transient hypoxia-induced step change in deoxy-hemoglobin
	10:20-10:40	20	Ian Driver	Measuring Pulse-wave Velocity in the Healthy Human Brain using inflow magnetic contrast MRI
	10:40-11:00	20	Aneurin Kennerly	Measurement and Modulation of Cerebral ATP flux: A 31P Magnetisation Transfer Magnetic Resonance Spectroscopy study with 670nm photobiomodulation.
	11:00-11:20	20		BREAK
				Session 1b - Blood
	11:20-11:40	20	Jiani Wu	Longitudinal changes in cerebral metabolic rate of oxygen (CMRO <sub>2</sub> ) in cognitively normal older adults
	11:40-12:00	20	Megan Aumann	Cerebral blood flow and oxygen extraction fraction responses to conservative and aggressive treatments in adults with sickle cell disease
	12:00-12:20	20	Yunjie Tong	Novel identifications of cerebral hemodynamics in BOLD fMRI associated with fetal hemoglobin in patients with sickle cell disease
	12:20-13:00	40	John Wood Professor of Paediatrics and Radiology	T.B.A. Clinic, Sickle Cell Disease
13:00-14:30		90		LUNCH: Posters + Demo's <u>RapidTide</u>
14:30-17:00				Session 2 - Clinical
	14:30-14:50	20	Cristina Comella	Mapping cerebrovascular reactivity and vascular lag in gliomas with multi-echo BOLD fMRI and breath holding
	14:50-15:10	20	Caleb Han	Cerebrovascular reactivity response time as revealed by time regression analysis is uniquely correlated to recent stroke symptomatology in moyamoya patients
	15:10-15:30	20	Stanley Pham	Association between small vessel function and progressive white matter injury in CADASIL using advanced 7T MRI
	15:30-15:50	20	Oluwateniola Akinwale	CO <sub>2</sub> and O <sub>2</sub> reactivity in brain gliomas
	15:50-16:10	20		BREAK
	16:10-17:00	50	Jorn Fierstra	Integration of BOLD cerebrovascular reactivity into clinical ischemic stroke management
18:30-22:00			DINNER + SOCIAL EVENT	Utrecht Rail Museum (Spoorweg Museum)



# Program

Imaging Cerebral Physiology

Network

Meeting, 5<sup>th</sup> Edition

**Day 2 – November 30th**

Time		Length (minutes)		
09:00-9:20		30		<b>Arrival, registration, coffee &amp; tea</b>
			Speaker	Title
09:20-10:00		40	<u>Lydiane Hirschler</u> Post-Doc	<b>Imaging techniques to assess the CSF-mediated brain clearance system in humans</b>
10:00-13:00				<b>Session 3 – vessels and neuro-fluids</b>
	10:00-10:20	20	Ellen van Hulst	Quantifying Cardiac-Induced Brain Tissue Deformations Using DENSE MRI: Insights from an Observational Study
	10:20-10:40	20	Manon Schipper	Does a manual determined threshold bias quantitative perivascular spaces measurements based on the <u>Frangi vesselness</u> filter?
	10:40-11:00	20	Lotte van der Voort	CO <sub>2</sub> as an engine for <u>neurofluid</u> flow: exploring the coupling between vascular reactivity, brain clearance and changes in tissue properties
	11:00-11:20	20		BREAK
	11:20-11:40	20	Lori Donaldson	Age-related differences in emotional fMRI responses after accounting for cerebrovascular reactivity decline
	11:40-12:00	20	Dinil Sasi Sankaralayam	Impact of caffeine on cerebrovascular reactivity in caffeine-naive healthy adults
	12:00-12:20	20	Beatriz Padrela	Blood-brain barrier permeability measured with ASL differs between cognitive stages and amyloid status
	12:20-13:00	40	<u>Zixuan Lin</u> Assistant Professor	<b>Non-contrast imaging of blood-brain-barrier permeability and its clinical application</b>
13:00-14:30		90		<b>LUNCH: Posters + Demo's <u>PhysioPy</u></b>
14:30-17:40				<b>Session 4 – structure and function</b>
	14:30-15:10	40	<u>Stephanie Forkel</u> Associate Professor,	<b>T.B.A., Mapping Brain connections; from anatomy to the clinic</b>
	15:10-15:30	20	Elisa Zamboni	Mapping curvature domains in human V4 using CBV-sensitive layer-fMRI at 3T
	15:30-15:50	20	Hendrik Mattern	Combining vessel distance mapping and non-negative matrix factorization to identify arterial and venous patterns in the putamen
	15:50-16:10	20	Wesley Richardson	Detectability of white matter perfusion across flow territories when using arterial spin labelling MRI: Impact of <u>hematocrit</u> and bolus arrival times
	16:10-16:30	20	Mathijs B.J. Dijkshof	Cerebral blood flow as an intermediary between cardiovascular and cerebrovascular health: results from the Insight46 study
	16:30-16:50	20		BREAK
	16:50-17:40	50	<u>Blaise Frederick</u> Associate Professor	<b>Using resting state fMRI to study everything but neuronal activity + the mysterious growing <u>sLFOs!</u></b>



# Program

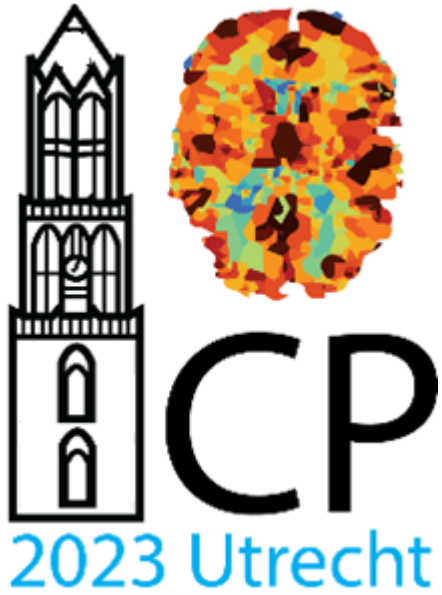
Imaging Cerebral Physiology

Network

Meeting, 5<sup>th</sup> Edition

**Day 3 – December 1st**

Time		Length (minutes)		
09:00-9:20		30		<b>Arrival, registration, coffee &amp; tea</b>
			Speaker	Title
09:20-10:00		40	<b>Hanzhong Lu</b> Professor of Radiology	<b>CVR as a candidate biomarker in vascular cognitive impairment: the MarkVCID Consortium experience</b>
10:00-13:00				<b>Session 5 - Cerebrovascular &amp; Metabolism</b>
	10:00-10:20	20	Ahlam Alzaidi	Preliminary data for using hyperoxia and multiparametric gBOLD to estimate the oxygen extraction fraction
	10:20-10:40	20	Hannah Chandler	Increased brain oxygen metabolism and oxygen extraction in patients with cystic fibrosis
	10:40-11:00	20	Eleonara Patitucci	Single image super resolution reconstruction of susceptibility maps for improved vessel segmentation and oxygen saturation estimation
	11:00-11:20	20	Zacharie Potvin-Jutras	Sex differences in the effects of physical activity on cerebrovascular reactivity
	11:20-11:40	20		<b>BREAK</b>
	11:40-12:00	20	Julia Huck	Vascular and metabolic changes in individuals with and without the ApoE ε4 allele
	12:00-12:20	20	Joseph Liu	Automated cerebral blood flow metrology and physiology in anesthetized children using phase contrast MRI
	12:20-12:40	20	Zhiyi Hu	Macrovascular-suppressed ASL MRI in neonates: quantification of cerebral blood flow and arterial transit time
	12:40-13:10	30	<b>Emma Hafkamp</b> Clinical Psychologist	<b>Something Different: How we can modulate our own physiology?</b>
13:10-14:30		90		<b>LUNCH: Respiratory systems, RespirAct, Clinical fixed inspired CVR Setup + Demo seeVR</b>
14:30-18:00				<b>Session 6 - pushing boundaries</b>
	14:30-15:10	40	<b>Jeroen Siero</b> Associate Professor	<b>Silent MRI using an ultra-sonic gradient coil: new frontier measuring brain function</b>
	14:50-15:10	20	Vanja Curcic	From microscopy data to hemodynamic simulations: a vascular graph approach to understand the fMRI signal formation
	15:10-15:30	20	Marius Burman Ingeberg	Estimating the viscoelastic properties of the human brain using intrinsic MRE and nonlinear inversion at 7T
	15:30-15:50	20	Emiel C.A. Roefs	Velocity selective Arterial Spin Labelling at 7T
	15:50-16:10	20		<b>BREAK</b>
	16:10-17:00	50	<b>Jurgen Claassen</b> , Associate Professor	<b>T.B.A.: Cerebral autoregulation in the clinic, Spaceflight, Physiology</b>
	17:00 - 18:00			Closing



Day 1: November 29th

# Model-free cerebral perfusion metrics calculated directly from a transient hypoxia-induced step- change in deoxyhemoglobin

James Duffin<sup>1</sup>, Ece Su Sayin<sup>1,2</sup>, Olivia Sobczyk<sup>2,3</sup>, Julien Poublanc<sup>2</sup>, David J. Mikulis<sup>2</sup>, Joseph A. Fisher<sup>1,3,4</sup>

<sup>1</sup>Departments of Physiology, University of Toronto, Toronto, Canada.

<sup>2</sup>Joint Department of Medical Imaging and the Functional Neuroimaging Laboratory, University Health Network, Toronto, Canada.

<sup>3</sup>Department of Anaesthesia and Pain Management, University Health Network, Toronto, Canada.

<sup>4</sup>Toronto General Hospital Research Institute, University Health Network, Toronto, Canada.

## Synopsis and/or Summary of Main Findings:

Indicator dilution methods have long been used for calculating resting perfusion measures such as cerebral blood flow, cerebral blood volume and mean transit time. A bolus of intravenously injected indicator such as gadolinium, arrives at tissue with its initial concentration profile dispersed to unknown extent. The arterial input function must be measured by deconvolution of the residue function at each voxel.

Here we use paramagnetic properties of transient hypoxia-induced deoxyhemoglobin as a susceptibility agent. Deoxyemoglobin in the venous return is reoxygenated in the lung within 1s providing a step arterial input function. We compared this model-free hemodynamic approach to that using standard deconvolution for calculating flow metrics and found the former was highly correlated to the conventional model-based gadolinium bolus deconvolution method.

## Abstract Body:

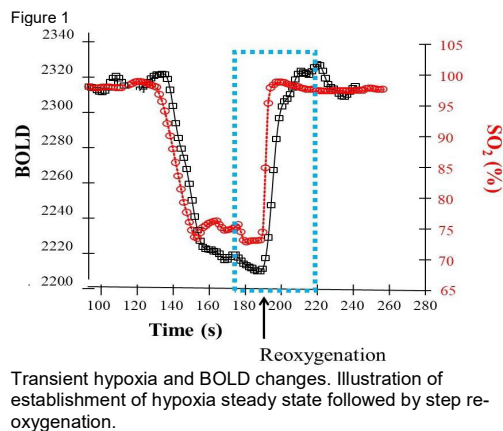
**Background:** Resting relative cerebral perfusion metrics are calculated by analysing the voxel-wise MRI susceptibility weighted T2\* signal during the first passage through the brain of an intravascular bolus injection of a contrast agent such as gadolinium-based contrast agents (GBCAs). This calculation requires the selection of an arterial input function (AIF), for example, from a middle cerebral artery. We introduce a novel non-invasive contrast agent, transient hypoxia-induced bolus of deoxyhemoglobin (THx-dOHb) and a model-free signal analysis to generate resting perfusion metrics.

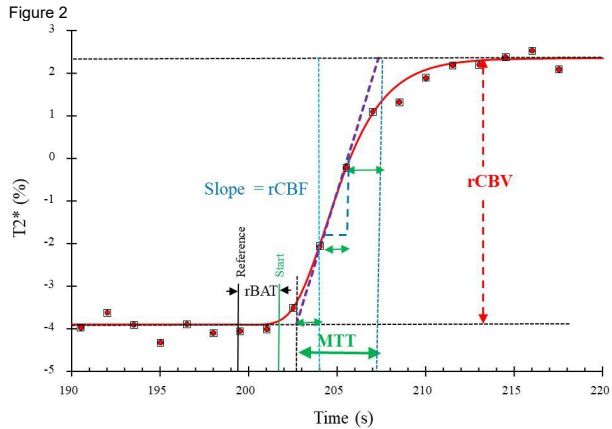
**Purpose:** To compare metrics from a model-free analysis of THx-dOHb to those obtained with an AIF from GBCA in the same individuals.

**Methods:** In 8 healthy volunteers we calculated cerebral perfusion metrics using THx-dOHb using a model-free analysis as illustrated in Figures 1 and 2, and compared values to those using susceptibility weighted T2\* signal changes as the deconvolution of an AIF for GBCA in the same participants.

**Results:** Mean transit time (MTT), relative cerebral blood flow (rCBF) and relative cerebral blood volume (rCBV) maps are virtually indistinguishable between methods, with the model free method exhibiting a smaller standard deviation (Figure 3).

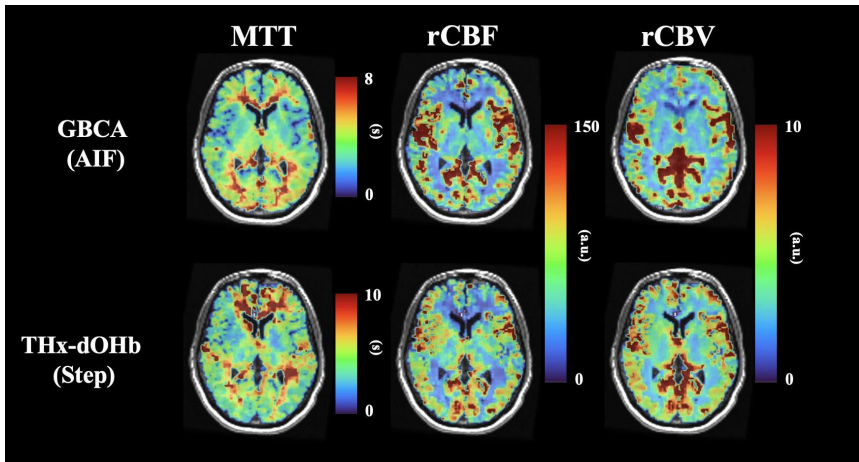
**Conclusion:** The model-free method benefits from rapid reoxygenation of deoxyhemoglobin yielding perfusion metrics that are highly comparable to those obtained from the standard approach using model-based analyses of the GBCA bolus. THx-dOHb is a promising "needle-free", environmentally friendly alternative measure of cerebral perfusion metrics.





Analysis of re-oxygenation for voxel-wise hemodynamic factors. Relative blood arrival time (rBAT) occurs between an arbitrary reference point and threshold change in signal. Amplitude of signal (red dashed line) is proportional to relative cerebral blood volume (rCBV), linear rate of signal change is proportional to relative cerebral blood flow (rCBF). Mean transit time (MTT) is the sum of the inflow time constant, time of linear progression and time constant of contrast exit.

Figure 3



Analysis of re-oxygenation for voxel-wise hemodynamic factors. Relative blood arrival time (rBAT) occurs between an arbitrary reference point and threshold change in signal. Amplitude of signal (red dashed line) is proportional to relative cerebral blood volume (rCBV), linear rate of signal change is proportional to relative cerebral blood flow (rCBF). Mean transit time (MTT) is the sum of the inflow time constant, time of linear progression and time constant of contrast exit.

# Measuring pulse-wave velocity in the healthy human brain using dynamic inflow magnitude contrast MRI

I.D. Driver, M.E. Wright, A. Crofts, S. Davies, H. Chandler, K. Murphy

<sup>1</sup>Cardiff University Brain Research Imaging Centre (CUBRIC), School of Physics and Astronomy, Cardiff University, Cardiff, United Kingdom

## Synopsis

This work demonstrates the concept of using a beat-to-beat measure of carotid and middle cerebral artery pulsatile blood flow velocity to measure pulse-wave velocity entering the healthy human brain. The arterial pulse-wave delay between the carotid artery and the middle cerebral artery was measured as  $29\pm 14$ ms, corresponding to a pulse-wave velocity of 4 m/s. These results are the first stage in establishing pulse-wave velocity as a new non-invasive MRI biomarker for cerebrovascular health, providing a new tool to investigate mechanisms underlying healthy ageing and brain pathology.

## Introduction

Pulse-wave velocity is a measure of arterial stiffness, providing a key marker of cardiovascular health<sup>1-4</sup>. It is commonly measured as the pulse-wave delay between carotid and femoral arteries divided by the difference in path length from the heart<sup>5</sup>. Compliant cerebral arteries act to attenuate the pulse-wave, protecting brain tissue from damage. Therefore, a measurement of pulse-wave velocity through the cerebral vasculature provides specific information about cerebral arterial stiffness and cerebrovascular health. MRI is uniquely able to non-invasively measure pulsatile flow in arteries deep within the skull. Dynamic inflow magnitude contrast (DIMAC) MRI<sup>5</sup> can measure the pulsatile flow waveform for individual heartbeats. In this work, we demonstrate the feasibility of measuring pulse-wave velocity between carotid and middle cerebral arteries (MCA) using the DIMAC signal in a small cohort.

## Methods

We present data from seven healthy female participants (aged 18-32). Data were acquired on a Siemens Prisma 3 Tesla system and peripheral pulse measurements were made using a Biopac photoplethysmograph (PPG; 500 Hz sampling frequency). Time-of-flight angiography (TR = 21ms, 0.6mm isotropic) was used for slice positioning and calculating path length between the carotid and MCA. Two DIMAC slices were acquired, positioned perpendicular to the right carotid and right MCA, respectively (Figure 1). Each DIMAC slice was acquired with TR=15ms, 2x2x10mm, GRAPPA=5, 4096 measurements in 1 minute. Pulse timings were determined by fitting a Fourier series basis set to each heartbeat period of each pulse waveform. As carotid and MCA waveforms were not acquired simultaneously, they were both aligned to the finger pulse as a reference point (Figure 2).

## Results

Delays from the DIMAC pulse to the finger pulse (PPG) are shown in Figure 3, averaged across all heartbeat periods for each subject. The carotid artery led the finger pulse by  $120\pm 6$ ms and the MCA led the finger pulse by  $91\pm 12$ ms. Therefore, the carotid pulse led the MCA pulse by  $29\pm 14$ ms (pWilcoxon=0.03, signed rank=27). Incorporating the path length from the carotid to the MCA (110mm) gives a pulse-wave velocity of 4m/s.

## Discussion

In this work we introduce the concept of measuring pulse-wave velocity in the healthy brain. Pulse-wave velocity is a key indicator of vascular compliance, how the pulse-wave is attenuated before reaching (and damaging) brain tissue. The DIMAC flow-sensitive signal allows the pulse to be resolved for individual heartbeats, so is less sensitive to heart rate variability than other MRI methods for studying flow velocity, such as phase-contrast MRI.

This is a small dataset, with a homogeneous demographic (young, female participants). The carotid pulse led the MCA pulse in 6/7 subjects, whilst the amplitude of the delay was driven by 2 subjects. Therefore, we will build on this initial demonstration of concept by expanding the sample size, to further understand the variability of the measurement.

In conclusion, we present an initial demonstration of MRI derived pulse-wave velocity measurements in the human brain. These measurements could provide valuable information on arterial stiffness, that would extend our understanding of vascular pathophysiology in neurodegeneration and related diseases<sup>2</sup>.

## References

1. Alastruey et al. *Am J Physiol Heart Circ Physiol* 325: H1–H29, 2023; doi: 10.1152/ajpheart.00705.2022
2. Scuteri and Wang. *J Alzheimers Dis.* 42 Suppl 4:S401-10, 2014; doi: 10.3233/JAD-141416
3. Li et al. *J Exerc Sci Fit.* 21(4):313-325, 2023; doi: 10.1016/j.jesf.2023.06.002
4. Pomeroy et al. *Sleep Med Rev.* 70:101794, 2023; doi: 10.1016/j.smrv.2023.101794
5. Milan et al. *J Hypertens.* 37(8):1547-1557, 2019; doi: 10.1097/HJH.0000000000002081
6. Whittaker et al. *Front Neurosci.* 17;15:795749, 2022; doi: 10.3389/fnins.2021.795749

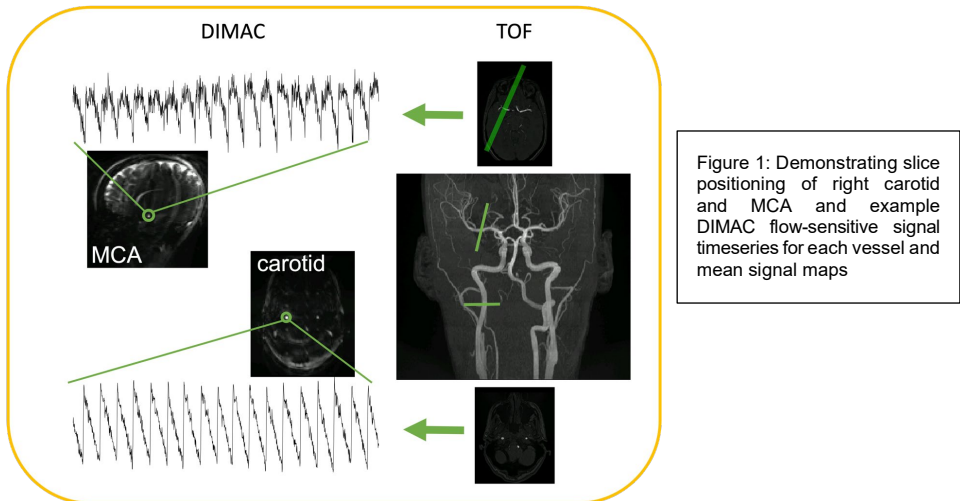


Figure 1: Demonstrating slice positioning of right carotid and MCA and example DIMAC flow-sensitive signal timeseries for each vessel and mean signal maps

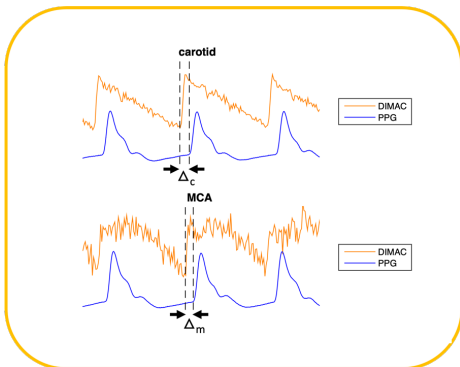


Figure 2: Demonstrating the delay from DIMAC flow-sensitive waveforms (cerebral arteries) to the PPG pulse (finger). The relative delay between carotid and MCA pulse is the difference between these delays (i.e.  $l'_c - l'_m$ )

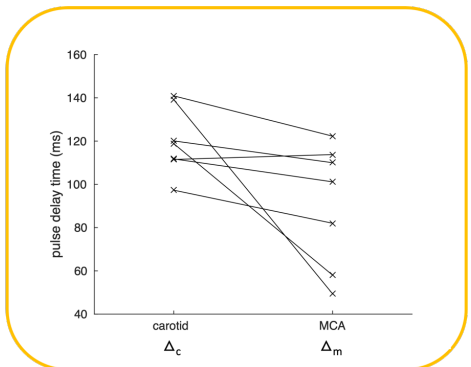


Figure 2: Demonstrating the delay from DIMAC flow-sensitive waveforms (cerebral arteries) to the PPG pulse (finger). The relative delay between carotid and MCA pulse is the difference between these delays (i.e.  $l'_c - l'_m$ )

# Measurement and Modulation of Cerebral ATP flux: A 31P Magnetisation Transfer Magnetic Resonance Spectroscopy study with 670nm photobiomodulation

E.J. Fear<sup>1</sup>, F.H. Torkelsen<sup>2</sup>, E. Zamboni<sup>3</sup>, H. Baseler<sup>4,5</sup> and A.J. Kennerley<sup>6</sup>\*

<sup>1</sup>Department of Biomolecular Sciences, University of Urbino Carlo Bo, 61029 Urbino, Italy; <sup>2</sup>Department of Chemistry, University of York, York, UK, YO10 5DD; <sup>3</sup>School of Psychology, University of Nottingham, Nottingham, UK, NG7 2RD; <sup>4</sup>Hull York Medical School, University of York, York, UK, YO10 5DD. <sup>5</sup>Department of Psychology, Stanford University, Stanford, California 94305, USA. <sup>6</sup>Institute of Sport, Department of Sports & Exercise Sciences, Manchester Metropolitan University, Manchester, UK, M15 6BH.

## Synopsis and/or Summary of Main Findings:

Mitochondrial function declines with age and many pathological processes of neurodegenerative diseases stem from this dysfunction when mitochondria fail to produce the necessary energy required. Photobiomodulation (PBM), long-wavelength light therapy, has been shown to rescue mitochondrial function in animal models and improve human health, but clinical uptake is limited due to uncertainty around efficacy and the mechanisms responsible. Using 31P Magnetisation Transfer Magnetic Resonance Spectroscopy (MT-MRS) we quantify, for the first time, the effects of 670 nm PBM treatment on healthy aging human brains. We find a significant increase in the rate of ATP synthase flux in brain after PBM in a cohort of older adults. Data is supported with theoretical Monte Carlo modelling of light transport to make inferences about treatment strategies to account for skin melanin and cerebrum size.

Our study provides direct evidence of PBM therapeutic efficacy for improving mitochondrial function and restoring ATP flux in age.

## Abstract Body:

Introduction: Mitochondrial function declines with age due to time related oxidative damage, cysteine toxicity, mitochondrial DNA mutations and impaired biogenesis[1,2]. Growing evidence suggests that non-invasive transcranial red/infrared photobiomodulation (PBM) therapy offers neuroprotective metabolic benefits[3]. Here we test the hypothesis that PBM therapy yields an increased rate of mitochondrial ATP production through light absorption by cytochrome-c[4].

## Methods:

Our 5-day longitudinal study implemented 31P MT-MRS measures to quantify cell metabolites (e.g., Pi, PCr & ATP) before (day 1) and after (day 5) PBM treatment (18W, Red Mini 670, Red Light Man Ltd., Manchester, UK) applied above theinion (days 1-4) for 20 minutes (figure 1). A 31P magnetisation transfer FID based pulse sequence, with varying number of 114ms adiabatic RF pulses to selectively saturate gamma-ATP, was implemented on a 3T MAGNETOM Prisma system (Siemens Healthcare, D). Signal saturation of the terminal phosphate ( $\gamma$ ) of ATP, induces a signal decrease in both PCr (due to the creatine kinase equilibrium) and Pi (due to oxidative phosphorylation) – see figure 1. The signal reductions as a function of saturation time can be fitted to estimate flux rates (kf) of ATP production[5]. A dual channel 1H/31P transmit- receive flexible surface coil (Rapid Biomedical, D) was used for RF transmission/detection. 31P spectral data of N = 10 healthy participants (mean age = 68 years; age range = 60-85 years; 6 females) were analysed offline in MATLAB. Data was supplemented by image informed Monte Carlo simulation of light transport (350-1000 nm) through a five-layer tissue model of the human head providing a quantitative estimate of the amount applied PBM light absorbed within the grey matter. The model consisted of optical layers representing skin, skull, cerebrospinal fluid (CSF), grey matter (GM) and white matter (WM) informed with high resolution MRI structural data of the cranium.

## Results:

Following PBM in aging brain we found a significant increase in mitochondrial/oxidative phosphorylation ATP production (kf rate from 0.158 s<sup>-1</sup>, pre-PBM, to 0.252 s<sup>-1</sup>, post PBM - Wilcoxon Signed Ranks test, two-tailed, Z = -2.366, p = 0.016 – figure 1). In contrast there was no significant change in creatine kinase flux before and after PBM treatment (Wilcoxon Signed Ranks test, two-tailed, Z = -0.338, p = 0.813). Light modelling demonstrated a dramatic 2/3 drop in the amount of 670nm photons being absorbed by cytochrome-c in grey matter under skin with high melanin fraction. The drop is less pronounced (1/2 photon count) at the optimum 820 nm peak (figure 2). This has important implications for the future application/treatment design for personalized PBM.

## Conclusion:

31P MT-MRS (with variable saturation time) validated the positive metabolic benefits of PBM in healthy aged individuals (60-85 years). Data validates the metabolic changes underpinning recent research exploring the wider cognitive benefits/changes induced by illumination of the cerebrum with light[6]. The proposed protocol will find benefit in people suffering with neurodegenerative diseases in which mitochondrial function (and hence ATP production) is impaired. PBM presents neuroprotective effects in aging and disease and is a ray of light in the fight against neurodegeneration.

**Acknowledgments / Funding Information:** We thank the staff at the York Neuroimaging Centre for support with 3 T MRI scanning and participant handling. We also thank Dr Alexandra Olaru from Siemens Healthineers for her MR technical support. Theoretical light transport modelling was undertaken on the Viking Cluster, which is a high-performance computing facility provided by the University of York. We are grateful for computational support from the University of York High Performance Computing service, Viking and the Research Computing team. This project was funded by an EPSRC Impact Accelerator Award and Wellcome Trust Centre for Future Health award.

**References:** [1] Balaban RS, et.al. Cell. 2005;120(4):483-495; [2] Ames BN, et.al. Biochimica Et Biophysica Acta-

Molecular Basis of Disease. 1995;1271(1):165-170. [3] Hamblin MR. *Bba Clinical*. 2016;6:113-124. [4] Begum R, et al. *Plos One*. 2013;8(2); [5] Forsen S & Hoffman RA. *Journal of Chemical Physics*. 1963;39(11):2892; [6] Waight JL et al. *Behavior Research Methods*. 2023.

**Figures**

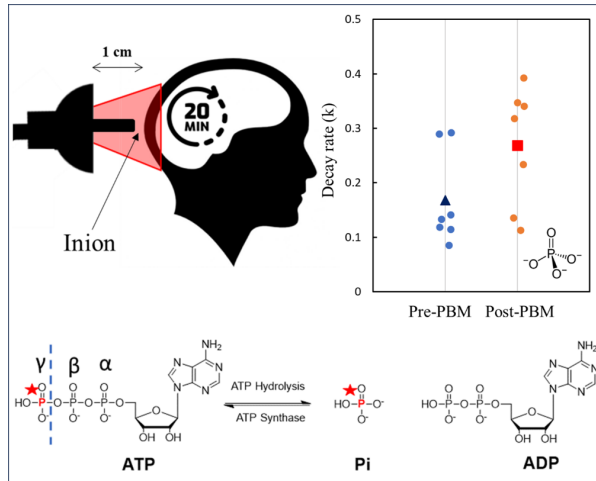


**Figure 1:** We used <sup>31</sup>P Magnetisation Transfer Magnetic Resonance Spectroscopy to quantify a significant increase in cerebral mitochondrial ATP flux (Pi + ADP  $\rightleftharpoons$  ATP) between pre and post photobiomodulation (670nm transcranial illumination for 20 minutes over 4 days).

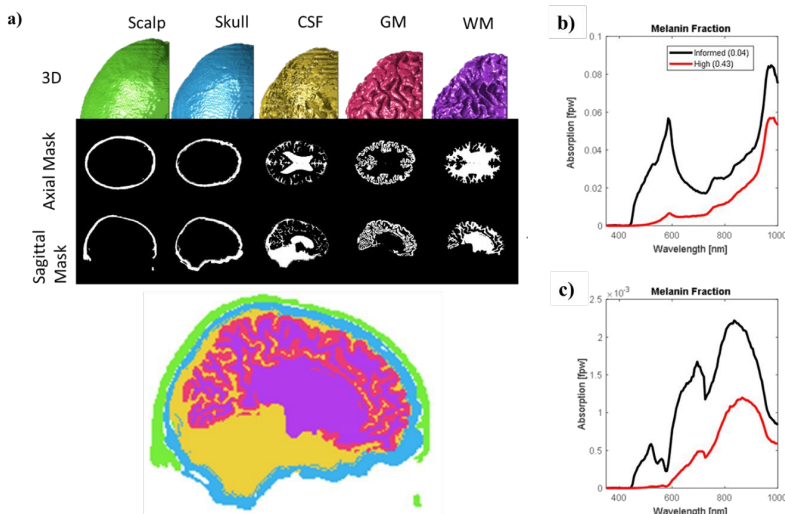


**Figure 2:** Our study was supplemented with light modelling simulations. (a) Layered tissue models were informed using personalised high resolution MRI structural data. Simulations allowed quantification of fraction photon weight (fpw) within each tissue layer. Absorption of light by cytochrome-c in the grey matter is hypothesised to be driving PBM neuroprotective effects. Data show dramatic effects of skin Melanin on the fraction of light reaching (b) the grey matter for absorption by (c) cytochrome-c.

# Longitudinal changes in cerebral metabolic rate of oxygen (CMRO<sub>2</sub>) in cognitively normal older adults

Jiani Wu<sup>1</sup>, Hanzhang Lu<sup>1,2</sup>

**1 Department of Biomedical Engineering, Johns Hopkins University School of Medicine, Baltimore, MD, USA**

**2 The Russell H. Morgan Department of Radiology & Radiological Science, Johns Hopkins University School of Medicine, Baltimore, MD, USA**

## Synopsis and/or Summary of Main Findings

Cerebral metabolic rate of oxygen (CMRO<sub>2</sub>) reflects the amount of O<sub>2</sub> that the brain consumes and represents an indirect index of the brain's aggregated neural activity. CMRO<sub>2</sub> alternations in the aging brain may be complex. On the one hand, compensatory neural activity may result in an elevation in CMRO<sub>2</sub>. On the other hand, neurodegeneration may result in a decrease in CMRO<sub>2</sub>. This present work used TRUST MRI and phase-contrast MRI to measure whole-brain CMRO<sub>2</sub>, and revealed a complex trajectory of CMRO<sub>2</sub> in aging through a longitudinal study in 174 cognitively normal older participants.

## Introduction:

Cerebral metabolic rate of oxygen (CMRO<sub>2</sub>) denotes the amount of O<sub>2</sub> that the brain consumes. Because the brain primarily uses oxidative metabolism to generate ATP, this index is often used as a measure of the brain's energy consumption status. Previous methods of measuring CMRO<sub>2</sub> in humans require the use of three radiotracers along with an arterial line using PET. Thus, CMRO<sub>2</sub> measurement has not been widely available in large cohort studies. With recent advances in MRI, it is now feasible to quantitatively measure CMRO<sub>2</sub> (in  $\mu\text{mol}/100\text{g}/\text{min}$ ) on a standard MRI scanner in less than 5 minutes. This present study reports longitudinal CMRO<sub>2</sub> changes in a group of cognitively normal older adults aged 50 to 89 years old.

## Methods:

Experimental procedure: A total of 174 participants were enrolled. They were part of the BIOCARD cohort that included comprehensive cognitive and clinical assessments, along with MRI, PET, and biofluid sampling. This report only concerns the MRI data. Each participant was scanned on a 3T MRI (Philips) in a longitudinal study design. A total of 424 MRI scans were performed. The number of MRI scans each participant has received ranged from 1 to 4 times. The CMRO<sub>2</sub> measurement method has been detailed previously<sup>1</sup>. Briefly, T<sub>2</sub>-Relaxation-Under-Spin-Tagging (TRUST)<sub>2,3</sub> was used to measure venous oxygenation (Y<sub>v</sub>). Phase-contrast MRI applied on the four feeding arteries was used to measure cerebral blood flow (CBF). CMRO<sub>2</sub> was then estimated from the arterio-venous difference in oxygen content, i.e.,  $\text{CMRO}_2 = \text{CBF} \cdot (\text{Y}_a - \text{Y}_v) \cdot \text{C}$ , where Y<sub>a</sub> is the arterial oxygenation and C is the oxygen-carrying capacity of the blood.

## Data analysis:

The relationship between CMRO<sub>2</sub> and age was studied using a linear mixed-effects model. CMRO<sub>2</sub> was the dependent variable; age at baseline, time since baseline, sex, and education were used as fixed-effect independent variables.

## Results:

Table 1 shows the relationship between CMRO<sub>2</sub> and related independent variables. As can be seen, there was a significant effect of baseline age on CMRO<sub>2</sub> ( $p=0.002$ ). From the fifties to the eighties, there was a general effect of decreasing CMRO<sub>2</sub> cross-sectionally. This observation is consistent with the general notion that neurodegeneration takes place at very advanced age. Longitudinally, there was an increase in CMRO<sub>2</sub> with time ( $p=0.002$ ), suggesting that the brain is using more energy. Note that the longitudinal follow-up time is on the order of 2-6 years, which is much shorter than the cross-sectional age range (~30 years). Therefore, the cross-sectional and longitudinal observation is not necessarily contradictory, because they are reporting CMRO<sub>2</sub> changes at different time spans. We then further examined the slope of the CMRO<sub>2</sub> change (in  $\mu\text{mol}/100\text{g}/\text{min}/\text{year}$ ) and the results are summarized in Table 2. It can be seen that there was an age dependence of the CMRO<sub>2</sub> slope ( $p=0.01$ ). Specifically, older adults less than an age of 75 years old tend to show a time-increase in CMRO<sub>2</sub> whereas those at more advanced age tend to show a time-decrease in CMRO<sub>2</sub> (Figure 1a). To better illustrate this point, the longitudinal change in CMRO<sub>2</sub> of each individual is plotted in Figure 1b.

## Discussion and Conclusion:

The findings from this report suggest that there is a "bell-shaped" curve in CMRO<sub>2</sub> in the aging brain. Older adults generally show an increase in CMRO<sub>2</sub>, which may be reflective of the brain "working harder" to compensate for its lower efficiency. At an advanced age, however, the brain's CMRO<sub>2</sub> tends to decrease which may be related to the brain running out of compensatory capacity and showing signs of neurodegeneration.

**Acknowledgments / Funding Information:** NIH grant R01 NS106702.

## References:

1. Lu H, Xu F, Rodrigue K M, et al. Alterations in cerebral metabolic rate and blood supply across the adult lifespan. *Cerebral cortex*, 2011, 21(6): 1426-1434.
2. Lu H, Ge Y. Quantitative evaluation of oxygenation in venous vessels using T<sub>2</sub>-relaxation-under-spin-tagging MRI. *Magnetic resonance in medicine*, 2008, 60(2): 357-363.
3. Lu H, Xu F, Grgac K, et al. Calibration and validation of TRUST MRI for the estimation of cerebral blood oxygenation. *Magnetic resonance in medicine*, 2012, 67(1): 42-49.

## Figures & Tables

**Table-1:**

Results of Linear Mixed-Effects Model Assessing the Relationship between CMRO<sub>2</sub> and Related Independent Variables

	Coefficient	P-value
(Intercept)	193.29	<0.001
Time since baseline	1.164	0.002
Age at baseline	-0.636	0.002
Sex (male)	-8.069	0.006
Education	0.571	0.386

**Table-2:**

Linear Fitting of the Slope of CMRO<sub>2</sub> Change (in  $\mu\text{mol}/100\text{g}/\text{min}/\text{year}$ ) and the Age at Baseline

	Coefficient	P-value
(Intercept)	18.16	0.005
Age at baseline	-0.240	0.010

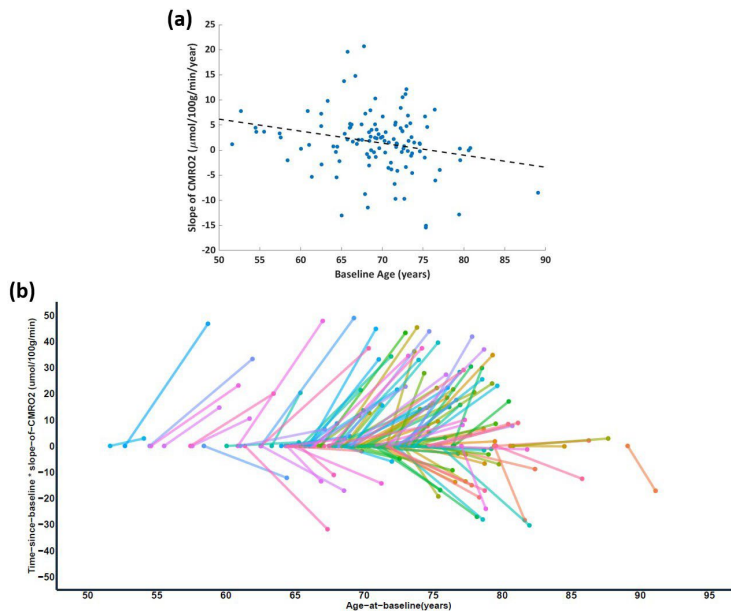


**Figure-1:** (a) Scatter plot between the slope of CMRO<sub>2</sub> change over time and age at baseline (total N=116). The dashed line is a linear fitting of the slope and the baseline age. (b) The longitudinal change in CMRO<sub>2</sub> of each individual. Each line corresponds to a subject and the slope of it is the slope of CMRO<sub>2</sub> change of this subject. If the subject has received more than two MRI scans, only two time points are shown here.

**Table-1:** Results of Linear Mixed-Effects Model Assessing the Relationship between CMRO<sub>2</sub> and Related Independent Variables

**Table-2:** Linear Fitting of the Slope of CMRO<sub>2</sub> Change (in  $\mu\text{mol}/100\text{g}/\text{min}/\text{year}$ ) and the Age at Baseline

**Figure-1:** (a) Scatter plot between the slope of CMRO<sub>2</sub> change over time and age at baseline (total N=116). The dashed line is a linear fitting of the slope and the baseline age. (b) The longitudinal change in CMRO<sub>2</sub> of each individual. Each line corresponds to a subject and the slope of it is the slope of CMRO<sub>2</sub> change of this subject. If the subject has received more than two MRI scans, only two time points are shown here.

# Cerebral blood flow and oxygen extraction fraction responses to conservative and aggressive treatments in adults with sickle cell disease

M.A. Aumann<sup>1</sup>, W. Richerson<sup>1</sup>, J.J. Eisma<sup>1</sup>, A.K. Song<sup>1</sup>, S.L. Waddle<sup>1</sup>, R.S. Jones<sup>1</sup>, M.R. Juttukonda<sup>1</sup>, S. Davis<sup>2</sup>, L. Milner<sup>2</sup>, L.T. Davis<sup>3</sup>, D. Martin<sup>3</sup>, L.C. Jordan<sup>1,2,3</sup>, M.J. Donahue<sup>1,4,5</sup>

<sup>1</sup>Department of Neurology, Vanderbilt University Medical Center, Nashville, TN, USA. <sup>2</sup>Department of Pediatrics, Division of Pediatric Neurology, Vanderbilt University Medical Center, Nashville, TN, USA.

<sup>3</sup>Department of Radiology, Vanderbilt University Medical Center, Nashville, TN, USA. <sup>4</sup>Department of Psychiatry, Vanderbilt University Medical Center, Nashville, TN, USA. <sup>5</sup>Department of Electrical and Computer Engineering, Vanderbilt University, Nashville, TN, USA.

## Synopsis

The overall goal of this work is to use quantitative functional neuroimaging to evaluate the impact of disease-modifying therapies on cerebral hemodynamics in sickle cell disease (SCD) patients across a variety of conservative (hydroxyurea) and more aggressive (red cell exchange transfusion and hematopoietic stem cell transplant, HSCT) treatments. Across all patients (n=44) and treatment groups, cerebral blood flow (CBF) decreased by 4.0 ml/100g/min per g/dl hemoglobin (Hb) increase, whereas oxygen extraction fraction (OEF) decreased by 1.78% per g/dl Hb increase. The largest changes were observed in HSCT patients, whereby a Hb increase from 8.91±1.89 g/dl to 12.93±2.7g/dl (p<0.001) paralleled a significant decrease in CBF from 68.16±20.2 to 47.4±12.2 ml/100g/min (p<0.001). These changes provide a framework for powering pharmacological studies that desire to use quantitative OEF or CBF as outcome measures to evaluate the impact of Hb modification on brain function.

## Introduction

Sickle cell disease (SCD) is a chronic hemolytic anemia resulting in hemoglobin-S (HbS) production, hemolysis and associated anemia, and elevated lifelong stroke risk. Standard-of-care in many patients without cerebral infarcts is oral hydroxyurea, which is myelosuppressive and increases fetal hemoglobin (HbF). Patients may also receive monthly blood transfusions which increase total Hb by 1-2 g/dl on average, or, in high-risk patients, hematopoietic stem cell transplantation (HSCT), which is a curative therapy following successful engraftment. Altered brain oxygen extraction fraction (OEF) 1–3 and cerebral blood flow (CBF) 4–8 have been identified as possible biomarkers for treatment selection; if so, these parameters should respond to treatments that aim to normalize hemodynamic impairment. The purpose of this study was to use quantitative MRI methods to assess how CBF and OEF change in response to SCD treatments across a spectrum of treatment-induced Hb changes.

## Methods

Adult participants (n=44) with SCD (Hb phenotype: HbSS or HbSC) and without (n=13) SCD (Hb phenotype: HbAA), were scanned at 3T at two time points (Table 1). Total Hb and HbS% were measured via venipuncture and arterial oxygen saturation (Ya) via pulse oximetry. A standard non-contrast head MRI was completed with 2D pseudo-continuous ASL (label delay=1900 ms; spatial resolution=3x3x7 mm<sup>3</sup>), and TRUST (TR/TE=1978/3.6 ms; spatial resolution=3.4x3.4x5 mm<sup>3</sup>; □CPMG=10ms; eTE=0, 40, 80, and 160ms) for anatomical, CBF, and OEF, respectively. Total gray matter CBF was quantified after accounting for effects of Hb on blood T 5 and OEF was calculated from TRUST upon pair-wise subtraction of data and quantification of venous blood water R2 and subsequently venous oxygen saturation using human calibration models calculated over a normal and anemic Hb range 1,9. Hemodynamic and metabolic measures were pair-wise compared within each cohort using a paired Student's t-test (significance: two-sided p<0.05) and regression applied to evaluate the dependence of change in OEF and CBF on Hb change.

## Results

In SCD patients receiving hydroxyurea, neither Hb (p=0.41), CBF (p=0.43), nor OEF (p>0.99) changed between time 1 (Hb=8.9±1.2 g/dl) and time 2 (Hb=9.00±1.76 g/dl) (Fig. 1). In patients receiving blood transfusions, Hb increased from 8.20±1.35 g/dl to 9.26±1.39 g/dl pre- vs. post-transfusion (p<0.001), which paralleled a CBF decrease of 14.2 ml/100g/min (p=0.003) (Fig. 2). OEF did not change significantly after transfusion (pre: 43.56%; post: 40.21%; p=0.32). In HSCT patients, a significant Hb increase from 8.91±1.89 g/dl to 12.93±2.7g/dl (p<0.001) pre- vs. post-transplant was observed, which paralleled significant CBF decreases from 68.16±20.2 to 47.4±12.2 ml/100g/min (p<0.001). OEF did not change significantly after HSCT (pre: 43.71%; post: 39.72%; p=0.38). Fig. 2 shows the change in CBF and OEF related to treatment-induced increases in Hb across all participants: CBF decreased by 4.0 ml/100g/min per g/dl increase in Hb, whereas OEF decreased by 1.78 per g/dl increase in Hb. OEF trends were largely preserved across calibration models used, although significance criteria differed.

## Discussion and Conclusion

Findings support that CBF and OEF are more dynamic following transfusion and transplant therapies than in patients on hydroxy urea; quantitative relationships between these parameters should provide a framework for motivating these measures as endpoints in emerging SCD therapy trials.

## References

1. Jordan LC, Gindville MC, Scott AO, et al. Non-invasive imaging of oxygen extraction fraction in adults with sickle cell anaemia. *Brain*. 2016;139(3):738-750. doi:10.1093/brain/aww397
2. Ford AL, Ragan DK, Fellah S, et al. Silent infarcts in sickle cell disease occur in the border zone region and are associated with low cerebral blood flow. *Blood*. 2018;132(16):1714-1723. doi:10.1182/blood-2018-04-841247

3. Vaclavu L, Petersen ET, VanBavel ET, Majoie CB, Nederveen AJ, Biemond BJ. Reduced Cerebral Metabolic Rate of Oxygen in Adults with Sickle Cell Disease. *Blood*. 2018;132(Supplement 1):11-11. doi:10.1182/blood-2018-99-116194
4. Buxton RB, Frank LR, Wong EC, Siewert B, Warach S, Edelman RR. A general kinetic model for quantitative perfusion imaging with arterial spin labeling. *Magn Reson Med*. 1998;40(3):383-396. doi:10.1002/mrm.1910400308
5. Juttukonda MR, Jordan LC, Gindville MC, et al. Cerebral hemodynamics and pseudo-continuous arterial spin labeling considerations in adults with sickle cell anemia. *NMR Biomed*. 2017;30(2):e3681. doi:10.1002/nbm.3681
6. Watchmaker JM, Juttukonda MR, Davis LT, et al. Hemodynamic mechanisms underlying elevated oxygen extraction fraction (OEF) in moyamoya and sickle cell anemia patients. *J Cereb Blood Flow Metab*. 2018;38(9):1618-1630. doi:10.1177/0271678X16682509
7. Lu H, Ge Y. Quantitative evaluation of oxygenation in venous vessels using T2-Relaxation-Under-Spin-Tagging MRI. *Magn Reson Med*. 2008;60(2):357-363. doi:10.1002/mrm.21627
8. Bush A, Borzage M, Detterich J, et al. Empirical model of human blood transverse relaxation at 3 T improves MRI T 2 oximetry. *Magn Reson Med*. 2017;77(6):2364-2371. doi:10.1002/mrm.26311
9. Juttukonda MR, Donahue MJ, Waddle SL, et al. Reduced oxygen extraction efficiency in sickle cell anemia patients with evidence of cerebral capillary shunting. *J Cereb Blood Flow Metab*. 2021;41(3):546-560. doi:10.1177/0271678X20913123

## Figures and Tables

**Table 1. Patient demographics and cerebrovascular profiles**

	N	Age (years)	Sex	Hemoglobin 1 (g/dl)	Hemoglobin 2 (g/dl)	Gray Matter CBF 1 (ml/100g/min)	Gray Matter CBF 2 (ml/100g/min)	OEF 1 (%)	OEF 2 (%)
Control	13	33.5 ± 12.2	6M/7F	13.7 <sup>#</sup>	13.7 <sup>#</sup>	61.5 ± 12.7	65.8 ± 9.6	36.4 ± 4.4	44.1 ± 5.1
Hydroxyurea	10	24.7 ± 5.2	4M/6F	8.9 ± 1.2	9.0 ± 1.8	89.4 ± 12.1	94.0 ± 20.1	40.5 ± 5.2	40.7 ± 9.5
Transfusion	19	26.5 ± 6.2	8M/11F	8.2 ± 1.4	9.3 ± 1.4	86.6 ± 18.1	72.4 ± 19.3	43.6 ± 7.5	40.2 ± 6.5
Transplant	15	31.4 ± 8.7	6M/9F	8.9 ± 1.9	12.9 ± 2.7	68.2 ± 20.2	47.4 ± 12.2	43.7 ± 8.6	39.7 ± 7.8

*CBF = cerebral blood flow; OEF = oxygen extraction fraction. Data shown are the mean ± standard deviation unless otherwise noted. <sup>#</sup> Mean Hb in healthy control participants was assumed and not measured.*

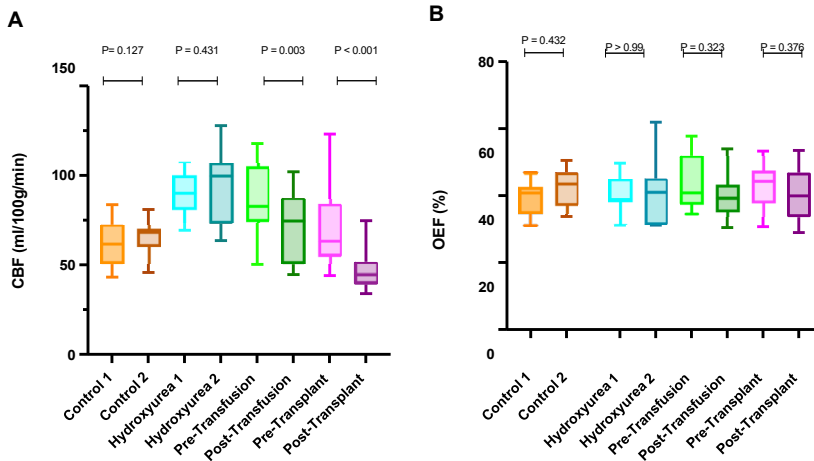


**Figure 1.** Box and whisker plots showing group changes from scan 1 to scan 2 of cerebral blood flow (CBF) (A), and oxygen extraction fraction percentage (OEF) (B).

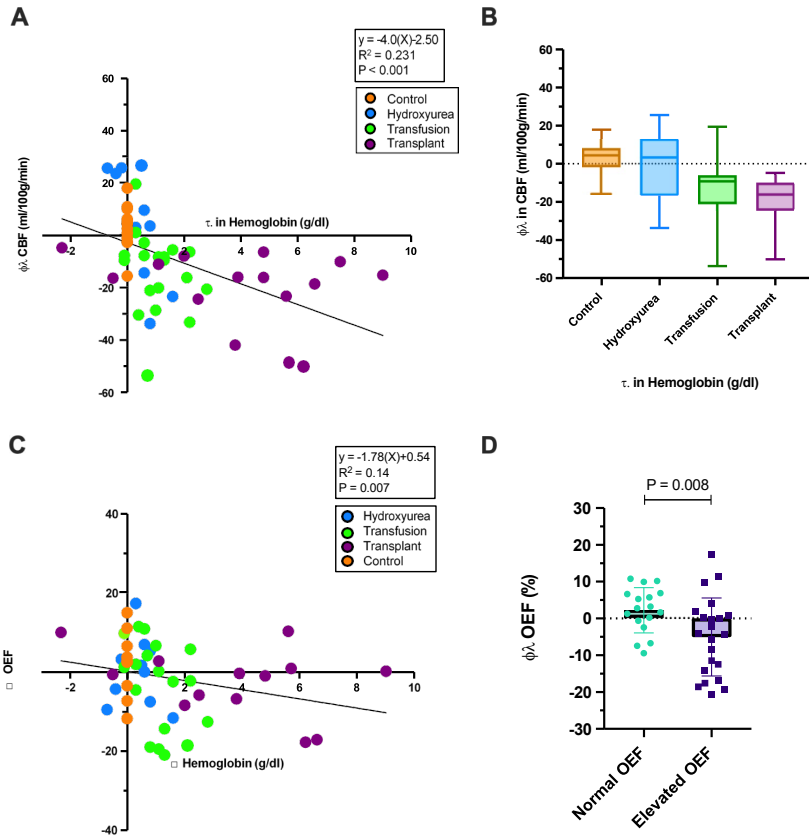


**Figure 2.** Regression showing the relationship between the change in hemoglobin and change in CBF (A) as well as change in OEF (B) across all subjects, with the average and standard deviation of each group's change in hemoglobin shown as a function of their change in CBF (B). Panel D shows a box and whisker plot depicting the change in OEF across subjects dichotomized into those with OEF within one standard deviation of commonly accepted normal ranges (e.g., OEF < 42%) or elevated at baseline (OEF > 42%).

# Novel identifications of cerebral hemodynamics in BOLD fMRI associated with fetal hemoglobin in patients with sickle cell disease

B. Kish<sup>1</sup>, J. Yao<sup>1</sup>, A. Frels<sup>1</sup>, N. Grom<sup>1</sup>, V. Vijayakrishnan Nair<sup>1</sup>, A. O'Brien<sup>2</sup>, Y. Wang<sup>2,3</sup> and Y. Tong<sup>1\*</sup>

<sup>1</sup>Weldon School of Biomedical Engineering, Purdue University, West Lafayette, IN

<sup>2</sup>Division of Hematology/Oncology, Indiana University School of Medicine, Indianapolis, IN

<sup>3</sup>Department of Anesthesia, Stark Neurosciences Research Institute, Indiana University School of Medicine, Indianapolis, IN

**Synopsis and/or Summary of Main Findings:** In this study, we aimed to investigate the hemodynamic mechanisms of sickle cell disease (SCD) through fMRI and their relationship with hematological parameters and pain, a common characteristic of SCD. Systemic low-frequency oscillations (0.01-0.1 Hz) in the BOLD signal were used to identify the maximum cross-correlation coefficient (MCCC) and delay between the average signals from the whole brain and the superior sagittal sinus. Uniquely, some SCD patients showed a negative correlation, a phenomenon only known to occur when correlating between BOLD signals falling above and below 86% oxygenation. Thus, we propose a model in which the average oxygenation in the brain falls above this threshold in some patients with SCD. Additionally, measures of MCCC and delay were positively correlated with levels of hemoglobin and hematocrit and negatively correlated with the level of hemoglobin S. Combined, these factors show promise in the development of non-invasive hemodynamic biomarkers for SCD severity.

**Abstract Body:** Sickle cell disease (SCD) is a genetic blood disorder caused by a mutation in the beta-globin gene, leading to the production of abnormal hemoglobin known as hemoglobin S [1,2]. This abnormal hemoglobin easily forms long, rigid chains, causing the formation of sickled erythrocytes which are prone to destruction, resulting in a reduced oxygen-carrying capacity of the blood. Consequently, SCD patients often have low hematocrit levels and decreased oxygen affinity in their blood. To maintain proper oxygen delivery to the brain at rest, the body compensates by increasing cerebral blood flow [3,4,5]. This can result in cerebral vascular shunting, in which cerebral blood velocity is increased to the point at which oxygen off-loading efficiency is reduced in the capillary bed. Chronic hypoxia due to vaso-occlusive events and vascular shunting can lead to cerebral vascular remodeling and cerebral vascular disease, which can further impair cerebral blood flow and oxygen delivery [6].

In this study, we aimed to investigate the hemodynamic mechanisms of SCD through functional magnetic resonance imaging and their relationship with hematological parameters and pain, a common characteristic of the disease. It was hypothesized that BOLD-fMRI signals in SCD patients will exhibit different hemodynamic features that are related to disease severity and pain in SCD. Systemic low-frequency oscillations (sLFO) (0.01-0.1 Hz) in the BOLD signal were used to identify the maximum cross-correlation coefficient (MCCC) and delay between the average signal from the whole brain (GMean) and the superior sagittal sinus (SSS).

Most control subjects, except for one individual, exhibited high positive MCCC values with negative delay times (MCCC:  $0.735 \pm 0.516$ , Delay:  $-2.014 \pm 2.310$  sec), indicating that the GMean-sLFO led the averaged SSS-sLFO. In contrast, 8 out of 15 SCD patients exhibited a similar pattern as the control subjects (MCCC:  $0.8 \pm 0.124$ , Delay:  $-3.225 \pm 1.552$  sec), while the remaining 7 SCD patients showed a negative MCCC value between the averaged SSS-sLFO and the GMean-sLFO, accompanied by positive delay times (MCCC:  $-0.748 \pm 0.105$ , Delay:  $3.708 \pm 0.710$  sec), suggesting that the SSS-sLFO led (Figure 1). This negative correlation is a phenomenon only known to occur when correlating between BOLD signals falling above and one below 86% oxygenation [7]. Additionally, measures of MCCC and delay were positively correlated with levels of hemoglobin and hematocrit and negatively correlated with the level of hemoglobin S (Figure 1, 2). Thus, we propose a model in which the average oxygenation in the brain falls above the 86% threshold in some patients with SCD (Figure 3). The model is based on two assumptions: 1) lower hemoglobin and high hemoglobin S lead to faster blood flow (shunting) and a wider affected region, resulting in higher oxygen saturation in more voxels of the brain; 2) The sign of the fMRI signal of a voxel depends on its oxygen saturation. Our results demonstrate a correlation between fMRI findings and important hematologic parameters and show promise as a potential novel marker of SCD severity which would be of tremendous value for therapeutic decisions.

**Acknowledgments / Funding Information:** This work was supported by NIH K99/R00 award (Grant # 4R00AT010012) and Indiana University Health – Indiana University School of Medicine Strategic Research Initiative funding to Y.W.

## References:

- [1] Arkuszewski, M., Krejza, J., Chen, R., & Melhem, E. R. (2013). Sickle Cell Anemia: Reference Values of Cerebral Blood Flow Determined by Continuous Arterial Spin Labeling MRI. *The Neuroradiology Journal*, 26(2), 191–200. <https://doi.org/10.1177/197140091302600209>
- [2] DeBaun, M. R., Derdeyn, C. P., & McKinstry, R. C. (2006). Etiology of strokes in children with sickle cell anemia. *Mental Retardation and Developmental Disabilities Research Reviews*, 12(3), 192–199. <https://doi.org/10.1002/mrdd.20118>
- [3] Jordan, L. C., DeBaun, M. R., & Donahue, M. J. (2021). Advances in neuroimaging to improve care in sickle cell disease. *The Lancet Neurology*, 20(5), 398–408. [https://doi.org/10.1016/S1474-4422\(20\)30490-7](https://doi.org/10.1016/S1474-4422(20)30490-7)
- [4] Juttukonda, M. R., Jordan, L. C., Gindville, M. C., Davis, L. T., Watchmaker, J. M., Pruthi, S., & Donahue, M. J. (2017). Cerebral hemodynamics and pseudo-continuous arterial spin labeling considerations in adults with sickle cell

anemia. *NMR in Biomedicine*, 30(2), e3681. <https://doi.org/10.1002/nbm.3681>

[5] Kassim, A. A., & DeBaun, M. R. (2013). Sickle Cell Disease, Vasculopathy, and Therapeutics. *Annual Review of Medicine*, 64(1), 451–466. <https://doi.org/10.1146/annurev-med-120611-143127>

[6] Halder, S. K., & Milner, R. (2021). The impact of chronic mild hypoxia on cerebrovascular remodelling; uncoupling of angiogenesis and vascular breakdown. *Fluids and Barriers of the CNS*, 18(1), 1–15. <https://doi.org/10.1186/S12987-021-00284-X/FIGURES/8>

[7] Tong, Y., Yao, J. (Fiona), Chen, J. J., & Frederick, B. de B. (2019). The resting-state fMRI arterial signal predicts differential blood transit time through the brain. *Journal of Cerebral Blood Flow and Metabolism : Official Journal of the International Society of Cerebral Blood Flow and Metabolism*, 39(6), 1148–1160. <https://doi.org/10.1177/0271678X17753329>

Figures and tables

### Blood Measurements vs. MCCC in SCD Patients

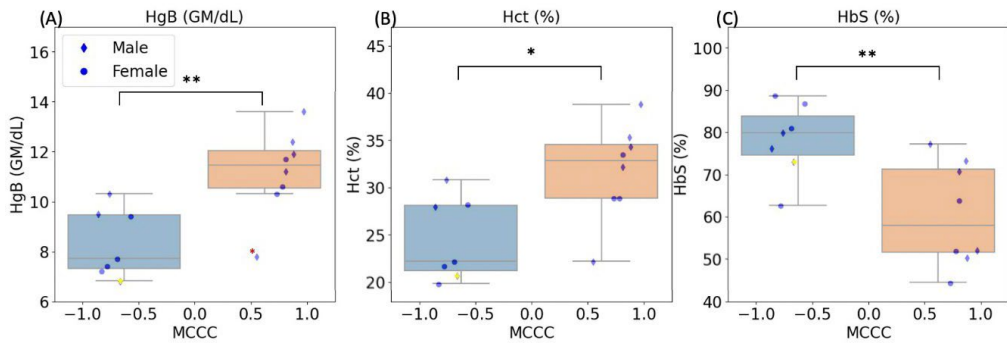


**Figure 1:** Blood measurements (A) HgB, (B) Hct, and (C) HbS (%) and MCCC values for all SCD subjects. SCD patients with negative MCCC values are shown to have significantly lower HgB and Hct values and significantly higher HbS values than those with positive MCCC values. (Female: circles; Male: diamonds; Outliers: red asterisk).

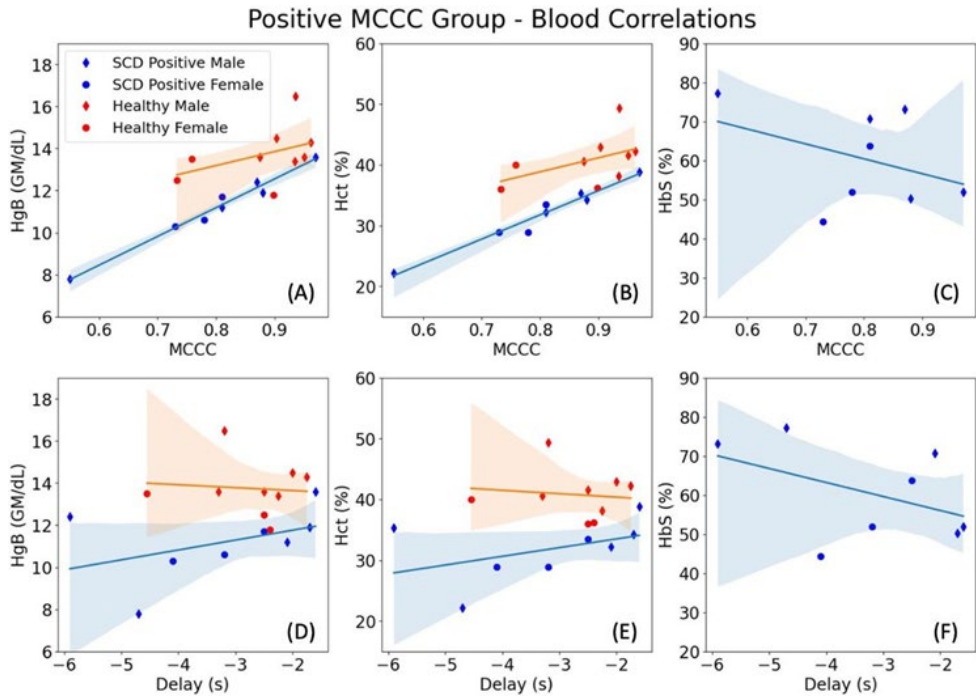


**Figure 2:** Correlations between blood measurements (A, D) HgB, (B, E) Hct, and (C, F) HbS and MCCC and delay values for unaffected (red) and SCD (blue) subjects. Only subjects with positive MCCC values are shown. The percentage of HgB and Hct exhibit high correlation with MCCC values in SCD with a p-value less than 0.05. HbS shows a moderate correlation with MCCC values and delay times as well.

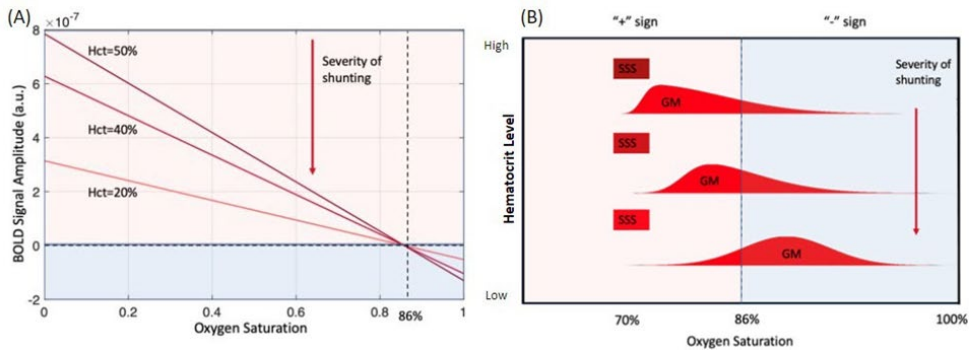


**Figure 3:** fMRI model for oxygen saturation in BOLD signal. A) BOLD amplitude versus percentage of  $SO_2$ . The relationship at different levels of hematocrit percentages is plotted. 86%  $SO_2$  produces negative amplitudes, but lower levels of hematocrit demonstrate weakened signals at all oxygen levels. B) Estimated voxel distribution of  $SO_2$  for different Hct %. Lower Hct % will lead to more voxels having higher  $SO_2$  values, thus leading to an eventual flipped sign (-) of the GMean.

# Mapping cerebrovascular reactivity and vascular lag in gliomas with multi-echo BOLD fMRI and breath-holding.

Cristina Comella<sup>1</sup>, Ileana Quiñones<sup>2</sup>, Santiago Gil Robles<sup>3,4</sup>, Iñigo Pomposo<sup>4</sup>, Manuel Carreiras<sup>1,2,3</sup>, César Caballero-Gaudes<sup>1</sup>

<sup>1</sup>Basque Center on Cognition, Brain and Language (BCBL); San Sebastian, Spain; <sup>2</sup>Universidad del País Vasco (UPV/EHU); San Sebastian, Spain; <sup>3</sup>Ikerbasque, Basque Foundation for Science; Bilbao, Spain; <sup>4</sup>BioCruces Research Institute, Bilbao, Spain; <sup>5</sup>Hospital Quiron, Madrid, Spain

**Synopsis and/or Summary of Main Findings:** 150 words.

This study explores the potential of multi-echo (ME) BOLD fMRI for mapping cerebrovascular reactivity (CVR) and vascular lag with an induced breath-holding (BH) task in glioma patients. Obtaining these maps with a simple BH task can offer valuable insights in patients into neurovascular alterations in tumour-affected regions, making this approach more accessible clinically. However, motion and susceptibility artefacts due to BH can substantially diminish the quality of MR images, hence reducing the accuracy and reliability of CVR mapping. By employing optimized ME-fMRI procedures in 16 patients with diverse glioma characteristics, including nuisance modelling with ME-Independent Component Analysis and lagged regression analysis, we observed a decrease in the CVR and an informative vascular lag in most subjects. These maps provided clinically valuable information on tumour and peritumoral areas, delimitating the functional boundaries of the lesion, which could help during the neurosurgical planning to maximize the extent of resection.

## Abstract Body:

**Introduction:** Cerebrovascular reactivity (CVR) measures the brain's ability to regulate blood flow in response to changes in arterial CO<sub>2</sub> levels [1]. A breath-holding (BH) task is a straightforward and self-induced manner to induce a vasoactive stimulus (i.e. vasodilation)[2]. BH-induced CVR has provided clinically relevant information in patients with glioma to assess neurovascular uncoupling or delimit regions affected by the tumour [3][4]. However, BH tasks might severely compromise data quality due to movement and susceptibility artefacts. These challenges can be addressed by means of multi-echo (ME) fMRI pre-processing and denoising approaches [5]. This study investigates the advantages of ME-fMRI data collection during a BH task to obtain accurate and reliable CVR and vascular lag maps for glioma patients. Vascular lag modelling can provide clinically relevant information about the vascular transit delay and variations in vasodilatory dynamics instigated by glioma.

**Methods:** Patients: Sixteen subjects (28-69 y.o.; 9 Female & 7 Male) with varying glioma characteristics (6 Astrocytoma, 4 Glioblastoma, 3 Oligodendroglioma, 1 Pleomorphic Xanthoastrocytoma, 1 Polymorphous neuroepithelial, 1 Cavernoma) were scanned at. MRI data acquisition (3T Siemens PrismaFit, 64-channel coil): T1-w MPRAGE (pre- and post-Gd injection), T2-w FLAIR images (voxel size=1 mm<sup>3</sup>), and ME-fMRI data during a BH task [5] [6] with T2\*-weighted gradient-echo multi-echo sequence (TEs=10.6/28.69/46.78/84.87 ms, TR= 1.5 s, 2.4 mm isotropic voxels, SMS=5, GRAPPA=2, 340 scans). Exhaled CO<sub>2</sub> and O<sub>2</sub> levels were recorded using a nasal cannula with an ADInstruments ML206 gas analyser (sampling frequency = 40 Hz). End-tidal CO<sub>2</sub> peaks were manually identified using Peakdet [7] and linearly interpolated to obtain the PetCO<sub>2</sub> signal. ME-fMRI data preprocessing (AFNI): Motion realignment of the 1st echo to a single-band reference image and apply this transformation to the rest of echoes. ME-ICA denoising with TEDANA [8] and manual evaluation of BOLD-related and noise-related components with RICA [9]. Data analysis: CVR and vascular lag maps were obtained with a conservative lagged regression analysis [6] using phys2cvr [10], considering a lagged PetCO<sub>2</sub> signal convolved with the canonical HRF (lag shifts=0.3s), the realignment parameters and their temporal derivatives, up to 4th-order Legendre polynomials, and the orthogonalized rejected ME-ICA time courses [6]. The bulk shift to compensate for the delay of the expired air between the brain and the gas analyser was estimated via cross-correlation between the PetCO<sub>2</sub>hrf signal and the average signal of non-tumor voxels.

**Results & Discussion:** Table 1 describes the study sample, showcasing the results of the CVR and vascular delay maps. Three patients were excluded due to poor task performance. All remaining thirteen subjects displayed significantly reduced CVR within glioma-affected regions. Notably, nine of them also exhibited increased vascular lag in both glioma-affected and peritumoral areas, mainly in high-grade tumours. However, the vascular delay maps in three subjects offered little information on tumour-affected areas. Figures 1 and 2 showcase four representative cases, illustrating different glioma types and performance task levels. In summary, employing ME-fMRI during a feasible BH task yields clinically informative CVR and vascular delay maps providing a good task performance, which can improve individualized diagnosis among glioma patients.

**Acknowledgments / Funding Information:** This study was supported by the Spanish Ministry of Economy and Competitiveness (Ramon y Cajal Fellowship, RYC-2017-21845), the Spanish State Research Agency (BCBL "Severo Ochoa" excellence accreditation CEX2020-001010/AEI/10.13039/501100011033) and the Basque Government (BERC 2022-2025 and Programa Investigo).

## Reference:

1. Chen J., & Fierstra J. (Eds.) (2022). Cerebrovascular Reactivity Methodological Advances and Clinical Applications. Humana Press.
2. Pinto J, et al, (2020). Front Physiol, 11: 608475. <https://doi.org/10.3389/fphys.2020.608475>
3. Iranmahboob, A., et al, (2015) J Neuroimaging 26(2): 232-239. <https://doi.org/10.1111/jon.12278>
4. Pillai J., & Mikulis, D.J., 2015 AJNR Am J Neuroradiol. 36(1):7-13. <https://doi.org/10.3174/ajnr.A3941>

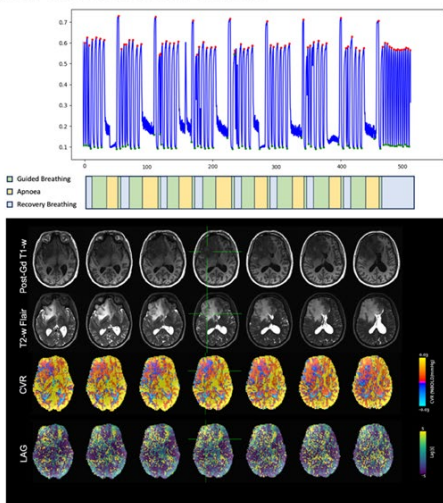
5. Moia S, et al, (2021) NeuroImage, 233, 117914. <https://doi.org/10.1016/j.neuroimage.2021.117914>
6. Bright, M. G. & Murphy, K. (2013). Neuroimage, 83, 559-568. <https://doi.org/10.1016/j.neuroimage.2013.07.007>
7. Markello, R & DuPre, E. (2018). Peakdet [Computer software]. <https://doi.org/10.5281/zenodo.7244954>
8. DuPre, E., et al. (2021) Journal of Open Source Software, 6(66), 3669. <https://doi.org/10.5281/zenodo.7244954>
9. Uruñuela, E. (2021). Rica (Version v1.0.17) [Computer software]. <https://doi.org/10.5281/zenodo.5788350>
10. Moia, S (2023). Phys2cvr (Version v.0.18.0) [Computer software]. <https://doi.org/10.5281/zenodo.6461353>

## Figures and tables

Patient Number	Type Glioma	Grade	Age	Sex	Task Performance	CVR	Lag
053	Polymorphous neuroepithelial	I	35	M	Good	Decrease	Informative
052	Pleomorphic Xanthoastrocytoma	II	38	F	Good	Decrease	Informative
046	Oligodendroglioma	II	42	F	Medium	Decrease	Non-Informative
058	Oligodendroglioma	II	42	F	Good	Decrease	Informative
062	Oligodendroglioma	II	43	M	Good	Decrease	LiQle-Informa#ve
054	Astrocytoma	II	28	F	Good	Decrease	Informative
059	Astrocytoma	II	32	F	Good	Decrease	Informative
060	Asytocytoma	II	42	M	Good	Decrease	LiQle-Informative
061	Astrocytoma	II	47	M	Good	Decrease	LiQle-Informative
064	Astrocytoma	III	35	F	Good	Decrease	Informative
050	Glioblastoma	IV	45	M	Good	Decrease	Informative
056	Glioblastoma	IV	68	M	Good	Decrease	Informative
057	Glioblastoma	IV	47	F	Good	Decrease	Informative
051	Glioblastoma	IV	69	F	Bad		
063	Astrocytoma	III	49	F	Bad		
066	Cavernoma		71	M	Bad		

**Table 1:** Dataset study information categorized by patient characteristics (age and sex), glioma type and grade, subject task performance, and CVR and vascular lag map outcomes. Green: Patients showing a decrease in CVR maps and informative vascular lag maps. Blue: Patients showing a decrease in CVR maps but less informative vascular lag maps. Yellow: Subjects with medium task performance. Red: Patients with poor task performance (excluded from further analyses).

**A) Sub-064: Astrocytoma Grade III**



**B) Sub-056: Glioblastoma Grade IV**

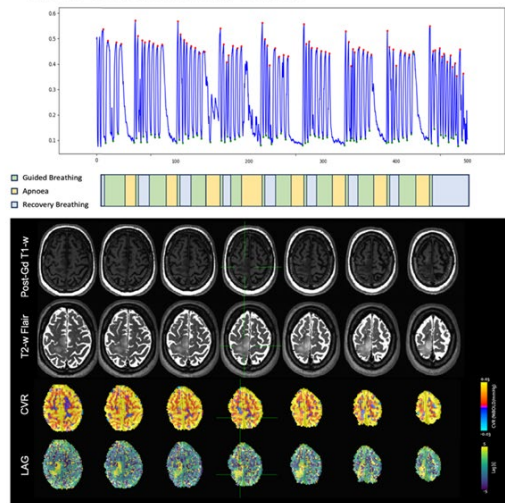
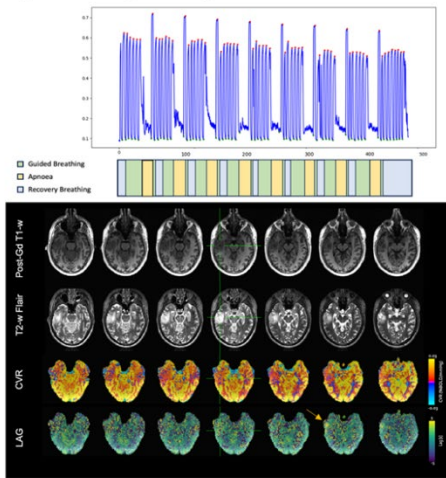


**Figure 1:** Two patients with good task performance: a) Astrocytoma Grade III, and b) Glioblastoma Grade IV. The CO2 traces (top) show that subjects performed the eight BH trials of the task properly (middle). Subject 064 (a) showed reduced CVR in tumoral areas and increased vascular lag in tumoral and peritumoral areas. Subject 056 (b) showed a smaller reduction of CVR in tumoral area, but a notable increase of the vascular lag in tumoral and peritumoral areas.

A) Sub-062: Oligodendrolioma Grade III



B) Sub-046: Oligodendrolioma Grade II

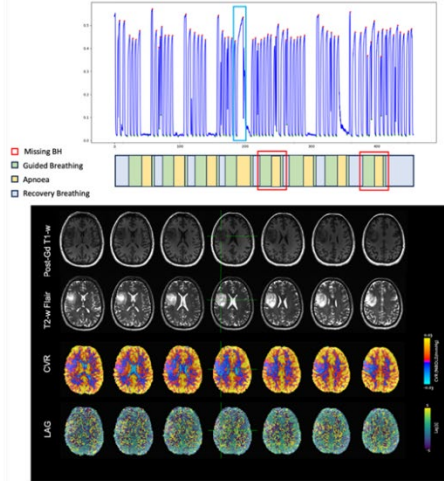


**Figure 2:** Two patients with Oligodendrolioma with: a) medium task performance, and b) good task performance. The CO<sub>2</sub> traces of subject 062 (a) performed the eight BH trials of the task properly; however subject 046 (b) inspired, instead of expired, before the 4<sup>th</sup> apnoea, and missed the 5<sup>th</sup> and 8<sup>th</sup> apnoea's (see boxes in panels). Both subjects show reduced CVR in the tumoral area, yet their vascular lag map offers no valuable information about the tumour.

# Cerebrovascular reactivity response time as revealed by time regression analysis is uniquely correlated to recent stroke symptomatology in moyamoya patients

Caleb Han<sup>1</sup>, Wesley T. Richerson<sup>1</sup>, Maria Garza<sup>1</sup>, L. Taylor Davis<sup>2</sup>, Matthew Fusco<sup>3</sup>, Rohan Chitale<sup>3</sup>, Murlu Mishra<sup>1</sup>, Lori C. Jordan<sup>4</sup>, Manus J. Donahue<sup>1</sup>

<sup>1</sup>Department of Neurology, Vanderbilt University Medical Center, Nashville, TN, USA; <sup>2</sup>Department of Radiology and Radiological Sciences, Vanderbilt University Medical Center, Nashville, TN, USA; <sup>3</sup>Department of Neurosurgery, Vanderbilt University Medical Center, Nashville, TN, USA <sup>4</sup>Department of Pediatrics, Vanderbilt University Medical Center, Nashville, TN, USA

## Synopsis

This work applies hypercapnic respiratory stimuli in a clinical radiology unit, in sequence with time-regression analyses, to understand how recent ischemic symptoms alter hemodynamic reactivity metrics in patients (n=73) with moyamoya vasculopathy. Reactivity delay times in the flow territory of ischemic symptoms were found to be lengthened in patients with vs. without ischemic symptoms in the prior six months (p<0.001). After accounting for response timing, maximum vasodilatory response to hypercapnia was observed to be related to recent ischemic symptoms (p=0.037) but this finding did not meet significance criteria following multiple comparisons correction. Findings are consistent with cerebrovascular reactivity timing profiles being potentially more sensitive to acute or early chronic ischemic symptomatology compared to the magnitude of the vasodilatory response itself. Exemplar reactivity values in non-symptomatic hemispheres are provided, and the use of these metrics as an exemplar to enable personalized, diagnostic reactivity assessments is discussed.

## Introduction:

Moyamoya disease (MMD) is a cerebrovascular condition characterized by non-atherosclerotic steno-occlusion of the intracranial carotid artery (ICA) and its proximal branches, corresponding to a high risk of new or recurrent stroke<sup>1</sup>. Impairment is assessed using anatomical MRI and catheter angiography<sup>2</sup>, however, these methods lack information on parenchymal impairment and are often complemented with parenchymal measures of cerebrovascular reserve capacity. For reactivity assessments to be accepted as biomarkers of treatment response or stroke risk, the relationship between these measures and ischemic symptomatology must be established. Here, we test the hypothesis that hypercapnia-induced cerebrovascular reactivity (CVR) and CVR response times, assessed from novel time-regression analyses<sup>3,4</sup> correlate with recent ischemic symptoms derived from the same flow territory.

## Methods:

Participants (n=73) with a diagnosis of moyamoya vasculopathy from clinically-indicated catheter angiography<sup>1</sup> and neurological assessment provided informed consent and underwent non-contrast anatomical MRI (T1-weighted, T2-weighted FLAIR, and DWI), in sequence with hypercapnic blood oxygenation level-dependent (BOLD; TE=35 ms; spatial resolution=3.5x3.5x3.5 mm, TR=2000 ms) <sup>5</sup>. A paradigm comprising two blocks of 180s hypercapnic hyperoxic gas (5% CO<sub>2</sub>/95% O<sub>2</sub>) interleaved with 180s normocapnic normoxic gas (21% O<sub>2</sub>/79% N<sub>2</sub>) was administered. Time regression exploited the hyperoxic balance as a diffusible tracer to quantify timing-uncorrected cerebrovascular reactivity (CVRRAW), maximum cerebrovascular reactivity (CVRMAX), and reactivity delay time (CVRDELAY)<sup>4</sup>. CVRRAW and CVRMAX were normalized by the end-tidal CO<sub>2</sub> change. Cortical masks were derived from middle cerebral artery (MCA) flow territory map and dichotomized along the midline to calculate each hemisphere's reactivity metrics separately. A board-certified neurologist organized symptomatology information for each hemisphere into symptomatic (ischemic symptoms within six-months) or asymptomatic (no history of ischemic symptoms). A logistic regression analysis with robust standard errors based on Huber-White sandwich estimator compared the CVR metrics between cohorts. Exemplar summary statistics as a function of age were also recorded. Significance criterion: Bonferroni-corrected two-sided p<0.05.

## Results:

Table 1 summarizes participant demographics and logistic regression analysis. Fig. 1 shows violin plots comparing each of the reactivity statistics between cohorts. The symptomatic hemispheres display significantly reduced cortical CVRRAW (p=0.007) and lengthened CVRDELAY (p<0.001); no differences were observed in the CVRMAX after controlling for multiple comparisons (p=0.037). Fig. 2 shows an example of the lateral effects unilateral strokes have on cortical CVR as well as age-dependent regression information for asymptomatic hemispheres.

## Discussion and Conclusion:

Findings support that CVR metrics are uniquely altered in hemispheres with recent ischemic symptoms, motivating the use of CVR as a surrogate of ischemic symptomatology<sup>6</sup>. Maximum CVR was observed to be less significantly related to symptoms than timing parameters, suggesting that the time of vascular compliance, rather than the magnitude, may be most sensitively related to ischemic symptoms. The relevance of timing, including mean transit time and time-to-peak, is well-known to have clinical relevance in acute stroke imaging<sup>7</sup>. Finally, the age-dependent ranges reported in patients may complement recent reports of normative ranges in healthy control volunteers<sup>8</sup> to provide an exemplar for quantitative interpretation of reactivity.

**Acknowledgments / Funding Information:** 5R01NS097763

## References

1. Scott RM, Smith ER. Moyamoya disease and moyamoya syndrome. *N Engl J Med.* 2009;360:1226-1237. doi: 10.1056/NEJMra0804622
2. Juttukonda MR, Donahue MJ. Neuroimaging of vascular reserve in patients with cerebrovascular diseases. *Neuroimage.* 2019;187:192-208. doi: 10.1016/j.neuroimage.2017.10.015
3. De Vis JB, Bhogal AA, Hendrikse J, Petersen ET, Siero JCW. Effect sizes of BOLD CVR, resting-state signal fluctuations and time delay measures for the assessment of hemodynamic impairment in carotid occlusion patients. *Neuroimage.* 2018;179:530-539. doi: 10.1016/j.neuroimage.2018.06.017
4. Donahue MJ, Strother MK, Lindsey KP, Hocke LM, Tong Y, Frederick BD. Time delay processing of hypercapnic fMRI allows quantitative parameterization of cerebrovascular reactivity and blood flow delays. *J Cereb Blood Flow Metab.* 2016;36:1767-1779. doi: 10.1177/0271678X15608643
5. Donahue MJ, Ayad M, Moore R, van Osch M, Singer R, Clemmons P, Strother M. Relationships between hypercarbic reactivity, cerebral blood flow, and arterial circulation times in patients with moyamoya disease. *J Magn Reson Imaging.* 2013;38:1129-1139. doi: 10.1002/jmri.24070
6. Liu P, Liu G, Pinho MC, Lin Z, Thomas BP, Rundle M, Park DC, Huang J, Welch BG, Lu H. Cerebrovascular Reactivity Mapping Using Resting-State BOLD Functional MRI in Healthy Adults and Patients with Moyamoya Disease. *Radiology.* 2021;299:419-425. doi: 10.1148/radiol.2021203568
7. Powers WJ. Acute Ischemic Stroke. *N Engl J Med.* 2020;383:252-260. doi: 10.1056/NEJMcp1917030
8. Sobczyk O, Battisti-Charbonney A, Poublanc J, Crawley AP, Sam K, Fierstra J, Mandell DM, Mikulis DJ, Duffin J, Fisher JA. Assessing cerebrovascular reactivity abnormality by comparison to a reference atlas. *J Cereb Blood Flow Metab.* 2015;35:213-220. doi: 10.1038/jcbfm.2014.184

## Figures and tables

	N (hemispheres)	N (participants)	Sex (percent female)	Race (count)			Reactivity parameters		
				Asian	Black	White	CVR <sub>RAW</sub> (z/ΔEtCO <sub>2</sub> )	CVR <sub>MAX</sub> (z/ΔEtCO <sub>2</sub> )	CVR <sub>DELAY</sub> (seconds)
Asymptomatic	70	59	64.3%	6	16	48	0.75 ± 0.41*	1.74 ± 0.66 <sup>#</sup>	38.50 ± 10.51 <sup>^</sup>
Symptomatic	39	32	69.2%	0	12	26	0.52 ± 0.37*	1.50 ± 0.68 <sup>#</sup>	49.16 ± 15.19 <sup>^</sup>

**Table 1:** Demographic summary for symptomatic and asymptomatic cohort and results of logistic regression analysis of the reactivity statistics comparing the average (i) cerebrovascular reactivity (CVRRAW), (ii) maximum cerebrovascular reactivity (CVRMAX), and (iii) cerebrovascular reactivity delay (CVRDELAY) among participants who have been stratified by their stroke history. \*p=0.007; #p=0.037;

<sup>^</sup>p<0.001. Values are mean standard ± deviation unless otherwise noted.

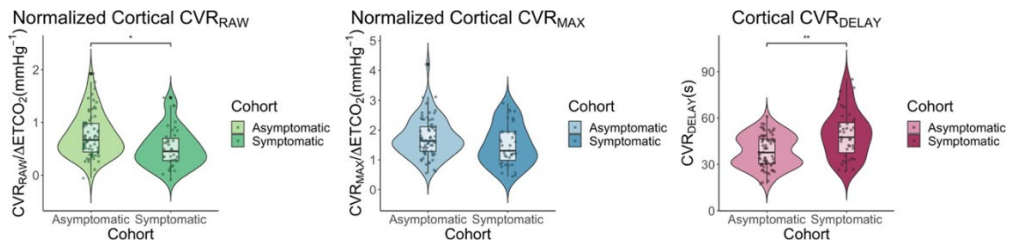


**Figure 1:** Violin plots compare the cortical cerebrovascular reactivity between participants who have (symptomatic) and have not (asymptomatic) experienced ischemic symptoms in the prior six-months. Upon logistic regression after controlling for age and sex, CVRRAW was significantly lower and the CVRDELAY significantly lengthened in the symptomatic cohort (\*p=0.007; \*\*p<0.001). CVRMAX was reduced in symptomatic hemispheres (p=0.037), which was insignificant after accounting for multiple comparisons.

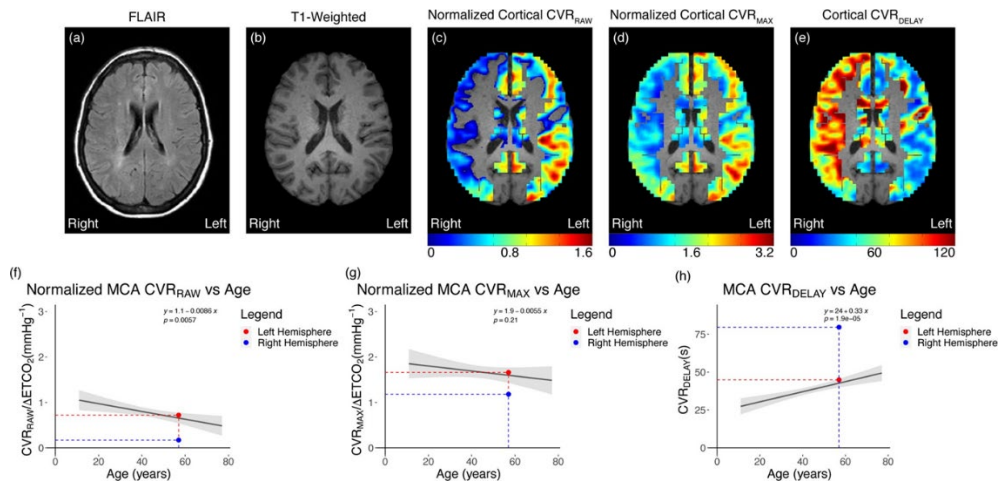


**Figure 2:** (a) FLAIR image of a 57-year-old female with right hemispheric ischemic symptoms. (b-e) T1-weighted image at the corresponding level superimposed with the cortical mask displays reduced reactivity and lengthened reactivity delay in the symptomatic right hemisphere. (f-h) Plots show age-dependent reactivity regression in asymptomatic hemispheres ( $n=70$ ) with the average reactivity metrics of the above case example plotted. Asymptomatic (left) hemisphere reactivity metrics fall within the normative range while the symptomatic hemisphere shows impairment.

# Association between small vessel function and progressive white matter injury in CADASIL using advanced 7T MRI

S.D.T. Pham<sup>1</sup>, H. van den Brink<sup>2</sup>, N. Vlegels<sup>3</sup>, A. Kopczak<sup>3</sup>, A. De Luca<sup>1</sup>, J.J.M. Zwanenburg<sup>1</sup>, N. Dieleman<sup>1</sup>, M. Duering<sup>3</sup>, G.J. Biessels<sup>1</sup>, J.C.W. Siero<sup>1</sup>

<sup>1</sup>University Medical Center Utrecht, Utrecht, the Netherlands;

<sup>2</sup>Massachusetts General Hospital, Boston, United States

<sup>3</sup>Ludwig-Maximilians-Universität, Munich, Germany

## Synopsis and/or Summary of Main Findings:

Small vessel function on 7T MRI is impaired in CADASIL and associated with baseline white matter injury. In previous work we found that several aspects of small vessel function were associated with white matter hyperintensity (WMH) burden and white matter integrity quantified as the peak width of the skeletonized mean diffusivity (PSMD). We studied if impaired small vessel function on 7T MRI was associated with white matter injury increase after two-year follow-up in terms of WMH volume and PSMD in CADASIL. Participants underwent a 3T brain MRI at baseline and follow-up to quantify WMH volume and PSMD. 7T brain MRI was performed at baseline to assess small vessel function. No significant associations between small vessel function and WMHs or PSMD increase were found. Further studies are warranted to assess the association between impaired small vessel function and progressive white matter injury on a voxelwise level.

## Introduction

White matter hyperintensities (WMH) and diffusion tensor imaging (DTI) metrics such as the peak width of the skeletonized white matter (PSMD) are associated with stroke and cognitive decline in cerebral small vessel diseases (cSVDs)[1-3].

CADASIL is a genetic form of cSVD with observed pathology in small cerebral arteries[4-6]. Using 7T MRI, small vessel function was found to be impaired in CADASIL and was associated with baseline WMH and PSMD[7,8]. In this study we studied if impaired small vessel dysfunction on 7T MRI was associated with WMH and PSMD increase in CADASIL.

## Methods

CADASIL patients were recruited through the ZOOM@SVDs study[9], a prospective observational cohort study with two-year follow-up. Participants underwent a 3T MRI at baseline and follow-up to quantify WMH and PSMD. A 7T MRI was performed at baseline to assess small vessel function[9] (Figure 1). The following aspects of small vessel function were assessed:

1. Blood flow velocity and pulsatility in perforating arteries at the level of the basal ganglia and centrum semioval using 2D phase-contrast angiography to assess arterial stiffness.
2. Reactivity to a visual stimulus was assessed in the visual cortex using the blood-oxygen-level dependent (BOLD) response, indicative of neurovascular coupling.

Baseline and follow-up WMH and PSMD were compared using a paired t-test. Small vessel function measures were related to baseline measures and change in WMH and PSMD using linear regression.

## Results

The characteristics of 22 CADASIL patients are shown in Table 1. There was a significant increase of WMH ( $p < 0.001$ ) and PSMD ( $p = 0.03$ ) after two-year follow-up.

Mean blood flow velocity within the perforating arteries of the centrum semioval was significantly associated with baseline WMH ( $\beta = -0.61$ ;  $p = 0.05$ ) and PSMD ( $\beta = -0.84$ ;  $p = 0.04$ ). None of the other small vessel function measures showed a significant association with baseline WMH and PSMD (Table 2).

There were no significant associations between any small vessel function measure and WMH or PSMD change (all  $p > 0.05$ ).

## Discussion

We found a significant negative association between mean blood flow velocity in centrum semioval perforating arteries and baseline WMH and PSMD, which we found before[8]. In this work we presented novel associations between cerebral small vessel dysfunction and progressive white matter injury in terms of WMH and PSMD change in CADASIL. Though WMH and PSMD increase was significant between baseline and two-year follow-up, we found no significant association with small vessel dysfunction. Despite not finding any significant associations between small vessel dysfunction and white matter injury progression on a whole-brain level, we have found in earlier work that small vessel dysfunction was associated with white matter injury at a voxelwise level in cSVDs[8]. We found that BOLD cerebrovascular reactivity (BOLD-CVR) to a hypercapnic stimulus was negatively correlated with mean diffusivity of the white matter[8] and we found that a lower BOLD-CVR was associated with voxels progressing to new WMH[10]. Those findings warrant further studies to assess the association between voxelwise small vessel dysfunction and longitudinal alterations in white matter injury in cSVDs to better understand the role of small vessel function in disease progression in cSVDs.

**Acknowledgments / Funding Information:** We want to thank all study participants in the ZOOM@SVDs study and all partners of the SVDs@target collaborative program for their efforts. ZOOM@SVDs is part of SVDs@target that has received funding from the European Union's Horizon 2020 research and innovative program under grant agreement No. 666881. JCWS and SDTP are funded by the UMCU Brain Center Young Talent Fellowship 2019.

## References

1. Wardlaw JM, et al. Small vessel disease: mechanisms and clinical implications. *Lancet Neurol.* 2019;18:684-696.
2. DeBette S, et al. Clinical Significance of Magnetic Resonance Imaging Markers of Vascular Brain Injury: A Systematic Review and Meta-analysis. *JAMA Neurol.* 2019;76:81-94.
3. Baykara, E, et al. "A novel imaging marker for small vessel disease based on skeletonization of white matter tracts and diffusion histograms." *Annals of neurology* 80.4 (2016): 581-592.
4. Chabriat H, et al. *Lancet Neurol.* 2009;8:643-653.
5. Di Donato I, et al. Cerebral Autosomal Dominant Arteriopathy with Subcortical Infarcts and Leukoencephalopathy (CADASIL) as a model of small vessel disease: Update on clinical, diagnostic, and management aspects. *BMC Med.* 2017;15:1-12.
6. Hervé D, et al. CADASIL. *J Geriatr Psychiatry Neurol.* 2010;23:269-276.
7. Van Den Brink, Hilde, et al. "CADASIL Affects Multiple Aspects of Cerebral Small Vessel Function on 7T-MRI." *Annals of Neurology* 93.1 (2023): 29-39.
8. Vlegels N, et al. The relation between small vessel function and white matter microstructure in monogenic and sporadic small vessel disease - the ZOOM@SVDs study, Manuscript in preparation
9. van den Brink H, Kopczak A, Arts T, et al. Zooming in on cerebral small vessel function in small vessel diseases with 7T MRI: Rationale and design of the "ZOOM@SVDs" study. *Cereb Circ Cogn Behav.* 2021;2:100013.
10. Pham, S, et al. Cerebrovascular reactivity on 7T MRI is associated with longitudinal white matter hyperintensity progression in small vessel disease on 7T MRI, Poster Presentation at ISMRM 2023, Toronto, 2023

## Tables and figures

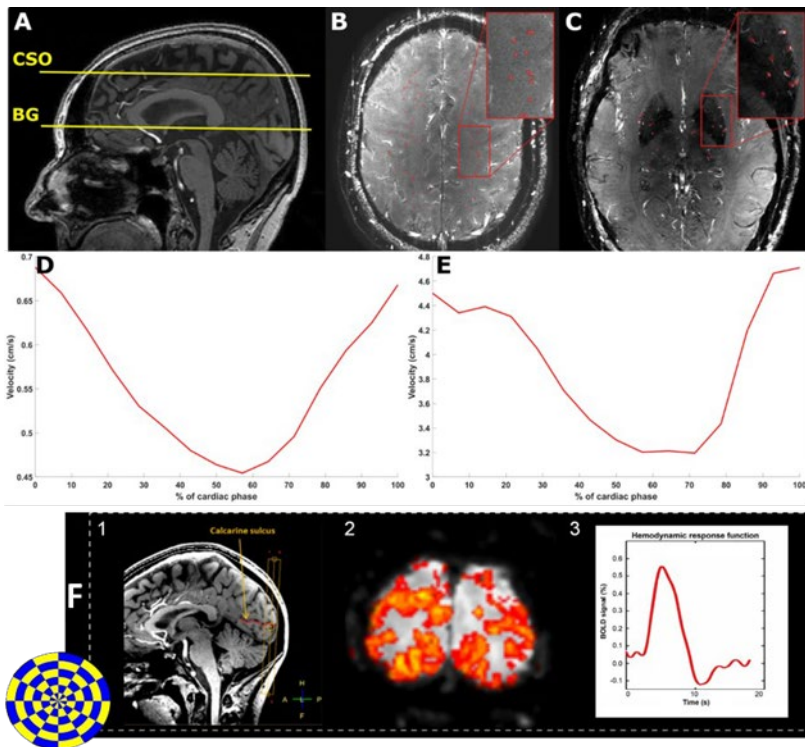


**Figure 1** A) 2D phase contrast slice planning of the CSO and BG. B) Magnitude image of the CSO and BG (C). Perforators are marked in red. D) Average velocity trace over the cardiac cycle of the perforators in the CSO and BG (E). F) BOLD acquisition of the visual stimulus with (1) slice planning in the visual cortex, (2) voxelwise reactivity maps, and (3) BOLD signal curves over time for small vessel reactivity.

CADASIL	
N	22
Age, mean±SD	51±10
Sex, female n (%)	12 (55%)
Follow-up time, months median [IQR]	25 [2]
<b>Imaging markers</b>	
WMHs baseline %ICV [SD]	4.8 [4.6] *
WMHs follow-up %ICV [SD]	5.3 [4.8] *
PSMD baseline mm <sup>2</sup> /s *10 <sup>-4</sup> [SD]	3.1 [0.6]**
PSMD follow-up mm <sup>2</sup> /s *10 <sup>-4</sup> [SD]	3.3 [0.8]**

**Table 1** Characteristics of CADASIL patients

ICV = intracranial volume; IQR = inter-quartile range; PSMD = Peak width of the skeletonized mean diffusivity; SD = standard deviation; WMH = white matter hyperintensities

\* paired t-test (P<0.001)

\*\* paired t-test (P=0.03)

	WMH baseline		PSMD baseline		WMH change		PSMD change	
	b	P-value	b	P-value	b	P-value	b	P-value
<b>HRF peak %BOLD change</b>	-0,05	0,6	-0.15	0.15	-0,0007	0,97	-0.04	0.46
<b>CSO Mean Velocity</b>	-0,61	0,05	-0.65	0.04	0,018	0,67	0.001	0.99
<b>CSO Pulsatility Index</b>	-0,1	0,34	-0.23	0.07	-0,0004	0,98	0.007	0.89
<b>BG Mean Velocity</b>	-0,05	0,17	-0.007	0.85	0,011	0,8	0.006	0.68

**Table 2** Results of linear regression between small vessel dysfunction and WMH and PSMD for baseline and two-year change in CADASIL

BG = basal ganglia; BOLD = blood-oxygen level-dependent; CSO = centrum semioval; HRF = hemodynamic response function; PSMD = Peak width of the skeletonized mean diffusivity

## CO<sub>2</sub> and O<sub>2</sub> reactivity in brain gliomas

Oluwateniola Akinwale<sup>1</sup>, Yang Li<sup>1,2</sup>, Peiyong Liu<sup>1</sup>, Shruti Agarwal<sup>1,3</sup>, Xirui Hou<sup>1</sup>, Shanshan Jiang<sup>1</sup>, Doris Lin<sup>1,3</sup>, Jay. J. Pillai<sup>1,3</sup>, and Hanzhang Lu<sup>1</sup>

<sup>1</sup>Department of Radiology, Johns Hopkins University School of Medicine, Baltimore, MD, United States,

<sup>2</sup>Graduate School of Biomedical Sciences, UT Southwestern Medical Center, Dallas, TX, United States,

<sup>3</sup>Department of Neurosurgery, Johns Hopkins University School of Medicine, Baltimore, MD, United States

### SYNOPSIS:

CVR, O<sub>2</sub>-reactivity and BAT maps were obtained for sixteen de novo brain tumor patients using a CO<sub>2</sub> and O<sub>2</sub> inhalation MRI technique. Region-of-interest analysis showed that CVR and O<sub>2</sub> reactivity were significantly lower while BAT was significantly higher in tumor regions compared to contralateral healthy tissue.

### INTRODUCTION:

Gas-inhalation MRI now allows us to obtain biomarkers such as O<sub>2</sub>-reactivity (thought to reflect venous cerebral blood volume, vCBV) and cerebrovascular reactivity (CVR) for brain tumors. CBV has already been established as a diagnostic marker for tumor grading and CVR potentially informing on tissue regions with neurovascular uncoupling [1]. Jointly, they may act as potential tools for the diagnosis and treatment of brain tumors. A limitation is that this information is normally collected during different scans. In this work, a novel MRI technique that allows for the collection of data to measure multiple hemodynamic parameters in a single 9- minute scan was applied. Analysis of the output multi-parametric maps showed that one may use them to reliably differentiate between tumor and normal brain tissue.

### METHODS:

**Patients:** Sixteen de novo brain tumor patients (age 21-81y, 11M/5F) were scanned on 3T (Siemens and Philips), after IRB-approved informed consent was obtained. Fifteen patients have since undergone surgical intervention and histopathologic tumor grades were obtained using 2016 WHO standards.

**Imaging parameters:** Concomitant CO<sub>2</sub>/O<sub>2</sub> breathing paradigm was performed while BOLD images were continuously collected [1]. The CO<sub>2</sub> and O<sub>2</sub> breathing periods were optimized previously and is illustrated in Fig. 1, and allows for the independent alteration of CO<sub>2</sub> and O<sub>2</sub> levels. The BOLD sequence used the following parameters: TR/TE=1550/21ms, 3.2×3.2×3.5mm, scan duration=9.3min. Clinical MR scans were also performed, including contrast-enhanced T1W, T2W, and FLAIR.

**Data processing:** Following a previously established analysis method [1], BOLD images and physiological recordings of end-tidal (Et) CO<sub>2</sub> and O<sub>2</sub> traces were used to obtain CVR (based on BOLD signal change to EtCO<sub>2</sub> change), CBV (based on BOLD signal change to EtO<sub>2</sub> change), and bolus arrival time (BAT; based on the time lag between the voxel and whole brain BOLD signal) maps.

**Statistical analysis:** Regions-of-interest (ROI) were manually drawn on solid tumor regions and contralateral healthy tissue and were applied to the CVR, CBV, and BAT maps to obtain regional values. Parametric values were compared between tumor and contralateral ROIs using paired t-tests. Correlation between tumor grade and the normalized tumor CVR was also examined.

### RESULTS:

Fig. 2a shows the anatomical images (T1W and FLAIR) and parametric (CVR, CBV, and BAT) maps for three patients: Patient A – WHO IV grade glioblastoma, Patient B – WHO III grade anaplastic glioma, and Patient C – WHO II grade astrocytoma. CVR and CBV is seen to be decreased in tumor regions. The dark tumor region is smaller in the CBV map indicating that there may be angiogenesis in outer tumor regions, however, the vessels are not mature enough to respond to stimuli. Tumor regions are green in the BAT map indicating a longer response time to the CO<sub>2</sub>/O<sub>2</sub> stimulus.

Fig. 2b shows the CVR, CBV, and BAT values for the tumor and contralateral side. Paired t-tests for the difference between ROIs were highly significant (all < 0.01) indicating that these maps enable differentiation between tumor and healthy tissue.

Fig. 3 shows the tumor CVR normalized by contralateral tissue CVR in low grade (Grade II) and high grade (Grades III and IV). The normalized CVR was lower high-grade tumors compared to low grade tumors, however, a paired t-test yielded a non-significant p- value.

### CONCLUSION:

We used an advanced technique to simultaneously evaluate CVR, CBV, and BAT in glioma patients. The multiparametric maps were found to be able to accurately distinguish between tumor and normal tissue. This methodology could be a cost-effective way to help with tumor classification and presurgical planning in glioma patients.

### REFERENCES:

1. Liu, P., Welch, B. G., Li, Y., Gu, H., King, D., Yang, Y., Pinho, M., & Lu, H. (2017). Multiparametric imaging of brain hemodynamics and function using gas-inhalation MRI. *NeuroImage*, 146, 715–723. <https://doi.org/10.1016/j.neuroimage.2016.09.063>

**Figures:**

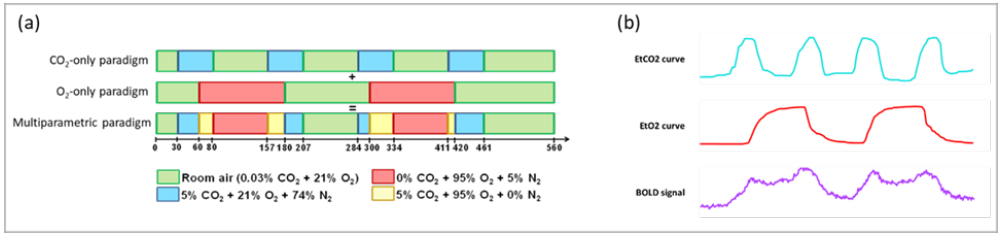


**Fig. 1:** (a) Illustration of breathing paradigm applied in the multiparametric MRI technique. (b) EtCO<sub>2</sub>, EtO<sub>2</sub>, and BOLD time courses used to obtain the parametric maps.

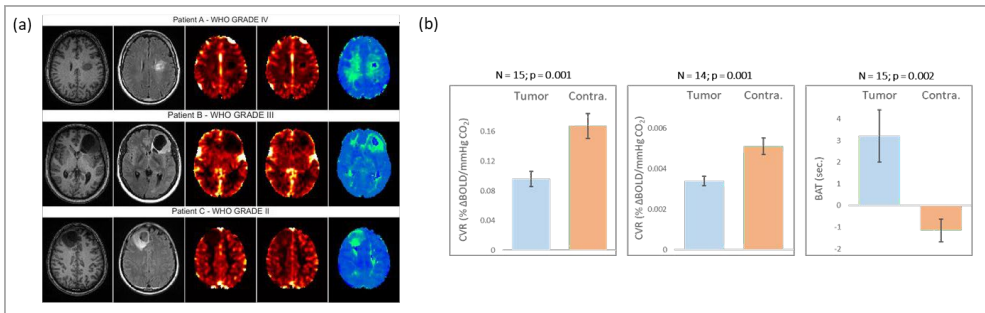


**Fig. 2:** (a) From left to right – TW1, FLAIR, CVR, CBV, and BAT maps – from grade IV (top), III (middle), and II (bottom) patients. (b) Comparison of the tumor and contralateral ROI values from the CVR (left), CBV (middle), and BAT (right) maps (N = 16 and error bars indicate standard error).

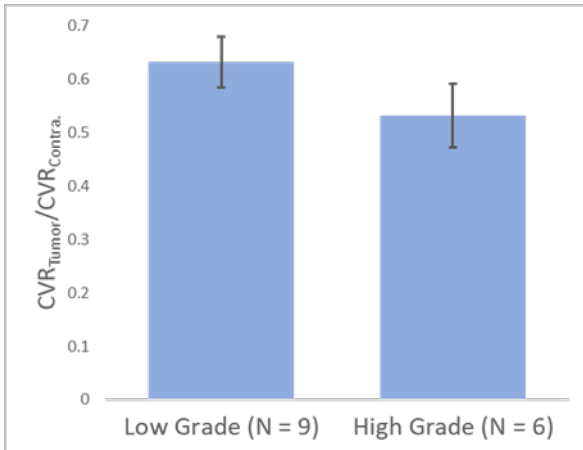
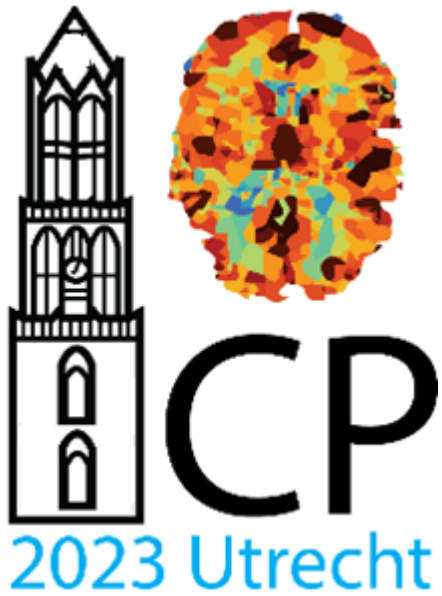


**Fig. 3:** Comparison of the tumor CVR normalized by contralateral tissue CVR of low and high grade (Error bars indicate standard error).



Day 2: November 30<sup>th</sup>

# Quantifying Cardiac-Induced Brain Tissue Deformations Using DENSE MRI: Insights from an Observational Study

E. van Hulst<sup>1</sup>, M.G. Báez-Yáñez<sup>1</sup>, G.J. Biessels<sup>2</sup>, J.J.M. Zwanenburg<sup>1</sup>

<sup>1</sup>Center for Image Sciences, University Medical Center Utrecht, Utrecht, The Netherlands

<sup>2</sup>Department of Neurology, University Medical Center Utrecht, Utrecht, The Netherlands

## Synopsis and/or Summary of Main Findings:

The heartbeat causes viscoelastic deformations and volumetric strain in the surrounding brain tissue which can be observed by an MRI acquisition method using Displacement Encoding with Stimulated Echoes (DENSE). This study reports observations of consistent brain tissue compression during the first (systolic) half of the cardiac cycle. Comparing simulated and measured volumetric strain curves suggest that the observations cannot be explained by measurement noise. The curves show a similar but opposite pattern for the expanding and the compressing regions of the brain following the cardiac cycle, which suggests that the observed compressions reflect a physiological process. Consistency in spatial distribution between different subjects further supports the interpretation of true compressions in brain tissue during the systolic phase of the heart cycle. Further work aims to establish whether the observations are not caused by systemic measurement errors.

## Introduction:

Blood volume changes in the microvasculature due to the cardiac cycle cause deformations and volumetric strain in surrounding brain tissue. MRI acquisition using Displacement Encoding with Stimulated Echoes (DENSE) allows us to measure these brain tissue deformations in vivo [1]. The current observational study reveals that while the majority of brain tissue primarily expands during systole, there is a considerable fraction of brain tissue that predominantly undergoes compression.

## Methods:

Data previously acquired by Sloots et al. [2] were further analyzed for the occurrence of compression. From this single-shot DENSE data the cardiac-induced volumetric strain over 8 cardiac phases between 0 and 52.5 percent of the cardiac interval was available (Figure A). For each cardiac phase, each voxel was labeled either +1 or -1 for a positive or negative volumetric strain, respectively. The labeled maps for the 8 cardiac phases were summed resulting in a single count map metric displaying a range from -8 (consistent compression for each cardiac phase of the first half of the cardiac cycle) to +8 (consistent expansion). In the process, registration and masking steps using a high-resolution t1w image were applied as needed. Based on the count map, two regions of interest were selected: an expanding (count>0) and compressing (count<0) ROI. To rule out measurement noise as explanation for the observations, volumetric strain data was simulated with an identical distribution at each cardiac phase as the whole brain measurement data. The analysis followed the same methodology. Distributions of one subject were used and data was generated 1000 times with different noise realizations to estimate the uncertainty in the volumetric strain curves of the compression- and expansion ROIs.

## Results and Discussion:

Figure B shows the mean and median volumetric strain curves for both ROIs and the whole brain. The expanding ROI covered  $65 \pm 3.6\%$  (mean $\pm$ sd) of the brain, whereas the compressing ROI covered  $22 \pm 1.8\%$ . On average, the brain tissue showed an expanding pattern over the cardiac cycle. The volumetric strain curves for the positive and negative ROIs showed similar but opposite patterns over the cardiac cycle, suggesting that the compressions seen are not solely artifacts but reflect a physiological process. The simulated curves showed different behavior for the compressing ROI, suggesting that measurement noise cannot explain the observations. The spatial distribution of compressive tissues showed similarities between different subjects. Notably, the area around the sagittal sinus showed compression in all subjects (Figure C). Compressions were also seen in deeper-lying areas, which contain few large blood vessels or CSF voids, making it probable that we are indeed looking at brain regions undergoing compression, rather than artifacts from partial volume effects that could affect the DENSE measurement.

Conclusion: The current analysis provides a first observation of compressions in brain tissue during the systolic phase of the cardiac cycle. These compressions could reflect compressed veins (like systolic coronary compression in the heart) or perivascular spaces. However, a more comprehensive analysis must be performed to ensure that the observed compressions are not caused by systemic measurement errors from e.g. large vessels or sulci.

## References

- [1] A. L. Adams, H. J. Kuijff, M. A. Viergever, P. R. Luijten, and J. J. M. Zwanenburg, "Quantifying cardiac-induced brain tissue expansion using DENSE," *NMR Biomed*, vol. 32, no. 2, Feb. 2018, doi: 10.1002/nbm.4050.
- [2] J. J. Sloots, G. J. Biessels, A. de Luca, and J. J. M. Zwanenburg, "Strain Tensor Imaging: Cardiac-induced brain tissue deformation in humans quantified with high-field MRI," *Neuroimage*, vol. 236, Aug. 2021, doi: 10.1016/j.neuroimage.2021.118078.

Figures and tables

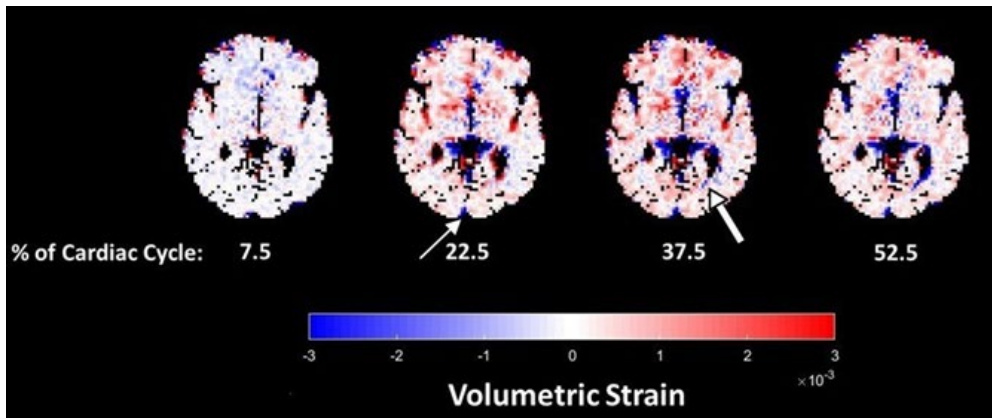


Figure 1: Volumetric strain maps for subject 1 at four different heart phases. Note the consistent apparent compression at the sagittal sinus (thin arrow) and in the white matter near the lateral horn of the left ventricle (wide arrow).

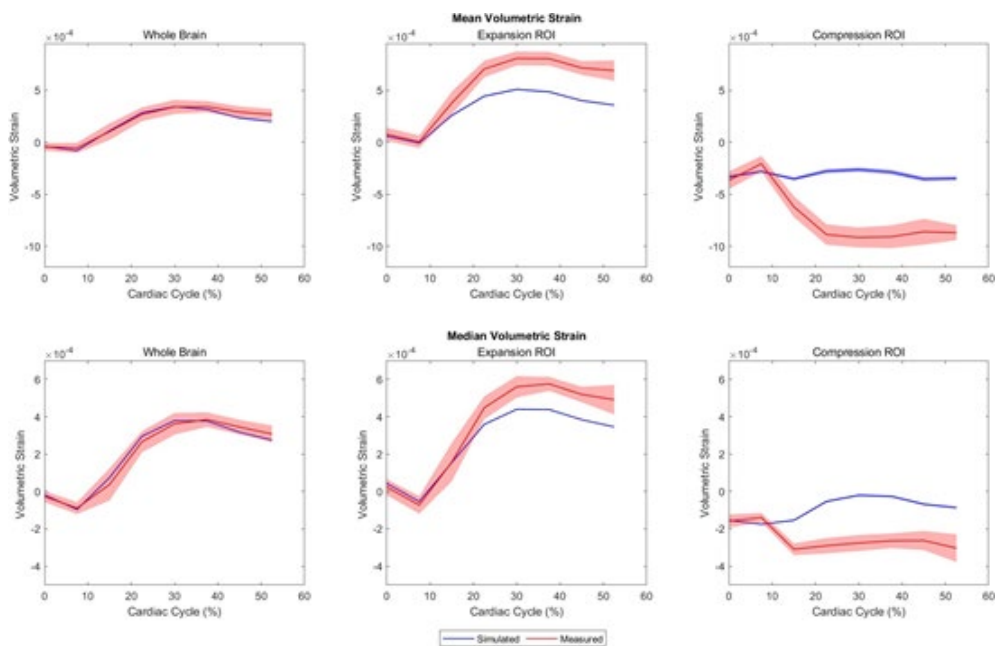
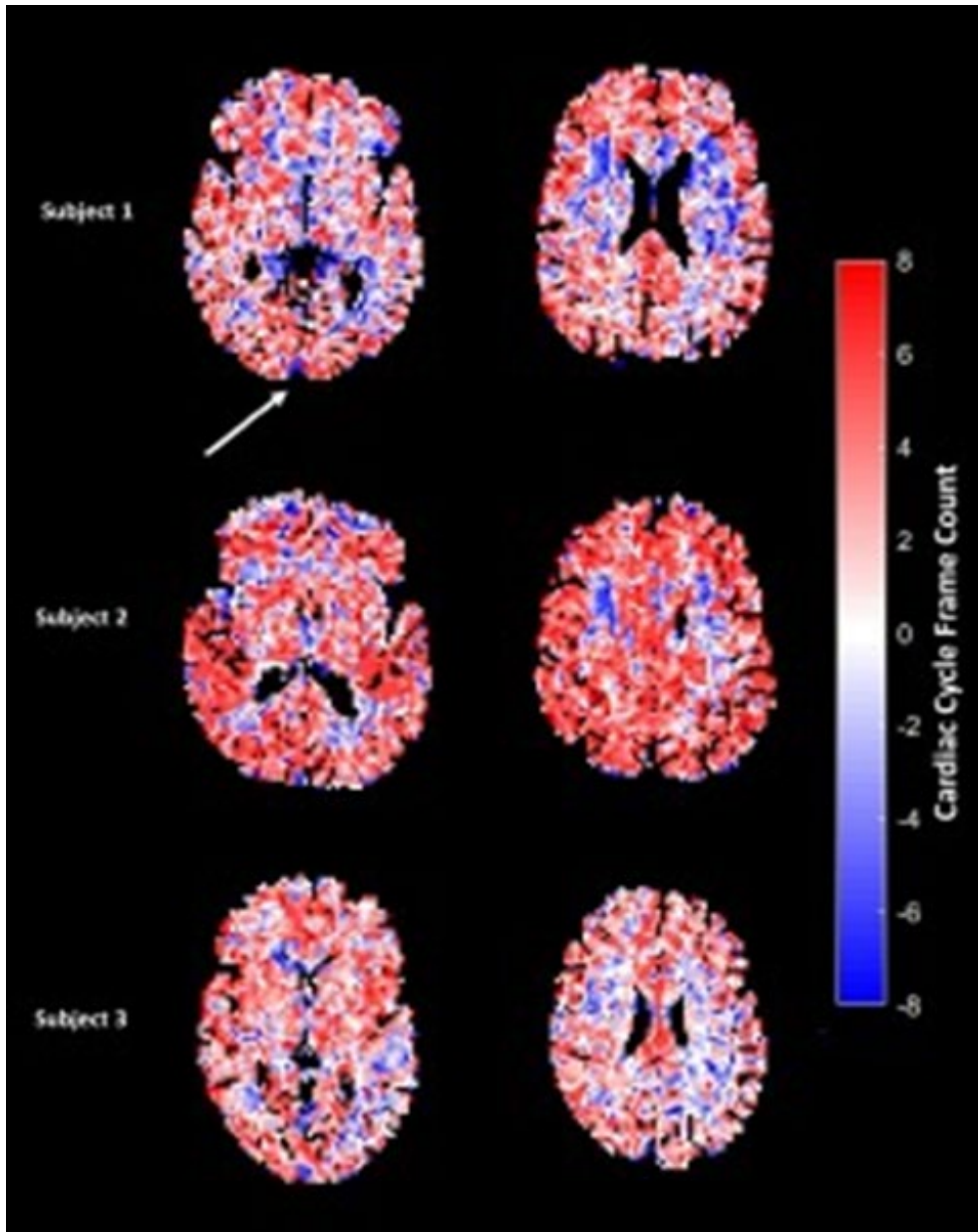


Figure 2: Mean and median volumetric strain curves for the measured and simulated data in the whole brain, expansion ROI and compression ROI. The measured data shows a characteristic pattern following the cardiac cycles, whereas the simulated data doesn't. The bold line indicates the mean over all data and the shaded regions the standard deviation.



**Figure 3:** Cardiac cycle frame count maps for three subjects. Note the compressing sagittal sinus indicated by the white arrow in the three left figures, and the compressing tissue in the deeper lying areas in the three right figures.

# Does a manual determined threshold bias quantitative perivascular spaces measurements based on the Frangi vesselness filter?

M. R. Schipper<sup>1</sup>, A. Razoux-Schultz<sup>1</sup>, T.W. van Harten<sup>1</sup>, M.J.H. Wermer<sup>2</sup>, M.J.P. van Osch<sup>1</sup>, M.A.A. van Walderveen<sup>1</sup>, S. van Rooden<sup>1</sup>

<sup>1</sup>Department of Radiology, Leiden University Medical Center, Leiden, The Netherlands

<sup>2</sup>Department of Neurology, University Medical Center Groningen, Groningen, The Netherlands

## Synopsis and/or Summary of Main Findings:

Variable settings for quantitative assessment of perivascular spaces (PVS), seem to be required for individual PVS assessment in a population with varying noise levels, artefacts, and pathology. However, adjusting e.g. the threshold per individual may introduce bias to the PVS measure. We studied the effect of the Frangi vesselness filter threshold on PVS volume assessment. Main findings show no significant relation between the filter threshold and the PVS volume assessment (unstandardized B = -1361.97, p = 0.093, Adjusted R<sup>2</sup> = 0.04). We recommend visually adjusting the filter threshold per person to optimize the WM-PVS segmentation by maximizing the PVS inclusion, while minimizing false positives and false negatives in the WM-PVS segmentation.

## Abstract Body:

Visual rating scales used to be the golden standard for scoring enlarged perivascular spaces (PVS). Main limitations of this method are a strong ceiling effect – blinding us for the most severe stages of disease progression – and a focus on a small part of the brain. To overcome these limitations, several research groups are looking into quantitative PVS assessment. In a previous study of PVS volume in Dutch-type Cerebral Amyloid Angiopathy (D-CAA) – an autosomal dominant hereditary form of one of the leading etiologies of intracerebral hemorrhage in elderly – we determined that, to deal with varying noise levels, artefacts, and pathology, it is needed to adjust the Frangi vesselness filter threshold on an individual basis. With the current study we aim to assess the effect of such a personal filter threshold on semi-automatically segmented total white matter PVS (WM-PVS) volume in D-CAA.

In our analyses we included 12 symptomatic D-CAA (mean 55±5.8yrs, range 45-63yrs, 6/12 were female), 9 presymptomatic D-CAA mutation carriers (mean 34±12.5yrs, range 20-51yrs, 8/9 were female), 12 older controls (mean 57±7.0yrs, range 46- 67yrs, 6/12 were female), and 14 young controls (mean 33±7.4yrs, range 20-45yrs, 12/14 were female). Total WM-PVS volume (mL) was determined using in-house developed software based upon the Frangi vesselness filter that is applied on white matter masked multi-slice T2-weighted images (TE/TR 80/4200ms, FA 90°, 40 slices, FOV 224x180x144 mm, slices thickness 3.6 mm, matrix 448x320 voxels, in-plane resolution 0.5x0.56 mm, scan duration ~3 min). For our region of interest (ROI) we excluded non-WM areas from the brain, i.e. cerebellum, brain stem, basal ganglia, and large CSF areas (ventricles, subarachnoid space, large sulci), resulting in a ROI mask covering only the WM of the cerebrum. This ROI was manually adjusted where needed (ARS) and afterwards checked by another assessor (MS) to reduce false positive PVS segmentations. Filtering thresholds were visually determined per participant, to minimize false positive and false negative segmentations. Thresholds were determined (ARS) and checked by two other assessors (MS and SvR). The relative WM-PVS volume was defined as total WM-PVS volume normalized by the total WM volume in mL per subject. Figure 1 shows an example of the ROI throughout the brain and the WM-PVS segmentation within this ROI. To test the association between the filter threshold and the WM-PVS volume, we performed a linear regression.

Linear regression modeling showed that no significant relationship between the filter threshold and WM-PVS volume in our study cohort, with a very small effect size (unstandardized B = -1361.97, 95% CI [-2957.65, 233.72], p = 0.093, Adjusted R<sup>2</sup>= 0.04). Figure 2 shows a scatterplot of the filter threshold and WM-PVS volume.

We demonstrated that adjustment of the Frangi vesselness filter threshold per person, does not introduce a systematic bias. A high threshold does not necessarily result in a low WM-PVS volume and vice versa. We propose that adjusting the filter threshold per person allows for optimization of the WM-PVS segmentation by maximizing the PVS inclusion, while minimizing false positives and false negatives in the WM-PVS segmentation.

**Acknowledgments / Funding Information:** M.R. Schipper reports independent support from the TRACK D-CAA consortium, consisting of Alnylam, Biogen, the Dutch CAA foundation, Vereniging HCHWA-D, and researchers from Leiden, Boston, and Perth.

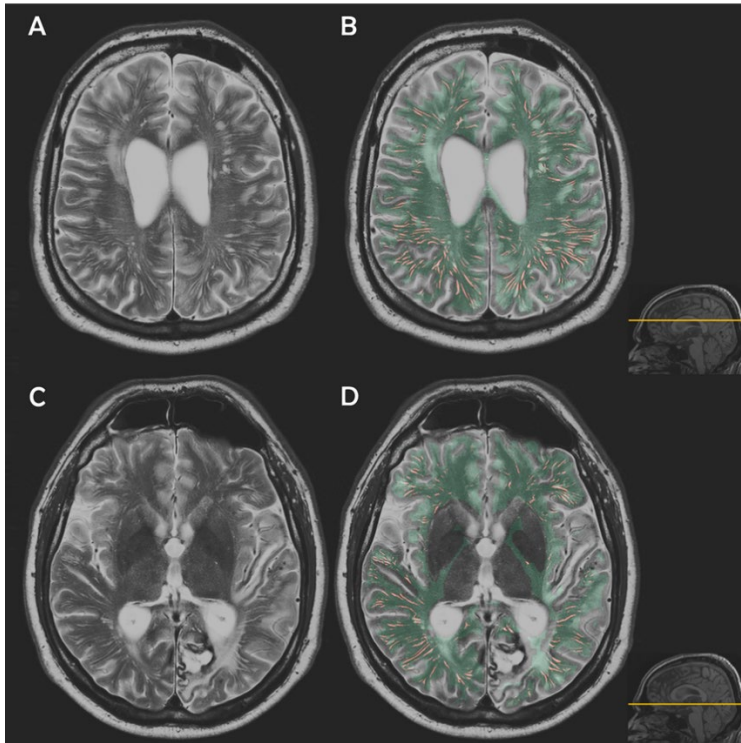


**Figure 1.** Example of WM-PVS segmentation in a participant with visible WM-PVS. A and C) T2-weighted image with visible WM-PVS. B and D) T2-weighted images from A and C with the region of interest in which the Frangi vesselness filter is applied, overlaid in green, and the resulting WM-PVS segmentation overlaid in red.

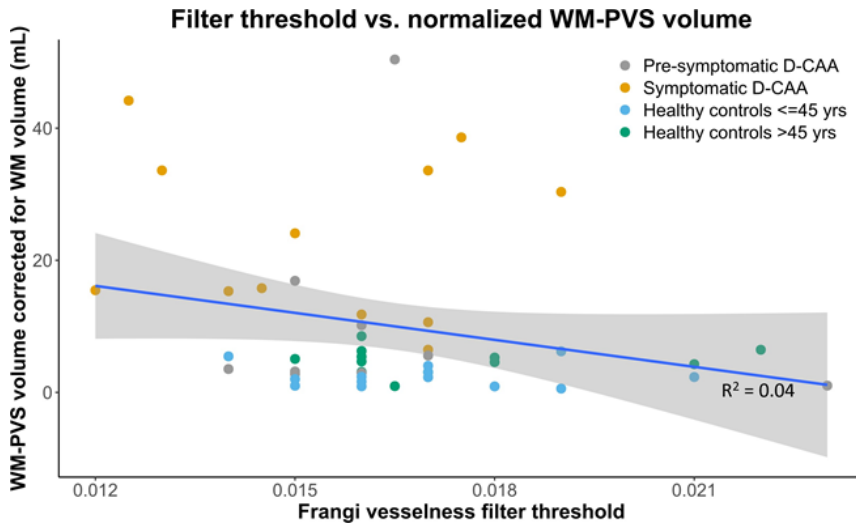


**Figure 2.** Scatterplot of the Frangi vesselness filter threshold and the normalized WM-PVS volume, with the different subgroups projected in different colours.

# CO<sub>2</sub> as an engine for neuro-fluid flow: exploring the coupling between vascular reactivity, brain clearance and changes in tissue properties

E.C. van der Voort<sup>1</sup>, Y. Tong<sup>2</sup>, E. van Grinsven<sup>3</sup>, J.J.M. Zwanenburg<sup>1</sup>, M.E.P. Phillipens<sup>3</sup>, A.A. Bhogal<sup>1</sup>

<sup>1</sup>Center for Image Sciences, UMC Utrecht, Utrecht, The Netherlands,

<sup>2</sup>Purdue University, West Lafayette, IN, United States,

<sup>3</sup>Radiotherapy department, UMC Utrecht, Utrecht, The Netherlands

## Synopsis

To assess CSF flow in the fourth ventricle, we use Blood Oxygen Level Dependent (BOLD) imaging in combination with controlled hypercapnic stimulus in a patient cohort presenting with brain metastases and varying amounts of peritumoral edema. Our findings revealed an association between alterations in arterial carbon dioxide levels (PaCO<sub>2</sub>) and CSF flow due to changes in cerebral blood volume (CBV), consistent with the principles of the Monro-Kellie doctrine. Furthermore, we observed a significant correlation between edema load and the rate of the hemodynamic response to alterations in PaCO<sub>2</sub>. This study is the first to explicitly demonstrate that modifying CBV using targeted PaCO<sub>2</sub> manipulations leads to CSF motion in the fourth ventricle, establishing a direct link between vascular responses and CSF flow. Additionally, our findings shed a new light on the interplay between CSF and hemodynamics and edema formation, expanding the understanding of cerebral physiology.

## Abstract Body

The brain's high metabolic rate necessitates an efficient clearance mechanism to eliminate byproducts and maintain homeostasis. However, due to absence of a conventional lymphatic system, the exact pathways for waste clearance remain subject of debate [1]. Consequently, research interest is growing, with specific focus on understanding the forces that facilitate waste removal through cerebrospinal fluid (CSF). Arterial dynamics (heartbeat and vasomotion) and respiration (abdominal and thoracic pressure changes) have been identified as potential driving forces [2-5]. It is suggested that respiration also affects CSF flow through changes in arterial carbon dioxide levels (PaCO<sub>2</sub>), linking it to cerebrovascular responses. Our goal is to first establish a direct connection between cerebrovascular reactivity (CVR) and CSF dynamics through controlled manipulations of arterial blood gases; and second, to investigate whether changes in mechanical properties of the brain, potentially influencing neurofluid flow, impact CVR.

We retrospectively analyzed fMRI Blood Oxygen Level Dependent (BOLD) data from a patient cohort presented with brain metastases undergoing radiotherapy treatment. A subset of 22 patients were included of which 12 had repeated measurements (prior/post radiotherapy). Patients were scanned on a 3T Philips (Best, The Netherlands) system using a multi-slice GE-EPI sequence (BOLD-fMRI) throughout controlled manipulation of arterial blood gases using RespirAct™ (Thornhill Medical, Toronto, Canada). MRI parameters were: TR=1050ms, TE=30ms,  $\alpha=65^\circ$ , resolution=2.3x2.3x2.5mm<sup>3</sup>, matrix=96x96, slices=51, volumes=1000, multi-band factor=3. The respiratory paradigm consisted of a 90s hypercapnic block (+10mmHg), 120s baseline, 180s progressively increasing hypercapnic ramp (max=+12mmHg), 90s baseline, 180s hyperoxic block (target 680mmHg) and final 120s baseline period. Data were preprocessed using FSL [6]. Respiratory traces were interpolated to the TR of the MRI scans and bulk alignment between the average whole brain signal and resampled PetCO<sub>2</sub> trace was done using functions from the seeVR toolbox [7]. The last two slices of the MRI data were used to calculate CSF inflow from manually segmented CSF voxels. CSF signals were smoothed and de-trended. The grey matter (GM) MRI signal was smoothed and the temporal derivative was calculated as a surrogate for CBV change [8]. The same was done for the PetCO<sub>2</sub> trace. The vascular response dynamics were assessed according to [9]. This resulted in a time constant, 'tau'.

In total, 17 patients showed clear inflow effects either prior or post radiotherapy. Figure 1 shows CSF inflow measured in the fourth ventricle in response to modifying CBV by manipulating PaCO<sub>2</sub>. No inflow is measured due to changes in O<sub>2</sub> levels, serving as a validation for our measurements. Furthermore, results suggest (Figure 2) that changes in tissue properties, due to formation of edema, affect both cerebrovascular response and CSF dynamics. When analyzing the complete dataset, subjects with higher edema loads exhibit a slower BOLD response (represented by the time constant, tau) to changes in PaCO<sub>2</sub> (Figure 3). These findings support the notion that widespread changes in the brain's mechanical properties may influence the vascular response and subsequently affect CSF flow, and lend convincing evidence to the notion that CSF flow, vascular dynamics and brain tissue properties are intricately linked to form a co-dependent system.

**Acknowledgments / Funding Information:** We thank Martijn Froeling for his contributions to the fitting of the CSF inflow signal.

## References

1. Agarwal, N., Lewis, L. D., Hirschler, L., Rivera, L. R., Naganawa, S., Levendovszky, S. R., ... & van Osch, M. J. (2023). Current Understanding of the Anatomy, Physiology, and Magnetic Resonance Imaging of Neurofluids: Update From the 2022 "ISMRM Imaging Neurofluids Study group" Workshop in Rome. *Journal of magnetic resonance imaging*.
2. Mestre, H., Tithof, J., Du, T., Song, W., Peng, W., Sweeney, A. M., ... & Kelley, D. H. (2018). Flow of cerebrospinal fluid is driven by arterial pulsations and is reduced in hypertension. *Nature communications*, 9(1), 4878.
3. van Veluw, S. J., Hou, S. S., Calvo-Rodriguez, M., Arbel-Omath, M., Snyder, A. C., Frosch, M. P., ... & Bacskai, B. J. (2020). Vasomotion as a driving force for paravascular clearance in the awake mouse brain. *Neuron*, 105(3), 549-561.

4. Dreha-Kulaczewski, S., Joseph, A. A., Merboldt, K. D., Ludwig, H. C., Gärtner, J., & Frahm, J. (2017). Identification of the upward movement of human CSF in vivo and its relation to the brain venous system. *Journal of Neuroscience*, 37(9), 2395-2402.
5. Wang, Y., van Gelderen, P., de Zwart, J. A., Özbay, P. S., Mandelkow, H., Picchioni, D., & Duyn, J. H. (2022). Cerebrovascular activity is a major factor in the cerebrospinal fluid flow dynamics. *Neuroimage*, 258, 119362.
6. Jenkinson, M., Beckmann, C. F., Behrens, T. E., Woolrich, M. W., & Smith, S. M. (2012). *Fsl. Neuroimage*, 62(2), 782-790.
7. Bhogal, A. A. (2023). abhogal-lab/seeVR: 1.55 (v1.55), Zenodo. doi:10.5281/zenodo.7875713.
8. Yang, H. C., Inglis, B., Talavage, T. M., Nair, V. V., Yao, J., Fitzgerald, B., ... & Tong, Y. (2022). Coupling between cerebrovascular oscillations and CSF flow fluctuations during wakefulness: An fMRI study. *Journal of Cerebral Blood Flow & Metabolism*, 42(6), 1091-1103.
9. Poubanc, J., Crawley, A. P., Sobczyk, O., Montandon, G., Sam, K., Mandell, D. M., ... & Fisher, J. A. (2015). Measuring cerebrovascular reactivity: the dynamic response to a step hypercapnic stimulus. *Journal of Cerebral Blood Flow & Metabolism*, 35(11), 1746-1756.

## Tables and Figures

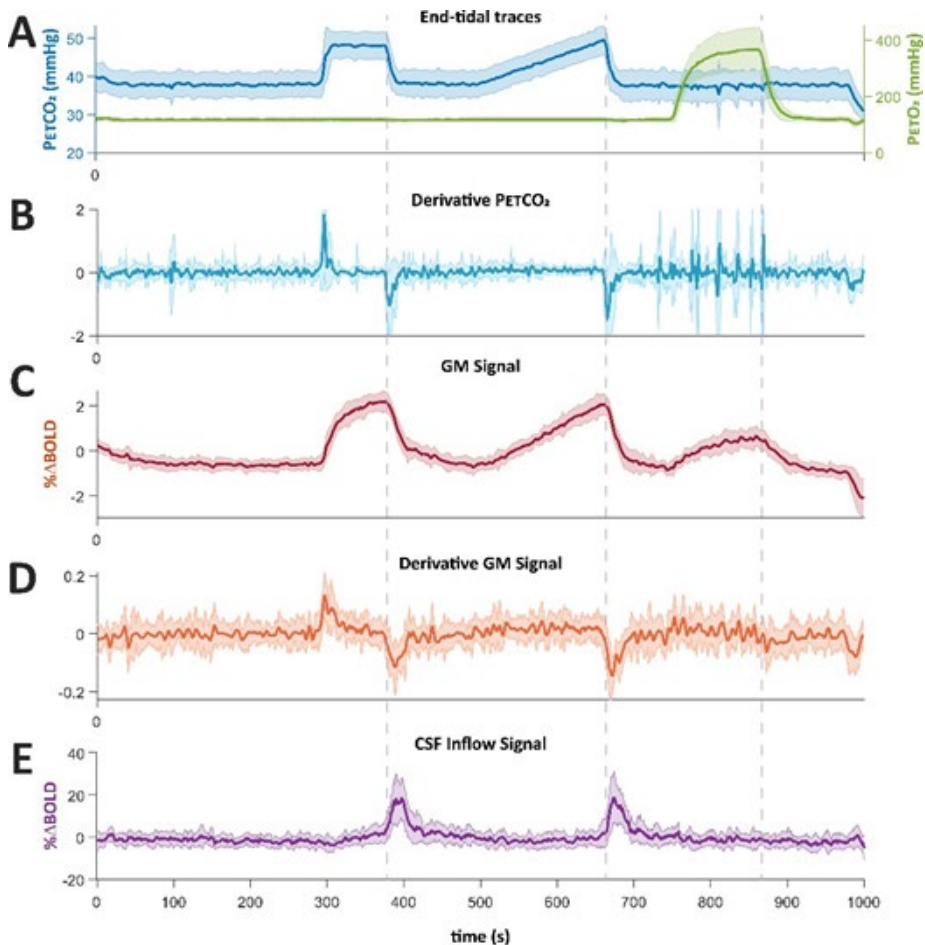


**Figure 1** A) Group-averaged end-tidal CO<sub>2</sub> (blue) and O<sub>2</sub> (green) traces and (B) corresponding time-derivative of the CO<sub>2</sub> trace. C) Group-averaged GM BOLD signal response and (D) corresponding time-derivative. E) Inflow signal resulting from CO<sub>2</sub>-mediated modulation of CBV. Note the timings between the peak response time-derivative and peak inflow signal and the fact that transient O<sub>2</sub> produces no inflow effect. The shaded areas indicate the standard deviation across subjects.

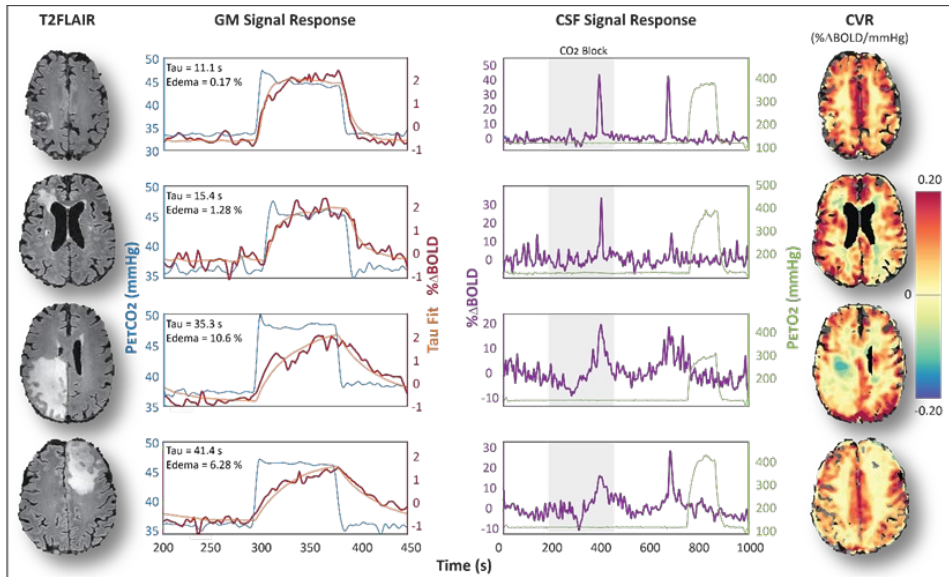


**Figure 2** Four patients with different edema loads depicted on T2FLAIR. End-tidal CO<sub>2</sub> trace (blue), BOLD response (red) and exponential fit (orange) for the hypercapnic block are shown. Note: tau increases with percent edema. Next, PetO<sub>2</sub> traces (green) and corresponding inflow signal (purple). Note: less sharp CSF peaks for higher edema loads and lack of strong inflow peaks during the hyperoxic period. CVR maps of the corresponding slices show decreased CVR for higher edema loads.

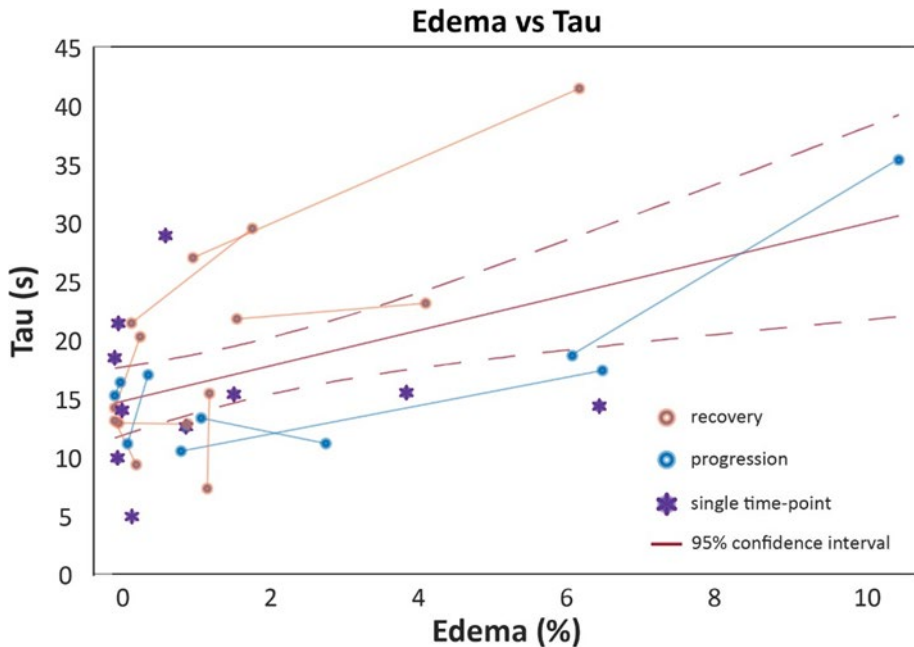


**Figure 3** Edema versus Tau for all patients. Lines indicate the two time points (prior and post radiotherapy) belonging to the same patient. Orange lines indicate a decrease in edema load and blue an increase. Single time point subjects are shown in purple. R<sup>2</sup> = 0.25, p = 0.003.

# Age-related Differences In Emotional fMRI Responses After Accounting for Cerebrovascular Reactivity Decline

L. Donaldson<sup>1</sup>, P. Joshi<sup>1</sup>, L. Kartchner<sup>1</sup>, S. Akar<sup>1</sup>, and P. Liu<sup>1</sup>

<sup>1</sup>Department of Diagnostic Radiology & Nuclear Medicine, University of Maryland School of Medicine, Baltimore, MD, USA

## Synopsis and/or Summary of Main Findings:

Age-related changes in emotional circuitry have been studied using BOLD fMRI and revealed age-related increases in the activation of the prefrontal cortex and inconsistent findings in the amygdala [1-3]. Since the BOLD response is based on neurovascular coupling, these findings could be confounded by vascular change, especially in view of the expected decline of vascular function with age [4]. In this study, using picture viewing task fMRI and CO<sub>2</sub>-inhalation MRI, we examined age-related differences in emotional fMRI responses in the context of vascular aging. We found that, after accounting for cerebrovascular reactivity (CVR) differences, increased age-related activation of prefrontal regions was observed compared to activation before vascular correction, whereas age-invariant activity was seen in the amygdala. Increased correlations between the fMRI responses and psychiatric measures were also seen in the prefrontal regions after accounting for CVR differences, while less correlations were observed in the amygdala.

## INTRODUCTION

Blood-Oxygenation-Level-Dependent (BOLD) functional MRI (fMRI) is an important tool to study neural activity. However, the BOLD response is based on neurovascular coupling, which could be confounded by vascular factors, especially with the expected decline of vascular function with age. Therefore, we conducted the present study to assess how the emotional circuit changes after accounting for age-related changes in cerebrovascular reactivity (CVR).

## METHODS

27 subjects (23-73yrs, 13F/14M) underwent a 10min task-evoked fMRI scan and a 7min hypercapnia-inhalation MRI scan on a 3T scanner using identical HCP BOLD-MRI protocols. The emotion perception task-fMRI used a block-designed paradigm with positive, negative, and neutral IAPS pictures (Figure 1a) [5]. CVR maps were obtained following standard GLM methods and CVR correction was performed as  $S_{fMRI,corr} = S_{fMRI,uncorr} / CVR$  [6,7]. Analysis was performed on three ROIs in the emotional network, the amygdala, the left and the right inferior frontal gyrus (IFG). Psychiatric measures of positive affectivity, cognitive reappraisal, agreeableness, extraversion, stress, and confusion were also obtained using self-report questionnaires. These measures were compared between the young and old groups, and their associations with the BOLD responses were evaluated before and after CVR correction.

## RESULTS AND DISCUSSION

Figure 1b shows the group activation map across all subjects in viewing the affective pictures. Amygdala, left and right IFGs were activated, confirming the involvement of the emotional circuit in our emotion perception task.

Figure 1c shows the group-averaged CVR maps. CVR in left and right IFGs were significantly lower in the older group ( $p=0.018$  and  $0.044$ , respectively, Figure 1d), although the age difference was not significant in the amygdala ( $p=0.14$ ). Figure 2 shows the group comparisons of fMRI signals between young and old in each ROI before and after CVR correction for different contrasts. The older subjects had significantly higher BOLD signals in the left IFG in all three contrasts, and became more significant after accounting for CVR differences. In the right IFG, before CVR correction, the older subjects showed a trend of higher fMRI signal only in the negative>positive contrast, but after CVR correction, this trend of higher fMRI signal was observed in all three contrasts. The age-related increase in frontal recruitment is thought to represent a compensatory activation that occurs in the aging brain to accommodate the decreased volume of neural tissue and declining efficiency of neural circuitry [8]. No significant group difference was found in the amygdala before or after correction, suggesting the function of the amygdala remains intact in aging.

For psychiatric measures, the older subjects generally had less negative feelings and higher positive moods compared to the young group, consistent with previous literature. Correlations of the psychiatric measures and the BOLD responses before and after CVR correction are shown in Table 1. Across all subjects, the frontal lobe responses showed positive associations with the psychiatric measures, which are more significant after CVR correction. In contrast, the amygdala showed less associations with the psychiatric measures after CVR correction.

## CONCLUSION

Accounting for age-related changes in vascular function could improve the examination of fMRI responses in emotional aging.

## References:

1. Tessitore A, Hariri AR, Fera F, Smith WG, Das S, Weinberger DR, et al. Functional changes in the activity of brain regions underlying emotion processing in the elderly. *Psychiatry Research*. 2005;139:9-18.
2. Leclerc CM, Kensinger EA. Age-related differences in medial prefrontal activation in response to emotional images. *Cognitive, Affective & Behavioral Neuroscience*. 2008a;8:153-164.
3. Mather M, Canli T, English T, Whitfield S, Wais P, Ochsner K, et al. Amygdala responses to emotionally valenced stimuli in older and younger adults. *Psychological Science*. 2004;15:259-263.
4. Lu H, Xu F, Rodrigue KM, Kennedy KM, Cheng Y, Flicker B, Hebrank AC, Uh J, Park DC. Alterations in cerebral metabolic rate and blood supply across the adult lifespan. *Cereb Cortex*. 2011 Jun;21(6):1426-34.
5. Lang PJ, Bradley MM, Cuthbert BN. International affective picture system (IAPS) Gainesville, FL: University of Florida; 1997.

6. Lu H, Kashani AH, Arfanakis K, Caprihan A, DeCarli C, Gold BT, Li Y, Maillard P, Satizabal CL, Stables L, Wang DJJ, Corveau RA, Singh H, Smith EE, Fischl B, van der Kouwe A, Schwab K, Helmer KG, Greenberg SM; MarkVCID Consortium. MarkVCID cerebral small vessel consortium: II. Neuroimaging protocols. *Alzheimers Dement*. 2021 Apr;17(4):716-725.
7. Liu P, De Vis JB, Lu H. Cerebrovascular reactivity (CVR) MRI with CO<sub>2</sub> challenge: A technical review. *Neuroimage*. 2019 Feb 15;187:104-115.
8. Cabeza R, Anderson ND, Locantore JK, McIntosh AR. Aging gracefully: compensatory brain activity in high-performing older adults. *Neuroimage*. 2002;17:1394-1402.

## Figures and Tables

Amygdala	Uncorrected			Corrected		
	c2 (pos-neu)	c3 (neg-neu)	c4 (neg-pos)	c2 (pos-neu)	c3 (neg-neu)	c4 (neg-pos)
Positive Affectivity	0.364*	0.371*	0.304	-0.117	0.242	0.321
Cognitive Reappraisal	0.024	0.00129	0.047	-0.357*	-0.139	0.0403
Stress	0.377*	0.477**	0.437**	0.057	0.357*	0.401*

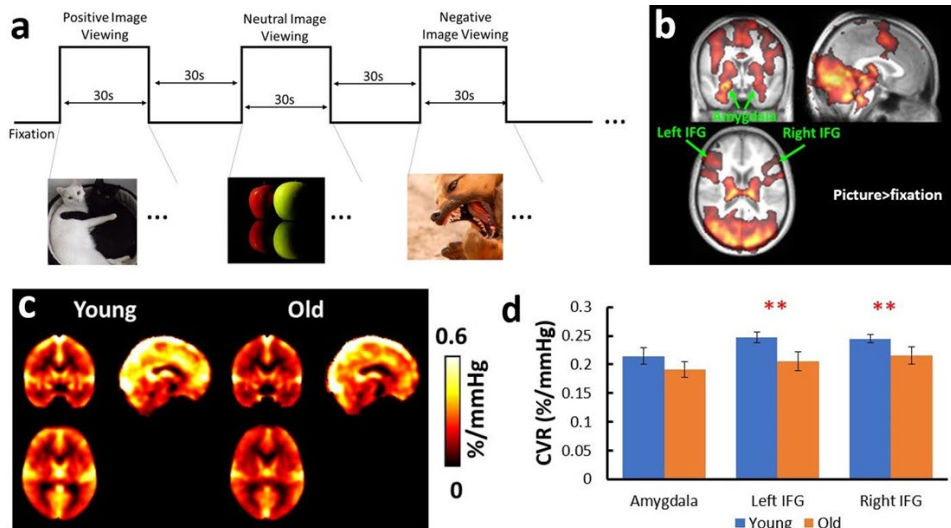
  

Left IFG	Uncorrected			Corrected		
	c2 (pos-neu)	c3 (neg-neu)	c4 (neg-pos)	c2 (pos-neu)	c3 (neg-neu)	c4 (neg-pos)
Positive Affectivity	0.362*	0.322	0.3	0.377*	0.374*	0.372*
Extraversion	0.288	0.326	0.334*	0.292	0.29	0.277
Agreeableness	0.282	0.341*	0.37*	0.497**	0.535***	0.524***
Confusion	0.257	0.283	0.312	0.313	0.315	0.314

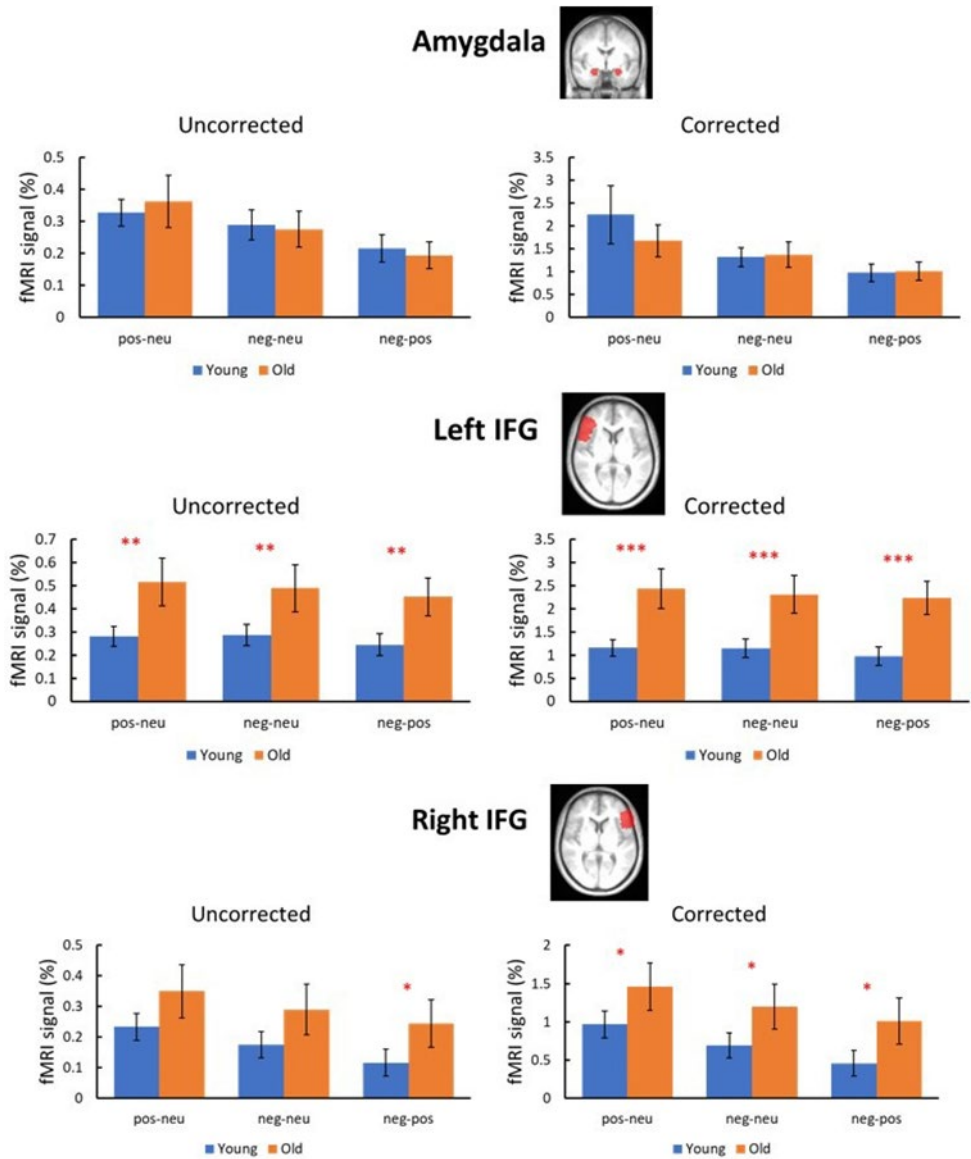
  

Right IFG	Uncorrected			Corrected		
	c2 (pos-neu)	c3 (neg-neu)	c4 (neg-pos)	c2 (pos-neu)	c3 (neg-neu)	c4 (neg-pos)
Positive Affectivity	0.439**	0.406**	0.369*	0.397*	0.442**	0.476**
Extraversion	0.368*	0.37*	0.42**	0.402*	0.399*	0.448**
Stress	0.452**	0.384*	0.336*	0.516***	0.457**	0.413**

**Table 1. Correlation coefficients between psychiatric measures and fMRI signal in the amygdala, left IFG, and right IFG. \* indicates  $0.05 < p < 0.1$ . \*\* indicates  $0.01 < p < 0.05$ . \*\*\* indicates  $p < 0.01$ .**



**Figure 1. Task-fMRI and CVR results. (a) Block diagram for the emotional task paradigm. (b) Group activation map showing the picture > fixation contrast. (c) Averaged CVR maps for the young and old groups. (d) Comparison of CVR values in the young and old groups in the amygdala, left IFG, and right IFG. \*\* indicates  $0.01 < p < 0.05$ .**



**Figure 2.** Comparisons of BOLD responses in amygdala, left IFG, and right IFG between young and old subjects before and after CVR correction. \* indicates  $0.05 < p < 0.1$ . \*\* indicates  $0.01 < p < 0.05$ . \*\*\* indicates  $p < 0.01$ .

# Impact of Caffeine on Cerebrovascular Reactivity in Caffeine-naïve healthy adults

Dinil Sasi S<sup>1</sup>, Cuimei Xu<sup>1</sup>, Zhiyi Hu<sup>1</sup>, Dengrong Jiang<sup>1</sup>, Abhay Moghekar<sup>2</sup>, Peiying Liu<sup>3</sup>, Hanzhang Lu<sup>1,4</sup>

<sup>1</sup> The Russell H. Morgan Department of Radiology & Radiological Science, Johns Hopkins University, Baltimore, Maryland, USA

<sup>2</sup>Department of Neurology, Johns Hopkins University, Baltimore, Maryland, USA

<sup>3</sup>Department of Radiology, University of Maryland, Baltimore, Maryland, USA

<sup>4</sup>F. M Kirby Center for Functional Brain Imaging, Kennedy Krieger Institute, Baltimore, Maryland, USA

## Synopsis:

Caffeine is a widely consumed psychoactive substance that acts as an adenosine receptor antagonist. This means that it blocks the effects of adenosine, a neuromodulator that plays a role in vasodilation and regulation of cerebral blood flow (CBF). However, the impact of caffeine on cerebrovascular reactivity (CVR) is not well understood. This study is designed to understand the impact of caffeine on whole brain CVR measured using quantitative CBF during a hypercapnia challenge in caffeine-naïve healthy adults. The results showed that caffeine caused a significant reduction in CVR and venous oxygenation (Yv). This suggests that caffeine reduces the ability of cerebral vessels to dilate in response to a vasoactive challenge in caffeine-naïve healthy adults. This could be due to the binding of caffeine molecules to adenosine receptors to reduce its capability for vasodilation.

## Introduction:

Caffeine is one of the most widely used psycho-active substances. It acts adversary to adenosine, a neuromodulator responsible for vasodilation and regulation of cerebral blood flow (CBF) to cause vasoconstriction and results in decrease in CBF and venous oxygenation<sup>1</sup>. Cerebrovascular reactivity (CVR) is an important neuroimaging biomarker which quantifies the ability of cerebral vessels to dilate or constrict in response to vasoactive challenges such as acetazolamide injection or hypercapnia<sup>2</sup>. However, the impact of caffeine on CVR is not well explored. So, this study is designed to understand the impact of Caffeine on whole brain CVR measured using phase contrast (PC) MRI during a hypercapnia challenge.

## Methods:

Experimental procedure: The study design consisted of a baseline (pre-caffeine) CVR measurement using PC-MRI<sup>3</sup> (to measure global change in blood flux (BF) (in ml/min)) during normal air breathing and hypercapnia using 5% CO<sub>2</sub> enriched gas mixture (5% CO<sub>2</sub>, 21% O<sub>2</sub>, 74% N<sub>2</sub>) and T2-Relaxation-Under-spin-Tagging (TRUST)<sup>4,5</sup> (to measure venous oxygenation (Yv)). Then, a 200 mg caffeine tablet (equivalent to 2 cups of coffee) was orally administered to the subjects followed by a break for 25 minutes, and repeated CVR and TRUST measurements were performed following that. The detailed setup for hypercapnia experiment is described elsewhere<sup>3</sup>. 7 healthy caffeine-naïve volunteers with a mean age 27.7±3.9 (4 male and 3 female) were scanned on Philips Ingenia 3T system using a 32 channel receiver head coil. The MRI parameters for PC-MRI were: field-of-view (FOV) = 240×240 mm<sup>2</sup>, matrix size = 400×400, thickness = 5mm, TR/TE = 18.7/9.1 ms and scan duration =62 s. TRUST sequence was acquired using previously published protocol<sup>5</sup>.

## Data analysis:

To compute BF from PC-MRI, region-of-interest was manually drawn on complex difference images, and the total flux was computed from phase images. The envelope for EtCO<sub>2</sub> was measured using an envelope detection algorithm, and PC-CVR was computed as Eq. (1).

$$CVR = 100 * ((BF_{HC} - BF_{RA}) / BF_{RA}) / (EtCO_{2HC} - EtCO_{2RA}) \quad (1)$$

Where, subscripts RA and HC represent values during room air and hypercapnia, respectively. TRUST images were processed using the previously published pipeline<sup>4</sup>. Relative percentage variation (RPV) and a paired t-test with 2-tail distribution was used as statistical measures to evaluate the results

## Results:

Figure-1 shows the EtCO<sub>2</sub> curves (a) and the corresponding ROIs in complex difference images (b) acquired during RA and HC state acquired before and after caffeine administration. Even though both RA and HC EtCO<sub>2</sub> values reduced post-caffeine, there was no effect on the difference in EtCO<sub>2</sub>. However, both RA and HC BF reduced after Caffeine administration. Figure-2 (a) and (b) shows the bar graphs of CVR and Yv and computed from all 7 subjects used in this study. CVR and Yv exhibited 32% and 23% RPV post caffeine with p < 0.001 (paired t tests).

## Discussion and Conclusion:

In this study, we evaluated the effect of Caffeine on CVR in Caffeine naïve healthy adults. The preliminary results show that caffeine introduced a significant reduction CVR and Yv in SSS. This could be due to the binding of caffeine molecules to adenosine receptors to reduce its capability for vasodilation.

**Acknowledgments / Funding Information:** NIH grant R01 NS106702.

## References:

- Xu, F., Liu, P., Pekar, J. J. & Lu, H. Does acute caffeine ingestion alter brain metabolism in young adults? *Neuroimage* 110, 39–47 (2015).
- Sleight, E., Stringer, M. S., Marshall, I., Wardlaw, J. M. & Thrippleton, M. J. Cerebrovascular Reactivity Measurement

Using Magnetic Resonance Imaging: A Systematic Review. *Frontiers in Physiology* vol. 12 Preprint at <https://doi.org/10.3389/fphys.2021.643468> (2021).

3. Sur, S. et al. CO<sub>2</sub> cerebrovascular reactivity measured with phase-contrast MRI: A potential biomarker of cognition and physical function in older adults. *Alzheimer's & Dementia* 16, (2020).

4. Lu, H. et al. Calibration and validation of TRUST MRI for the estimation of cerebral blood oxygenation. *Magn Reson Med* 67, 42–49 (2012).

5. Jiang, D. et al. Cross-vendor harmonization of T2-relaxation-under-spin-tagging (TRUST) MRI for the assessment of cerebral venous oxygenation. *Magn Reson Med* 80, 1125–1131 (2018).

**Figures:**

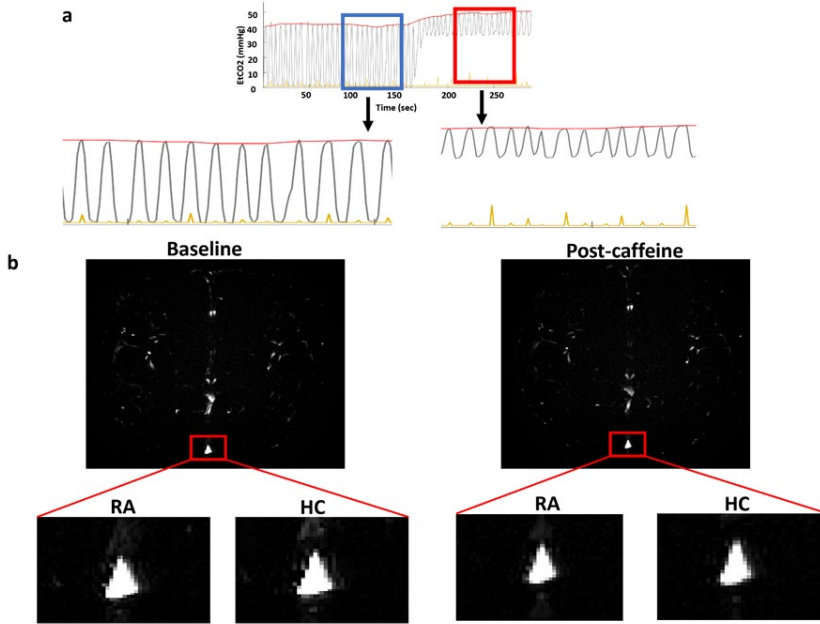


**Figure-1:** (a) End-tidal CO<sub>2</sub> (EtCO<sub>2</sub>) curve acquired from a representative subject during room air (RA) (highlighted with blue box) and hypercapnia (HC) (highlighted with red box). Corresponding region of interest (superior sagittal sinus (SSS)) in the complex difference images acquired before and after caffeine administration is shown in (b)

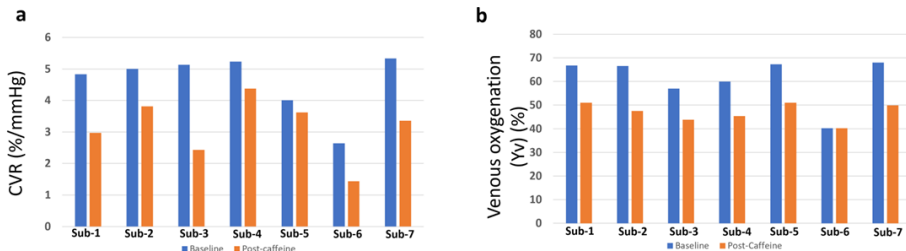


**Figure 2:** Subject-wise barplots of (a) Phase contrast CVR (in %/mmHg) , and (b) venous oxygenation (Y<sub>v</sub> (%)) computed before and after Caffeine administration

# Blood-brain barrier permeability measured with ASL differs between cognitive stages and amyloid status

Beatriz E. Padrela<sup>a,b</sup>, Sandra Tecelão<sup>c</sup>, Oliver Geier<sup>d</sup>, Markus Sneve<sup>e</sup>, David Vallez Garcia<sup>a,b</sup>, Lene Pålhaugen<sup>c,f</sup>, Bjørn-Eivind Kirsebom<sup>g,h</sup>, Atle Bjørnerud<sup>g,i</sup>, Anders M. Fjell<sup>g,i</sup>, Kristine B. Walhovde<sup>j</sup>, Frederik Barkhof<sup>a,b,j</sup>, Per Selnes<sup>c</sup>, Jan Petr<sup>a,c,k</sup>, Tormod Fladby<sup>c,f</sup>, Henk J.M.M. Mutsaerts<sup>a,b</sup>

<sup>a</sup>Department of Radiology and Nuclear Medicine, Amsterdam University Medical Center, Location VUmc, Amsterdam, the Netherlands;

<sup>b</sup>Brain Imaging, Amsterdam Neuroscience, Amsterdam, the Netherlands;

<sup>c</sup>Department of Neurology, Akershus University Hospital, Oslo, Norway;

<sup>d</sup>Department of Physics and Computational Radiology, Division of Radiology and Nuclear Medicine, Oslo University Hospital, Oslo, Norway;

<sup>e</sup>Department of Psychology, Center for Lifespan Changes in Brain and Cognition, University of Oslo, Oslo, Norway;

<sup>f</sup>Institute of Clinical Medicine, Campus Ahus, University of Oslo, Oslo, Norway;

<sup>g</sup>Department of Neurology, University Hospital of North Norway, Tromsø, Norway;

<sup>h</sup>Department of Psychology, Faculty of Health Sciences, UiT The Arctic University of Norway, Tromsø, Norway;

<sup>i</sup>Computational Radiology and Artificial Intelligence, Division of Radiology and Nuclear Medicine, Oslo University Hospital, Oslo, Norway;

<sup>j</sup>Queen Square Institute of Neurology and Centre for Medical Image Computing (CMIC), University College London, London, UK

<sup>k</sup>Helmholtz-Zentrum Dresden-Rossendorf, Institute of Radiopharmaceutical Cancer Research, Dresden, Germany

## Summary of Main Findings:

In this study, we investigated the permeability of the blood-brain barrier (BBB) non-invasively with a multi-post-labeling delay and multi-echo 3D GRASE ASL-MRI sequence. This sequence was used to calculate time of exchange (Tex) maps of the brain, where lower Tex is a proxy of higher BBB water permeability. We included 116 participants from two different centers. Our results show that Tex GM values were significantly different between cognitively normal and mild cognitive impaired patients, as well as between amyloid negative and amyloid positive groups, even corrected for age, sex and CBF. This suggests that BBB-ASL maps can be a potential early imaging biomarker in AD pathophysiology.

## Introduction

Blood-brain barrier (BBB) permeability changes may affect early mechanisms of Alzheimer's Disease (AD). Here, we evaluate changes in BBB water permeability between cognitive and amyloid status, measured non-invasively using arterial spin labeling (ASL) MRI.

## Methods

Participants older than 50 years were selected from the Dementia Disease Initiation (DDI) and from the Center for Lifespan Changes in Brain and Cognition (LCBC) cohorts (Table 1). All LCBC participants were cognitively normal (CN), while DDI included both CN and mild cognitive impairment (MCI)[1] participants. We separated the groups as CN\_LCBC, CN\_DDI, and MCI\_DDI. A recently developed multi-delay multi-echo BBB-ASL MRI sequence [2] was used to estimate cerebral blood flow (CBF) and time of exchange (Tex) of labeled blood water across the BBB [3]. Lower Tex is a proxy of higher BBB water permeability. Images were processed with ExploreASL[3,4], using a modified version of FSL FABBER[5] to quantify CBF and Tex[6] maps.

Amyloid status was defined from the CSF amyloid-beta 42/40 ratio (cut-off  $\leq 0.077$ ), or amyloid-PET when available. Tex and CBF associations with cognition and amyloid status were assessed using general linear models (GLMs) adjusted for age and sex. Statistical analyses were performed in R 4.1.2.

## Results

CBF tended to be higher in the A+ group but not statistically significant ( $t=-1.94$ ,  $p=0.06$ , Figure 1A)[7,8]. Tex was lower in A+ than A- ( $t=2.75$ ,  $p=0.01$ , Figure 1B). GLM analysis showed that both amyloid status and cognitive staging were predictive of BBB water permeability (Tex), with higher permeability in amyloid positive compared to amyloid negative groups, when correcting for age, sex, and CBF ( $\beta = -35.2$ ,  $p < 0.001$ ) (Table 2A). The same pattern was found in MCI subjects compared to healthy controls (Table 2B).

## Conclusion

Our findings suggest that BBB water permeability is increased in amyloid-positive participants as well as in MCI participants compared to CN, suggesting that BBB water permeability is a potential early imaging biomarker in AD pathophysiology.

## References

1. Fladby T, Pålhaugen L, Selnes P, Waterloo K, Bråthen G, Hessen E, et al. Detecting At-Risk Alzheimer's Disease Cases. *J Alzheimers Dis.* 2017;60: 97–105.
2. Cordes C, Konstantin S, Porter D, Günther M. Portable and platform-independent MR pulse sequence programs. *Magn Reson Med.* 2020;83: 1277–1290.

3. Mahroo A, Buck MA, Huber J, Breutigam N-J, Mutsaerts HJMM, Craig M, et al. Robust Multi-TE ASL-Based Blood-Brain Barrier Integrity Measurements. *Front Neurosci.* 2021;15: 719676.
4. Mutsaerts HJMM, Petr J, Groot P, Vandemaele P, Ingala S, Robertson AD, et al. ExploreASL: An image processing pipeline for multi-center ASL perfusion MRI studies. *Neuroimage.* 2020;219: 117031.
5. Clement P, Petr J, Dijsselhof MJB, Padrela B, Pasternak M, Dolui S, et al. A Beginner's Guide to Arterial Spin Labeling (ASL) Image Processing. *Frontiers in Radiology.* 2022;2. doi:10.3389/fradi.2022.929533
6. Chappell MA, Groves AR, Whitcher B, Woolrich MW. Variational Bayesian Inference for a Nonlinear Forward Model. *IEEE Trans Signal Process.* 2009;57: 223–236.
7. Fazlollahi A, Calamante F, Liang X, Bourgeat P, Raniga P, Dore V, et al. Increased cerebral blood flow with increased amyloid burden in the preclinical phase of alzheimer's disease. *J Magn Reson Imaging.* 2020;51: 505–513.
8. Padrela BE, Lorenzini L, Collij LE, Garcia DV, Coomans E, Ingala S, et al. Genetic, vascular, and amyloid components of cerebral blood flow in a preclinical population. *J Cereb Blood Flow Metab.* 2023; 271678X231178993.

## Figures and tables

	Total sample (n=116)	
	LCBC (n=77)	DDI (n=39)
Age (years)	64.6 ± 8.4	67.7 ± 7.94
Sex (female)	49 (64%)	20 (51%)
Cognitively normal (n)	77	24
MCI (n)	0	15
Total GM CBF (mL/100g/min)	58.3 ± 13.4	75.7 ± 23.2
Females (mL/100g/min)	61.4 ± 14.0	86.9 ± 21.9
Males mean value	52.9 ± 10.3	63.7 ± 18.2
Total GM Tex (s)	0.21 ± 0.04	0.18 ± 0.04
Females mean value	0.22 ± 0.04	0.20 ± 0.04
Males mean value	0.19 ± 0.02	0.17 ± 0.03

**Table 1:** Sample characteristics. Units are given as mean ± SD.

A	Amyloid status		Amyloid status + age + sex						Amyloid status + age + sex + CBF							
	$\beta$	<i>p</i>	$\beta$ (A+)	<i>p</i> (A+)	$\beta$ (age)	<i>p</i> (age)	$\beta$ (male)	<i>p</i> (male)	$\beta$ (A+)	<i>p</i> (A+)	$\beta$ (age)	<i>p</i> (age)	$\beta$ (male)	<i>p</i> (male)	$\beta$ (CBF)	<i>p</i> (CBF)
CBF total GM	10.7	*	13.3	**	-0.5	*	-8.4	*	-	-	-	-	-	-	-	-
Tex total GM	-0.028	**	-0.22	*	-0.001	**	-0.028	***	-0.035	***	-0.001	N.S.	-0.02	**	0.001	***

B	Cognitive staging				Cognitive staging + age + sex + CBF											
	$\beta$ (CN)	<i>p</i> (CN)	$\beta$ (MCI)	<i>p</i> (MCI)	$\beta$ (CN)	<i>p</i> (CN)	$\beta$ (MCI)	<i>p</i> (MCI)	$\beta$ (age)	<i>p</i> (age)	$\beta$ (male)	<i>p</i> (male)	$\beta$ (CBF)	<i>p</i> (CBF)		
CBF total GM	19.17	**	-0.5	*	-	-	-	-	-	-	-	-	-	-		
Tex total GM	-0.22	*	-0.001	**	-0.053	***	-0.051	***	-0.02	N.S.	-0.0002	N.S.	0.0014	***		

**Table 2:** CBF and Tex GM values associated with amyloid status (A) and cognitive staging (B) corrected for age and sex – and CBF in the case of Tex. Reference groups: CN\_LCBC for cognitive staging and female for sex. CBF: Cerebral blood flow; CN: CN corresponds to cognitively normal subjects from DDI, since the reference group is CN from LCBC; GM: Gray matter; Tex: time of exchange (proxy of BBB water permeability).  $p < 0.05$  \*,  $p < 0.01$  \*\*,  $p < 0.001$  \*\*\*.

# Mapping curvature domains in human V4 using CBV-sensitive layer-fMRI at 3T.

E. Zamboni<sup>1</sup>, I. Watson<sup>2</sup>, R. Goebel<sup>3</sup>, R. Stirnberg<sup>4</sup>, R. Huber<sup>5</sup>, A.J. Kennerley<sup>6</sup>, A.B. Morland<sup>7</sup>

<sup>1</sup>School of Psychology, University of Nottingham, Nottingham, UK, NG7 2RD;

<sup>2</sup>School of Physics, Engineering and Technology, University of York, York, UK, YO10 5DD;

<sup>3</sup>Department of Cognitive Neuroscience, Maastricht University, Maastricht, Netherlands;

<sup>4</sup>German Centre for Neurodegenerative Diseases, Bonn, Germany;

<sup>5</sup>National Institute of Health, Bethesda, USA;

<sup>6</sup>Institute of Sport, Department of Sports & Exercise Sciences, Manchester Metropolitan University,

Manchester, UK, M15 6BH; <sup>7</sup>Department of Psychology, University of York, York, YO10 5DD.

## Synopsis and/or Summary of Main Findings:

Understanding how cerebral physiology and brain functional properties are linked can inform on how we interpret the world: how does our visual brain recognise objects? Visual area V4 represents a vital intermediate stage of processing spatial and curvature information preceding object recognition<sup>1,2</sup>. Electrophysiological recordings and optical imaging studies<sup>3,4</sup> in macaques have identified a modular organisation of curvature responses in V4, that has not been observed in humans. Understanding how the functional architecture and hierarchical integration of local contours (curvature) contributes to formation of shapes can inform computational models of object recognition. Using Vascular Space Occupancy (VASO) fMRI, a Cerebral Blood Volume (CBV)-sensitive approach, which provides much higher specificity than standard BOLD acquisition, we probe the fine spatial organisation of the human visual system with high precision. By quantifying changes in CBV related to curvature/straight lines we unveil, for the first time, a modular organisation of curvature responses in human V4.

## Introduction:

The intermediate processing steps in human vision are not well characterised. It seems likely that simple features are combined into progressively more complex structures (curves, junctions, outlines). This intuition has been bolstered recently by the observation that macaque monkeys have 'patches' of visual cortex sensitive to curves<sup>3,4</sup> organised in a modular fashion known as curvature domains. fMRI work in humans<sup>5</sup> has reported a possible extended network of 'patches' involved in processing curvature, including area V4. Unfortunately, standard BOLD fMRI methods of assessing cerebral function reflect complex interplay between activity, blood oxygenation, blood volume, and other physiological parameters (including blood vessel geometry), rendering quantifiability and interpretability of the signal difficult. Vascular Space Occupancy (VASO) presents as the solution in providing measurements of Cerebral Blood Volume changes. Importantly these changes are spatially localised to cerebral microvasculature, thus enhancing spatial specificity and physiological interpretability (reduced effect of oxygenation related vascular changes and biases from large vasculature through and at the surface of the cortex<sup>6,7</sup>). Here we image the functional organisation of curvature responses in human V4 by measuring CBV responses using VASO at clinically relevant MR field strengths.

## Methods:

A 3D-EPI based VASO sequence was implemented and optimised<sup>8</sup> for use on Siemens MAGNETOM Prisma 3T scanner. CBV-based images had a nominal resolution of 1.2mm isotropic (20 slices, T1/TI2/TR/TE=1145/2115/2610/17.2 ms) and slice position and orientation were adjusted to cover ventrolateral visual cortex. During functional scans, participants (n=4) fixated at the centre of the screen while concentric circles (curved stimulus) and concentric squares (straight contours) were presented in a block design (31.32s ON-OFF; contrast of stimuli reversed every 522ms – Figure 1). Supporting retinotopic mapping data were acquired using standard BOLD sequence (52 slices, 2.5mm isotropic, TR/TE=1000/30ms), together with structural imaging using MP2RAGE for high resolution segmentation of grey/white matter. Data were analysed using custom MATLAB scripts and LAYNI was used for BOLD contamination correction. Curvature preference maps were obtained by computing, for each voxel in V4, the difference in peak haemodynamic response between visual stimuli.

## Results:

Following identification of visual field map for each hemisphere and participant, we identified the topography of curvature preference in area V4 (Figure 2) by colour coding preference for curvature (red) and straight lines (blue) and displaying these maps on a flat surface. These maps show a modular organisation of functional responses, with blobs and stripes alternating between visual functional areas with a preference for curvature and preference for straight lines. This is observed across the cortical depth (Figure 3). Furthermore, comparing topographies from CBV measures with BOLD data, it emerges how the former details improved organisation, suggesting that VASO indeed provides higher spatial specificity for studying the cerebral physiology underlying specific functions.

## Conclusion:

Using high resolution Vascular Space Occupancy at 3T we unmask, for the first time, curvature domains in human V4. To date, this has only been shown using invasive imaging methods in animal models, thus we demonstrate the feasibility and specificity of CBV-based measures to understand the fine-scale cortical organisation of human vision.

**Acknowledgments / Funding Information:** We thank the staff at the York Neuroimaging Centre for access of 3T MRI scanner and participants for enduring testing. We also thank Dr Omer Faruk Gulban from Brain Innovation and FPN Maastricht for his support with data visualisation. This project was funded by the York-Maastricht Partnership to RH-AJK & RG-AMB.

**References:** [1] Kobatake E, et al. J Neurophysiol. 1994;71(3):856-67; [2] Pasupathy A, et al. J Neurophysiol. 1999;82, 2490- 2502; [3] Hu JM, et al. eLife. 2020; 9:e57261; [4] Tang R, et al. eLife 2020; 9:e57502; [5] Yue X, et al. NeuroImage 2020; 222:117295; [6] Polimeni JR, et al. NeuroImage 2010; 52(4):1334-46; [7] Huber L, et al. NeuroImage 2019; 197:742-760; [8] Stirnberg R, et al. Mang Reson Med. 2020; 85(0):1540-1551

**Figures:**

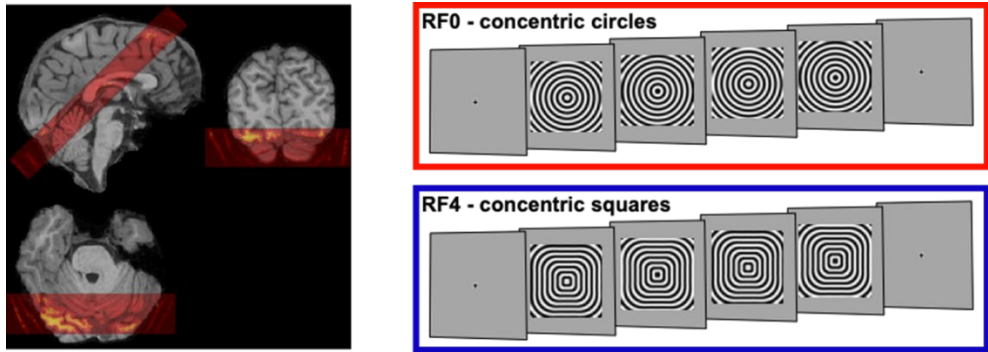


**Figure 1:** Slice coverage overlaid on whole brain MP2RAGE image. The panel on the left shows the schematic of stimulus blocks (concentric circles and concentric squares) presented during functional scans VASO acquisition.

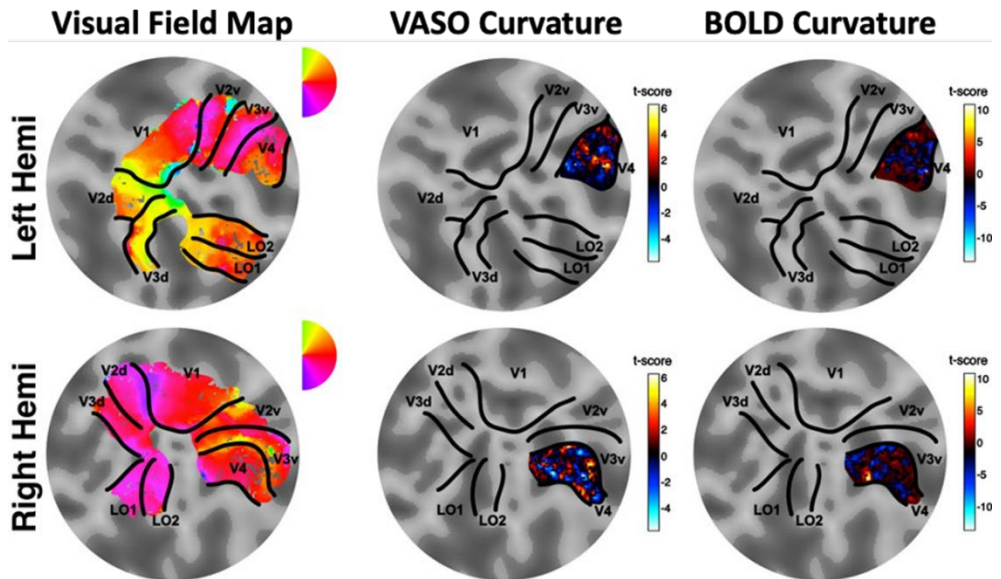


**Figure 2:** Overview of curvature maps for each hemisphere and participant. Column 1 shows visual field maps for left (top row) and right (bottom row) hemispheres; Column 2 shows curvature preference maps for CBV-based measures; Column 3 shows curvature preference maps for BOLD contrast. Modular organization has higher specificity in VASO compared to BOLD maps.

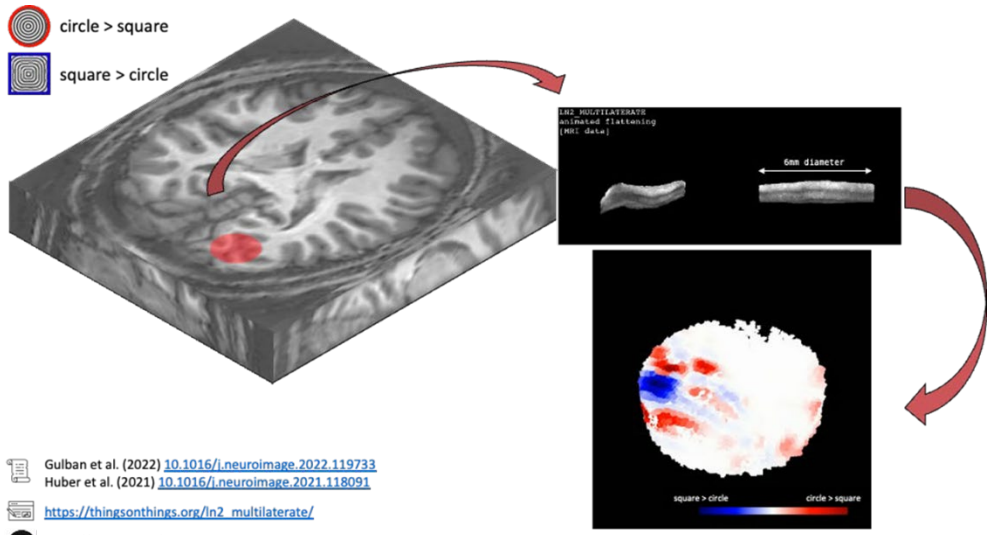


**Figure 3:** Schematic of curvature domains across cortical depth for one representative participant. Area V4 is segmented and extracted from the acquisition slab, flattened into a 6mm diameter disk, and the curvature preference map is projected across the cortical depth highlighting curvature domain organization in a laminar-resolved fashion.

# Combining vessel distance mapping and non-negative matrix factorization to identify arterial and venous patterns in the putamen

H. Mattern<sup>1,2,3</sup>, S. Schreiber<sup>2,3,4</sup>, O. Speck<sup>1,2,3,5</sup>

<sup>1</sup>Department of Biomedical Magnetic Resonance, Otto-von-Guericke University, Magdeburg, Germany;

<sup>2</sup>German Center for Neurodegenerative Disease, Magdeburg, Germany;

<sup>3</sup>Center for Behavioral Brain Sciences, Magdeburg Germany;

<sup>4</sup>Department of Neurology, Otto-von-Guericke University, Magdeburg Germany;

<sup>5</sup>Leibniz Institute for Neurobiology, Magdeburg, Germany

## Synopsis and/or Summary of Main Findings

Anatomical variability of the vascular structure, starting from the circle of Willis up to anastomoses of the pial vasculature, contribute to interindividual variance in MR-based physiology metrics. In this proof-of-principle study, we assess vascular patterns, i.e. vessel branching and distribution patterns, by combining vessel distance mapping (VDM) and non-negative matrix factorization (NMF) to identify distinct arterial and venous patterns in the human putamen of healthy volunteers. Distinct arterial and venous patterns can be identified with the proposed approach in an automatic and interpretable manner, requiring follow-up investigations to prove robustness and applying them in physiology studies.

## Abstract Body

Given the immense anatomical variability of the vascular structure, starting from the circle of Willis up to anastomoses of the pial vasculature, assessing vascular patterns, i.e. vessel branching and distribution patterns, is key to understand interindividual variance in MR-based physiology metrics. Here we leverage vessel distance mapping (VDM) and non-negative matrix factorization (NMF) to identify distinct arterial and venous patterns in the human putamen of healthy volunteers.

In a nutshell, VDM quantifies the distance of each point in space to the vasculature of interest and has been used to assess vascular resilience in cerebral small vessel disease<sup>1</sup>. NMF decomposes an input matrix with the constraint of only positive values, unlike other decomposition techniques. By enforcing orthogonal projections in NMF, i.e. OPNMF, this provides interpretable and sparse parcellations of brain structures<sup>2</sup>.

As a proof-of-principle, high resolution Time-of-Flight angiography and T2\*-weighted data from publicly available "StudyForrest" dataset was re-used in this study<sup>3,4</sup>. In total, arterial and venous distance maps of 40 hemispheres (20 volunteers) were generated as follows (see Fig.1): i) enhance vessels with Frangi filter and automatic thresholding for binary segmentation as provided by the OMELETTE toolbox<sup>5,6</sup>, ii) computation of VDM by computing the Euclidian distance of each voxel to its closest segmented vessel, iii) spatial normalization into MNI space. To identify patterns via OPNMF, the distance maps per hemisphere were cropped to the putamen and flattened to generate an input matrix so size (#putamen voxels × #hemispheres). The OPNMF decomposes the input into the component matrix  $W$  (#voxels ×  $k$ ) and weight matrix  $H$  ( $k$  × #hemispheres) with  $k$  being the number of components set by the user. In this preliminary study,  $k$  was empirically set to 3 for arterial and venous decomposition, respectively. After reshaping  $W$ , the components can be viewed as 3D patterns while  $H$  provides per hemisphere the weights of the components required to reconstruct the input data<sup>2</sup>. These weights enable hierarchical clustering of subjects (Ward linkage used).

Results for arterial and venous patterns, i.e. reshaped  $W$ , and the clustered weights, i.e.  $H$ , are shown in Fig.2 and Fig.3, respectively. Enforced by the orthogonality, the components represent distinct parts of the putamen, e.g. pattern #3 and #2 represent increased arterial and venous distances at the putamen head, respectively. Overall, these patterns agree with visually perceived variances in the data. The weights show that hemispheres can be clustered into distinct groups. Within this preliminary study, the feasibility of VDM and OPNMF to automatically identify vessel patterns in an interpretable manner has been shown. Follow-up investigations are required to enable data-driven selection of the number of components, show the robustness of the approach, and compare the found patterns to expert ratings. In the future, automatic pattern identification could be used to assess interindividual variability in the brain physiology and move the field beyond the assumption of a global, normative vascular structure towards individualized vessel architecture assessment.

**Acknowledgments / Funding Information:** This work was funded by the Deutsche Forschungsgemeinschaft (DFG) (MA 9235/3-1/SCHR 1418/5-1 (501214112), MA 9235/1-1 (446268581), CRC 1436 (B04, 425899996), and RTG 2413 (SynAGE, 362321501)) and by the Deutsche Alzheimer Gesellschaft (DAG) e.V. (MD-DARS project).

## References

1. Garcia-Garcia, Berta, et al. "Vessel distance mapping: a novel methodology for assessing vascular-induced cognitive resilience." *Alzheimer's & Dementia* 18 (2022): e063391.
2. Robert, Corinne, et al. "Analyses of microstructural variation in the human striatum using non-negative matrix factorization." *NeuroImage* 246 (2022): 118744.
3. <https://www.studyforrest.org/data.html>
4. Hanke, Michael, et al. "High-resolution 7-tesla fmri data on the perception of musical genres—an extension to the studyforrest dataset." *F1000Research* 4 (2015): 174.
5. <https://gitlab.com/hmattern/omelette>
6. Mattern, Hendrik. "Openly available sMall vEssel sEGmenTaTion pipelinE (OMELETTE)." *Proc. 883 Intl. Soc. Mag. Reson. Med* 884 (2021).

Figures

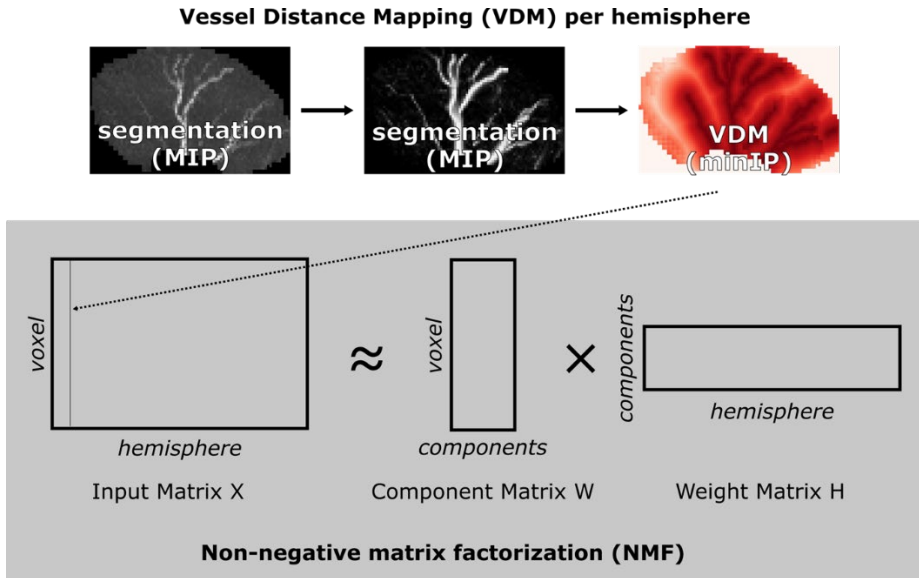


**Fig.1:** Analysis pipeline. Per putamen, vessels are segmented and vessel distance maps computed (displayed as maximum intensity projections (MIP) and minimum intensity projections (minIP)). The flattened distance maps (40 in total) are stacked to create the input matrix (#putamen voxels x #hemispheres). The input matrix is decomposed via NMF to create a component matrix  $W$  (#putamen voxels x components) and weight matrix  $H$  (components x #hemispheres).

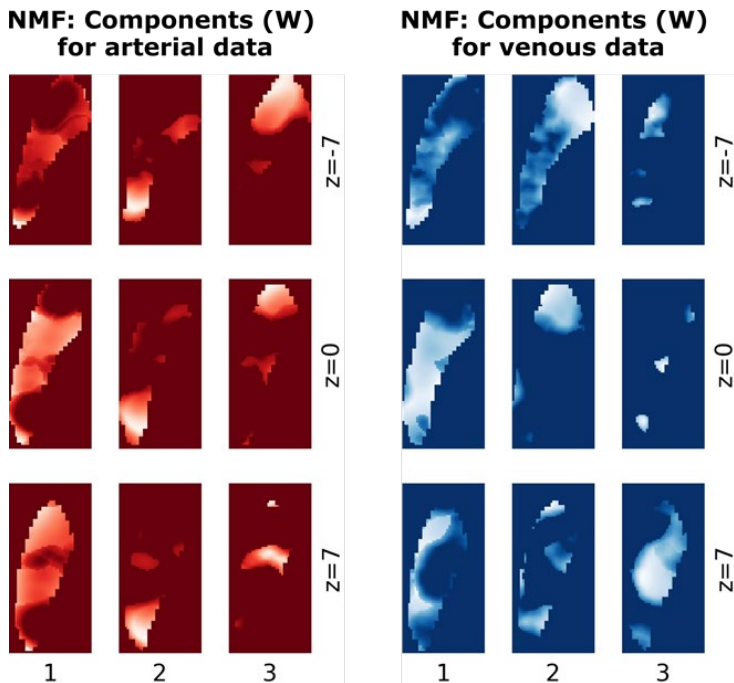


**Fig.2:** Overview of the three arterial and venous patterns found, respectively, via NMF after reshaping the  $W$  matrix. Patterns are shown in axial views at three different levels along the head-foot-direction.

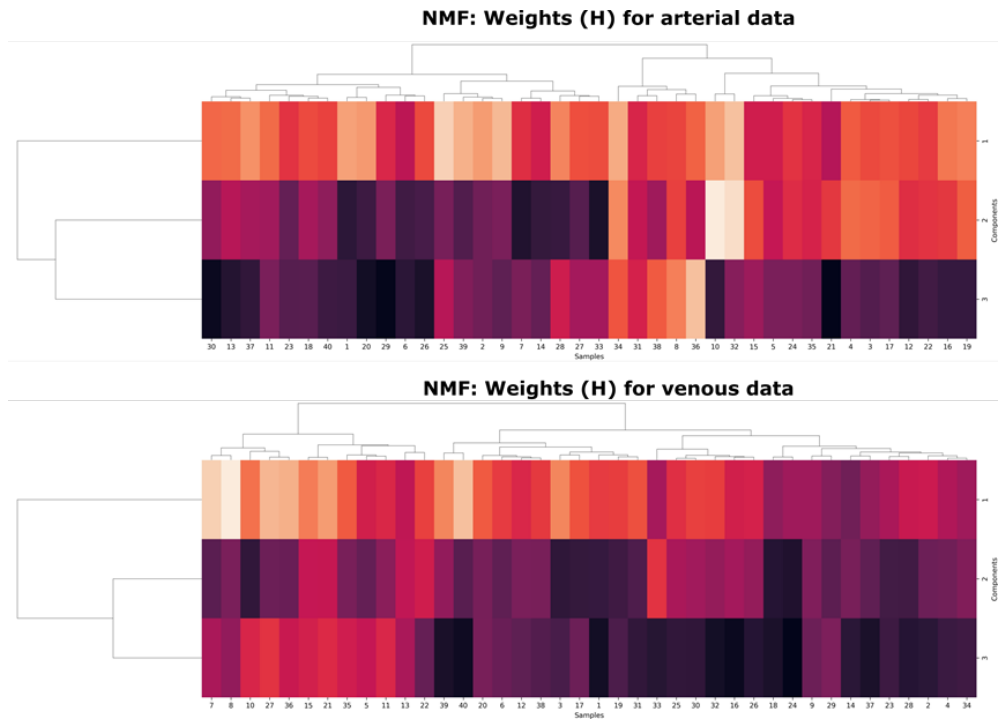


**Fig.3:** Overview of the arterial and venous weights matrix  $H$ , respectively. Based on the weights, representing the contribution of each component/pattern for each hemisphere, the putamen can be clustered, indicating the presence of distinct, interindividual vascular patterns in the human putamen.

# Detectability of White Matter Perfusion Across Flow Territories When Using Arterial Spin Labeling MRI: Impact of Hematocrit and Bolus Arrival Times

W.T. Richerson<sup>1</sup>, M.A. Aumann<sup>1</sup>, A.K. Song<sup>1,2</sup>, S. Davis<sup>3</sup>, N.J. Patel<sup>3</sup>, J.J. Eisma<sup>1</sup>, L.C. Jordan<sup>3</sup>, and M.J. Donahue<sup>1</sup>

<sup>1</sup>Neurology, Vanderbilt University Medical Center, Nashville, TN, United States;

<sup>2</sup>Vanderbilt Brain Institute, Vanderbilt University, Nashville, TN, United States;

<sup>3</sup>Pediatrics, Division of Pediatric Neurology, Vanderbilt University Medical Center, Nashville, TN, United States

## Synopsis and/or Summary of Main Findings

The goal of this work is to revisit white matter (WM) cerebral blood flow (CBF) quantification with 3-Tesla arterial spin labeling (ASL) MRI, using recent sequence advances, over a range of inversion times (TIs) and CBF in healthy adults (n=12) and adults with elevated CBF and reduced bolus arrival time (BAT) secondary to sickle cell disease (SCD) (n=33). WM border-zone signal was detectable in SCD patients, but not in controls. WM CBF was observed to be higher across all flow territories in SCD vs. control participants, but BAT was only marginally reduced in SCD relative to healthy participants. WM CBF trended weakly with hematocrit (Spearman- $\rho$ =-0.20;  $p$ =0.26), but BAT was strongly associated with hematocrit (Spearman- $\rho$ =0.55;  $p$ <0.001) suggesting that BAT is more dependent on hematocrit than CBF. Findings suggest that WM CBF can be quantified reliably in SCD, and in all but border-zone regions in healthy adults, using appropriately parameterized ASL scans.

## Abstract Body

**INTRODUCTION:** The goal of this work is to revisit the possibility of quantifying white matter (WM) cerebral blood flow (CBF) with 3-Tesla arterial spin labeling (ASL) MRI, using recent sequence and hardware advances, over a range of inversion times (TIs) and CBF in healthy adults and adults with elevated CBF and reduced bolus arrival time (BAT) secondary to sickle cell disease (SCD). Despite the majority of silent and overt infarcts being localized to WM, ASL has been suggested to lack WM CBF sensitivity owing to lower WM CBF and longer WM BAT compared to blood-water T11,2. However, increased CBF, decreased BAT in SCD patients and recent ASL advances may enable WM CBF quantification<sup>3,4</sup>. We performed multi-delay Look-Locker ASL in healthy and SCD participants and quantified signal reliability over a range of CBF and BAT, as well as relationships between CBF, BAT, and hematocrit (Hct).

## METHODS:

33 SCD (hemoglobin-SS) and 12 healthy age-matched (hemoglobin-AA) adults provided informed consent. Total hemoglobin and hemoglobin-S fraction were recorded in SCD patients. On the same day, participants were scanned at 3-Tesla using a novel pulsed ASL (PASL) sequence (repetitions=25; TIs=16; TI-range=200-3200ms; resolution=3x3x7mm; slices=9; acquisition time=6min56s) with Look-Locker readout and labeling 100 mm proximal to the imaging volume. Using the CBF-weighted signal ( $\Delta M/M_0$ ), we performed one-sample t-tests at each TI comparing the signal measured to null signal<sup>5</sup> and used mean  $\Delta M/M_0$  over time and FSL-BASIL to fit the three-stage kinetic model for CBF and BAT, accounting for Hct on arterial blood T16,7,8. CBF was quantified in total gray matter (GM) and WM; as well as anterior, middle, and anterior-middle cerebral artery border-zone WM territories<sup>9</sup>. Group level CBF and BAT was contrasted in each region using a Wilcoxon rank-sum test; group one-sample t-statistic curves were plotted against significant detection ( $p$ <0.05), and relationships between

(i) CBF and (ii) BAT with hemoglobin were evaluated with Spearman rank-correlation. Significance was defined as  $p$ <0.05.

## RESULTS:

Signal was one standard deviation above  $p$ <0.05 over the WM for each group (controls: TI=1400ms, SCD: TI=800-1800ms), peaking at TI=1200ms in SCD and TI=1400ms in controls (Figure 1). Border-zone ASL signal was detected at TI=1400ms in SCD, but was not detected in controls. SCD CBF was observed to be significantly higher across all regions (SCD CBF: GM=63.7±19.5mL/100g/min WM=19.3±7.2mL/100g/min; Control CBF: GM=35.2±10.0mL/100g/min WM=8.6±1.8mL/100g/min), but only whole WM BAT was reduced in SCD relative to healthy participants (Control BAT: GM=632±88ms WM=920±75ms; SCD BAT: GM=601±85ms WM=866±86ms) (Figures 2-3), indicating that low CBF, rather than prolonged BAT, may be most relevant to WM CBF detectability. WM CBF trended weakly with Hct (Spearman- $\rho$ =-0.20;  $p$ =0.26), but BAT was significantly associated with Hct (Spearman- $\rho$ =0.55;  $p$ <0.001) suggesting that BAT is more dependent on Hct than CBF.

## CONCLUSION:

We used a novel PASL sequence to demonstrate WM CBF quantitation feasibility in healthy and SCD participants and report that WM CBF quantification in major flow territories is more viable than previously appreciated even for healthy hemoglobin levels; the predominant contributor to lower WM CBF detectability was observed to be CBF magnitude rather than BAT prolongation.

## References:

1. Ford, A. L. et al. Silent infarcts in sickle cell disease occur in the border zone region and are associated with low cerebral blood flow. *Blood* 132, 1714–1723 (2018).
2. van Gelderen, P., de Zwart, J. a. & Duyn, J. h. Pitfalls of MRI measurement of white matter perfusion based on arterial spin labeling. *Magnetic Resonance in Medicine* 59, 788–795 (2008).
3. Bush, A. et al. Pseudo Continuous Arterial Spin Labeling Quantification in Anemic Subjects with Hyperemic Cerebral Blood Flow. *Magn Reson Imaging* 47, 137–146 (2018).
4. Juttukonda, M. R. et al. Cerebral hemodynamics and pseudo-continuous arterial spin labeling considerations in adults

with sickle cell anemia. *NMR in Biomedicine* 30, 1–9 (2017).

5. van Osch, M. J. P. et al. Can arterial spin labeling detect white matter perfusion signal? *Magnetic Resonance in Medicine* 62, 165–173 (2009).

6. Buxton, R. B. et al. A general kinetic model for quantitative perfusion imaging with arterial spin labeling. *Magnetic Resonance in Medicine* 40, 383–396 (1998).

7. Chappell, M. A. et al. Separation of macrovascular signal in multi-inversion time arterial spin labelling MRI. *Magnetic Resonance in Medicine* 63, 1357–1365 (2010).

8. Lu, H., Clingman, C., Golay, X. & Van Zijl, P. C. M. Determining the longitudinal relaxation time ( $T_1$ ) of blood at 3.0 Tesla. *Magnetic Resonance in Medicine* 52, 679–682 (2004).

9. Liu, C.-F. et al. Digital 3D Brain MRI Arterial Territories Atlas. *Sci Data* 10, 74 (2023).

## Figures

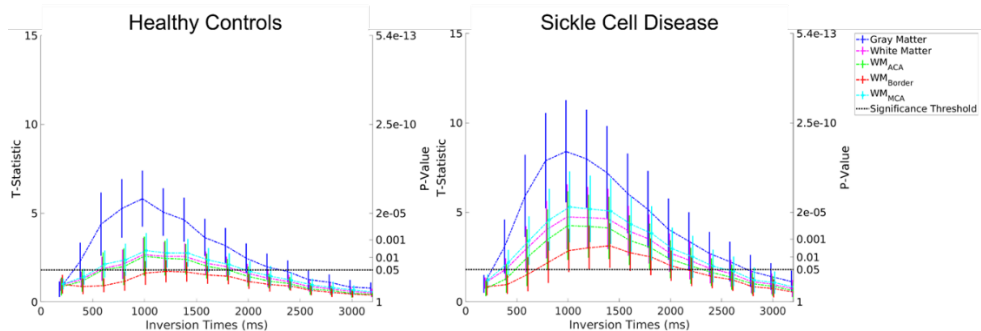


**Figure 1:** Resulting t-statistic of a one-sample t-test relative to zero perfusion, using all 25 repetitions at each inversion time (TI) as a sample distribution of perfusion in each region and white matter flow territory. The time courses are the group mean t-statistic at each TI while the vertical lines are the standard deviation at each TI. The dashed horizontal line is at  $p=0.05$ , where we considered the signal to be significantly detected relative to no perfusion.

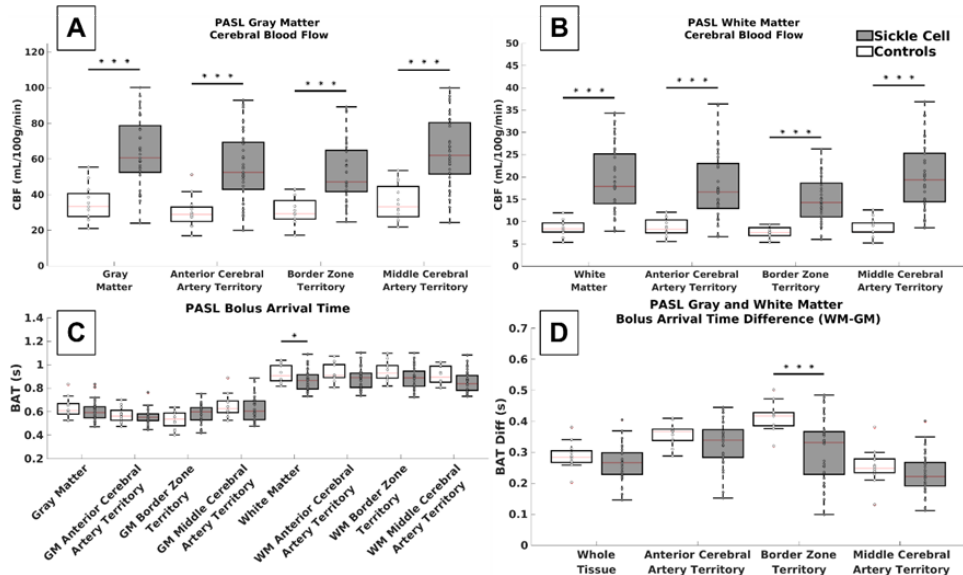
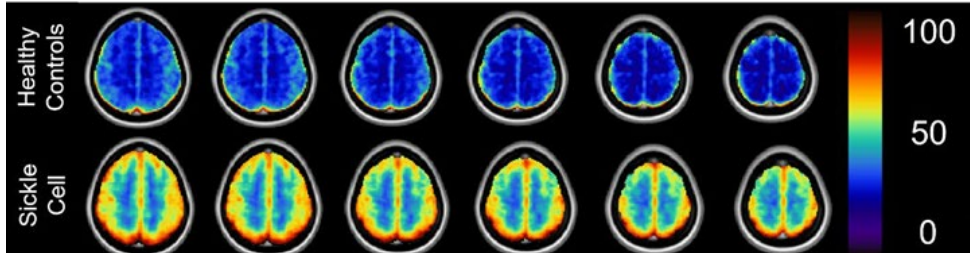


**Figure 2:** Mean cerebral blood flow (CBF; A and B), bolus arrival time (BAT; C) and BAT difference between white and gray matter (D) across all flow territories. CBF is significantly increased in Sickle Cell Disease (SCD) patients across all regions. BAT is only significantly longer in SCD patients in the gray matter border-zone region, while most territories are shorter in SCD patients, non-significant differences indicate that BAT is not a limiting factor in perfusion detection.

## Cerebral Blood Flow (mL/100g/min)



## Bolus Arrival Time (s)

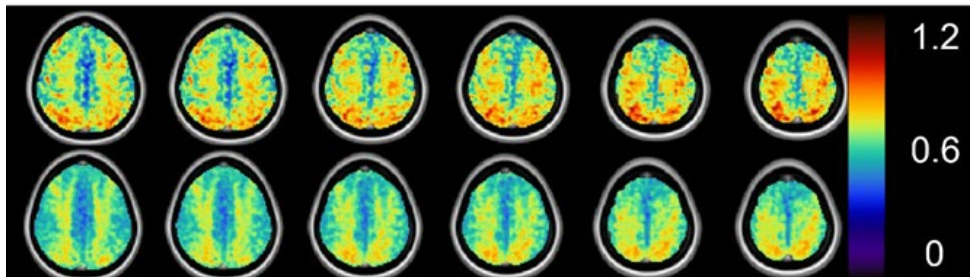


**Figure 3:** Group averaged cerebral blood flow (CBF) and blood tissue arrival time (BAT) overlaid in MNI152 T1 2 mm space in sickle cell disease patients and healthy controls. CBF is much higher across all regions in the brain and BAT is shorter in sickle cell disease patients. Longest BAT can be found in the border-zone region of the white matter in both groups.

# Cerebral blood flow as an intermediary between cardiovascular and cerebrovascular health: results from the Insight46 study

Mathijs B.J. Dijsselhof<sup>1,2</sup>, Sarah-Naomi James<sup>3</sup>, Luigi Lorenzini<sup>1,2</sup>, Lyduine E. Collij<sup>1,2</sup>, David L. Thomas<sup>4,5</sup>, Catherine J Scott<sup>5</sup>, Emily Manning<sup>5</sup>, Tamás I. Józsa<sup>1,2</sup>, Dave Cash<sup>5</sup>, Insight 46 study team<sup>5</sup>, Carole Sudref<sup>3</sup>, Alun D. Hughes<sup>3</sup>, Marcus Richards<sup>3</sup>, Frederik Barkhof<sup>1,2,6</sup>, Jonathan Schott<sup>5</sup>, Jan Petr<sup>1,2,7</sup>, Henk J.M.M. Mutsaerts<sup>1,2</sup>

<sup>1</sup>. Dept. of Radiology and Nuclear Medicine, Amsterdam University Medical Centers, Vrije Universiteit, NL

<sup>2</sup>. Amsterdam Neuroscience, Brain Imaging, NL

<sup>3</sup>. MRC Unit of Lifelong Health at Ageing at UCL, University College London, UK.

<sup>4</sup>. Neuroradiological Academic Unit, Department of Brain Repair and Rehabilitation, UCL Queen Square Institute of Neurology, London, United Kingdom

<sup>5</sup>. Dementia Research Centre, UCL Queen Square Institute of Neurology, London, United Kingdom

## Synopsis and/or Summary of Main Findings

Mid-life cardiovascular and late-life structural cerebrovascular pathology contribute in accelerating cognitive decline in normal aging and dementia. Cerebral blood flow (CBF) may be a haemodynamic biomarker of future cognitive decline, however, our understanding of normal CBF variability and its relation with the aforementioned parameters is limited. We explored associations of life-long cardiovascular parameters and white matter hyperintensity WMH volume (at 69-71 years) with ASL MRI CBF and spatial coefficient of variation (sCoV) at 69-71 years in Insight46, a cognitively healthy population-based sample. Cardiovascular parameters showed strongest associations with late-life sCoV and CBF at 69-71 years. Here, higher systolic blood pressure (SBP) and mean arterial pressure (MAP) were associated with lower GM CBF in men and stable GM CBF in women; higher DBP was associated with lower GM CBF. Higher WMH volume was related to higher GM and WM CBF, and lower GM and WM sCoV.

## Introduction

Mid-life cardiovascular and late-life structural cerebrovascular pathology play a major role in accelerating cognitive decline in normal aging<sup>1</sup> and dementia<sup>2–4</sup>. Cerebral blood flow (CBF) may be a critical intermediate biomarker of future cognitive decline, however our understanding of normal CBF variability and its relation with mid-life cardiovascular and late-life structural cerebrovascular parameters is limited.

The MRC National Survey of Health and Development neuroimaging sub-study 'Insight 46' provides a unique opportunity to study the effects of cardiovascular and cerebrovascular health on CBF in a cohort with a fixed chronological age<sup>5</sup>. We explored associations of life-long cardiovascular parameters and WMH volume with ASL MRI CBF in this cognitively healthy population-based sample.

## Methods

3D T1-weighted, FLAIR, and pseudo-continuous ASL (labelling duration = 1800ms; post-labelling delay = 1800ms) data (3T) were acquired in 295 participants (Table 1) at 69-71 years. MRI scans were processed with ExploreASL6.

Grey matter (GM), white matter (WM) and white matter hyperintensity (WMH) volume were segmented from the T1w and FLAIR images. ASL-derived partial volume-corrected CBF and the spatial coefficient of variation (sCoV) were obtained in whole-brain GM and WM7.

Life-long cardiovascular health measures (acquired at ages 43, 53, 60-64, 69, and 69-71 years) included systolic blood pressure (SBP), diastolic blood pressure (DBP), mean arterial pressure (MAP), pulse pressure (PP), and the Framingham Risk Score (FRS). Linear regression models examined associations between life-long cardiovascular health (ages 43, 53, 60-64, 69, and 69-71 years), ASL metrics (at 69-71 years), and WMH load (at 69-71 years). Models were corrected for sex, and sex interactions were tested if applicable.

## Results

While mid-life cardiovascular parameters were associated with late-life sCoV and CBF, the strongest associations were seen at 69-71 years. At this time point, higher SBP and MAP were associated with lower GM CBF in men (Figure 1A-B,  $\beta=-0.16, -0.28$ ) and relatively stable GM CBF in women (Figure 1A-B,  $\beta=0.02, -0.02$ ); higher DBP was associated with lower GM CBF ( $\beta=-0.18$ ). Higher WMH volume was related to higher GM and WM CBF (Figure 2A-B,  $\beta=2.04, 1.45$ ), and lower GM and WM sCoV (Figure 2C-D,  $\beta=-0.04, 0.05$ ).

## Conclusion

These sex-dependent associations encourage further investigation into the potential mediatory role of CBF between mid-life cardiovascular and late-life structural decline of cerebrovascular health, leading to cognitive impairment.

**Acknowledgments / Funding:** Dutch Heart Foundation 2020T049 — MD, JP, and HM — Eurostars-2 joint programme with co-funding from European Union Horizon 2020 research and innovation programme (ASPIRE E113701), provided by the Netherlands Enterprise Agency (RVO) — MS, JP, and HM — and the EU Joint Program for Neurodegenerative Disease Research, provided by the Netherlands Organisation for Health Research and Development and Alzheimer Nederland DEBBIE JPN2020-568-106 — JP, HM. FB is supported by the NIHR biomedical research centre at UCLH. The Insight46 study is principally funded by grants from Alzheimer's Research UK (ARUK-PG2014-1946, ARUK-PG2017-1946), the Medical Research Council Dementias Platform UK (CSUB19166), the British Heart Foundation

(PG/17/90/33415) and the Wolfson Foundation (PR/ylr/18575). Florbetapir amyloid tracer is provided by AVID Radiopharmaceuticals (a wholly owned subsidiary of Eli Lilly) who had no part in the design of the study. The National Survey of Health and Development is funded by the Medical Research Council (MC\_UU\_12019/1, MC\_UU\_12019/3).

## References

1. Pettigrew, C. et al. Cognitive reserve and rate of change in Alzheimer's and cerebrovascular disease biomarkers among cognitively normal individuals. *Neurobiol. Aging* 88, 33–41 (2020).
2. Iturria-Medina, Y. et al. Early role of vascular dysregulation on late-onset Alzheimer's disease based on multifactorial data-driven analysis. *Nat. Commun.* 7, 11934 (2016).
3. Plassman, B. L., Williams, J. W., Jr, Burke, J. R., Holsinger, T. & Benjamin, S. Systematic review: factors associated with risk for and possible prevention of cognitive decline in later life. *Ann. Intern. Med.* 153, 182–193 (2010).
4. Leritz, E. C., McGlinchey, R. E., Kellison, I., Rudolph, J. L. & Milberg, W. P. Cardiovascular Disease Risk Factors and Cognition in the Elderly. *Curr. Cardiovasc. Risk Rep.* 5, 407–412 (2011).
5. Lane, C. A. et al. Study protocol: Insight 46 – a neuroscience sub-study of the MRC National Survey of Health and Development. *BMC Neurol.* 17, (2017).
6. Mutsaerts, H. J. M. M. et al. ExploreASL: An image processing pipeline for multi-center ASL perfusion MRI studies. *Neuroimage* 219, 117031 (2020).
7. Mutsaerts, H. J. et al. The spatial coefficient of variation in arterial spin labeling cerebral blood flow images. *J. Cereb. Blood Flow Metab.* 37, 3184–3192 (2017).

## Figures and tables

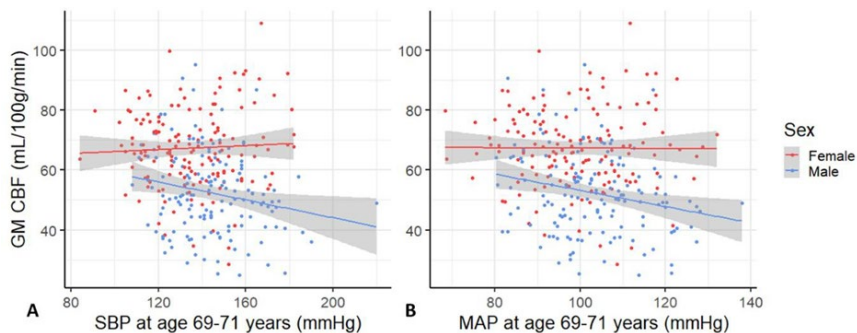


**Figure 1:** The relationship, stratified for sex, between GM CBF, SBP (A) and MAP (B) at age 69-71 years. Abbreviations: CBF = cerebral blood flow; GM = grey matter; MAP = mean arterial pressure; SBP = systolic blood pressure.

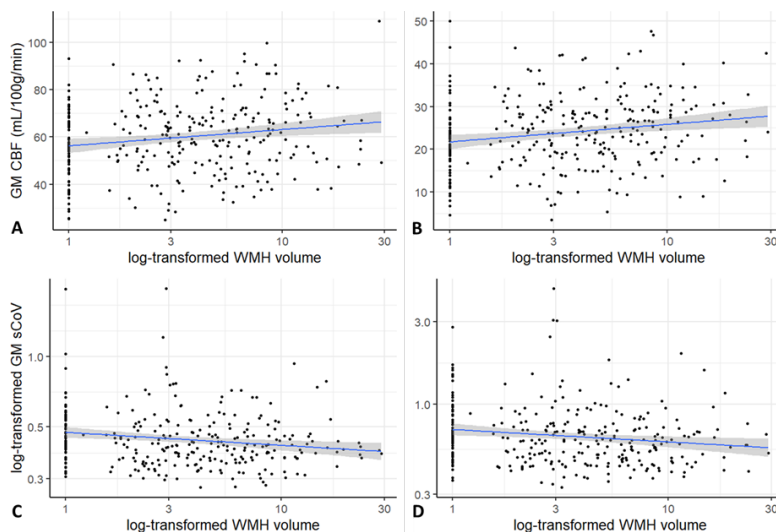
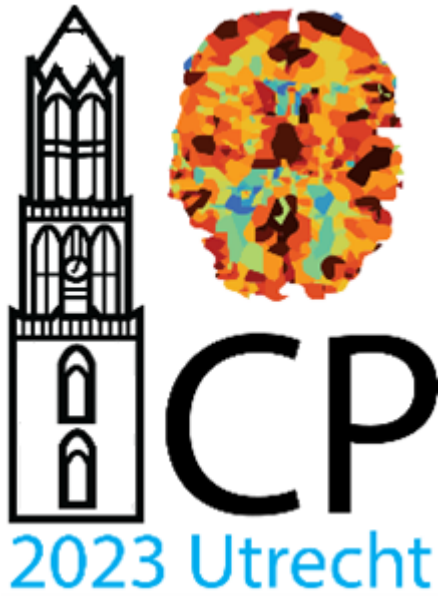


**Figure 2:** The relationship, stratified for sex, between GM and WM CBF (A and B), and GM and WM CoV (C and D), and log-transformed WMH volume. Abbreviations: CBF = cerebral blood flow; CoV = spatial coefficient of variation; GM = grey matter; WM = white matter, WMH = white matter hyperintensity

	N	Overall	Males	Females	p-value
<b>Number of participants in total sample</b>	295		145 (49.2%)	150 (50.8%)	
<b>Age at imaging baseline (years)</b>	295	70.6 (70.1-71.2)	70.53 (70.1-71.2)	70.65 (70.1-71.3)	0.341
<i>Imaging derivatives</i>					
<b>Whole brain volume (mL)</b>	295	1093 (1015 - 1174)	1159 (1098 - 1199)	1032 (973-1091)	<0.001*
<b>GM volume (mL)</b>	295	593 (556 - 626)	618 (593 - 643)	560 (540 - 594)	<0.001*
<b>WM volume (mL)</b>	295	500 (456 - 546)	539.1 (500 - 570)	470 (434 - 501)	<0.001*
<b>CSF volume (mL)</b>	295	365 (315 - 411)	398 (365 - 445)	324 (284 - 366)	<0.001*
<b>WMH volume (mL)</b>	295	2.3 (0.8 - 5.8)	2.3 (0.6 - 4.9)	2.8 (0.9 - 6.3)	0.292
<b>GM CBF (mL/min/100g)</b>	295	60.0 (15.4)	52.4 (13.7)	67.3 (13.3)	<0.001*
<b>WM CBF (mL/min/100g)</b>	295	23.9 (8.43)	19.9 (7.27)	27.9 (7.6)	<0.001*
<b>GM sCoV (<math>\sigma/\mu</math>)</b>	295	0.4 (0.4-0.5)	0.5 (0.4-0.6)	0.4 (0.4-0.5)	<0.001*
<b>WM sCoV (<math>\sigma/\mu</math>)</b>	295	0.6 (0.5-0.8)	0.7 (0.6-1.0)	0.5 (0.5-0.7)	<0.001*
<i>Cardiovascular health age 43</i>					
<b>SBP (mmHg)</b>	281	120.8 (112.0-130.4)	123.8 (114.6-134.6)	117.6 (110.2-126.7)	<0.001*
<b>DBP (mmHg)</b>	281	77.9 (72.0-84.9)	79.6 (74.4-87.4)	75.1 (70.0-82.2)	<0.001*
<b>MAP (mmHg)</b>	281	91.9 (85.6-99.3)	95.7 (87.9-102.1)	89.8 (83.2-96.7)	<0.001*
<b>PP (mmHg)</b>	281	42.1 (36.4-49.2)	42.6 (35.9-50.7)	42.0 (36.8-48.7)	0.831
<i>Cardiovascular health age 53</i>					
<b>SBP (mmHg)</b>	289	131 (119-148)	140.5 (126-153)	125 (115-138)	<0.001*
<b>DBP (mmHg)</b>	289	81 (75-95)	86 (79-95)	78 (72-8)	<0.001*
<b>MAP (mmHg)</b>	289	98 (90-107.6)	103.5 (95.4-116.5)	94 (86-100.8)	<0.001*
<b>PP (mmHg)</b>	289	49 (41-60)	53 (43-63.8)	46 (39-56.5)	<0.001*
<b>FHS-CVS (%)</b>	289	9.8 (5.5-15.1)	15.0 (11.8-18.0)	5.6 (4.4-7.9)	<0.001*
<i>Cardiovascular health age 60-64</i>					
<b>SBP (mmHg)</b>	295	134.0 (123.0-147.0)	140.0 (127.0-150.0)	130.0 (120.0-142.0)	<0.001*
<b>DBP (mmHg)</b>	295	77.6 (10.0)	80.5 (10.1)	74.8 (9.1)	<0.001*
<b>MAP (mmHg)</b>	295	96.3 (88.0-105.8)	101.0 (91.3-109.3)	92.3 (86.3-100.9)	<0.001*
<b>PP (mmHg)</b>	295	57.0 (50-65)	59.0 (51.0-67.0)	56.0 (47.3-63.0)	0.007*
<i>Cardiovascular health age 69-71</i>					
<b>SBP (mmHg)</b>	288	135.8 (17.1)	139.33 (16.2)	132.3 (17.4)	<0.001*
<b>DBP (mmHg)</b>	288	74.9 (10.0)	75.75 (10.6)	73.99 (9.3)	0.136
<b>MAP (mmHg)</b>	288	95.2 (11.3)	96.9 (11.2)	93.42 (11.0)	0.008*
<b>PP (mmHg)</b>	288	60.0 (51.0-68.0)	62.0 (55.0-71.0)	58.0 (50.0-64.0)	<0.001*
<b>FHS-CVS (%)</b>	286	21.1 (13.3-32.3)	32.3 (25.9-37.3)	13.3 (9.8-16.7)	<0.001*

**Table 1:** Sample characteristics at imaging baseline. Values shown are n (%), mean (SD) or median (q1, q3). The asterisk denotes significant differences for male/female. Abbreviations: WMH, white matter hyperintensity; GM, grey matter; CBF, cerebral blood flow; WM, white matter; sCoV, spatial coefficient of variation; SBP, systolic blood pressure; DBP, diastolic blood pressure; MAP, mean arterial pressure; PP; pulse pressure.



Day 3: December 1st

# Preliminary data for using hyperoxia and multiparametric qBOLD to estimate the oxygen extraction fraction

A.A. Alzaidi<sup>1,2</sup>, R. Panek<sup>3</sup>, Sebastian Rieger<sup>4</sup>, Susan Francis<sup>5</sup>, G.Hoffmann<sup>6</sup>, S.Kaczmarz<sup>6</sup>, N.Blockley<sup>1</sup>

<sup>1</sup>School of Life Science, University of Nottingham, Nottingham, United Kingdom.

<sup>2</sup>Taif University, Taif, Saudi Arabia.

<sup>3</sup>Medical Physics and Clinical Engineering Nottingham Hospitals NHS Trust, Nottingham, United Kingdom.

<sup>4</sup>Wellcome Centre for Integrative Neuroimaging, University of Oxford, Oxford, United Kingdom.

<sup>5</sup>School of Physics & Astronomy, University of Nottingham, Nottingham, United Kingdom.

<sup>6</sup>Technical University of Munich, School of Medicine, Munich, Germany.

## Synopsis and/or Summary of Main Findings: (140/150 words)

Quantitative BOLD (qBOLD) maps the oxygen extraction fraction (OEF) in the brain but is limited by the need for specialist pulse sequences. Multiparametric qBOLD (mqBOLD) addresses this using product sequences but estimating deoxygenated blood volume (DBV) requires dynamic susceptibility contrast (DSC), which is not an absolute measure of venous blood volume(1). Administering hyperoxia and acquiring BOLD-weighted data can directly quantify DBV without the need for contrast agents(2). This study combines mqBOLD and hyperoxia-BOLD, to produce a non-invasive and widely implementable technique for mapping OEF. Both mqBOLD and hyperoxia-BOLD data were acquired in five healthy subjects. TRUST data were also obtained for comparison with global OEF. Preliminary results showed R2' values were generally in agreement with the literature and DBV values agreed with the literature. In combination, OEF values were found to be outside the physiological range i.e. greater than 100%.

## Introduction

The balance of oxygen delivery and consumption in the brain is measured by the oxygen extraction fraction (OEF). Even small fluctuations in OEF can signal physiological disturbance, making a quick and non-invasive method of measurement valuable for clinical assessments. While conventional qBOLD techniques can measure OEF, they require a high signal-to-noise ratio and may overestimate DBV. One solution is to use a separate measurement of CBV, as used by the multiparametric-qBOLD (mqBOLD) technique. This approach measures total blood volume, not the deoxygenated blood volume (DBV) required by qBOLD(1). However, by acquiring BOLD-weighted data and administering hyperoxia we can directly quantify DBV without contrast agents(2). Combining mqBOLD and hyperoxia-BOLD may produce a widely implementable technique for mapping OEF.

Aim: Estimate OEF using mqBOLD with a hyperoxia-BOLD measurement of DBV and compare it to OEF estimated from the TRUST technique.

## Methods

Five healthy participants, aged 18-40 years old, were scanned using a 3T Ingenia (Philips Healthcare, Best, NL). MRI data were acquired as follows:

TRUST: 64x64 matrix, TR=3s, TE=2.9ms. T2 of venous blood was quantified from this data and converted to Yv by following the standard analysis approach(3). Assuming arterial blood is fully saturated, an estimate of whole brain OEF is given by  $1 - Yv$ .

mqBOLD: Multi echo GRE (R2\*) and 3D-GRASE (R2) data were acquired following parameters from Kaczmarz et al., 2020(4).

Hyperoxia-BOLD: Hyperoxia challenges were generated using an electronically controlled gas delivery system. Three 2 mins blocks of normoxia interleaved with two 2 mins blocks of hyperoxia were performed (duration 10mins).

Analysis: A high-resolution structural image was acquired and segmented using FAST(6) to produce subject-specific ROIs of grey matter (GM), which were further refined to the cortex by masking with the MNI atlas. Hyperoxia-BOLD data were analysed with FEAT(5). DBV was calculated from voxel-wise estimates of percentage BOLD signal change ( $\delta\delta S$ ) using Eq. 2, where  $A=27ms$ ,  $B=0.2$ ,  $C=245.1mmHg$  and  $D=0.1$ . OEF was then calculated by combining DBV and R2' parametric maps using Eq. 1. Due to extreme outliers, particularly in the OEF maps, the median values of R2', DBV and OEF were estimated from voxels in the cortical GM ROIs.

$$OEF = \frac{R_2'}{DBV \cdot \gamma \cdot \pi \cdot \Delta \chi_0 \cdot Hct \cdot B_0} \quad (1) \quad DBV = \left( \frac{A}{TE} + B \right) \left( \frac{C}{\Delta P_{ET} O_2} + D \right) \cdot \delta S \quad (2)$$

## Results

Preliminary results showed an average R2' of 6.87s-1, DBV of 0.80% and OEF-hmqBOLD of 219.53% (Table 1). For these data the median was calculated instead of the mean because this data was skewed (Fig. 1). The OEF-TRUST average was 38.5%.

## Discussion

The GM R2' value of 6.87s-1 is similar to values reported in the mqBOLD literature(7). However, others reported lower values using different techniques, such as GESSE (2.9s-1)(8) and ASE (4.4s-1)(9). DBV values of 0.46-1.31% are similar to past measurements (2.18%)(10). OEF-hmqBOLD values are not in agreement with OEF-TRUST and outside of the physiological range i.e. greater than 100%. This may be due to the higher R2' values. Future work aims to acquire more

subjects to assess the correlation between OEF-hmqBOLD and OEF-TRUST and hence whether hmqBOLD can be used as a relative measure of OEF.

**Acknowledgments / Funding Information:** This project is funded by Taif University, Saudi Arabia.

### References

- (1) Jiang, D. and Lu, H., 2022. Cerebral oxygen extraction fraction MRI: Techniques and applications. *Magnetic resonance in medicine*, 88(2), pp.575- 600.
- (2) Blockley, N. P., Griffeth, V. E. M., Germuska, M. A., Bulte, D. P., & Buxton, R. B. (2013). An analysis of the use of hyperoxia for measuring venous cerebral blood volume: Comparison of the existing method with a new analysis approach. *Neuroimage*, 72, 33–40.
- (3) Lu, H. and Ge, Y., 2008. Quantitative evaluation of oxygenation in venous vessels using T2-relaxation-under-spin-tagging MRI. *Magnetic Resonance in Medicine: An Official Journal of the International Society for Magnetic Resonance in Medicine*, 60(2), pp.357-363.
- (4) Kaczmarz, S., Hyder, F., & Preibisch, C. (2020). Oxygen extraction fraction mapping with multi-parametric quantitative BOLD MRI : Reduced transverse relaxation bias using 3D-GrASE imaging. *NeuroImage*, 220, 117095.
- (5) Jenkinson, M., Beckmann, C.F., Behrens, T.E., Woolrich, M.W. and Smith, S.M., 2012. *Fsl. Neuroimage*, 62(2), pp.782-790.
- (6) Zhang, Y., Brady, M. and Smith, S., 2001. Segmentation of brain MR images through a hidden Markov random field model and the expectation- maximization algorithm. *IEEE transactions on medical imaging*, 20(1), pp.45-57.
- (7) Sedlacik, J., Boelmans, K., Löbel, U., Holst, B., Siemonsen, S. and Fiehler, J., 2014. Reversible, irreversible and effective transverse relaxation rates in normal aging brain at 3 T. *Neuroimage*, 84, pp.1032-1041.
- (8) He, X. and Yablonskiy, D.A., 2007. Quantitative BOLD: mapping of human cerebral deoxygenated blood volume and oxygen extraction fraction: default state. *Magnetic Resonance in Medicine: An Official Journal of the International Society for Magnetic Resonance in Medicine*, 57(1), pp.115- 126.
- (9) An, H. and Lin, W., 2003. Impact of intravascular signal on quantitative measures of cerebral oxygen extraction and blood volume under normo- and hypercapnic conditions using an asymmetric spin echo approach. *Magnetic Resonance in Medicine: An Official Journal of the International Society for Magnetic Resonance in Medicine*, 50(4), pp.708-716.
- (10) Blockley, N.P., Griffeth, V.E., Germuska, M.A., Bulte, D.P. and Buxton, R.B., 2013. An analysis of the use of hyperoxia for measuring venous cerebral blood volume: comparison of the existing method with a new analysis approach. *Neuroimage*, 72, pp.33-40.

### Tables and figures

Subject #	$RR_{22}$ (Hz)	DBV (%)	OEF-hmqBOLD (%)	OEF-TRUST (%)
1	6.65	1.10	182.47	33.0
2	7.10	1.31	134.65	39.1
3	7.51	0.61	294.01	48.9
4	6.22	0.46	161.70	38.8
5	6.88	0.54	324.84	32.6
<b>Mean</b>	6.87	0.80	219.53	38.5

**Table 1.** Median values of grey matter  $R_2'$ , DBV, OEF-hyperoxia mqbBOLD (hmqBOLD) and OEF-TRUST for all the subjects.

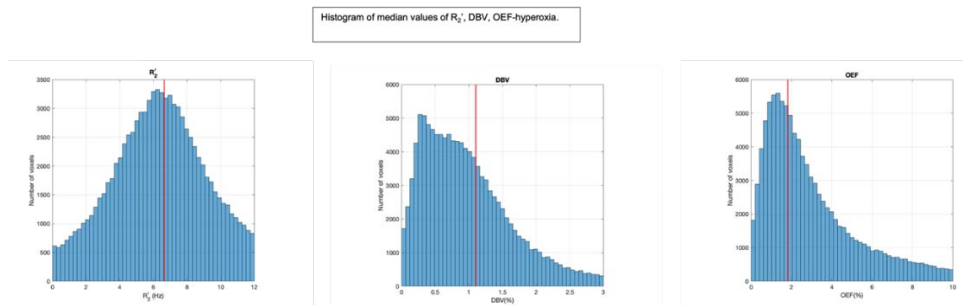


**Figure1.** histogram for  $R_2'$ , DBV, OEF-hyperoxia median values for subject 3, redline indicating median value. DBV and

OEF data are skewed to the right by 2,77, respectively.

## Abstract title: Increased brain oxygen metabolism and oxygen extraction in patients with cystic fibrosis

H L Chandler<sup>1</sup>, M Germuska<sup>1</sup>, TM Lancaster<sup>2</sup>, C Xanthe<sup>3</sup>, K Murphy<sup>1</sup>, C Metzler-Baddeley<sup>1\*</sup>, R G Wise<sup>4</sup>, J Duckers<sup>3</sup>

<sup>1</sup>Cardiff University Brain Research Imaging Centre (CUBRIC), Cardiff University, Cardiff.

<sup>2</sup>University of Bath, School of Psychology, Bath

<sup>3</sup>Department of Respiratory Medicine, University Hospital Wales, Cardiff and Vale University Health Board.

<sup>4</sup>Department of Neurosciences, Imaging and Clinical Sciences, University "G. d'Annunzio" of Chieti-Pescara, Chieti, Italy.

### Synopsis and/or Summary of Main Findings.

We use pseudo-continuous arterial spin labelling (pCASL) and T2-Relaxation-Under-Spin-Tagging (TRUST) to estimate grey matter cerebral blood flow (gmCBF), global oxygen extraction fraction (OEF) and global cerebral metabolic rate of oxygen consumption (CMRO<sub>2</sub>) in 14 patients with cystic fibrosis (PwCF) compared to 56 age and sex matched healthy controls. PwCF had increased global OEF and CMRO<sub>2</sub>, but comparable / intact gmCBF. These alterations may reflect changes in mitochondrial function, possibly explained by the effects of chronic hypoxia.

### Background:

Cystic fibrosis (CF) is a progressive inherited disorder that primarily affects the lungs (1). In addition to respiratory symptoms, PwCF frequently present with significant cognitive changes in executive function, memory and attention (2), but the reason for these alterations is not understood. In other respiratory diseases, cognitive symptoms have been linked to neuronal damage explained by chronic hypoxia (3). With recent breakthroughs in effective treatments for CF that increase life-expectancy, there has been a higher prevalence of age-related comorbidities associated with the disease including stroke, cardiovascular disease, and cognitive decline (4). Therefore, cerebrovascular research in CF is crucial to understand the trajectory of disease pathophysiology. Here, we use pseudo-continuous ASL (pCASL) to quantify cerebral perfusion in grey-matter and T2-Relaxation-Under-Spin-Tagging (TRUST) to estimate global OEF and CMRO<sub>2</sub>.

### Methods:

We studied 14 PwCF and 56 healthy age/sex matched controls. All MRI data were collected on a Siemens Prisma 3T MRI scanner (Siemens Healthineers, Erlangen, Germany), with a 32-channel receive only head coil. A magnetisation-prepared rapid acquisition with gradient echo (MPRAGE) T1-weighted scan was used for registration and brain segmentation purposes (matrix 165 x 203 x 197, 1 mm isotropic resolution, TR/TE = 2100/3.24ms). To quantify gmCBF, an in house PCASL sequence was collected (TR/TE= 4600ms / 11ms; slices = 22; Slice thickness = 5mm; PLD = 2000ms; tag duration = 1800ms; GRAPPA acceleration factor = 2). A T2-Relaxation-Under-Spin-Tagging (TRUST) MRI sequence was acquired to estimate global venous oxygenation and OEF (TR/TE = 3000ms/3.9ms, slice thickness = 5mm, eTE =0ms, 40ms, 80ms, 160ms, GRAPPA acceleration factor = 3). We further collected a T1 inversion recovery sequence to calculate Hb ( $\Delta$ TR/TE = 150ms/22ms, flip angle= 90 degrees, and GRAPPA acceleration factor= 2). The venous oxygen saturation was derived from exponential fitting of the TRUST signal in the sagittal sinus. We estimated gmCBF from the PCASL data, with partial volume correction. Global CMRO<sub>2</sub> was estimated using the gmCBF, calculated CaO<sub>2</sub>, and OEF.

### Results:

Thirteen patients (mean age  $\pm$  SD = 34.57  $\pm$  10.92, 3/13 female) and 55 healthy controls (mean age  $\pm$  SD = 34.48  $\pm$  11.78, 14/55 female) were included in the final analysis after outlier removal (3 x interquartile range). There were significant increases in CMRO<sub>2</sub> (PwCF vs. controls: 190.46 vs. 169.36 $\mu$ mol/100 g/min,  $t(19.38)$  = -2.88,  $p$  = 0.009) and OEF (PwCF vs. controls: 0.41 vs. 0.37,  $t(15.39)$  = -2.24,  $p$  = 0.040) in PwCF compared to healthy controls. There were no significant between-group differences in grey-matter CBF (PwCF vs. controls: 65.32 vs. 62.93ml/100 g/min,  $t(21.40)$  = -0.96,  $p$  = 0.347).

### Discussion:

PwCF have increased global OEF and CMRO<sub>2</sub>, but comparable gmCBF. PwCF and other acute / chronic lung diseases are more likely to show altered mitochondrial function (5, 6), where increases in CMRO<sub>2</sub> have been linked to chronic hypoxia (7). Future research could benefit from exploring regional alteration in OEF and CMRO<sub>2</sub> via dual-calibrated MRI protocols (and alike). With these approaches, we can also estimate the partial pressure of oxygen at the mitochondrial level (8), which may be useful in assessing more localised microvascular alterations in PwCF.

### References

1. Batten J. Cystic Fibrosis: A Review. Br J Dis Chest. 1965;59:1-9.
2. Piasecki B, Turska-Malinska R, Matthews-Brzozowska T, Mojs E. Executive function in pediatric patients with cystic fibrosis, inflammatory bowel disease and in healthy controls. Eur Rev Med Pharmacol Sci. 2016;20(20):4299-304.
3. Zheng GQ, Wang Y, Wang XT. Chronic hypoxia-hypercapnia influences cognitive function: a possible new model of cognitive dysfunction in chronic obstructive pulmonary disease. Med Hypotheses. 2008;71(1):111-3.
4. Hussain N, Hussain F, Malik A, Rizvi M, Patel P, Chittivelu S. A devastating cardiovascular event in an adult cystic fibrosis patient: An unforeseen outcome of increasing life expectancy. Respir Med Case Rep. 2018;25:233-4.
5. Favia M, de Bari L, Bobba A, Atlante A. An Intriguing Involvement of Mitochondria in Cystic Fibrosis. J Clin Med.

2019;8(11).

6. Patergnani S, Vitto VAM, Pinton P, Rimessi A. Mitochondrial Stress Responses and "Mito-Inflammation" in Cystic Fibrosis. *Front Pharmacol.* 2020;11:581114.

7. Bernthman L, Carlsson C, Siesjo BK. Cerebral oxygen consumption and blood flow in hypoxia: influence of sympathoadrenal activation. *Stroke.* 1979;10(1):20-5.

8. Chandler HL, Stickland RC, Patitucci E, Germuska M, Chiarelli AM, Foster C, et al. Reduced brain oxygen metabolism in patients with multiple sclerosis: Evidence from dual-calibrated functional MRI. *J Cereb Blood Flow Metab.* 2023;43(1):115-28.

#### Figures

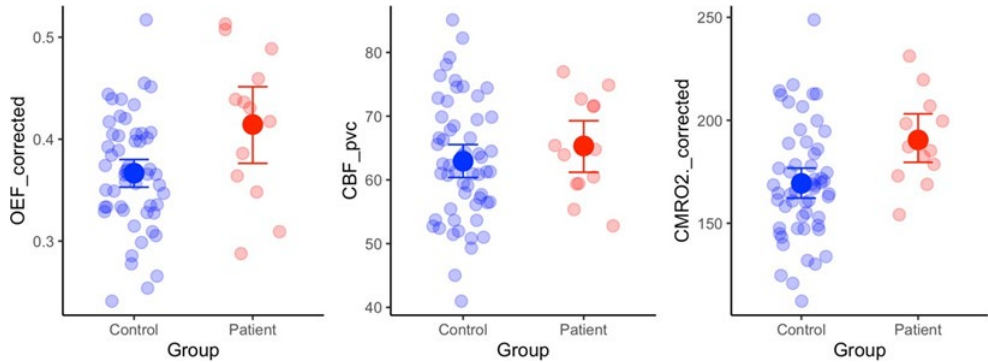


**Figure 1.** Results reveal significant increases in global OEF ( $p = .040$ ) and CMRO2 ( $p = .009$ ) in the patient group compared to age / sex matched controls. Our results show no significant grey-matter difference in CBF ( $p = .347$ ).

# Single Image Super Resolution Reconstruction of Susceptibility Maps for Improved Vessel Segmentation and Oxygen Saturation Estimation

Eleonora Patitucci\*<sup>1</sup>, Stefano Zappalà\*<sup>2</sup>, Richard Wise\*<sup>3,1</sup>, Michael Germuska<sup>1,2</sup>

\*These authors have contributed equally to the work

<sup>1</sup>Cardiff University Brain Research Imaging Centre (CUBRIC), School of Psychology, Cardiff University, Cardiff, United Kingdom;

<sup>2</sup>Cardiff University Brain Research Imaging Centre (CUBRIC), School of Physics and Astronomy, Cardiff University, Cardiff, United Kingdom;

<sup>3</sup>Institute for Advanced Biomedical Technologies, Department of Neurosciences, Imaging, and Clinical Sciences, University G. D'Annunzio of Chieti-Pescara, Via Luigi Polacchi 13, Chieti, Italy, 66100

## Synopsis and/or Summary of Main Findings

This study adapts a deep learning method for super-resolution reconstruction to enhance quantitative susceptibility mapping (QSM) images, with the aim of improving brain vasculature segmentation for venous oxygen saturation quantification. The 3D densely-connected super resolution network (DCSRN) has shown promising results in reconstructing T1w high-resolution (HR) images from low-resolution (LR) pairs.

Performance of the network was gauged on 1113 T1w images from the HCP dataset, and then applied to 101 QSM maps acquired from a 7T scanner. Training was based on LR volumes derived from k-space truncation of the HR volumes, with 7:1.5:1.5 splits for training, validation and testing respectively.

Results demonstrated an improvement in the reconstruction of the vasculature network, with susceptibility values distribution close to the true distribution. These initial findings show the promise of the DCSRN architecture in QSM SR reconstruction, giving robust results without the need of more powerful systems or longer acquisition sessions.

## Abstract Body

QSM quantitatively measures the spatial distribution of magnetic susceptibility within a tissue. Susceptibility differences allow the accurate segmentation of the brain vasculature and the estimation of venous oxygen saturation [1]. The reliability of such maps critically depends on their contrast and spatial resolution. High-resolution QSM data requires lengthy acquisitions and high field systems.

Single image super resolution (SISR) reconstruction attempts to solve the problem of generating HR images from a LR version. The DCSRN architecture [2] demonstrated promising results in reconstructing T1w HR images from LR pairs. The model proved to be efficient and less prone to overfitting due to weight sharing and the reuse of features.

In this work, we aim to train and fit the same deep learning model to QSM images, to increase the resolution of the images and improve the segmentation of the brain vasculature to quantify venous oxygen saturation in cortical vessels.

Two datasets were used in the present study: first, 1113 T1w images of Human Connectome Project (HCP) dataset [3] (Siemens 3T "Connectome Skyra", voxel resolution=0.7 mm3); second, 101 QSM maps generated from magnitude and phase GRE scans acquired in CUBRIC with a 7T Siemens Magnetom scanner (0.67 mm3, 7 TEs between 5 and 35 ms). QSM generation consisted of an initial phase unwrapping (ROMEO [4]), followed by projection onto dipole fields (MEDI suite [5]) and non-linear dipole inversion [6].

For both datasets (HCP and QSM), LR volumes were obtained by cropping the k-space of the HR volumes by a factor 2 in each direction. DCSRN model was separately trained on both datasets. Splits of 7:1.5:1.5 were used for training, validation, and testing, respectively. Intensity normalisation (mean/std) was applied to the whole 3D volumes, before the division into 200 randomly located patches used during training. The QSM dataset was further augmented by applying affine deformations with randomly generated rotation angles from normal distribution around 3° [7], and random shearing around 0.05.

Networks were implemented in TensorFlow and run on the GPU cluster at CUBRIC.

Table 1 shows the performance metrics obtained on the test set. The DCSRN architecture improved the similarity between HR and SR images relative to the other interpolation methods tested. Training on T1w, shows SSIM metric results similar to Chen et al. [2], although we used a different weight initialisation and different intensity normalisation. Figure 1 shows the improvement in the captured vasculature network achieved with the DCSRN architecture on QSM data. Smaller vessels could be more reliably identified from the SR image (blue) than the LR (orange) (Figure 1-A), and the noise that affected the HR image (brown) is discarded in SR (blue) (Figure 1-B). QSM susceptibility values within the vessels (range [0.2, 0.6] ppm) were extracted for each image (mean±std= LR: 0.2599±0.1031; HR: 0.3027±0.1205; SR: 0.2995±0.0898). We observed SR susceptibility values were similar to the true susceptibility values obtained from HR.

Taken together, our results show the promise of DCSRN architecture in QSM SR reconstruction, giving robust results without the need of more powerful systems or longer acquisition sessions.

**Acknowledgments / Funding Information:** The project was funded by EPSRC grant.

## References:

1. Murdoch, R., et al., A Comparison of MRI Quantitative Susceptibility Mapping and TRUST-Based Measures of Brain Venous Oxygen Saturation in Sickle Cell Anaemia. *Frontiers in physiology*, 2022. 13: p. 913443-913443.
2. Yuhua Chen, Y.X., Zhengwei Zhou, Feng Shi, Anthony Christodoulou, Debiao Li, Brain MRI Super Resolution Using

3D Deep Densely Connected Neural Networks. 2018.

3. Glasser, M.F., et al., The minimal preprocessing pipelines for the Human Connectome Project. *Neuroimage*, 2013. 80: p. 105-24.

4. Dymerska, B., et al., Phase unwrapping with a rapid opensource minimum spanning tree algorithm (ROME0). *Magnetic Resonance in Medicine*, 2021. 85(4): p. 2294-2308.

5. Liu, T., et al., Accuracy of the morphology enabled dipole inversion (MEDI) algorithm for quantitative susceptibility mapping in MRI. *IEEE transactions on medical imaging*, 2012. 31(3): p. 816-824.

6. Polak, D., et al., Nonlinear dipole inversion (NDI) enables robust quantitative susceptibility mapping (QSM). *NMR in biomedicine*, 2020. 33(12): p. e4271-n/a.

7. Gallichan, D., J.P. Marques, and R. Gruetter, Retrospective correction of involuntary microscopic head movement using highly accelerated fat image navigators (3D FatNavs) at 7T. *Magn Reson Med*, 2016. 75(3): p. 1030-9.

8. Gourdeau, D., S. Duchesne, and L. Archambault, On the proper use of structural similarity for the robust evaluation of medical image synthesis models. *Medical Physics*, 2022. 49(4): p. 2462-2474.

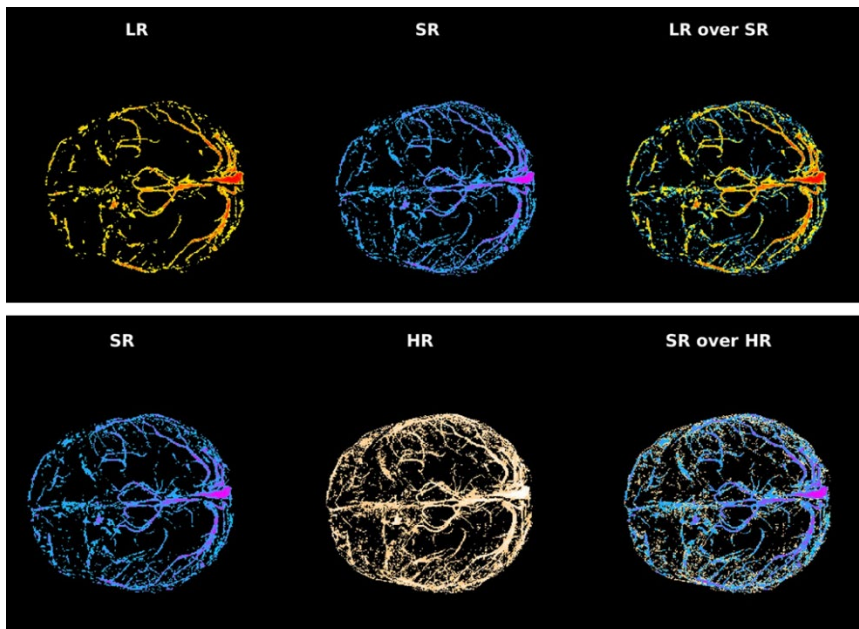
## Tables and figures

		SSIM	PSNR	NRMSE
T1w	<i>NN</i>	0.9550±0.0026	22.95±0.54	0.1574±0.0232
	<i>bicubic</i>	0.9594±0.0020	26.66±0.55	0.1383±0.0109
	<i>cubic</i>	0.9618±0.0020	28.34±0.65	0.1286±0.0098
	<i>DCSRN</i>	0.9739±0.0064	36.90±1.06	0.1965±0.0222
QSM	<i>NN</i>	0.8103±0.0107	28.75±0.42	1.0071±0.0515
	<i>bicubic</i>	0.8218±0.0099	28.87±0.45	1.0242±.062
	<i>cubic</i>	0.8271±0.0097	28.86±0.46	1.0342±0.067
	<i>DCSRN</i>	0.9274±0.0054	35.62±0.54	0.5800±0.0222

DCSRN optimal parameters					
	Batch size	Number of Epochs	Iterations	Weights Initialization	Learning Rate
T1w	2	50	5000	normal distribution (std 0.01)	10 <sup>-5</sup> fixed rate
QSM	2	50	5000	normal distribution (std 0.01)	variable learning rate (10 <sup>-5</sup> – 10 <sup>-2</sup> )

**Table 1.** Metrics and optimal parameters. Accuracy metrics on the test sets for training on HCP (T1w) and QSM datasets: structural similarity index measure (SSIM), peak signal-to-noise ratio (PSNR) and normalised root mean squared error (NRMSE) [8]. Different learning rates in the two datasets were used: a fixed rate of 10<sup>-5</sup> performed better in the T1w images, whereas a variable learning rate (exponential decay from 10<sup>-5</sup> to 10<sup>-2</sup>) performed better on the QSM maps. N words= 74/75



**Figure 1.** SR image. Maximum intensity projections of QSM map for one subject showing the improvements in the reconstruction of the vasculature network (display values in the range [0.2, 0.6] ppm). (A) LR image as input to the

DCSRN model (yellow – orange) is superimposed over the SR output (blue – light blue). (B) the SR output is now superimposed over the original HR image (brown – light copper)

## Sex differences in the effects of physical activity on cerebrovascular reactivity

Z. Potvin-Jutras<sup>1,2</sup>, B. Intzandt<sup>3</sup>, P. Liu<sup>4</sup>, J.J. Chen<sup>5,6</sup>, C.J. Gauthier<sup>2,7</sup>

<sup>1</sup>Physics, Concordia University, Montreal, Canada;

<sup>2</sup>Research Center, Montreal Heart Institute, Montreal, Canada;

<sup>3</sup>Hurvitz Brain Sciences Program - BrainLab, Sunnybrook Research Institute, Toronto, Canada;

<sup>4</sup>Radiology, University of Maryland, School of Medicine, Baltimore, United States;

<sup>5</sup>Rotman Research Institute, Baycrest Health Sciences, Toronto, Canada;

<sup>6</sup>Medical Biophysics, University of Toronto, Toronto, Canada; <sup>7</sup>PERFORM Center, Concordia University, Montreal, Canada;

### Synopsis and/or Summary of Main Findings:

Here we evaluated the sex-specific associations of physical activity (PA) [dose and intensity] and body mass index (BMI) on vascular brain health using cerebrovascular reactivity (CVR).

Females showed a positive relationship between total, moderate, moderate to vigorous PA and CVR in the frontal cortex. Moreover, a negative relationship was identified between total, low and vigorous PA and CVR in the temporal cortex in females. Males demonstrated a negative relationship between total, as well as low intensity PA and CVR in the frontal cortex. Only females exhibited a significant positive relationship between BMI and CVR. These findings suggest that there are significant sex differences on the influence of BMI and PA, two modifiable lifestyle factors, on vascular brain health.

### Abstract Body:

Physical inactivity and obesity are important risk factors for cardiovascular diseases<sup>1</sup>, stroke<sup>2</sup> and dementia<sup>3</sup>. Physical activity (PA) can help prevent the development of these conditions by maintaining brain health in aging.<sup>4</sup> Current PA recommendations from the World Health Organisation are identical for males and females<sup>5</sup>, but recent work suggests that there might be significant sex differences in the relationship between PA and brain health.<sup>6</sup> Therefore, recommendations could be optimized to better reflect the needs of each sex.<sup>7</sup> Cerebrovascular health may be sensitive to the effects of PA<sup>8</sup> and changes in cerebral blood flow and cerebrovascular reactivity (CVR) have been documented.<sup>9</sup> The effects of PA on CVR are unclear however and may depend on fitness.<sup>9,10</sup> Obesity has similarly been shown to have complex effects on the brain.<sup>6,12</sup>

**Objectives and hypotheses:** The primary objective of this study was to evaluate the effects of dose and intensity of PA on CVR in both sexes. The secondary objective was to investigate the relationship between body mass index (BMI) and CVR. Females were hypothesised to benefit (higher CVR) more from overall volume and all intensities of PA as compared to males. Males were hypothesised to demonstrate a stronger negative relationship between higher CVR and lower BMI compared to females.

### Methods:

The Human Connectome Project – Aging dataset was used here including preprocessed resting state fMRI data from 220 females and 215 males ( $\geq 36$  years). The international physical activity questionnaire (IPAQ) was used to quantify weekly PA<sup>13</sup>, categorized as: walking metabolic equivalent of task (METs) ( $< 3$  METs), moderate (3 to 6 METs) moderate- vigorous (greater than 3.0 METs), vigorous METs (greater than 6.0 METs), and total weekly PA (combining all intensities). Relative CVR maps were obtained from a gas-free technique<sup>11</sup>. Regions of interest (ROI) analyses were performed, stratifying by sex, and controlling for age, BMI and systolic blood pressure.

### Results:

Females showed a positive relationship between total, moderate, moderate-vigorous PA and CVR in the frontal cortex (see Fig 1A-C). Moreover, females demonstrated a negative relationship between total, low and vigorous PA and CVR in temporal cortex (see Fig 1D-E). Males showed a negative relationship between total and low intensity PA with CVR in the frontal cortex (see Fig 2). Further, females exhibited a positive relationship between BMI and CVR, but no significant relationships were found in males (see Fig 3).

### Discussion:

The effects of dose and intensity of PA on cerebrovascular health was sex- and region-specific. While the negative effects observed in females in temporal areas and frontal areas in males seem to indicate poorer vascular health with PA, these results must be interpreted with caution and are consistent with previous results showing a negative effect of fitness on CVR in Master athletes and very healthy older adults.<sup>9,10</sup> The PA and BMI relationships support sex differences in gray matter brain health as shown in previous work.<sup>6,14</sup> Future work should further investigate the physiological underpinning of CVR methods to better understand what underlies the negative relationship between PA and CVR, and positive relationship between BMI and CVR in females.

**References:** [1] Elagizi, A. et al. (2020). A Review of Obesity, Physical Activity, and Cardiovascular Disease. *Current obesity reports*, 9(4), 571–581. <https://doi.org/10.1007/s13679-020-00403-z> [2] Guzik, A., & Bushnell, C. (2017). Stroke Epidemiology and Risk Factor Management. *Continuum (Minneapolis, Minn.)*, 23(1, Cerebrovascular Disease), 15–39.

<https://doi.org/10.1212/CON.0000000000000416> [3] Kivipelto, M. et al. (2018). Lifestyle interventions to prevent cognitive impairment, dementia and Alzheimer disease. *Nature reviews. Neurology*, 14(11), 653–666.

<https://doi.org/10.1038/s41582-018-0070-3> [4] Tsao, C. W. et al. (2022). Heart Disease and Stroke Statistics-2022 Update: A Report From the American Heart Association. *Circulation*, 145(8), e153–e639.

<https://doi.org/10.1161/CIR.000000000001052> [5] Bull, F. C. et al. (2020). World Health Organization 2020 guidelines on physical activity and sedentary behaviour. *British journal of sports medicine*, 54(24), 1451–1462.

<https://doi.org/10.1136/bjsports-2020-102955> [6] Intzandt, B. et al. (2023). Sex-specific relationships between obesity, physical activity, and gray and white matter volume in cognitively unimpaired older adults. *GeroScience*, 45(3), 1869–1888. <https://doi.org/10.1007/s11357-023-00734-4> [7] Di Liegro, C. M. et al. (2019). Physical Activity and Brain Health. *Genes*, 10(9), 720. <https://doi.org/10.3390/genes10090720> [8] Kivipelto, M. et al. (2022). Trials and Treatments for Vascular Brain Health: Risk Factor Modification and Cognitive Outcomes. *Stroke*, 53(2), 444–456. <https://doi.org/10.1161/STROKEAHA.121.032614> [9] Intzandt, B. et al. (2020). Higher cardiovascular fitness level is associated with lower cerebrovascular reactivity and perfusion in healthy older adults. *Journal of cerebral blood flow and metabolism : official journal of the International Society of Cerebral Blood Flow and Metabolism*, 40(7), 1468–1481. <https://doi.org/10.1177/0271678X19862873> [10] Thomas, B. P. et al. (2013). Life-long aerobic exercise preserved baseline cerebral blood flow but reduced vascular reactivity to CO<sub>2</sub>. *Journal of magnetic resonance imaging : JMRI*, 38(5), 1177–1183. <https://doi.org/10.1002/jmri.24090> [11] Liu, P. et al. (2017). Cerebrovascular reactivity mapping without gas challenges. *NeuroImage*, 146, 320–326. <https://doi.org/10.1016/j.neuroimage.2016.11.054> [12] Sui, S. X., & Pasco, J. A. (2020). Obesity and Brain Function: The Brain-Body Crosstalk. *Medicina (Kaunas, Lithuania)*, 56(10), 499. <https://doi.org/10.3390/medicina56100499> [13] Lee, P. H. et al. (2011). Validity of the International Physical Activity Questionnaire Short Form (IPAQ-SF): a systematic review. *The international journal of behavioral nutrition and physical activity*, 8, 115. <https://doi.org/10.1186/1479-5868-8-115> [14] Barha, C. K. et al. (2019). Biological Sex: A Potential Moderator of Physical Activity Efficacy on Brain Health. *Frontiers in aging neuroscience*, 11, 329. <https://doi.org/10.3389/fnagi.2019.003>

## Figures and tables

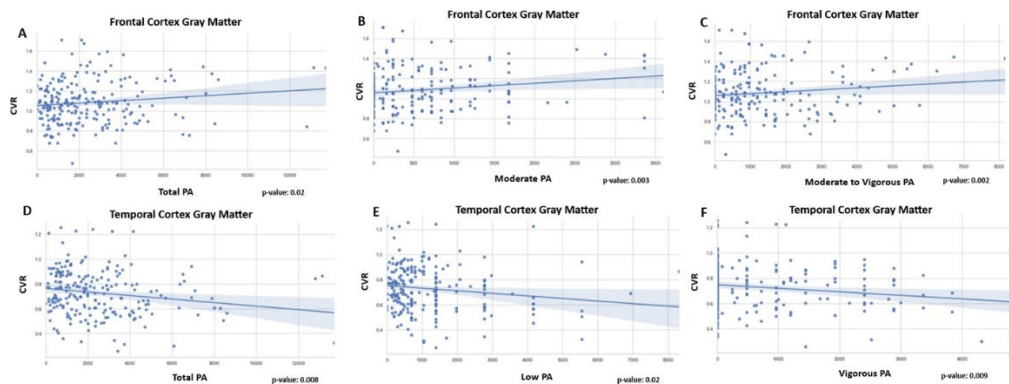


**Figure 1:** Linear relationships between PA in METs in females and CVR ROIs; A-C relationships in the frontal cortex; D-F relationships in the temporal cortex. CVR was measured in relative units and PA was categorized into walking metabolic equivalent of task.

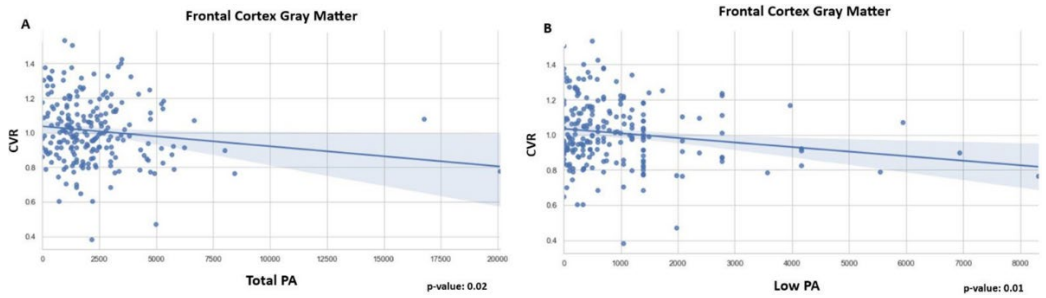


**Figure 2:** Linear relationships between PA in METs in males and CVR in the frontal cortex. CVR was measured in relative units and PA was categorized into walking metabolic equivalent of task.

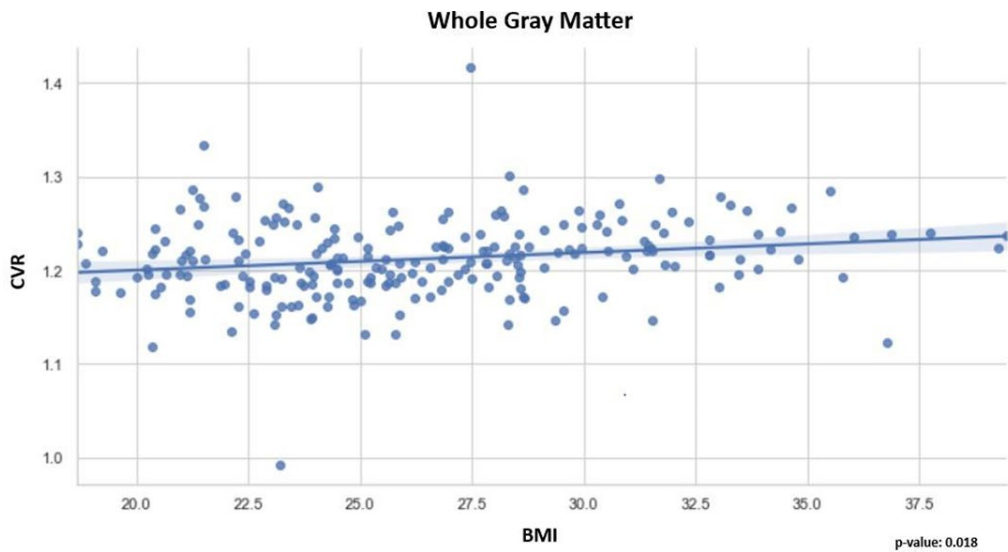


**Figure 3:** Linear relationship between BMI in females and CVR in the whole gray matter. CVR was measured in relative units and BMI in kilograms per squared meters.

# Vascular and metabolic changes in individuals with and without the ApoE $\epsilon$ 4 allele

J. Huck<sup>1,2</sup>, N. Spreng<sup>3,4</sup>, B. Intzandt<sup>2,5,6</sup>, S. Sanami<sup>2</sup>, PREVENT-AD Research Group<sup>7</sup>, S. Villeneuve<sup>4,7</sup>, M. Chakravarty<sup>7</sup>, P.-L. Bazin<sup>8</sup>, and C. J. Gauthier<sup>2,6</sup>

<sup>1</sup>Université de Sherbrooke, Sherbrooke, CA;

<sup>2</sup>Concordia University, Montreal, CA;

<sup>3</sup>McGill University, Montreal, CA,

<sup>4</sup>Montreal Neurological Institute (MNI), McGill University, Montreal, CA;

<sup>5</sup>Hurvitz brain Sciences Research Program, Sunnybrooke research institute, Toronto, CA;

<sup>6</sup>Institut de Cardiologie de Montreal, Montreal, CA;

<sup>7</sup>StoP-AD Centre, Douglas Mental Health Institute Research Centre, Montreal, CA;

<sup>8</sup>Full Brain Picture Analytics, Leiden, Netherlands;

## Synopsis and/or Summary of Main Findings

This study investigates potential early biomarkers of Alzheimer's Disease (AD) through the examination of cerebral blood flow (CBF) and oxygen extraction fraction (OEF). 150 participants with and without the Apolipoprotein E (ApoE)  $\epsilon$ 4 allele, were included. Individuals carrying at least one ApoE  $\epsilon$ 4 allele had significantly lower OEF in several brain regions compared to those with only ApoE  $\epsilon$ 3 alleles. This suggests an imbalance between blood supply and metabolic demand in the ApoE  $\epsilon$ 4 group, possibly indicating early AD-related changes. No significant differences in CBF were observed. These results highlight OEF as a promising and sensitive biomarker for AD risk assessment, which is of crucial importance for early intervention strategies. Further research is needed to elucidate the role of OEF in AD prediction and progression and its promise as a biomarker for preventive interventions.

## Abstract Body:

Alzheimer's Disease (AD) is a neurodegenerative disorder associated in more advanced stages with physiological alterations to Cerebral Blood Flow (CBF) and Oxygen Extraction Fraction (OEF)<sup>1–4</sup>. Preventative interventions that employ sensitive biomarkers early in the disease process are crucially needed in the face of population aging and limited treatment options. The Apolipoprotein E (ApoE)  $\epsilon$ 4 allele is the strongest genetic risk factor for late-onset sporadic AD<sup>5</sup>, and is associated with physiological changes years prior to the development of cognitive impairment in AD<sup>6</sup>. Here, we investigated differences in OEF and CBF between those with and without the ApoE  $\epsilon$ 4 allele.

## Methods:

Data from 150 participants (average age:  $68 \pm 4.87$ , 110 females; see table 1) were obtained from the Pre-symptomatic Evaluation of Novel or Experimental Treatments for Alzheimer's Disease (PREVENT-AD) program (release 6.0 2020). The datasets were acquired on a 3 T Siemens MAGNETOM PRISMA scanner (Siemens Medical Solutions, Erlangen, Germany) with a 32-channel head coil. MoCA scores were measured in a previous release of the dataset. For this study we employed the following: pseudo-continuous arterial spin labelling (pCASL) and an M0 map (for CBF quantification), a high- and low- resolution gradient echo sequence for the QSM reconstruction, and a T1w image for registrations and GM segmentation.

CBF was quantified with FSL BASIL7. The low-resolution GRE images allowed for calculation of the phase offset between the channels using POEM8 and applied to the high-resolution GRE phase images. The TGV-QSM9 algorithm was used to reconstruct the QSM images. Veins were segmented<sup>10</sup> and OEF values were calculated inside veins<sup>11,12</sup>. The MNI structural atlas was registered to QSM and CBF native space. Venous OEF values and CBF values were separately averaged across whole brain and within regions of interest (ROIs), restricted to GM for CBF. OEF and CBF values were compared between the two allele groups utilizing an ANCOVA (with sex and age as covariates). P-values were corrected for multiple comparisons.

## Results:

The results demonstrated that those with APOE  $\epsilon$ 4 allele have significantly lower OEF in all ROIs compared to the ApoE  $\epsilon$ 3 group ( $p < 0.05$ ) (see figure 1). The CBF analysis revealed no significant differences ( $p > 0.05$ ). However, the median CBF values in the frontal, parietal and temporal lobe were higher in the ApoE  $\epsilon$ 4 compared to the ApoE  $\epsilon$ 3.

## Discussion and Conclusion:

Here we revealed lower OEF in whole brain and ROIs in the ApoE  $\epsilon$ 4 group compared to  $\epsilon$ 3 carriers. The lower OEF in the ApoE  $\epsilon$ 4 group likely indicates an imbalance between blood supply and oxidative metabolism. This is consistent with other work in more severely affected AD patients, where a graded decrease in OEF with a greater number of ApoE  $\epsilon$ 4 copies have been shown<sup>13</sup>. Furthermore, no significant differences in CBF were observed, indicating this imbalance is likely not due to hyperperfusion alone. These results demonstrate the utility of OEF as a biomarker for AD risk and its potential in early detection. Future work should investigate these relationships longitudinally to gain a deeper understanding of the complex interplay of the vascular and metabolic alterations in the development of AD.

**Acknowledgments / Funding Information:** Data used in preparation of this abstract were obtained from the Pre-symptomatic Evaluation of Novel or Experimental Treatments for Alzheimer's Disease (PREVENT-AD) program (<https://douglas.research.mcgill.ca/stop-ad-centre>), data release 6.0 (2020). A complete listing of PREVENT-AD

Research Group can be found in the PREVENT-AD database: [https://preventad.loris.ca/acknowledgements/acknowledgements.php?date=\[2019-06-03\]](https://preventad.loris.ca/acknowledgements/acknowledgements.php?date=[2019-06-03]). The investigators of the PREVENT-AD program contributed to the design and implementation of PREVENT-AD and/or provided data but did not participate in analysis or writing of this report. The authors would also like to thank the Fonds de recherche en Santé - Nature et technologies (FRQNT) (JH), the Natural Science and Engineering Research Council (NSERC RGPIN-2015-04665) (JH), and the Heart and Stroke Foundation (Grant-in-Aid G-17-0018336) (C.JG).

#### References:

1. Nagata, K. et al. Can PET Data Differentiate Alzheimer's Disease from Vascular Dementia? *Annals NY Acad Sci* 903, 252–261 (2000).
2. Nagata, K. et al. Vascular and metabolic reserve in Alzheimer's disease. *Neurobiol Aging* 21, 301–307 (2000).
3. Chen, J. J. Functional MRI of brain physiology in aging and neurodegenerative diseases. *NeuroImage* 187, 209–225 (2019).
4. Li, D. et al. Quantitative Study of the Changes in Cerebral Blood Flow and Iron Deposition During Progression of Alzheimer's Disease. *JAD* 78, 439–452 (2020).
5. Corder, E. H. et al. Gene Dose of Apolipoprotein E Type 4 Allele and the Risk of Alzheimer's Disease in Late Onset Families. *Science* 261, 921–923 (1993).
6. Iturria-Medina, Y., Sotero, R. C., Toussaint, P. J., & et al. Early role of vascular dysregulation on late-onset Alzheimer's disease based on multifactorial data-driven analysis. *Nature Communications* 7, 11934 (2016).
7. Chappell, M. A., Groves, A. R., Whitcher, B. & Woolrich, M. W. Variational Bayesian Inference for a Nonlinear Forward Model. *IEEE Trans. Signal Process.* 57, 223–236 (2009).
8. Sun, H. et al. Extracting more for less: multi-echo MP2RAGE for simultaneous T1-weighted imaging, T1 mapping, mapping, SWI, and QSM from a single acquisition. *Magn Reson Med* 83, 1178–1191 (2020).
9. Langkammer, C. et al. Fast quantitative susceptibility mapping using 3D EPI and total generalized variation. *NeuroImage* 111, 622–630 (2015).
10. Bazin, P.-L., Plessis, V., Fan, A. P., Villringer, A. & Gauthier, C. J. Vessel segmentation from quantitative susceptibility maps for local oxygenation venography. in 2016 IEEE 13th International Symposium on Biomedical Imaging (ISBI) 1135–1138 (IEEE, 2016). doi:10.1109/ISBI.2016.7493466.
11. Fan, A. P. et al. Elevated brain oxygen extraction fraction measured by MRI susceptibility relates to perfusion status in acute ischemic stroke. *J Cereb Blood Flow Metab* 40, 539–551 (2020).
12. Uwano, I. et al. Noninvasive Assessment of Oxygen Extraction Fraction in Chronic Ischemia Using Quantitative Susceptibility Mapping at 7 Tesla. *Stroke* 48, 2136–2141 (2017).
13. Lin, Z. et al. Brain Oxygen Extraction by Using MRI in Older Individuals: Relationship to Apolipoprotein E Genotype and Amyloid Burden. *Radiology* 292, 140–148 (2019).

#### Tables and figures

	<b>ApoE <math>\epsilon</math>4-4 &amp; ApoE <math>\epsilon</math>4-3</b> (n = 61; 43 Females)	<b>ApoE <math>\epsilon</math>3-3</b> (n = 89, 60 Females)
<b>Age</b> (female; male)[years]	66.9 $\pm$ 4.9; 66.2 $\pm$ 3.5	67.9 $\pm$ 4.9; 69.2 $\pm$ 6.6
<b>Education</b> (years)	15.2 $\pm$ 3.5	15.4 $\pm$ 3.4
<b>MoCA</b> (out of 30)	28.4 $\pm$ 1.5	28.1 $\pm$ 1.5

**Table 1:** Demographics of the participants included in this study. Individuals were split into two groups (ApoE E4, which included individuals with at least one  $\epsilon$ 4 allele (ApoE  $\epsilon$ 4-3 and ApoE  $\epsilon$ 4-4) and individuals without the  $\epsilon$ 4 allele (ApoE  $\epsilon$ 3)).

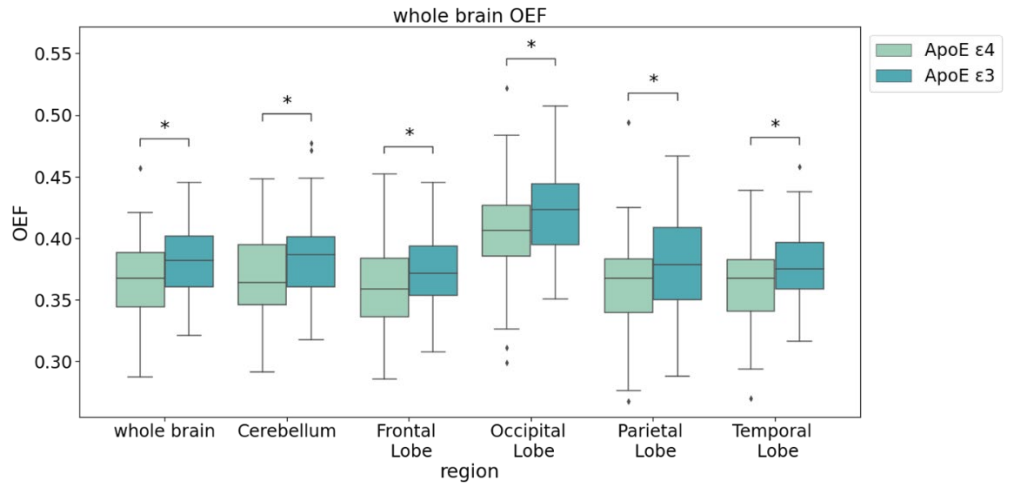


**Figure 1:** Average OEF values across the entire brain and in different brain regions for individuals with ApoE  $\epsilon 4$  and  $\epsilon 3$ . Individuals with ApoE  $\epsilon 4$  show significant lower OEF values in all brain regions. Values are corrected for sex, age and multiple comparison.

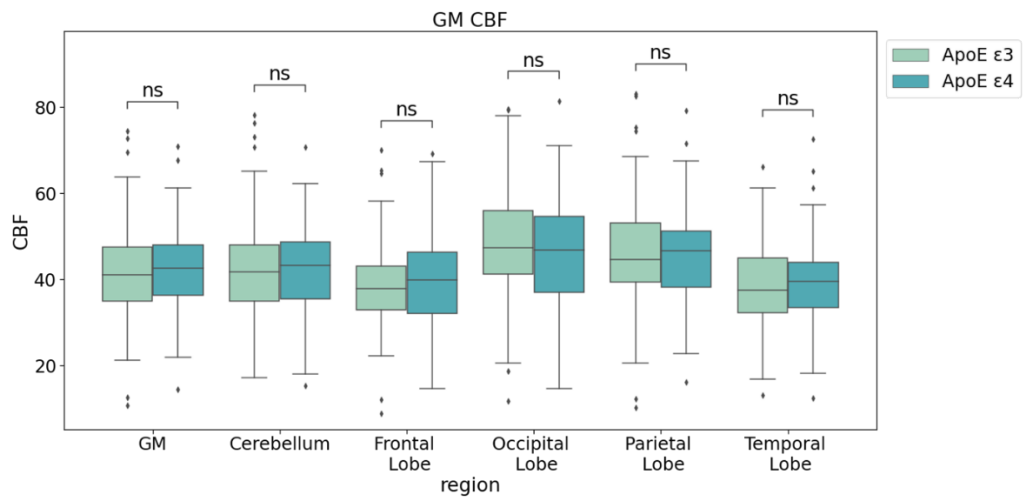


**Figure 2:** Average CBF values across the entire GM and in different brain regions inside the GM for individuals with ApoE  $\epsilon 4$  and  $\epsilon 3$ . No significant differences between the two groups were found. Values are corrected for sex, age and multiple comparison.

# Automated Cerebral Blood Flow Metrology and Physiology in Anesthetized Children Using Phase Contrast MRI

J. Liu<sup>1</sup>, I. Torres<sup>2,3</sup>, S. Ranganathan<sup>1,4</sup>, A. Karnwal<sup>5</sup>, B.S. Peterson<sup>6,7</sup>, J. Wood<sup>4</sup>, M. Borzage<sup>1</sup>

<sup>1</sup>Division of Neonatology, Department of Pediatrics, Children's Hospital Los Angeles, Keck School of Medicine, University of Southern California, Los Angeles, USA;

<sup>2</sup>Department of Radiology, Children's Hospital Los Angeles, Keck School of Medicine, University of Southern California, Los Angeles, USA;

<sup>3</sup>Rudi Schulte Research Insitute, Santa Barbara, USA;

<sup>4</sup>Division of Cardiology, Department of Pediatrics, Children's Hospital Los Angeles, Keck School of Medicine, University of Southern California, Los Angeles, USA;

<sup>5</sup>Anesthesia Critical Care Medicine, Children's Hospital Los Angeles, Keck School of Medicine, University of Southern California, Los Angeles, USA;

<sup>6</sup>Institute for the Developing Mind, Children's Hospital Los Angeles, USA;

<sup>7</sup>Department of Psychiatry, Keck School of Medicine, University of Southern California, Los Angeles, USA

## Summary of Main Findings

We developed and used a new algorithm to measure changes in cerebral blood flow in anesthetized children (N=29) using phase contrast magnetic resonance imaging. During anesthesia, our results show there is no significant change ( $p=0.99$ ) in cerebral blood flow between 3 measurements at times (A)  $19.1\pm 13.0$ min, (B)  $22.3\pm 13.2$ min, and (C)  $65.6\pm 21.5$ min.

## Introduction

Using phase contrast magnetic resonance imaging (PC-MRI) to measure cerebral blood flow in children is possible, yet difficult due to smaller vessels, lower blood velocities, and aliased blood flows. We developed an algorithm to address these challenges and assessed putative effects of anesthesia on cerebral blood flow.

## Methods

PC-MRI was acquired from children undergoing clinical MRI whose parents provided informed consent (CHLA-18-00439). All images were obtained using a Philips 3T magnet and head coil and acquired at C2 vertebrae level, perpendicular to the arteries. Sequence parameters included velocity encoding 30-60cm/s, number of signals averaged 12-36, compressed sensitivity encoding (SENSE) factor 2, and in-plane resolution 0.50-0.89mm. Each scan included 3 measurements: as soon as possible after anesthetic induction (A) and (B) for test-retest variability (Intraclass Correlation Coefficient: ICC), and at the end of the clinical MRI (C) for overall change (one-way Analysis of Variance: ANOVA). Cerebral blood flow was calculated with algorithmic and manual approaches. Our algorithm comprised: unwrapping aliased vessels, evaluated using Mean Absolute Error (MAE) versus manual unaliasing; creating vessel masks, evaluated using Matthew's Correlation Coefficient (MCC) versus manual regions of interest; computing cerebral blood flow, evaluated by measuring reliability (ICC) versus the manual approach; identifying vessels, tested using MCC (Fig. 1). The manual approach, performed by 2 trained personnel, included: drawing regions of interest delineating internal carotid and vertebral arteries (48 and 39 images each) and correcting aliasing on 10 artificially aliased ground truth images (5 images each).

## Results

We imaged N=29 children (1.10-5.15years,  $2.96\pm 1.10$ years). MAE for unaliasing was similar for algorithm and manual methods (0.07 and 0.03mL/min). Vessel masks generated by algorithm and manually were compared for each image (median MCC=0.79). Vessel identification performed by algorithm and manually were comparable (MCC=1.00). We report high reliability between algorithm and manual methods (ICC=0.92). Mean cerebral blood flow for measurements A, B, and C was  $526.2\pm 192.6$ mL/min,  $529.5\pm 225.1$ mL/min, and  $521.3\pm 222.1$ mL/min, respectively. The one-way ANOVA showed no significant difference ( $p=0.99$ ) between cerebral blood flow measurements A, B, and C. The test-retest reliability between measurements A and B was high (ICC=0.95). We calculated mean percent changes and confidence intervals (CI) in measurements from A to B (-0.38% and 95% CI -4.57%, 3.81%) and A to C (-0.53% and 95% CI -9.00%, 7.95%). The one-way ANOVA showed no significant difference between percent blood flow changes ( $p=0.97$ ). The time elapsed (minutes) from induction of anesthesia to measurements were (A)  $19.1\pm 13.0$ , (B)  $22.3\pm 13.2$ , and (C)  $65.6\pm 21.5$ , and varied depending on anesthesia team and duration of clinical MRI exam.

## Conclusion

We addressed challenges in measuring cerebral blood flow in children. We expected anesthetic exposure to reduce cerebral blood flow rapidly, and initial results indicate no significant change between measurements A, B, and C. Absence of significant change in flow over time may be attributable to delays between anesthetic induction and measurement (A), and our measurements could be during a low, but stable period. Our validation with metrics and preliminary results show that our algorithm is valuable for measuring cerebral blood flow and studying cerebral hemodynamics.

## Figures

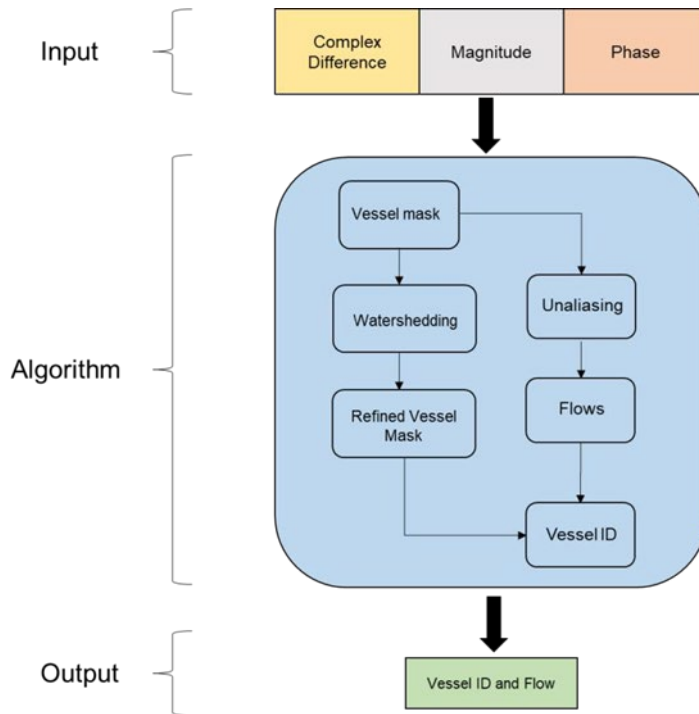


**Figure 1:** Phase Contrast MRI Analysis Algorithm Our algorithm automatically processes phase contrast magnetic resonance imaging. The algorithm includes (1) unwrapping aliased vessels, (2) creating vessel masks, (3) computing cerebral blood flow, and (4) identifying vessels.

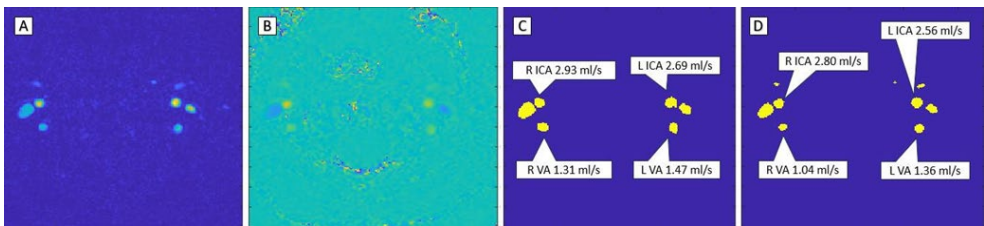


**Figure 2:** Raw Phase Contrast Data and Calculation of Cerebral Blood Flow Raw phase contrast MRI data consists of the (A) complex difference image which shows the cross-sections of vessels, and (B) phase image which shows the velocity in each voxel in yellow (positive) and blue (negative). The images are analyzed by creating vessel masks (C) manually, and (D) using the algorithm. Images C & D both show flows for internal carotid arteries (ICA) and vertebral arteries (VA).

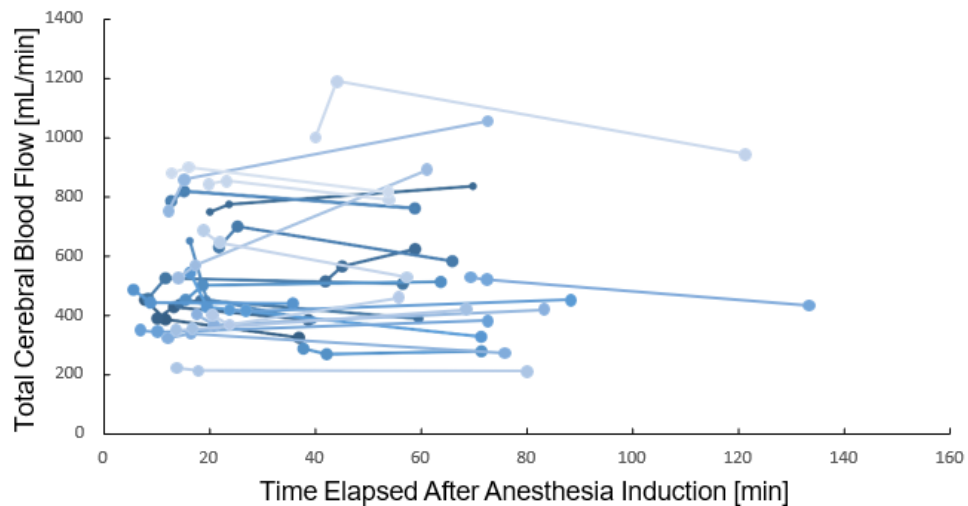


**Figure 3:** Cerebral Blood Flow At 3 Measurements Post-Anesthesia Induction Cerebral blood flow was calculated at measurements A, B, and C after induction of anesthesia for N=29 children (each represented by a different color shade). The time elapsed from induction of anesthesia to the measurements were (A)  $19.1 \pm 13.0$  min, (B)  $22.3 \pm 13.2$  min, and (C)  $65.6 \pm 21.5$  min. The cerebral blood flow measurements may represent potential confounding effects of other hemodynamic changes.

# Macrovasculature-suppressed ASL MRI in neonates: quantification of cerebral blood flow and arterial transit time

Zhiyi Hu<sup>1</sup>, Dengrong Jiang<sup>2</sup>, Jennifer Shepard<sup>3</sup>, Yuto Uchida<sup>2</sup>, Kenichi Oishi<sup>2</sup>, Peiying Liu<sup>2,4</sup>, Doris Lin<sup>2</sup>, Vivek Yedavalli<sup>2</sup>, Aylin Tekes<sup>2</sup>, W. Christopher Golden<sup>3</sup>, Hanzhang Lu<sup>1,2,5</sup>

<sup>1</sup>Department of Biomedical Engineering, Johns Hopkins University School of Medicine, Baltimore, US;

<sup>2</sup>Department of Radiology, Johns Hopkins University School of Medicine, Baltimore, US;

<sup>3</sup>Department of Pediatrics, Johns Hopkins University School of Medicine, Baltimore, US;

<sup>4</sup>Department of Diagnostic Radiology and Nuclear Medicine, University of Maryland School of Medicine, Baltimore, US;

<sup>5</sup>F.M Kirby Research Center for Functional Brain Imaging, Kennedy Krieger Research Institute, Baltimore, US;

## Synopsis

A prominent feature in neonatal cerebral blood flow (CBF) measurement is the hyperperfusion in the deep brain region. Given the rich presence of large arteries in this region, it is plausible that macrovascular artifacts may play a major role in the hyperintense signals observed. This study presented a new MRI technique, pCASL with arterial suppression and flow suppression (AFS-pCASL) to minimize the macrovascular artifacts in neonates. We demonstrated that macrovascular artifacts in neonatal pCASL can be substantially suppressed, from which quantitative CBF and arterial transit time (ATT) can be measured when applying the sequence in a multi-delay setting. Our results showed that ATT in neonates is slightly longer than that in adults, but not substantially longer. Macrovasculature-suppressed CBF in neonatal deep gray matter is the highest across the brain, which is similar to previous neonatal perfusion findings.

## INTRODUCTION

Cerebral blood flow (CBF) is crucial for assessing neonatal brain development and metabolic demand.<sup>1-3</sup> Arterial-spin-labeling (ASL) MRI has been established in adults for CBF assessment,<sup>4</sup> but its application in neonates remains challenging. A prominent feature in prior neonatal ASL CBF images is the hyperintense signal in the deep brain region, spanning from the mid-brain to the deep gray nuclei.<sup>5,6</sup> Additionally, arterial transit time (ATT) in neonates has not been reliably determined, impacting the selection of optimal labeling delay in neonatal ASL. Therefore, this study introduced a new scheme to suppress macrovascular signals in pseudo-continuous ASL (pCASL) and quantified CBF and arterial transit time (ATT) in healthy term-born neonates.

## METHODS

General Experimental method: The non-sedated neonates were retained in natural sleep when scanned on a Siemens 3T Prisma system. Two sub-studies were performed.

Study 1: Evaluation of macrovasculature-suppression schemes: Two macrovasculature-suppression schemes were developed and compared with a standard 3D GRASE pCASL sequence (Figure 1a).

Figure 1b depicts pCASL with arterial-suppression (AS-pCASL), which employed saturation RF pulses during PLD to suppress the incoming arterial blood after the labeling module. An additional flow-suppression preparation module ( $v_{enc}=4\text{cm/s}$ ) was applied in pCASL with arterial-suppression and flow-suppression (AFS-pCASL, Figure 1c) to attenuate the remaining macrovascular signals.

The three sequences were tested on 8 neonates (5 females,  $39.2\pm 1.1$ weeks): labeling duration=1800ms, PLD=3000ms, voxel size= $3.5\times 3.5\times 4\text{mm}^3$ , TR/TE=5370/24.76ms.

Study 2: Multi-delay scan to estimate CBF and ATT: Based on the results of Study 1 (see below), the AFS-pCASL sequence was used to minimize macrovascular contaminations. 12 neonates (8 female,  $39.0\pm 0.9$ weeks) were studied and 5 PLDs were acquired: 800ms, 1400ms, 2175ms, 2700ms and 3000ms. ATT was estimated in 4 ROIs (Figure 3b) using the method of signal-weighted delay.<sup>7</sup> CBF values were also calculated.

## RESULTS AND DISCUSSION

Figure 2a displays the average CBF maps acquired with the three pCASL sequences, while the temporal standard deviation map (STD) is also shown (Figure 2b) to illustrate the most pulsatile signal. Despite the long PLD of 3000ms, the conventional pCASL sequence still exhibited a hyperintense macrovascular signal and prominent signal variation aligning with major brain arteries (e.g. near Circle of Willis, COW). Arterial-suppression mitigated these hyperintensities and pulsatile signals, which were further reduced by additional flow-suppression. Figure 2c quantifies CBF and STD within the COW and brain parenchyma. COW CBF signal was reduced by 53% and 59% in the AS-pCASL and AFS-pCASL, respectively, with similar STD reduction. In contrast, the macrovasculature-suppressed parenchymal CBF and STD showed less decrease.

Figure 3a displays group average PLD-dependent ASL images. Quantitative ASL kinetic curves in 4 ROIs (Figure 3b) are also shown (Figure 3c). Figure 3d summarizes the average ATT and CBF values. We found a slightly longer ATT in neonates than that in adults. Of note, a short ATT and high CBF were observed in the deep gray matter, similar to previous 15O-PET CBF findings.<sup>8</sup>

## CONCLUSION

Using an AFS-pCASL sequence, we demonstrated that macrovascular artifacts in neonatal pCASL can be substantially suppressed, from which quantitative CBF and ATT in neonates can be measured when applying the sequence in a multi-delay setting.

Acknowledgments / Funding Information: This work was supported by the National Institutes of Health: R01 NS106711, R01 NS106702, R01 AG064792, UF1 NS100588, R01 NS109029, RF1 AG071515, P41 EB031771.

**Acknowledgments / Funding Information:** This work was supported by the National Institutes of Health: R01 NS106711, R01 NS106702, R01 AG064792, UF1 NS100588, R01 NS109029, RF1 AG071515, P41 EB031771.

**Reference**

1. Proisy M, Corouge I, Legouhy A, Nicolas A, Charon V, Mazille N, Leroux S, Bruneau B, Barillot C, Ferre JC. Changes in brain perfusion in successive arterial spin labeling MRI scans in neonates with hypoxic-ischemic encephalopathy. *Neuroimage Clin* 2019;24:101939.
2. Mabray P, Thewamit R, Whitehead MT, Kao A, Scafi J, Gaillard WD, Chang T, Tsuchida TN. Increased cerebral blood flow on arterial spin labeling magnetic resonance imaging can localize to seizure focus in newborns: A report of 3 cases. *Epilepsia* 2018;59:e63-e67.
3. Tortora D, Lo Russo FM, Severino M, Parodi A, Massirio P, Ramenghi LA, Rossi A. Regional impairment of cortical and deep gray matter perfusion in preterm neonates with low-grade germinal matrix-intraventricular hemorrhage: an ASL study. *Neuroradiology* 2020;62:1689-1699.
4. Alsop DC, Detre JA, Golay X et al. Recommended implementation of arterial spin-labeled perfusion MRI for clinical applications: A consensus of the ISMRM perfusion study group and the European consortium for ASL in dementia. *Magn Reson Med* 2015;73:102-116.
5. Tortora D, Mattei PA, Navarra R, Panara V, Salomone R, Rossi A, Detre JA, Caulo M. Prematurity and brain perfusion: Arterial spin labeling MRI. *Neuroimage Clin* 2017;15:401-407.
6. Kim HG, Lee JH, Choi JW, Han M, Gho SM, Moon Y. Multidelay Arterial Spin-Labeling MRI in Neonates and Infants: Cerebral Perfusion Changes during Brain Maturation. *AJNR Am J Neuroradiol* 2018;39:1912-1918.
7. Dai W, Robson PM, Shankaranarayanan A, Alsop DC. Reduced resolution transit delay prescan for quantitative continuous arterial spin labeling perfusion imaging. *Magn Reson Med* 2012;67:1252-1265.
8. Andersen JB, Lindberg U, Olesen OV, Benoit D, Ladefoged CN, Larsson HB, Hojgaard L, Greisen G, Law I. Hybrid PET/MRI imaging in healthy unsedated newborn infants with quantitative rCBF measurements using (15)O-water PET. *J Cereb Blood Flow Metab* 2019;39:782-793.

**Figures**

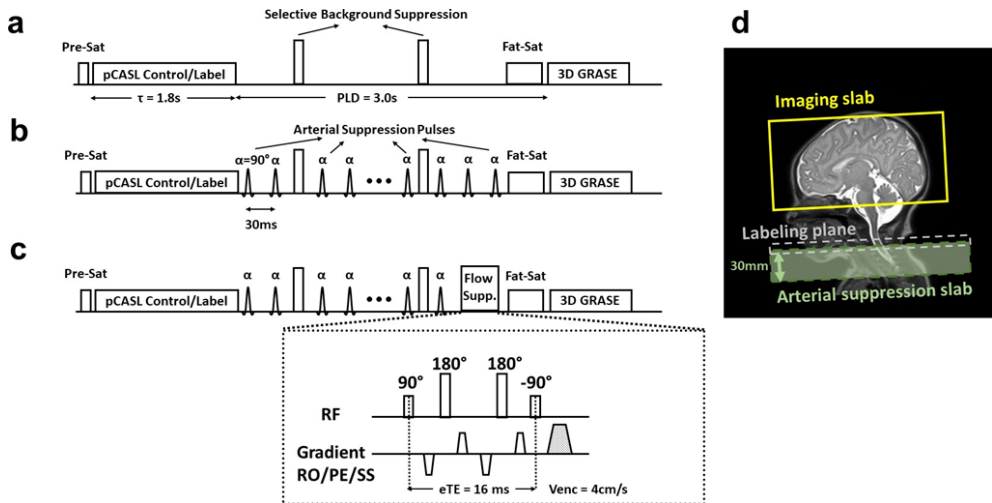


**Fig 1.** Sequence diagram of macrovasculature-suppressed pCASL. (a) Conventional pCASL. (b) pCASL with arterial suppression (AS-pCASL). (c) pCASL with arterial suppression and flow suppression (AFS-pCASL). (d) Positioning illustration.

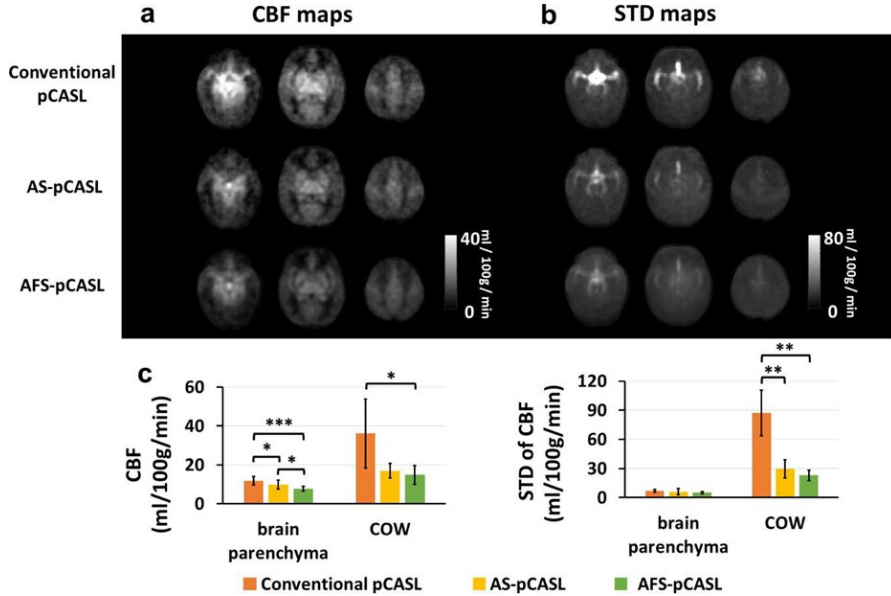


**Fig 2.** Comparison among macrovasculature-suppression schemes. (a) Group average CBF maps. (b) Temporal standard deviation maps, illustrating the most prominent pulsating signal. (c) Quantitative CBF and temporal standard deviation of CBF within the brain parenchyma and circle of Willis.

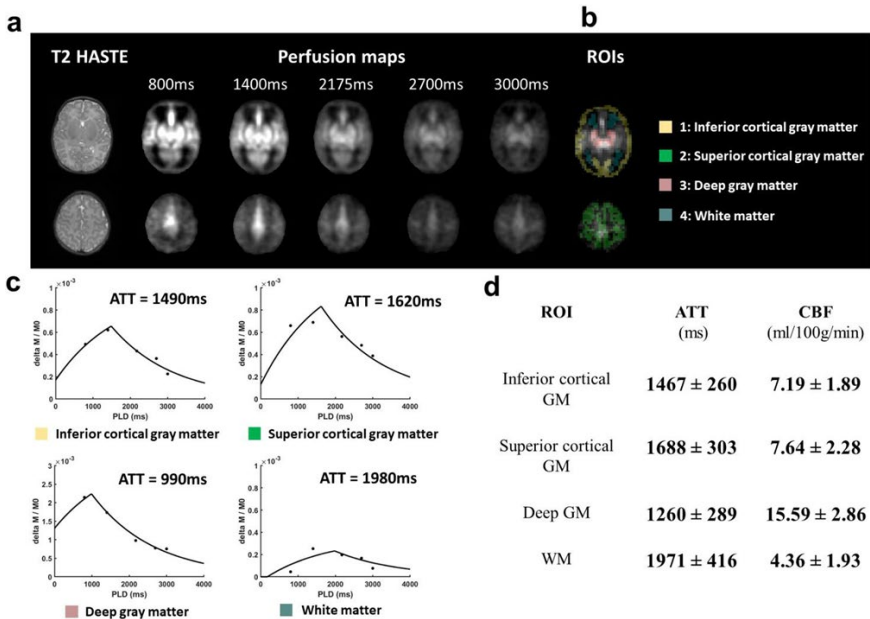


**Fig 3.** CBF and ATT estimation with multi-delay AFS-pCASL. (a) Group average PLD-dependent ASL images. (b) Illustration of 4 ROIs. ROI 1: inferior cortical gray matter at the level of the third ventricle, ROI 2: superior cortical matter at the level of superior frontoparietal cortex, ROI 3: deep gray matter, ROI 4: white matter. (c) Quantitative ASL kinetic curves for each ROI of a representative subject. (d) Summary of group average ATT values and ATT-corrected CBF in different ROIs

# From microscopy data to hemodynamic simulations: a vascular graph approach to understand the fMRI signal formation

V. Curcic<sup>1</sup>, M.G. Báez-Yáñez<sup>1</sup>, C. Liu<sup>2</sup>, P. Kara<sup>2</sup>, M.J.P. van Osch<sup>3</sup>, N. Petridou<sup>1</sup>

**1**Department of Radiology, UMCU, Utrecht, Netherlands, **2**University of Minnesota, Minnesota, USA, **3**Department of Radiology, Leiden UMC, Leiden, Netherlands

## Synopsis:

This study presents a pipeline for extracting realistic vascular models from cortical mouse data obtained with 2-photon microscopy. The pipeline employs graph theory to represent the cortical vasculature as a network composed by nodes and links providing detailed information on the cortical vascular architecture and vessel properties. Then, hemodynamic simulations were conducted using the extracted vascular graphs allowing the investigation of cerebral blood flow, blood volume, local blood pressure, and vascular resistance changes resulting from virtual arterial dilation. This framework is valuable for studying how the vascular architecture and vessel properties influence the spatiotemporal features of hemodynamic responses, and thus enhancing the interpretation of fMRI signals.

## Introduction:

Interpretation of fMRI signals requires a deep understanding of the intrinsic biophysical effects induced by the cortical vascular architecture and its functioning. Moreover, this knowledge might help to characterize the contribution of vessel dysfunction to cerebrovascular diseases. Towards this end, we have developed a pipeline that utilizes graph theory to extract realistic virtual models of the vascular architecture from the mouse cortex based on 2-photon microscopy data. Using these realistic vascular models, we have simulated hemodynamic changes, e.g. cerebral blood flow, cerebral blood volume, and local blood pressure, caused by a virtual arterial dilation.

## Methods and Results:

Our pipeline represents the cortical vasculature as a graph composed of nodes and links [1]. Initially, we extracted the centerlines (skeleton) of the vasculature (Fig 1 panel 2). From the skeleton, we identified the branching and ending points of the vessels, which serve as nodes in the vascular graph (Fig 1 panel 3). Using the node coordinates, we divided the skeleton into vessel segments or vascular graph links, labeled each segment, and characterized its properties (Fig 1 panels 4, 5 and 5 a). This information was used to construct the vascular graph (Fig 1. panel 6) and convert it into a 2D binary connectivity matrix (Fig 1. panel 7) that accurately represents the vascular topology. Hemodynamic simulations are based on the conservation of energy and they involve converting the graph's connectivity matrix into a connected dynamic system modeled by RC circuits [3]. To mimic the hemodynamic response, we simulated a virtual arterial dilation of 50% and heart rate with a frequency of 1.7 Hz, which results in a modification of the vascular resistance throughout the vascular network (Fig 2 panel 3), [2,3, 5]. Considering the blood viscosity, hematocrit, and vessel properties in Fig 2 panel 3, changes in the cerebral blood flow ( $\Delta$ CBF) and volume ( $\Delta$ CBV), local blood pressure ( $\Delta$ BP), and vascular resistance ( $\Delta$ R) were calculated [4].

## Discussion:

Using the developed pipeline, we extracted and described two realistic vascular models from cortical mouse data acquired with two-photon microscopy. The vascular graph approach offers a high degree of flexibility, allowing easy modification of blood vessel characteristics such as radius and compliance. Hemodynamic changes can be studied spatially at any vessel, and the simulations are based on physiologically relevant assumptions (hematocrit = 45%; blood viscosity is dependent on vessel radius, panel 10).  $\Delta$ CBF,  $\Delta$ CBV, and  $\Delta$ BP change according to the anatomical and physiological vessel properties (e.g. Fig 2 panel 2). A nonlinear relation between the radius and the vascular resistance is demonstrated together with the dependence on vessel length (Fig 2 panel 3). Note that our vascular model includes vessels running in the boundary of GM/WM (Fig 1 panel 5 b).

## Conclusion:

The presented pipeline offers a flexible approach for extracting realistic vascular models, by converting the vascular architecture into a vascular graph representation. The framework presented here can serve as a valuable approach for investigating how the structure and functional properties of the vasculature affect the spatiotemporal characteristics of the hemodynamic response, thereby facilitating the interpretation of fMRI signals. Moreover, this approach is suitable for simulating different vascular conditions associated with various cerebrovascular diseases.

**Acknowledgments / Funding Information:** Top Sector Life Sciences & Health (LSH) – Dutch Research Council (NWO) TTW award 18969

References: [1] Reichold et al. (2009) JCBFM; 29(8):1429-43. [2] Boas et al., (2008) Neuroimage 40:1116-29. [3] Báez-Yáñez et al. (2023) NMR Biomed, 2020.10. 05.326512 [4] Gagnon L et al. (2015) J Neurosci 35:3663–3675. [5] Hartung et al. 2022 Proc. ISMRM 2022, abstract: 0682.

## Figures

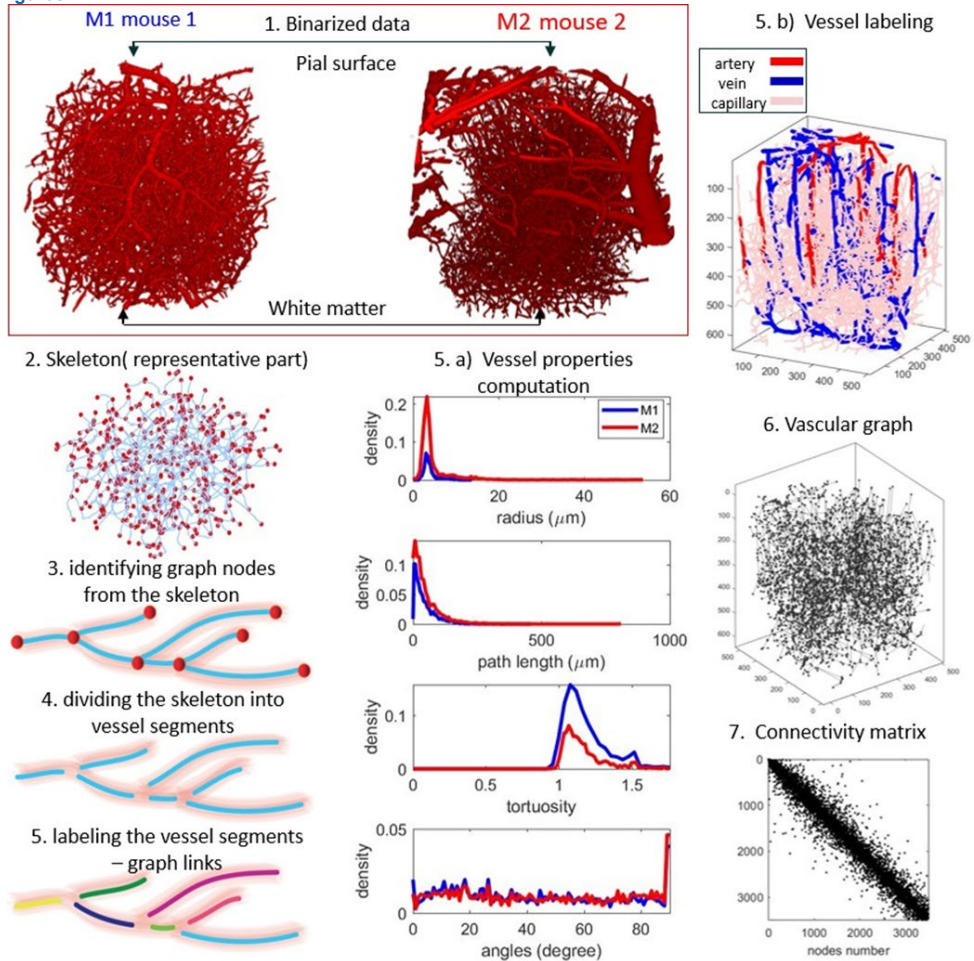


**Figure 1:** Pipeline for creating vascular graphs and computation of vascular properties: 1) Binarized data for mouse M1 and M2, 2) Data is skeletonized, 3-5) Graph nodes and links are extracted from the skeleton, 4) Vessel properties: radius, length, tortuosity, and angle (with respect to the axis normal to the cortical surface) for M1 and M2, 5a) Vessels are labeled according to computed properties, 6) Vascular graph is generated and 7) converted to connectivity matrix.

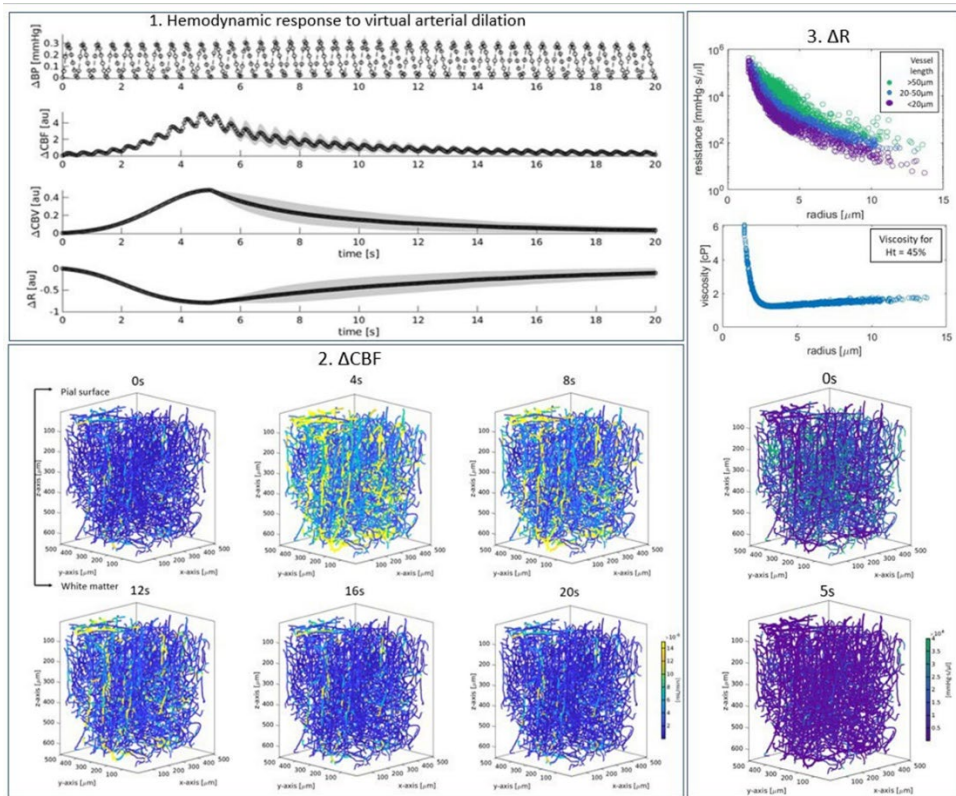


**Figure 2:** Hemodynamic simulations: 1) Changes in BP, CBF, CBV, and R averaged across the entire vascular graph, 2) Spatial distribution of CBF changes across vasculature at different time points, 3) From the top to bottom: dependency of resistance to the radius and length (color-coded according to 3 groups of vessel lengths), dependency of viscosity to vessel radius, spatial distribution of R changes across vasculature at different time points.

# Estimating the viscoelastic properties of the human brain using intrinsic MRE and nonlinear inversion at 7T

M. Burman<sup>1</sup>, J. Zwanenburg<sup>1</sup>, E. van Houten<sup>2</sup>

<sup>1</sup>Centre for image sciences, UMC Utrecht, Utrecht, The Netherlands; <sup>2</sup>Department of Mechanical Engineering, Sherbrooke University, Sherbrooke, Canada

## Synopsis and/or Summary of Main Findings:

Mechanical properties of the human brain can be altered by a variety of pathologies. These properties can be estimated from in vivo MRI measurements of brain tissue displacements as induced by the heartbeat. Previously obtained 7T MRI displacements measurements were used to reconstruct stiffness parameters using a subzone-based non-linear inversion scheme. Various structures of the brain can be observed in the reconstructed parameter distributions, and the results show good test-retest reliability. The preliminary results show promise of this approach to yield non-invasive assessment of brain tissue microstructure as a tool to investigate brain disease.

## Introduction

A variety of pathologies can alter the microstructure of human brain tissue. In general, changes in human tissue can be quantified using Magnetic Resonance Elastography (MRE), where harmonic steady-state mechanical waves are induced at a region of interest. The resulting tissue displacements can then be measured using phase-contrast MRI, and the measurements can be used to reconstruct mechanical properties of the tissue. However, the brain is enveloped in cerebral meninges and the cranium, which dampen extrinsically applied vibrations. Additionally, the porous nature of the brain results in it having a frequency dependent response, causing such vibrations to affect the brain stiffness<sup>1</sup>. Alternatively, mechanical properties of the brain can be estimated from in vivo MRI measurements of brain tissue deformation as induced by the heartbeat<sup>2,3</sup>. Recently, the quality of these deformation measurements was improved significantly using ultrahigh field (7T) MRI<sup>4</sup>. The purpose of this project is to reconstruct brain stiffness parameters from 7T MRI measurements of the displacements resulting from intrinsic, cardiac-induced vibrations, and to assess the test-retest reliability.

## Method

The displacement measurements used in this analysis were previously acquired for a separate study<sup>4</sup>, where eight healthy subjects (27 ± 7 years) were imaged with repeated scans (spatial resolution approx. 2 mm isotropic, temporal resolution 75 ms, motion sensitivity 0.35 mm/2π for displacements in Anterior-Posterior and Left-Right directions, and 0.7 mm/2π for Feet- Head displacements). The viscoelastic properties of the brain were estimated using a subzone based non-linear inversion scheme<sup>5</sup>.

## Results

Figure 1 shows a representative axial slice in one subject of the shear stiffness and the damping ratio, along with the equivalent slice in the repeated scan which has been co-registered to the original scan. The mean over all subjects and repeats for the  $\mu$  and  $\xi$  distributions are shown in Figure 2, where each image has been registered to the MNI-ICBM2009c non-linear template. The results show comparable consistency to that of extrinsic MRE between the viscoelastic property maps obtained from repeated displacement measurements. The shear stiffness maps showed consistent spatial patterns. A subject-wise Bland-Altman analysis is presented in Figure 3. The whole-brain repeatability coefficient (RC) for shear stiffness was (mean ± standard deviation) 8% ± 8% relative to the mean whole-brain stiffness, and the damping ratio RC was 28% ± 17% relative to the whole-brain damping ratio. The shear stiffness maps showed similar statistically significant regional trends as demonstrated in a publicly available atlas of viscoelastic properties obtained with extrinsic actuation MRE at 50 Hz. The damping ratio maps showed less consistency, likely due to data-model mismatch of describing the brain as a viscoelastic material under low frequencies.

## Conclusion

While artifacts induced by fluid flow within the brain remain a limitation of the technique in its current state, intrinsic actuation based MRE allow for consistent and repeatable estimation of the mechanical properties of the brain. The method provides enough sensitivity to investigate regional variation in such properties in the normal brain, which is likely sufficient to also investigate pathological changes.

**Acknowledgments / Funding Information:** This work was supported by a Vici Grant from the Netherlands Organization for Scientific Research (NWO) awarded to Jaco J.M. Zwanenburg under grant agreement no. 18674, and by the European Research Council under the European Union's Seventh Framework Programme (FP7/2007-2013) / ERC grant agreement n°337333.

## References:

1. Testu J et al. Viscoelastic power law parameters of in vivo human brain estimated by MR Elastography, *J Mech Behav Biomed Mater.* 2017;74:333-341
2. Zorgani A. et al. Brain palpation from physiological vibrations using MRI, *PNAS*, 2015;112(42):12917-21.
3. Weaver J. et al. Brain mechanical property measurement using MRE with intrinsic activation, *PMB*, 2012;57(22):7275-87.
4. Adams A. et al. Validating faster DENSE measurements of cardiac-induced brain tissue expansion as a potential tool for investigating cerebral microvascular pulsations, *Neuroimage*, 2020;208:116466.
5. Van Houten E.E.W. et al. Three-dimensional subzone-based reconstruction algorithm for MR elastography, *Magn Reson Med.* 2001;45(5):827-37.

## Figures

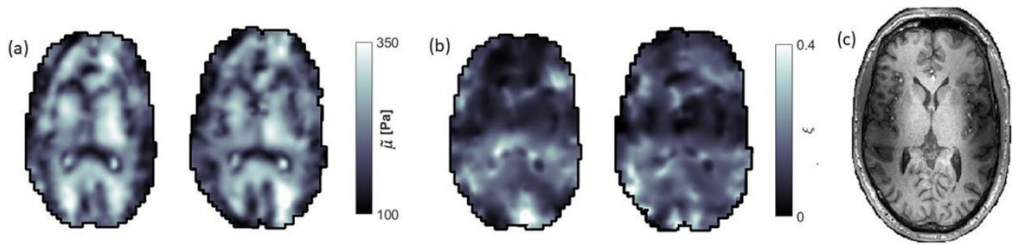


**Figure 1** Representative axial slices of the (a) shear stiffness,  $\mu$  [Pa], and the (b) damping ratio,  $\xi$ , for one subject along with repeat scans that have been co-registered to the initial scan. A T1-weighted image of the equivalent slice is shown in (c).

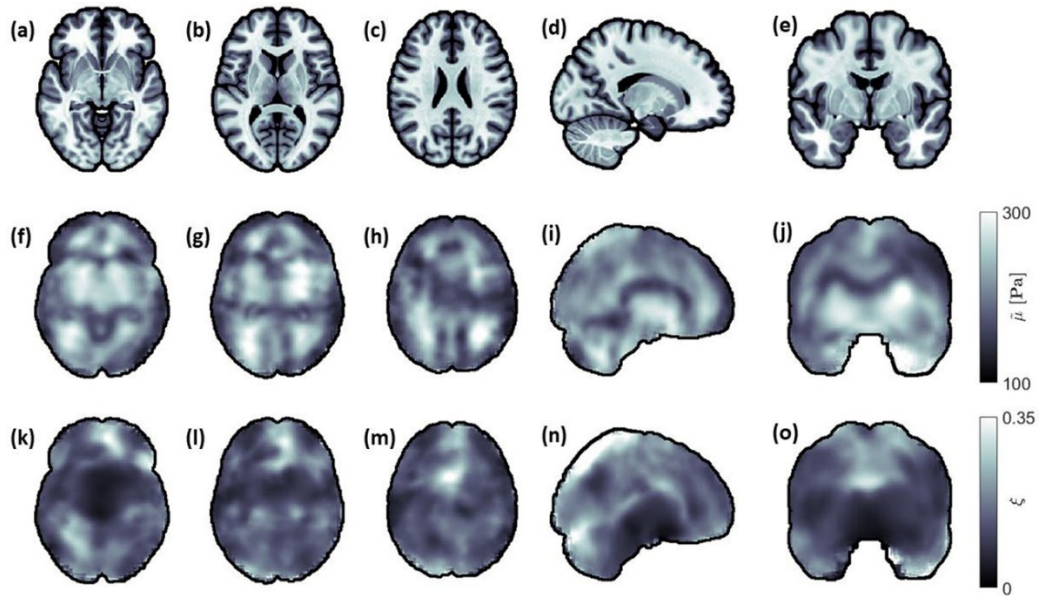


**Figure 2.** Transverse (a, b, c), sagittal (d), and coronal (e) anatomical representations of the brain in common space (MNI-ICBM2009c template), and respective shear stiffness (f-j) and damping ratio (k-o) maps, obtained from averaging over all subjects and repeats. Each individual parameter map has been registered to the MNI-ICBM2009c brain atlas.

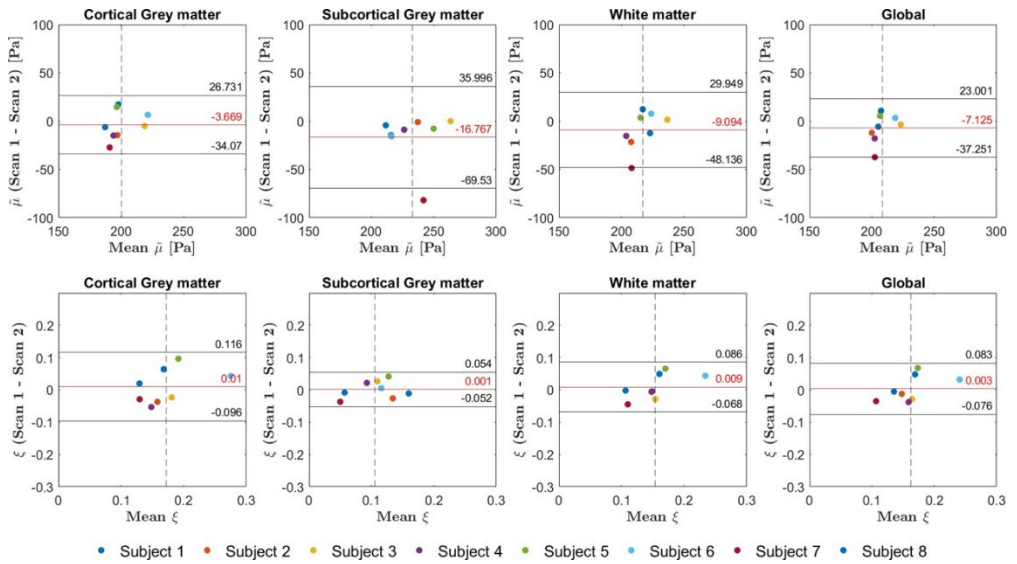


**Figure 3:** Bland-Altman plots of the mean shear stiffness (top row) and damping ratio (bottom row) in cortical GM, subcortical GM, WM, and global ROIs for all subjects. The horizontal red line represents the bias  $bb$  which is the mean of the differences between the two measurements. The upper and lower horizontal black lines represent the upper and lower limits of agreement respectively, defined as  $bb \pm 1.96 \cdot ssssss$ . The vertical dashed line indicates the mean over all subjects.

# Velocity selective Arterial Spin Labeling at 7T

Emiel C.A. Roefs<sup>1</sup>, Lydiane Hirschler<sup>1</sup>, Natalia Petridou<sup>2</sup>, Matthias J.P. van Osch<sup>1</sup>

<sup>1</sup>Department of Radiology, C.J. Gorter MRI Center, Leiden University Medical Center, Leiden, Netherlands;

<sup>2</sup>Department of Radiology, Center for Image Sciences, UMCU, Utrecht, Netherlands;

## Synopsis and/or Summary of Main Findings:

We showed the feasibility of velocity selective arterial spin labeling (VSASL) at 7T. VSASL perfusion images showed in general good visual agreement with FAIR ASL. However, VSASL still suffered from regions with low labeling efficiency and has lower tSNR compared to FAIR. The use of parallel transmit could potentially improve the VSASL labeling efficiency and would make it a valuable tool for fMRI purposes at high field.

## Background:

Despite the longer T1 and therefore less severe loss of label, arterial spin labeling (ASL) at ultra-high field (7T and above) has been found to be challenging mainly due to magnetic field inhomogeneities, B1-inhomogeneities, increase in physiological noise, shorter T2, and high specific absorption rate (SAR) (1). Over the last year, pCASL (2) and PASL using FAIR (3) have shown to provide robust perfusion maps at 7T. However, both these techniques can suffer from severe arterial-transit-time (ATT) artifacts. In this study, we show the feasibility of velocity selective (VS)ASL at 7T. VSASL creates label within the imaging volume by saturating the blood flowing above a certain cut-off velocity ( $V_{cut}$ ) and is therefore insensitive to ATT delays. We compared VSASL to the robust FAIR in terms of tSNR-efficiency.

## Methods:

A velocity selective saturation (VSS)ASL module was implemented and optimized on a Philips 7T Achieva (Best, Netherlands) equipped with a 32Rx 2Tx Nova head coil. To overcome B0 and B1-inhomogeneities, adiabatic excitation and refocusing is required for sufficient labeling efficiency. Therefore, the single refocused BIR4 labeling module was chosen (Figure 1). A BIR8-module would be more robust against eddy currents, however, this would double SAR and increases the effective echo time resulting in more severe loss of label due to T2.

Additional background suppression (BGS)-pulses are normally used to reduce physiological noise (4). However, since SAR is the limiting factor in ASL at 7T, the use of BGS-pulses will increase the TR considerably. In VSASL, suppressing CSF is most important to reduce diffusion-weighting. Therefore, the BIR4-segment is given a  $\pi/2$  phase offset to invert the static spins resulting in 'intrinsic' BGS without additional SAR (Figure 1) (5). Imaging was performed using a 3D EPI read-out with  $V_{cut}=2\text{cm/s}$  at a PLD of 1500ms after labeling to suppress the signal of CSF for  $\approx 90\%$ , GM 65% and WM 50%. VSASL (TR=4500ms) was compared to FAIR ASL (TR=7000ms).

## Results and Discussion:

We showed the feasibility of VSASL at 7T (Figure 2). Visual comparison of perfusion images (20 averages) for VSASL and FAIR is shown in Figure 2. Better GM/WM contrast can be observed for FAIR, possibly meaning VSASL is measuring WM perfusion better or suffers more from noise in the WM. More subjects are necessary to confirm this. FAIR shows 1.35x higher tSNR in the GM compared to VSASL (Figure 3). tSNR-efficiency, defined as  $tSNR/\sqrt{TR}$ , is only 1.07x higher for FAIR. VSASL still suffered from low inversion efficiency in some parts of the temporal lobes indicated with the red arrows (Figure 2) also reflected in regions with low tSNR.

## Next steps:

The current study was performed using dual transmission, whereas parallel transmit could potentially increase the B1-homogeneity and thereby improve the labeling efficiency. Validation of this technique is required in more participants (currently N=1) and under different conditions, e.g. visual stimulation, to prove perfusion weighting instead of CSF diffusion weighting. Once fully optimized, this VSASL at high field can be a very promising fMRI technique with high specificity to the arterial tree and capillary bed.

**Acknowledgments / Funding Information:** TTW-ZonMW-SGF-LHS Human Measurement models grant # 18969-Virtual Cerebrovascular Responses

## References:

1. Teeuwisse WM, Webb AG, van Osch MJ. Arterial spin labeling at ultra-high field: all that glitters is not gold. *International Journal of Imaging Systems and Technology*. 2010;20(1):62-70.
2. Zhao C, Shao X, Shou Q, Ma SJ, Gokyar S, Graf C, et al. Whole-Cerebrum distortion-free three-dimensional pseudo-Continuous Arterial Spin Labeling at 7T. *NeuroImage*. 2023:120251.
3. Kashyap S, Ivanov D, Havlicek M, Huber L, Poser BA, Uludağ K. Sub-millimetre resolution laminar fMRI using Arterial Spin Labelling in humans at 7 T. *PLOS ONE*. 2021;16(4):e0250504.
4. Qin Q, Alsop DC, Bolar DS, Hernandez-Garcia L, Meakin J, Liu D, et al. Velocity-selective arterial spin labeling perfusion MRI: A review of the state of the art and recommendations for clinical implementation. *Magnetic Resonance in Medicine*. 2022;88(4):1528-47.
5. Guo J. Robust dual-module velocity-selective arterial spin labeling (<sc>dm-VSASL</sc>) with velocity-selective saturation and inversion. *Magnetic Resonance in Medicine*. 2023;89(3):1026-40.

Figures

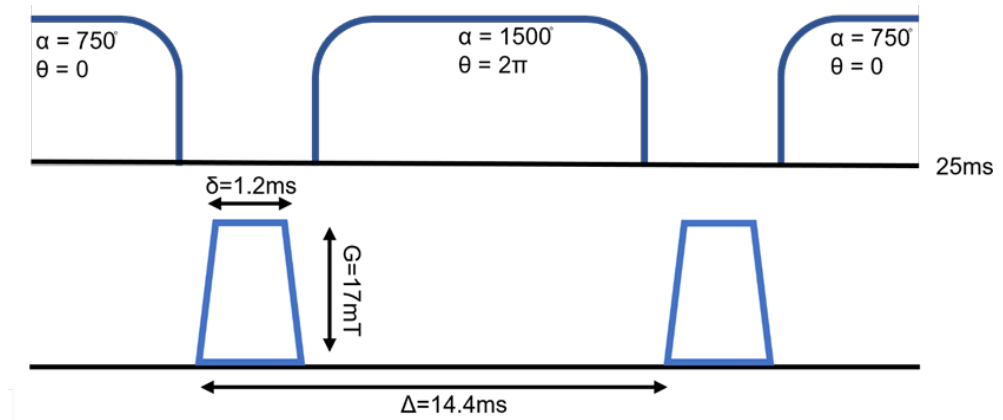


**Figure 1.** VSS labelling module used in this study with dur=25ms,  $G=17\text{mT/m}$ ,  $\delta=1.2\text{ms}$ ,  $V_{\text{cut}}=2\text{cm/s}$ . Last segment of the BIR4 containing  $\pi/2$  phase offset compared to normal BIR4 to invert static magnetization.

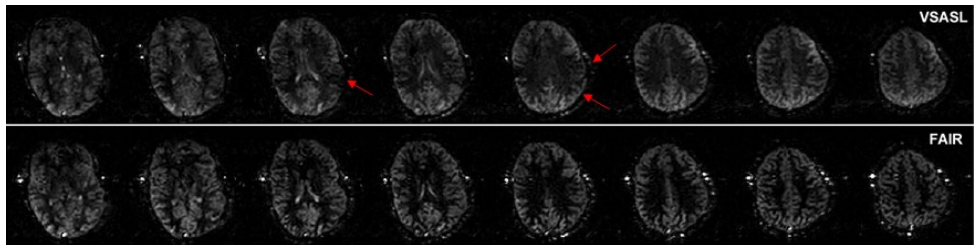


**Figure 2.** Comparison perfusion-weighted images for VSSinv ASL (top row) and FAIR (bottom row). Red arrows indicate regions with low labeling efficiency. Visible that FAIR ASL has more GM/WM contrast compared to VSASL. In general, good visual agreement between the two techniques. Imaging parameters: 3D EPI, res=3x3x3mm, 17 slices, SENSEap=2.5, 20 averages.

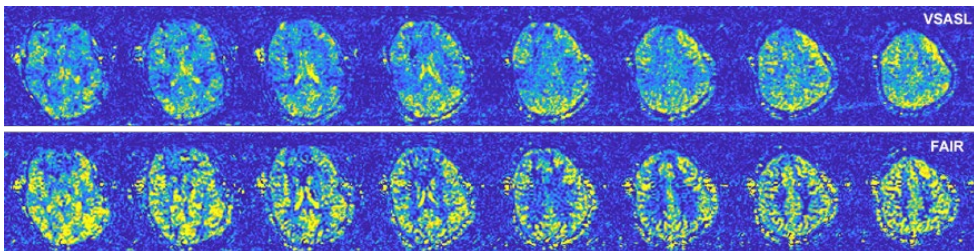
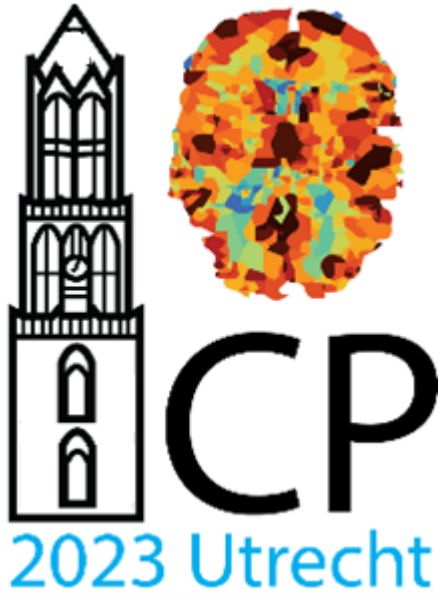


**Figure 3.** tSNR comparison VSSinv ASL (top row) and FAIR (bottom row). tSNR in GM 1.35x higher for FAIR than for VSASL. However, in terms of tSNR-efficiency defined as  $\text{tSNR}/\sqrt{\text{TR}}$ , they are comparable.



Posters

# Longitudinal Changes of BBB Permeability in Alzheimer's Disease Mice: A Non- Contrast MRI Study

Chuhan Xiong<sup>1</sup>, Yu Yin<sup>2</sup>, Qinfeng Zhu<sup>1</sup>, Ruicheng Ba<sup>1</sup>, Zhecheng Jin<sup>1</sup>, Zhiliang Wei<sup>3</sup>, Dan Wu<sup>1</sup>, Zixuan Lin<sup>1</sup>

<sup>1</sup>Key Laboratory for Biomedical Engineering of Ministry of Education, College of Biomedical Engineering and Instrument Science, Zhejiang University, Hangzhou, China;

<sup>2</sup>Department of Chemistry, Zhejiang University, Hangzhou, China;

<sup>3</sup>Department of Radiology, Johns Hopkins University, Baltimore, MD

## Synopsis and/or Summary of Main Findings:

Key words: Alzheimer's disease, Arterial spin labelling, Blood brain barrier

BBB disruptions has been demonstrated as a contributing factor in the pathophysiology of Alzheimer's disease (AD). This study investigated the longitudinal changes of BBB permeability in AD mice using a novel non-invasive MRI technique, WEPCAST MRI. Water extraction fraction (E) and permeability surface-area product (PS) in AD mice was significantly higher than in normal controls, implying BBB impairment in AD mice. Cerebral blood flow (CBF), brain volume, and PS decreased significantly with age in both AD and normal control mice, indicating a profound aging effect.

## Introduction

Blood-brain barrier (BBB) is a specialized structure in the brain, which plays an important role in regulating material transportation and waste clearance[1]. Numerous studies have demonstrated the significance of BBB disruptions as a contributing factor in the pathophysiology of Alzheimer's disease (AD)[2]. Several investigations have proposed arterial spin labeling (ASL) techniques exploiting water spins as an endogenous tracer to investigate BBB permeability, which have been postulated to be more sensitive to the subtle BBB damages in brain diseases due to the smaller molecular weight of water[3]. However, most of these methodologies have been primarily applied in human subjects, with limited research conducted on rodent models (mice and rats). Recently, a novel technique, based on water-extraction-with-phase-contrast-arterial-spin-tagging (WEPCAST) MRI that has been applied to humans, was proposed to assess BBB permeability in a mouse model[1,3]. This pioneering approach quantifies the fraction of labeled spins exchange into the cerebral tissue, yielding BBB permeability-surface-product (PS). In this study, we hypothesized that this method could serve as a novel biomarker for AD pathology and employed it to investigate the longitudinal change of BBB permeability in the 3xTg-AD mouse model.

## Methods Animals:

Female 3xTg-AD and normal control (NC) C57BL/6 mice were imaged at 5, 6, 7 and 8 months of age (NAD,5=5, NNC,5=5; NAD,6=5, NNC,6=5; NAD,7=4, NNC,7=5; NAD,8=5, NNC,8=5). All MRI data were acquired on a 7.0 T Bruker Biospec scanner, and mice were induced with 3% isoflurane and maintained at 1.5% during the experiments, while monitoring breathing rate and temperature. MRI acquisition: BBB permeability datasets were acquired using pseudo-continuous arterial spin labeling-echo planar imaging (pCASL-EPI), with labeling duration=2038.2 ms, post labeling delay (PLD)=25 ms, pulse width=0.4 ms, pulse interval=1 ms and flip angle (FA)=40°. The imaging slice was positioned to cover the midline of the mouse brain in the sagittal orientation. CBF data were obtained using phase contrast (PC) MRI, with encoding velocity (VENC) of ICA and VA=20/10 cm/s, respectively, FA=25°. The imaging locations are shown in Figure 1b.

## MRI data analysis:

For pCASL data, the difference image ( $\Delta M$ ) was obtained by pairwise subtraction between the control image and the labeled image. A ROI was manually delineated on  $\Delta M/M_0$  images including vein of Galen (VG) to obtain  $\Delta M_{vein}/M_0$ [1] (Figure 1a). According to Eq.1, E can be calculated[1]:

$$\Delta M_{vein} = 2\alpha(1 - E)M_{0,blood}e^{-\frac{BAT_{vein}}{T_{1b}}}$$

For PC MRI data, manually sketch arteries of interest (left/right internal carotid artery (LICA/RICA) and left/right vertebral artery (LVA/RVA)) and the total blood flow was calculated by the integration of the arterial voxels through the four arteries on the velocity map (acquired by Eq.2[4]) (Figure 1b), which was divided by the brain weight to obtain CBF[4]:

$$M_{CD} = 2M_0 \left| \sin \left( \frac{\pi v}{2VENC} \right) \right|$$

Then according to Renkin-Crone Model, PS can be determined by Eq.3[5]:

$$PS = -\ln(1 - E) \times CBF$$

Linear mixed-effect model (LMM) was used to examine the time-dependence of physiological parameters. Student's t-test was employed to examine the statistical difference between AD and NC mice. In all analyses, a p-value less than 0.05 was considered statistically significant.

## Results

Figure 2 presents the age-dependent curves of different parameters of the two groups of mice, namely CBF, brain volume, E, and PS. The mean values of CBF and brain volume of AD mice were smaller than those of the control group, while the mean values of E and PS were larger, however, only E and PS (at 6 and 8 months of age) showed significant differences.

LMM (Table 1) showed that CBF, brain volume, and PS all decreased significantly with age in both groups of mice, while the slight increase in E was not significant.

## Discussion

In our study, we have investigated BBB permeability in a mouse model of AD. The results showed that E was significantly greater in AD mice than in normal controls at all ages, which seems to suggest BBB impairment in AD mice. However, the significance of PS only appeared at 6 and 8 months, which may be related to occasionality due to the limited amount of data. The CBF, brain volume, and PS of both AD and normal control mice all decreased significantly with age, indicating that aging has a profound impact on these physiological parameters.

## Conclusion

Current study measured longitudinal changes of BBB permeability in AD mice, which started as early as 5 months of age, indicating an important role of BBB in the early detection of AD.

## Reference

- [1] Wei Z, Liu H, Lin Z, et al. Non-contrast assessment of blood-brain barrier permeability to water in mice: An arterial spin labeling study at cerebral veins[J]. *NeuroImage*, 2023, 268: 119870.
- [2] Lin Z, Sur S, Liu P, et al. Blood-Brain Barrier Breakdown in Relationship to Alzheimer and Vascular Disease[J]. *Annals of Neurology*, 2021, 90(2): 227-238.
- [3] Lin Z, Li Y, Su P, et al. Non-contrast MR imaging of blood-brain barrier permeability to water[J]. *Magnetic Resonance in Medicine*, 2018, 80(4): 1507-1520.
- [4] Wei Z, Chen L, Lin Z, et al. Optimization of phase-contrast MRI for the estimation of global cerebral blood flow of mice at 11.7T[J]. *Magnetic Resonance in Medicine*, 2019, 81(4): 2566-2575.
- [5] Renkin E M. Transport of potassium-42 from blood to tissue in isolated mammalian skeletal muscles[J]. *The American Journal of Physiology*, 1959, 197: 1205-1210.

## Tables and figures

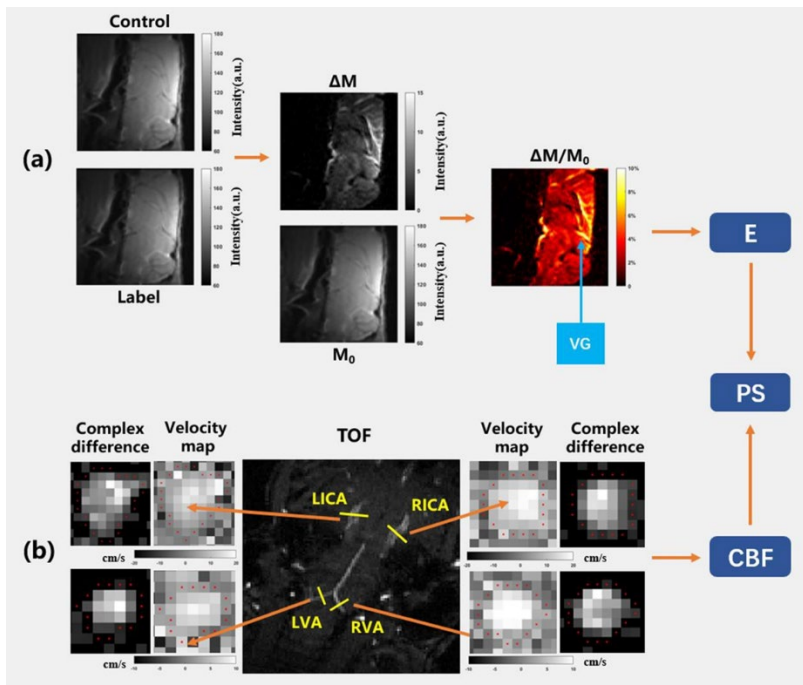


**Figure 1:** A sample dataset used in BBB permeability measurement. (a) shows the control, labeled, difference,  $M_0$ , and  $\Delta M/M_0$  images at the mid-sagittal plane. (b) shows the complex difference images and velocity maps of the four blood supply arteries (LICA, RICA, LVA, and RVA) by reference to a TOF image.

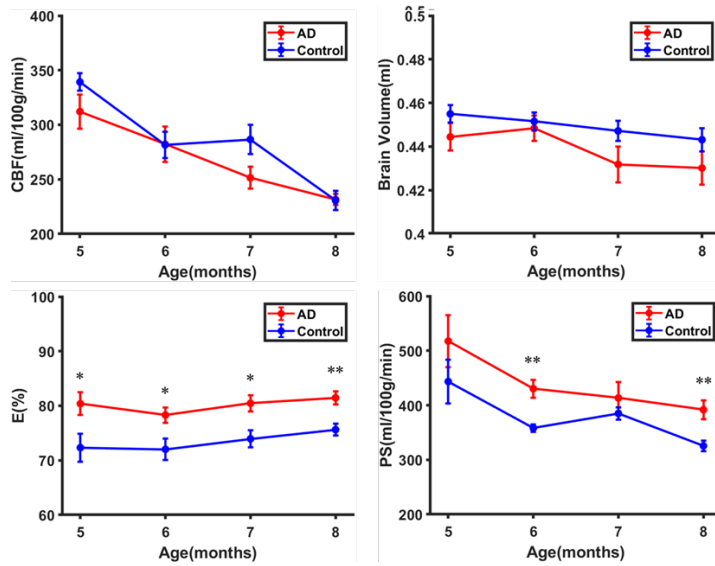


**Figure 2:** Cerebral blood flow, brain volume and BBB permeability of AD and control mice as a function of age. Error bar stands for standard error across mice. Significant differences between groups are marked with \* for  $p < 0.05$  and \*\* for  $p < 0.01$ .

LMM	AD			Control		
	Coefficient	SE	p-value	Coefficient	SE	p-value
CBF (ml/100g/min)	-27.34	5.44	<0.001	-32.05	5.14	<0.001
Brain volume(ml)	-0.0051	0.0016	0.005	-0.0040	0.0010	0.0012
E(%)	0.51	0.46	0.29	1.18	0.76	0.14
PS (ml/100g/min)	-41.64	12.49	0.0042	-32.68	9.79	0.0037

Table 1 Results of the relationship between mice age and various physiological parameters (CBF, brain volume, E and PS) by using linear mixed-effects models. Left and right representing the AD model mice and control mice, respectively.

<sup>1</sup>LMM, linear mixed effects model; SE, standard error; CBF, cerebral blood flow; E, water extraction fraction; PS, permeability surface-area product.

# Acute changes of cerebral hemodynamics, metabolism and blood-brain barrier permeability in response to aerobic exercise

Yizhe Hu<sup>1</sup>, Zixuan Lin<sup>1</sup>

<sup>1</sup>College of Biomedical Engineering & Instrument Science, Zhejiang university, Hangzhou, China

## Synopsis:

Keywords : Aerobic exercise; blood-brain barrier; cerebral blood flow; cerebral oxygen metabolism; magnetic resonance; T2-Relaxation-Under-Spin-Tagging Magnetic Resonance Imaging (TRUST MRI); Water-Extraction-with-Phase-Contrast- Arterial-Spin-Tagging Magnetic Resonance Imaging (WEPCAST MRI); Acute changes

Aerobic exercise was shown to be an effective tool in the prevention or treatment of neurodegenerative diseases through its regulation of cerebral physiology. However, how does single bout of exercise affect brain oxygen metabolism and blood-brain barrier (BBB) permeability in addition to perfusion remains unclear. This study aims to dynamically monitor the acute changes in multiple indices, including cerebral blood flow (CBF) as gauged by Phase-Contrast (PC) MRI, venous oxygenation (Yv) and cerebral metabolic rate of oxygen (CMRO2) as assessed by TRUST MRI, BBB water extraction (E) and permeability-surface- area-product (PS) as determined via WEPCAST MRI, subsequent to a singular aerobic exercise training session. We found a significant increase in participants' CBF and CMRO2 post-exercise, as well as an elevated PS, suggesting that a singular bout of moderate-intensity aerobic exercise can induce acute alterations in cerebral metabolism, and BBB permeability.

## Introduction:

Previous studies have demonstrated the longitudinal benefit of aerobic exercise on cerebrovascular health[1], thereby playing a pivotal role in thwarting the onset of a multitude of neurological disorders, including Alzheimer's disease. Nevertheless, the literature remains deficient in comprehensive understanding of the alterations engendered by short-term aerobic exercise interventions. Existing studies, employing alternative techniques, primarily focused on CBF, neglecting other cerebral physiological factors such as oxygen metabolism and BBB permeability due to a limit of methodologies. Recent advances in MRI techniques allows a completely non-contrast assessment of these physiological parameters within ten minutes. Thus, in this study, we investigated the dynamic alterations in a multitude of physiological parameters in healthy individuals, following a single regimen of moderate-intensity aerobic exercise.

## Methods:

The study engaged 23 healthy participants (10 females, 13 males), within an age range of 18-35 years. The experiment was conducted in a sequence of steps as shown in Figure 1.A. MRI acquisitions and data processing: [2]PC MRI was performed at four major feeding arteries (left/right internal carotid arteries and left/right vertebral arteries) to quantify global CBF. The following parameters were used: encoding velocity (Venc)=40 cm/s. Total flux of these four arteries was normalized by individual brain volume obtained from a 3D T1-weighted MPRAGE scan with the following parameters: shot interval=2100ms, inversion time (TI)=1100ms. Additionally, venous oxygenation (Yv) was measured by TRUST MRI [3] :four effective TEs (eTE=0, 40, 80, and 160ms) with a  $\tau\tau$ CPMG of 10 ms. CMRO2 was then calculated as follows[4].

$$CMRO2 = CBF * (Ya - Yv) * Ch$$

To assess BBB permeability, WEPCAST MRI[5] was conducted in mid-sagittal plane with a labeling duration of 4000 ms and a post-labeling delay of 3000 ms. E and PS was then quantified from the labeled spin signals at superior sagittal sinus.

## Statistical analysis:

The time dependence of the physiological parameters was studied with a mixed-effect model, in which the age, gender, and exercise duration of the subjects were fixed effects, while individual differences among the subjects were random effects.

## Results and Discussion:

Figure 2 delineates the experimental outcomes, while Table 3 elucidates the analytical findings derived from the linear mixed- effects model. As depicted in Figure 2, there was first drop followed by a significant augmentation in the participants' CBF ( $p=0.016$ ), while Yv showed a significant decrease ( $p=0.002$ ), i.e. an increased oxygen extraction, and returned to baseline level at later time points. CMRO2 gradually increased ( $p=0.012$ ), which could be attributable to an escalation in metabolic activity within the body and a higher demand for oxygen. The intergroup difference is only significant inCMRO2, indicating a complex interaction between oxygen metabolism and exercise duration. In addition, our data showed that E remains relatively stable post-exercise ( $p=0.36$ ), while PS significantly increased ( $p=0.009$ ). It could be due to the elevation of blood pressure after exercise, leading to a stretching of endothelial and vascular smooth muscles.

## Conclusion:

The findings of our investigation suggest that a singular bout of moderate-intensity aerobic exercise can induce acute alterations in cerebral hemodynamics, metabolic processes, and blood-brain barrier permeability.

**Acknowledgments / Funding Information:** This work is supported by College of Biomedical Engineering & Instrument Science, Zhejiang university.

**References:**

[1] B. P. Thomas et al., "Brain Perfusion Change in Patients with Mild Cognitive Impairment After 12 Months of Aerobic Exercise Training," *J Alzheimers Dis*, vol. 75, no. 2, pp. 617-631, 2020, doi: 10.3233/JAD-190977.  
 [2] S. L. Peng et al., "Age-related increase of resting metabolic rate in the human brain," *Neuroimage*, vol. 98, pp. 176-83, Sep 2014, doi: 10.1016/j.neuroimage.2014.04.078.  
 [3] H. Lu and Y. Ge, "Quantitative evaluation of oxygenation in venous vessels using T2-Relaxation-Under-Spin-Tagging MRI," *Magnetic Resonance in Medicine*, vol. 60, no. 2, pp. 357-363, 2008, doi: <https://doi.org/10.1002/mrm.21627>.  
 [4] F. Mielck, H. Stephan, W. Buhre, A. Weyland, and H. Sonntag, "Effects of 1 MAC desflurane on cerebral metabolism, blood flow and carbon dioxide reactivity in humans," *Br J Anaesth*, vol. 81, no. 2, pp. 155-60, Aug 1998, doi: 10.1093/bja/81.2.155.  
 [5] Z. Lin et al., "Non-contrast MR imaging of blood-brain barrier permeability to water," *Magnetic Resonance in Medicine*, vol. 80, no. 4, pp. 1507-1520, 2018, doi: <https://doi.org/10.1002/mrm.27141>.

**Tables and figures**

	Coefficient	SE	F-Values	p-Values (Time Effect)	p-Values (Group difference)
CBF	4.18	1.98	3.21	0.016	0.146
Y <sub>v</sub>	-0.15	0.64	4.51	0.002	0.947
CMRO <sub>2</sub>	0.08	0.72	3.42	0.012	0.009
E	4.27	2.72	0.36	0.996	0.893
PS	4.12	1.89	3.61	0.009	0.459

**Table 1.** Summary of linear mixed effect model results for CBF, Y<sub>v</sub>, CMRO<sub>2</sub>, E and PS

(A)



(B)

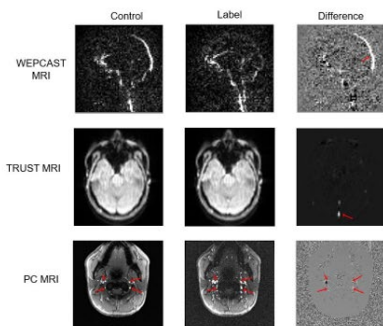


**Figure 1.** (A) Experimental procedures. The participants were stratified into two cohorts. The first cohort underwent a regimen of aerobic exercise training for a duration of 10 minutes, while the other was subjected to a training session lasting 20 minutes. (B) Representative MRI image results. The blood vessel pointed to by the red arrow is the region of interest.

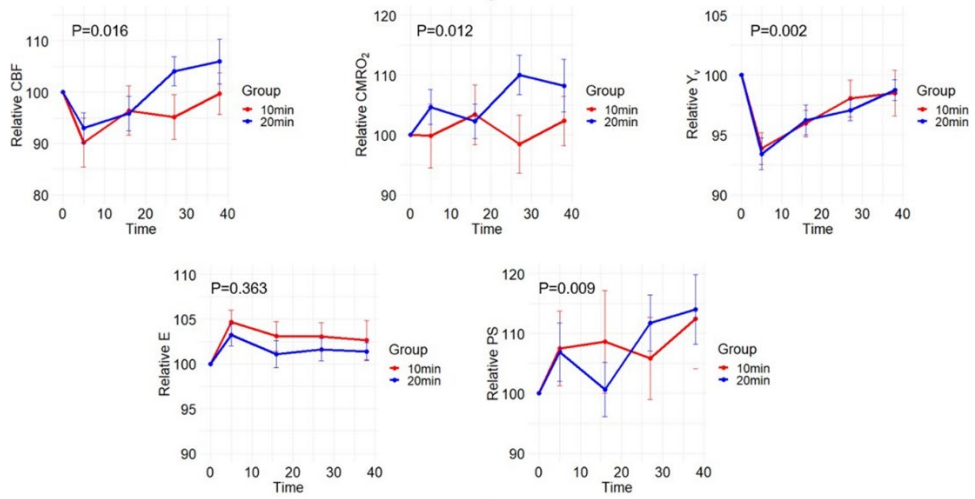


**Figure 2.** Time course of cerebral blood flow (CBF), venous oxygenation ( $Y_v$ ), cerebral metabolic rate of oxygen (CMRO<sub>2</sub>), water extraction fraction (E), and BBB permeability-surface-area product (PS) after single bout of aerobic exercise (10min or 20min). t=0 indicates baseline measurement. Other time points are labeled with the measurement start time (t = 5, 16, 27, and 38min) after exercise. Error bars denote standard error across participants.

# Accuracy of automatic detection of the cerebral arteries inside the Circle of Willis and its application

J. Huck<sup>1,2</sup>, D. Vanderweyen<sup>1,3</sup>, Félix Dumais<sup>2</sup>, T. Rundek<sup>4</sup>, M.S.V. Elkind<sup>5,6</sup>, J. Gutierrez<sup>5</sup>, M. Descoteaux<sup>2</sup>, K. Whittingstall<sup>3</sup>

<sup>1</sup>Department of Nuclear Medicine and Radiobiology, Université de Sherbrooke, Sherbrooke, CA;

<sup>2</sup>Department of Computer Science, Université de Sherbrooke, Sherbrooke, CA;

<sup>3</sup>Department of diagnostic radiology, Université de Sherbrooke, Sherbrooke, CA ;

<sup>4</sup>Evelyn F. McKnight Brain Institute and Department of Neurology, Miller School of Medicine, University of Miami, Miami, USA;

<sup>5</sup>Department of Neurology, Columbia University, New York, USA;

<sup>6</sup>Department of Epidemiology, Columbia University, New York, USA

## Synopsis and/or Summary of Main Findings

This study assesses the Circle of Willis (CW), a vital brain blood supply network, using the express IntraCranial Arteries Breakdown (eICAB), an open-source software for automated CW assessment.

Using the Northern Manhattan Study dataset, manual CW artery diameter measurements were compared to eICAB's estimates. eICAB's sensitivity in detecting major arteries was 100% for the basilar artery (BA), but lower for other CW arteries with accuracy of 72% for Anterior Cerebral Arteries (ACA). The study also explored how different resampling resolutions affected eICAB's diameter estimations, displaying higher accuracy with higher voxel resolution. It's crucial to consider that manual measurements were taken at a single point within the arteries, while eICAB averaged across the entire artery, with results falling within  $\pm 0.62\text{mm}$  of error.

Furthermore, the study investigated correlations between CW artery diameters and hippocampus volumes but found no significant associations after accounting for intracranial volume.

## Abstract Body

The brain's continuous demand for essential nutrients is met by arterial blood delivered through four major extracranial arteries, interconnected by an anastomotic ring known as the Circle of Willis (CW)<sup>1</sup>, which can be imaged by Magnetic Resonance Angiography (MRA). The CW is known for its morphological variants, which can impact brain physiology.

To alleviate time-consuming manual CW assessment, we compare diameter estimations from express IntraCranial Arteries Breakdown (eICAB)<sup>2</sup>, an in-house open-source software which can recognize and describe the CW variations, against manual measurements. Additionally, we explore the connection between diameters of some major arteries in the CW, Anterior Cerebral Arteries (ACA), Middle Cerebral Arteries (MCA), Posterior Cerebral Arteries (PCA) P1 segment, Posterior Communicating Arteries (PCOM), and Basilar (BA) with hippocampus volumes.

## Methods:

The Northern Manhattan Study (NOMAS) dataset of 1209 participants with available 1.5T MRA images was used for manual CW artery diameter measurements<sup>3,4</sup>. The principal CW arteries were segmented using eICAB on  $0.3 \times 0.3 \times 0.7\text{mm}$  time-of-flight MRA images<sup>2</sup>. Correct classification over all predictions was gauged using a neurologist's identification on a subset of 16 randomly selected participants. Diameter estimations followed post-resampling with nearest neighbor interpolation at diverse resolutions (0.625, 0.5, 0.4, and 0.3125). A comparison, using an independent t-test with Bonferroni correction was made with the manual measurements. Hippocampal volumes were extracted using FastSurfer<sup>5</sup> on T1w images. After the data was log-transformed to meet the normality assumption, the hippocampal volume was correlated to artery diameters using partial correlation coefficients factoring intracranial volume followed by a Bonferroni correction.

## Results:

Table 1 shows eICAB's accuracy to identify arteries accurately. There was a high accuracy of 100% for the BA, and the lowest accuracy was 72% for the ACAs. Figure 1 illustrates a comparison between manually measured diameters and eICAB's diameter estimations under different resampling parameters, highlighting a closer alignment with manual measurements when using a resampling resolution of 0.3125mm. In Figure 2 the partial correlation coefficient results are depicted. ACA, MCA, PCA P1, PCOM, and BA have no significant partial correlation between hippocampal volume and diameter after controlling for intracranial volume.

## Discussion and Conclusion:

Our findings highlight the accuracy of eICAB for CW artery segmentation. The lower ACA accuracy stemmed from hypoplastic A1 segments that were not manually measured but detected by eICAB. Optimal resampling (Figure 1) enhances precision of diameter measurements by eICAB. While the artery diameters are significantly higher in MCA and PCA P1 in eICAB compared to the manual measures, it is important to note that the manual measurements were taken at only one location in the arteries and the results from eICAB were averaged across the entire artery. The overall results are within  $\pm 0.62\text{mm}$  of error to manual measurements. Although ACA, MCA, and PCA P1 exhibited positive correlations between diameter and hippocampus volume, these correlations were not statistically significant after adjusting for intracranial volume. These preliminary results do not account for additional factors such as age and sex. The role of CW morphology and its precise measurements may be important in hippocampal injury and needs further exploration.

**Acknowledgments / Funding Information:** The authors would like to acknowledge the funding agencies which have supported this research: NINDS R37 NS029993 (Elkind), Fonds de recherche du Québec - Nature et technologies (FRQNT) (Huck), the Natural Science and Engineering Research Council (NSERC) (Whittingstall).

**References:**

1. Trepel, M. Neuroanatomie: Struktur und Funktion; mit 27 Tabellen. (Elsevier, Urban & Fischer, 2007).
2. Dumais, F. et al. eICAB: A novel deep learning pipeline for Circle of Willis multiclass segmentation and analysis. NeuroImage 260, 119425 (2022).
3. Gutierrez, J. et al. Dolichoectasia Diagnostic Methods in a Multi-Ethnic, Stroke-Free Cohort: Results from the Northern Manhattan Study: A Population-Based Study of Intracranial Dolichoectasia. J Neuroimaging 24, 226–231 (2014).
4. Gutierrez, J. et al. Determinants of cerebrovascular remodeling: Do large brain arteries accommodate stenosis? Atherosclerosis 235, 371–379 (2014).
5. Henschel, L. et al. FastSurfer - A fast and accurate deep learning based neuroimaging pipeline. NeuroImage 219, 117012 (2020).

**Tables and figures**

	Accuracy
ACA	72%
MCA	97%
PCA P1	88%
PCOM	84%
BAS	100%

**Table 1:** Accuracy of artery detection between arteries measured on 16 randomly selected participants by a vascular neurologist and arteries detected by eICAB. BA had a remarkably high accuracy of 100%, followed by MCA (97%), PCA P1 (88%), PCOM (84%), and ACA (72%).

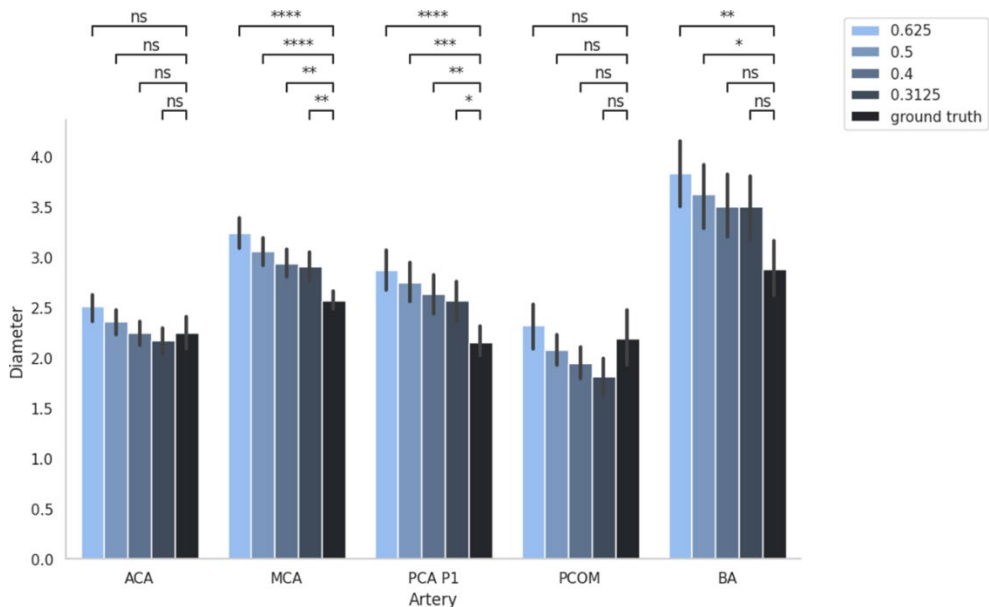


**Figure 1:** Results of the estimated diameters from eICAB on 16 participants with a resampling resolution of 0.625, 0.5, 0.4 and 0.3125 mm of the anterior cerebral artery (ACA), middle cerebral artery (MCA), the P1 segment of the posterior cerebral artery (PCA), Posterior Communicating Arteries (PCOM) and Basilar (BA) in comparison to the manually measured ground truth. Resampling to smaller resolutions tends to improve diameter estimation accuracy.

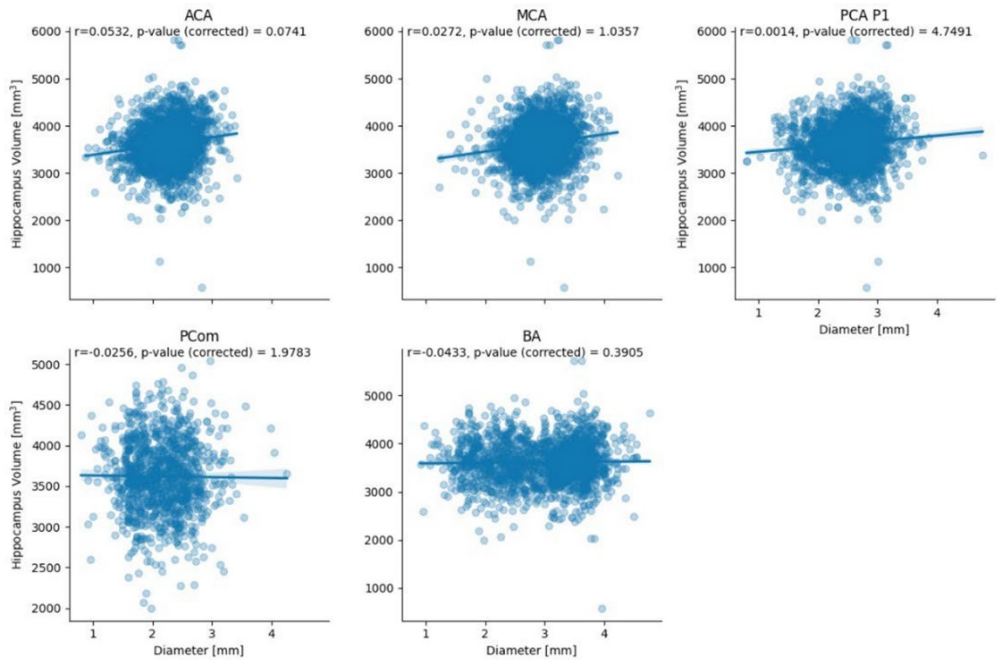


**Figure 2:** Relationship between diameters of ACA, MCA, PCA P1, PCOM, and BA and the hippocampus volume on 1209 participants. A partial correlation was done controlling for intracranial volume.

# Accuracy, repeatability, and sensitivity of breath-hold calibrated fMRI for the mapping of absolute CMRO<sub>2</sub>

I. Driver<sup>1</sup>, A.M. Chiarelli<sup>2</sup>, R.G. Wise<sup>2</sup>, M. Germuska<sup>1</sup>

<sup>1</sup>Cardiff University Brain Research Imaging Centre (CUBRIC), School of Physics and Astronomy, Cardiff University, Cardiff, United Kingdom.

<sup>2</sup>Institute for Advanced Biomedical Technologies, Department of Neurosciences, Imaging, and Clinical Sciences, University G. D'Annunzio of Chieti-Pescara, Chieti, Italy

## Synopsis:

We acquired breath-hold calibrated fMRI (bhc-fMRI) and T2-Relaxation-Under-Spin-Tagging (TRUST) datasets in 35 healthy volunteers at rest and during visual stimulation. The bhc-fMRI data were analysed integrating the standard Davis Model of the BOLD signal with an oxygen diffusion constrained model to map cerebral blood flow (CBF), oxygen extraction fraction (OEF), and cerebral metabolic rate of oxygen consumption (CMRO<sub>2</sub>). We found moderate agreement between grey matter OEF and global OEF measured with TRUST ( $r=0.55$ ,  $p<0.05$ ). The within session repeatability of OEF estimates was moderate to high ( $r=0.76$ ,  $p<0.05$ ). An ROI analysis in the visual cortex found a CBF increase of 15% during continuous visual stimulation, CMRO<sub>2</sub> increased by 11%, and OEF decreased by 3%. The bhc-fMRI measurement of CMRO<sub>2</sub> is simple to implement, has good repeatability, is sensitive to local changes in metabolism, and has comparable accuracy to existing gas-based methods.

## Background:

Dual-calibrated fMRI measurement of cerebral metabolism [1] is a sensitive method of mapping multi-parametric physiological parameters in the brain such as cerebral oxygen consumption. However, the method requires specialized equipment, long acquisition times, experienced operators, and can be uncomfortable for participants. We recently introduced a single-gas (CO<sub>2</sub>) alternative [2] that constrains the Davis Model of the BOLD signal with a diffusion model of oxygen transport from capillaries to mitochondria to infer OEF and cerebral blood volume. Here, we replace the CO<sub>2</sub> stimulus with a repeated breath-holding paradigm, increasing subject comfort and removing the need for ancillary equipment. The performance of the method was assessed in healthy volunteers at rest and during a visual task.

## Methods:

We studied 35 healthy volunteers (24±5.6yrs, 16 female). MRI data were collected on a Siemens Prisma 3T MRI scanner with a 32-channel receive-only head coil. An MPRAGE T1-weighted scan was used for registration and brain segmentation purposes (matrix 165x203x197, 1 mm isotropic resolution, TR/TE = 2100/3.24ms). A dual-excitation (DEXI) pCASL sequence with background suppression was used to collect simultaneous BOLD and ASL data (TR = 4400ms; TE<sub>1</sub>/TE<sub>2</sub> = 10ms/30ms; slices=15; Slice thickness=6mm; PLD = 1500ms; tag duration=1500ms). The breath-holding protocol had 10 repeats of 20 seconds of breath-holding at end expiration. This was repeated at rest and during visual stimulation (reversing radial checkerboard at a frequency of 8Hz). A T2-Relaxation-Under-Spin-Tagging (TRUST) MRI sequence was acquired to estimate global OEF. We further collected a T1 inversion recovery sequence to calculate Hb ( $\Delta TR / TE = 150ms / 22ms$ , flip angle = 90 degrees). OEF estimates were made from the DEXI-pCASL data using an exhaustive search as in [2]. However, the end-tidal regressor was replaced with the average grey matter response to breath-holding. The arterial oxygen content at rest was 127±8 mmHg, and 104±14 mmHg at the end of 20 seconds of breath-holding. These average values were used in the analysis of individual subjects.

## Results and Discussion:

Figure 1 shows a scatterplot and Bland-Altman analysis of the mean grey matter OEF and the global TRUST estimate for each subject. The Pearson's correlation coefficient between TRUST and bhc-fMRI is 0.55 ( $p<0.05$ ) and is similar to that found for dual-calibrated fMRI (0.58) [2]. Within session repeatability had a correlation coefficient of 0.76 ( $p<0.05$ ). Figure 2 shows the regions of significant average CBF and CMRO<sub>2</sub> change between the rest and visual stimulation. Within the ROI defined by significant CBF increase there is a 15±2% CBF increase, a 11±2% CMRO<sub>2</sub> increase, and a 3±1% OEF decrease. Figure 3 shows a boxplot for parameters values in the visual ROI. The average neurovascular coupling constant (1.44) is in good agreement with the 1.4 coupling ratio found with dual-calibrated fMRI [3] and the 3.6% OEF decrease observed with a 5-minute R<sub>2'</sub> measurement [4]. This in-vivo study demonstrates that breath-hold calibrated fMRI has similar accuracy to dual-calibrated fMRI for quantification of cerebral oxygen metabolism and is sensitive to neurovascular uncoupling in healthy volunteers. Further studies will investigate the applicability of the method in disease.

**Acknowledgments / Funding Information:** We acknowledge the members of the Welsh Advance Neuroimaging Database for acquiring this dataset and the support from the Wellcome Trust (WT104943/Z/14/Z and 220575/Z/20/Z), and the EPSRC (EP/S025901/1)

## References

- [1] Bulte et al. Quantitative measurement of cerebral physiology using respiratory-calibrated MRI'. *Neuroimage*. 2012. 60(1):582-91
- [2] Chiarelli and Germuska, et al. 'A flow-diffusion model of oxygen transport for quantitative mapping of cerebral metabolic rate of oxygen (CMRO<sub>2</sub>) with single gas calibrated fMRI'. *JCBFM*. 2022. 42(7): 1192–1209.
- [3] Germuska et al. 'Dual-calibrated fMRI measurement of absolute cerebral metabolic rate of oxygen consumption and effective oxygen diffusivity'. *Neuroimage*. 2019. 184: 717–728.
- [4] Arzanforoosh et al. 2023 'Streamlined quantitative BOLD for detecting visual stimulus-induced changes in oxygen

Figures

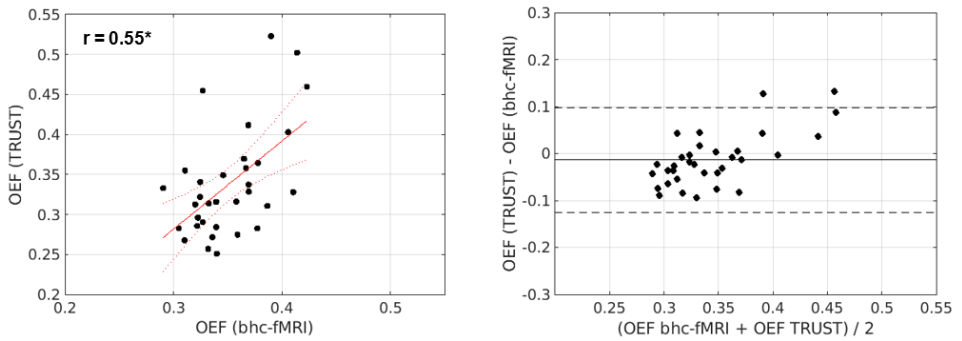


Figure 1. Scatterplot and Bland-Altman plot comparing grey matter OEF estimates from breath-hold calibrated fMRI and global OEF estimated from TRUST. \* $p < 0.05$ .

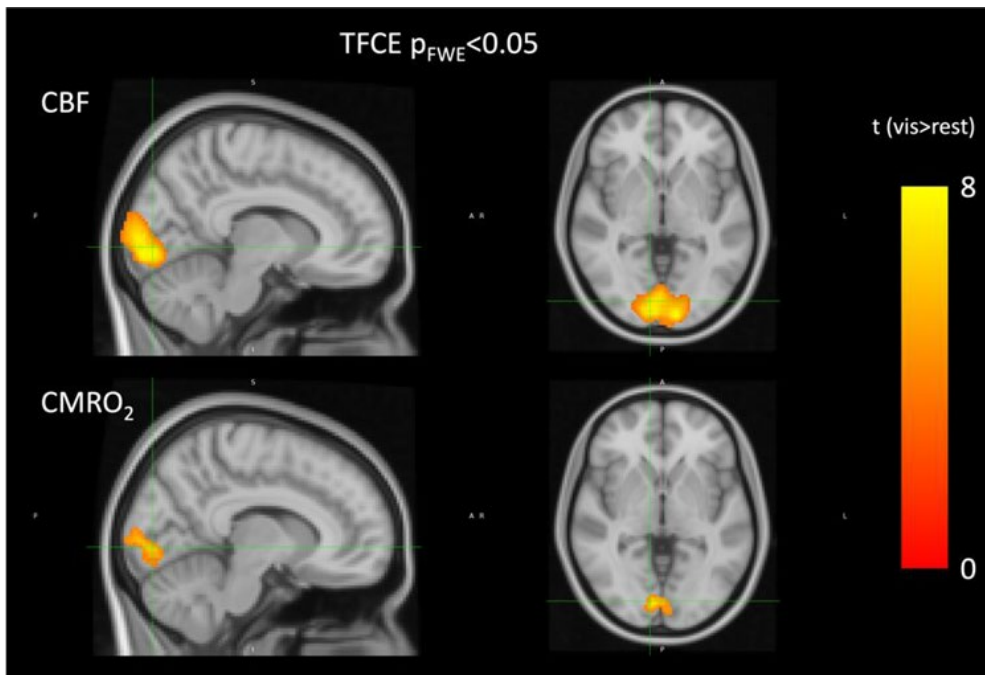
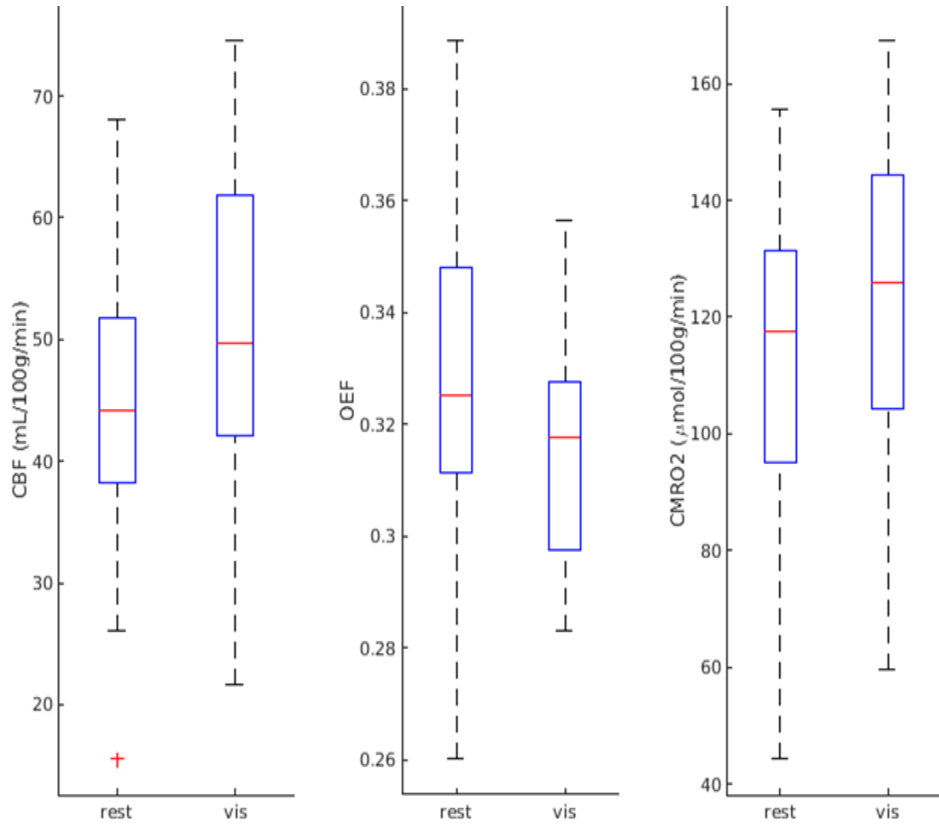


Figure 2. Group maps of CBF and CMRO<sub>2</sub> where the visual condition > resting condition ( $p_{FWE} < 0.05$ ).



**Figure 3:** Box plots of visual ROI-averaged CBF, OEF and CMRO2 for rest and visual task conditions. N.B. The two conditions are significantly different for all three parameters (Bonferroni-corrected  $p < 0.05$ ).

# Cerebrovascular changes associated with testosterone level in Polycystic Ovary Syndrome (PCOS).

M.E. Wright<sup>1,2</sup>, C.T. Richards<sup>3</sup>, S. Davies<sup>1,2</sup>, R.N. Lord<sup>3</sup>, A. Rees<sup>3,4</sup>, K. Murphy<sup>1,2</sup>

<sup>1</sup>Cardiff University Brain Research Imaging Centre (CUBRIC), Cardiff University, UK;

<sup>2</sup>School of Physics and Astronomy, Cardiff University, UK

<sup>3</sup>School of Sport and Health Sciences, Cardiff Metropolitan University, UK;

<sup>4</sup>Neuroscience and Mental Health Research Institute, Cardiff University, UK

## Synopsis and/or Summary of Main Findings

It has been suggested that Polycystic Ovary Syndrome (PCOS) patients have an increased risk of vascular abnormalities, potentially due to hyperandrogenism characteristic of the condition. However, the influence of PCOS and elevated testosterone levels on the cerebrovascular system has been under researched. Here we present preliminary data investigating the relationship between PCOS and testosterone level and various aspects of cerebrovascular functioning. 12 PCOS patients and 9 BMI-matched healthy controls completed a 3T MRI session. Variation in cerebral blood flow and arterial arrival time were found to be influenced by testosterone level when PCOS status was controlled for, but not vice versa. From the subsample that also completed an Oxygen Extraction Fraction measurement, linear models did not show statistical significance ( $p=0.15$ ). This provides information into how testosterone may influence the cerebrovascular system and highlights possible mechanisms by which vascular alterations occur in PCOS patients.

## Introduction

Patients with Polycystic Ovary Syndrome (PCOS), a condition associated with hyperandrogenism, demonstrate an increased risk of cardiovascular abnormalities. The exact mechanism is unknown, but may involve a direct action of testosterone on the vascular system (1). The impact of testosterone on the cerebrovascular system in PCOS has not been previously investigated.

The current study investigates multiple aspects of cerebrovascular functioning in PCOS patients compared to healthy controls and specifically investigates associations with testosterone. Presented here are preliminary results.

## Methods

12 PCOS patients (age mean[SD]=32.20[8.21]; testosterone mean[SD]=1.48[0.42]nmol/l) and 9 BMI-and-age-matched healthy controls (age mean[SD]=30.16[4.25]; testosterone mean[SD]=1.16[0.35]) completed an MRI session (Siemens MAGNETOM Prisma 3T scanner, 32-channel head-coil). A multi-post labelling delay pseudocontinuous arterial spin labelling (MPLD-pCASL) perfusion scan was completed (maximum TR=5.6s; TE=11s; voxel resolution=3.4x3.4x6.0mm, tag duration=1800, post-labelling delays=250-3000ms in steps of 250ms, GRAPPA=2). Cerebral Blood Flow (CBF) and Arterial Arrival Time (AAT) were mapped using BASIL software (2). Median values were extracted from Desikan-Killiany structural atlas regions (3). A subsample (6 PCOS, 5 controls) completed a T2-relaxation-under-spin-tagging (TRUST) sequence (TR=3s; TE=3.9ms) to estimate Oxygen Extraction Fraction (OEF). Linear models investigated the amount of CBF/AAT/OEF variance that could be explained by testosterone and group (i.e., PCOS vs controls). Additionally, CBF/AAT models included interaction terms with ROIs. In all models, a visual inspection of residual plots ensured no notable deviations from homoskedasticity or normality.

## Results

Global OEF results are illustrated in Figure 1. Qualitatively, there is lower OEF in PCOS patients compared to controls (PCOS mean=0.32; control mean=0.39). A linear model of OEF as a function of group and testosterone was statistically non-significant ( $F(2,7)=2.58$ ;  $p=0.15$ ).

The CBF data are illustrated in Figure 2, collapsed across ROI. A mixed linear model suggested that the ROI/group interaction contributed a non-significant amount of CBF variance ( $\chi^2(82)=43.99$ ;  $p=0.93$ ) but the ROI/testosterone interaction was significant ( $\chi^2(82)=121.50$ ;  $p=0.003$ ). Post-hoc tukey-corrected pairwise tests suggest that ROIs in the left hemisphere, particularly those in the anterior cortex (e.g. precuneus, fusiform gyrus, temporal pole, middle temporal cortex) and subcortex (e.g. hippocampus, putamen, thalamus) show CBF increases with increasing testosterone. Finally, the AAT results are illustrated in Figure 3, collapsed across ROI. A mixed linear model found the ROI/group interaction has a non-significant influence ( $\chi^2(82)=101.80$ ;  $p=0.068$ ). However, the ROI/testosterone interaction did significantly contribute to AAT ( $\chi^2(82)=130.46$ ;  $p=0.0005$ ). Post-hoc tukey-corrected pairwise tests suggest that ROIs in the right subcortex (e.g. amygdala, accumben's area) demonstrate decreasing AAT with increasing testosterone.

## Discussion

These preliminary results illustrate the cerebrovascular impact of PCOS, which appear due to testosterone level rather than the condition per se. We found that increasing testosterone is associated with increasing CBF and decreasing AAT in a region-dependent manner when PCOS diagnosis was controlled for, while PCOS diagnosis had a non-significant effect on these parameters when testosterone was controlled for. A larger sample is needed to test the OEF metric statistically.

This provides information into how testosterone may influence the cerebrovascular system and highlights possible mechanisms by which vascular alterations occur in PCOS patients.

**Acknowledgments / Funding Information:** Funded by the Waterloo Foundation.

## References

1. Kilic D, Kilic ID, Sevgican CI, Kilic O, Alatas E, Arslan M, et al. Arterial stiffness measured by cardio-ankle vascular index is greater in non-obese young women with polycystic ovarian syndrome. *J Obstet Gynaecol Res.* 2021 Feb;47(2):521–8.
2. Chappell MA, Groves AR, Whitcher B, Woolrich MW. Variational Bayesian Inference for a Nonlinear Forward Model. *IEEE Trans Signal Process.* 2009 Jan;57(1):223–36.
3. Desikan RS, Ségonne F, Fischl B, Quinn BT, Dickerson BC, Blacker D, et al. An automated labeling system for subdividing the human cerebral cortex on MRI scans into gyral based regions of interest. *NeuroImage.* 2006 Jul;31(3):968–80.

## Figures

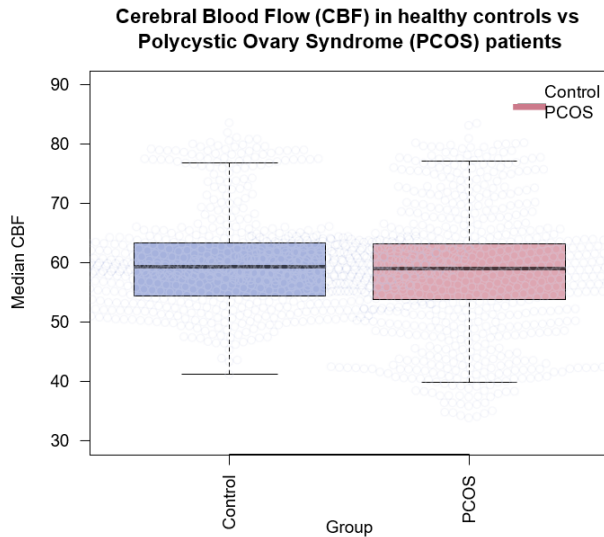


**Figure 1** - Oxygen Extraction Fraction (OEF) in Polycystic Ovary Syndrome (PCOS) patients against healthy controls. Unfilled circles show individual datapoints. Whiskers illustrate the interquartile range.

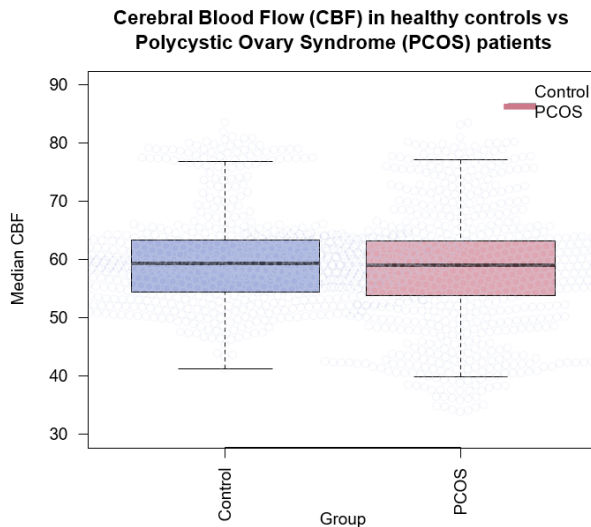


**Figure 2** - Cerebral Blood Flow (CBF) in Polycystic Ovary Syndrome (PCOS) patients against healthy controls, collapsed over region-of-interest (ROI). Data from all ROIs are included. Unfilled circles show individual datapoints. Whiskers illustrate the interquartile range.

**Arterial Arrival Time (AAT) in healthy controls vs Polycystic Ovary Syndrome (PCOS) patients**

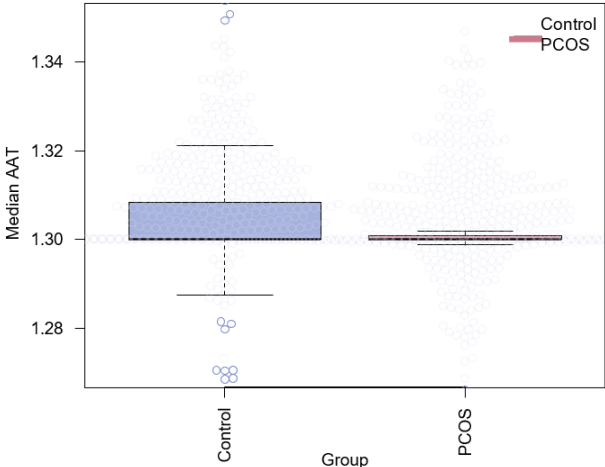


**Figure 3** - Arterial Arrival Time (AAT) in Polycystic Ovary Syndrome (PCOS) patients against healthy controls, collapsed over region-of-interest (ROI). Data from all ROIs are included. Unfilled circles show individual datapoints. Whiskers illustrate the interquartile range.

# Automatic Rejection based on Tissue Signal (ARTS) for motion-corrected quantification of cerebral venous oxygenation in neonates and older adults

Yifan Gou<sup>1</sup>, W. Christopher Golden<sup>1</sup>, Zixuan Lin<sup>1</sup>, Jennifer Shepard<sup>1</sup>, Aylin Tekes<sup>1</sup>, Zhiyi Hu<sup>1</sup>, Xin Li<sup>1</sup>, Kumiko Oishi<sup>2</sup>, Marilyn Albert<sup>1</sup>, Hanzhang Lu<sup>1</sup>, Peiyong Liu<sup>1,3</sup>, and Dengrong Jiang<sup>1</sup>

<sup>1</sup>School of Medicine, Johns Hopkins University, Baltimore, Maryland, USA.

<sup>2</sup>Whiting School of Engineering, Johns Hopkins University, Baltimore, Maryland, USA.

<sup>3</sup>School of Medicine, University of Maryland, Baltimore, Maryland, USA.

## Synopsis:

Cerebral venous oxygenation (Yv) is an important biomarker for various brain diseases such as hypoxic-ischemic-encephalopathy in neonates and Alzheimer's disease in the elderly. T2-Relaxation-Under-Spin-Tagging (TRUST) MRI is a widely used technique to measure global Yv level. However, subject motion during TRUST scan can cause considerable errors in Yv quantification. In this work, we developed an Automatic-Rejection-based-on-Tissue-Signal (ARTS) algorithm to identify and exclude motion-corrupted images in TRUST Yv estimation. This algorithm was trained using datasets of non-sedated healthy neonates, which contain considerable motion. The generalizability of this algorithm was tested on datasets of older adults. We demonstrated that ARTS significantly reduced the motion-induced uncertainties in Yv quantification in both the neonatal datasets and the older adult datasets, suggesting that this algorithm may be useful in enhancing the utility of Yv as a biomarker for brain diseases.

## INTRODUCTION

Cerebral venous oxygenation (Yv) is a biomarker for many brain diseases such as hypoxic-ischemic-encephalopathy<sup>1,2</sup> in neonates and Alzheimer's disease in the elderly.<sup>3,4</sup> T2-Relaxation-Under-Spin-Tagging (TRUST) MRI is a widely-used and validated technique to measure global Yv level.<sup>5</sup> Although TRUST has a short scan time (1.2min), for noncompliant subjects such as neonates, subject motion can still cause considerable errors in Yv quantification.<sup>6</sup> In this work, to improve the precision of Yv quantification, we propose an Automatic-Rejection-based-on-Tissue-Signal (ARTS) algorithm to identify and exclude motion-corrupted images in TRUST Yv estimation. This algorithm was trained using datasets of non-sedated healthy neonates, which contain considerable motion. The generalizability of this algorithm was tested on datasets of older adults.

## METHODS

TRUST MRI: TRUST utilizes subtraction between control and venous-labeled images to isolate pure blood signal in the superior-sagittal-sinus (SSS) and employs T2-preparation with varying effective-TEs (eTEs) to quantify blood T2, which can then be converted to Yv.<sup>7</sup> Each TRUST scan acquires 4 eTEs (0,40,80,160ms) with 3 dynamics for each eTE, and duration=1.2min.

Experiments:

Neonates: 37 healthy neonates received TRUST scans during natural sleep, with 14 of them undergoing 2-3 scans, resulting in a total of 54 TRUST scans.

Older adults: TRUST data were collected from 233 older adults, each undergoing one TRUST scan.

ARTS algorithm:

The ARTS algorithm is based on the fact that a motion-free difference image contains only a few bright pixels in the SSS (Figure 1A, yellow arrow); while a motion-corrupted difference image (Figure 1A, red-highlighted) contains considerable residual tissue signals. Therefore, ARTS first computes a tissue mask for each dataset (Figure 1B) and then calculates a motion index  $\epsilon$  for each difference image using their normalized tissue signal (Figure 1C). Difference images with large  $\epsilon$  were excluded, where the optimal threshold for  $\epsilon$  was trained using the neonatal datasets (Study 1). Yv was estimated using the remaining images.<sup>8,9</sup> The uncertainty of Yv ( $\Delta R2$ ) was also computed.

Study 1:

To serve as a gold-standard, motion-contaminated difference images in the neonatal datasets were manually identified. The optimal threshold for  $\epsilon$  in the ARTS algorithm was determined through fivefold cross-validation, using receiver-operating-characteristic curves to compare ARTS with manual identification, and selecting the threshold with the highest Youden Index<sup>10</sup>. Yv results computed with and without ARTS were compared.

Study 2:

We introduced random motions to the older adult datasets to match the motion occurrence rate of the neonatal datasets. We then compared Yv values with and without ARTS, using the optimal threshold from Study 1.

## RESULTS

Study 1: The optimal  $\epsilon$  threshold was determined to be 0.03. Compared to no motion exclusion, ARTS yielded lower  $\Delta R2$  (3.68Hz vs. 4.89Hz,  $P=0.0002$ , Figure 2B), with no difference in Yv (66.66% vs. 66.54%,  $P=0.88$ , Figure 2A). In neonates with multiple scans, ARTS reduced the coefficient-of-variation of Yv (2.57% vs. 6.87%,  $P=0.0005$ , Figure 2C).

Study 2: In older adult datasets, ARTS resulted in lower  $\Delta R2$  (2.15Hz vs. 3.54Hz,  $P<0.0001$ , Figure 3B), with no difference in Yv (58.20% vs. 58.50%,  $P=0.75$ , Figure 3A).

## CONCLUSION

We developed an automatic motion exclusion algorithm to improve the precision of Yv quantification in motion-prone subjects.

**Acknowledgments / Funding Information:** This work was supported by the National Institutes of Health: R21 AG079098, R01 AG064792, UF1 NS100588, R01 NS109029, RF1 AG071515, R01 NS106711, R01 NS106702, P41

### Reference:

- Shetty AN, Lucke AM, Liu P, Sanz Cortes M, Hagan JL, Chu ZD, Hunter JV, Lu H, Lee W, Kaiser JR. Cerebral oxygen metabolism during and after therapeutic hypothermia in neonatal hypoxic-ischemic encephalopathy: a feasibility study using magnetic resonance imaging. *Pediatr Radiol* 2019;49:224-233.
- De Vis JB, Petersen ET, Alderliesten T, Groenendaal F, de Vries LS, van Bel F, Benders MJ, Hendrikse J. Non-invasive MRI measurements of venous oxygenation, oxygen extraction fraction and oxygen consumption in neonates. *Neuroimage* 2014;95:185-192.
- Thomas BP, Sheng M, Tseng BY, Tarumi T, Martin-Cook K, Womack KB, Cullum MC, Levine BD, Zhang R, Lu H. Reduced global brain metabolism but maintained vascular function in amnesic mild cognitive impairment. *J Cereb Blood Flow Metab* 2017;37:1508-1516.
- Jiang D, Lin Z, Liu P et al. Brain Oxygen Extraction Is Differentially Altered by Alzheimer's and Vascular Diseases. *J Magn Reson Imaging* 2020;52:1829-1837.
- Jiang D, Deng S, Franklin CG, O'Boyle M, Zhang W, Heyl BL, Pan L, Jerabek PA, Fox PT, Lu H. Validation of T(2) - based oxygen extraction fraction measurement with (15) O positron emission tomography. *Magn Reson Med* 2021;85:290-297.
- Stout JN, Tisdall MD, McDaniel P, Gagoski B, Bolar DS, Grant PE, Adalsteinsson E. Assessing the effects of subject motion on T(2) relaxation under spin tagging (TRUST) cerebral oxygenation measurements using volume navigators. *Magn Reson Med* 2017;78:2283-2289.
- Lu H, Xu F, Grgac K, Liu P, Qin Q, van Zijl P. Calibration and validation of TRUST MRI for the estimation of cerebral blood oxygenation. *Magn Reson Med* 2012;67:42-49.
- Jiang D, Deng S, Franklin CG, O'Boyle M, Zhang W, Heyl BL, Pan L, Jerabek PA, Fox PT, Lu H. Validation of T2 - based oxygen extraction fraction measurement with (15) O positron emission tomography. *Magn Reson Med* 2021;85:290-297.
- Liu P, Parkinson C, Jiang D, Ouyang M, De Vis JB, Northington FJ, Tekes A, Huang H, Huisman T, Golden WC. Characterization of MRI techniques to assess neonatal brain oxygenation and blood flow. *NMR Biomed* 2019;32:e4103.
- Youden WJ. Index for rating diagnostic tests. *Cancer* 1950;3:32-35.

### Figures

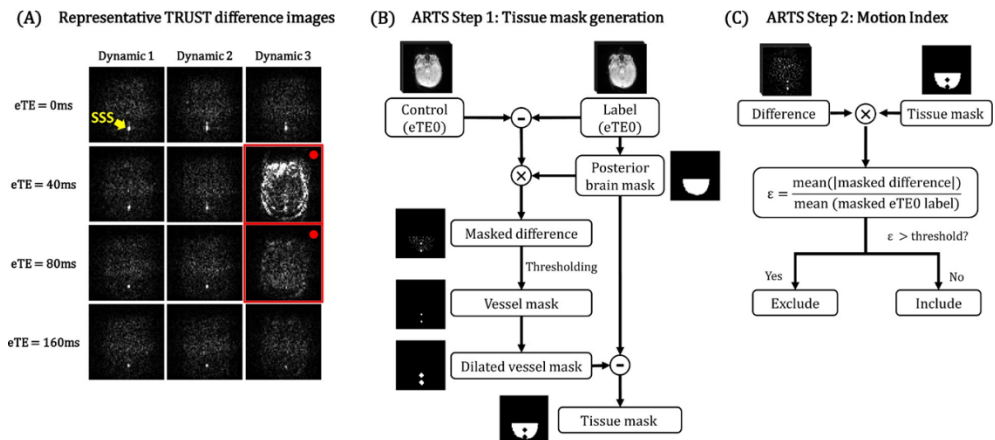


**Figure 1:** Representative TRUST images and flowchart of the ARTS algorithm. (A) TRUST data from a neonate, consisting of 12 difference images (3 dynamics  $\times$  4 eTEs). Motion-contaminated images are red-highlighted. (B) Tissue mask generation in ARTS. A brain mask was segmented from the labeled image and a vessel mask was segmented from the difference image. Subtraction of the vessel mask from the brain mask gave the tissue mask. (C) Motion index calculation and exclusion.

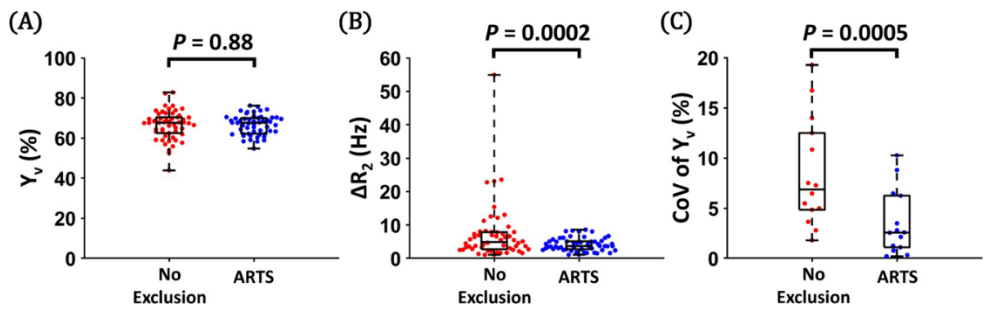


**Figure 2:** Comparison of (A)  $Y_v$ , (B)  $\Delta R_2$  and (C) CoV of  $Y_v$  values obtained without motion exclusion in contrast to those computed with ARTS motion exclusion in the neonatal datasets.

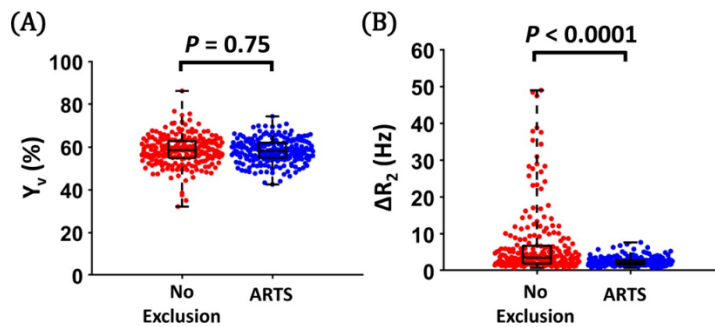


**Figure 3:** Comparison of (A)  $Y_v$  and (B)  $\Delta R_2$  values computed without motion exclusion in contrast to values obtained with ARTS motion exclusion in older adult datasets with simulated motion.

# Comparing BOLD and ASL for cerebrovascular reactivity (CVR) measurements under hypercapnia

G. Hoffmann<sup>1,2</sup>, M. van Osch<sup>3,4</sup>, L. Václavů<sup>3</sup>, J. Kufer<sup>1,2</sup>, L. Schmitzer<sup>1,2</sup>, F. Richter<sup>1,2</sup>, C. Zimmer<sup>1,2</sup>, S. Kaczmarz<sup>1,2,5</sup>, C. Preibisch<sup>1,2</sup>

<sup>1</sup>Department of Diagnostic and Interventional Neuroradiology, Klinikum rechts der Isar of the Technical University of Munich, Munich, Germany;

<sup>2</sup>TUM-Neuroimaging Center, Klinikum rechts der Isar of the Technical University of Munich, Munich, Germany;

<sup>3</sup>C.J. Gorter MRI Center, Department of Radiology, Leiden University Medical Center, Leiden, The Netherlands;

<sup>4</sup>Leiden Institute of Brain and Cognition, Leiden University, Leiden, The Netherlands;

<sup>5</sup>Philips GmbH Market DACH, Hamburg, Germany

## Synopsis and/or Summary of Main Findings:

Cerebrovascular reactivity (CVR) is a promising indicator of the cerebrovascular health status, which is commonly measured indirectly using relative changes in the blood oxygenation level dependent (BOLD) MRI signal. Compared to BOLD, pseudo-continuous arterial spin labelling (pCASL) allows direct assessment of hypercapnia induced perfusion changes. However, standard single post label delay (PLD) pCASL-based CVR may be biased in areas with delayed blood arrival, which can be avoided by using multiple PLD acquisitions by more advanced (time-encoded) Hadamard pCASL. To explore its applicability for patient studies, we compare robust BOLD-CVR to CBF-CVR obtained with single-PLD and Hadamard pCASL. For CBF-CVR, we found good correlations between both ASL techniques as well as homogenous CVR throughout the brain, where single-PLD pCASL systematically underestimated CVR compared to Hadamard ASL. BOLD-CVR on the other hand showed GM-WM contrast which may be due to the strong dependence of the BOLD effect on blood volume.

## Introduction

Cerebrovascular reactivity (CVR) measurements are promising for assessing the status of the vascular system, especially in cerebrovascular diseases.<sup>1,2</sup> While most applications indirectly probe CVR by blood oxygenation level dependent (BOLD) MRI,<sup>4,5</sup> arterial spin labeling (ASL) allows direct assessment of perfusion. However, current single post label delay (PLD) pseudo-continuous ASL (pCASL) implementations only capture ASL signal at a single timepoint and assume a uniform arterial transit time (ATT),<sup>6</sup> resulting in impaired sensitivity especially in white matter (WM) regions with longer ATT. Time-encoded Hadamard pCASL<sup>7</sup> allows time-efficient data collection at multiple PLDs within clinically reasonable scan times. To explore its applicability, we compared hypercapnia-induced CVR as measured by Hadamard pCASL against single-PLD pCASL and commonly used BOLD-MRI.

## Methods

22 healthy subjects (26.1±3.0y,14f) underwent MRI on a 3T Elition X (Philips,NL). Medical and hypercapnic (5% CO<sub>2</sub>) air were supplied by a gas-mixer (AltiTrainer,SMTec,CH). For details of MRI parameters and protocols, see Fig.1. Hadamard- encoded pCASL data were decoded prior to modelling CBF and ATT using FSL BASIL.<sup>8</sup> CVR was calculated as percent signal increase. Hadamard pCASL-based CVR was correlated (Pearson-Correlation,  $p < 0.05$ ) with BOLD- and pCASL- based CVR, and Bland-Altman analysis was conducted for single-PLD and Hadamard. Regional analysis comprised volumes-of-interest (VOIs) in GM, WM, and atlas-based vascular perfusion territories of the anterior (ACA), middle (MCA), and posterior cerebral artery (PCA).

## Results

Axial slices of group-average CVR parameter maps (Fig.1) show clear GM-WM contrast for BOLD-MRI, which is not present for CBF-CVR. While absolute values of BOLD and ASL-based CVR cannot be compared directly, Hadamard pCASL yields higher CBF-CVR than (single-PLD) pCASL (Fig.2A). It was also better correlated with pCASL in GM ( $r=0.51$ , Fig.2B) than BOLD-CVR ( $r=0.22$ , Fig.2C). Regional analyses (Fig.3) substantiate distinct GM-WM contrast for BOLD-MRI, with comparably larger CVR in the PCA territory. In comparison, both pCASL techniques showed similar CVR across different VOIs.

## Discussion

Based on our results, single-PLD pCASL correlates well with multi-PLD Hadamard pCASL but seems to systematically underestimate CVR. This agrees with a previous study in which single-PLD pCASL underestimated acetazolamide-based CVR compared to multi-PLD ASL and PET,<sup>9</sup> while Turbo-QUASAR (pulsed) ASL showed similar CVR as single-PLD pCASL.<sup>10</sup> BOLD CVR correlated rather moderately with Hadamard pCASL ( $r_{\text{BOLD-Hadamard}}=0.11$ ), not unexpectedly, due to the different contrast mechanism. BOLD-MRI yields lower CVR in WM than GM, which agrees with literature,<sup>11,12</sup> but contrasts to homogenous CBF-CVR that has been reported from ASL and PET.<sup>9,12</sup> The present study substantiates these findings as Hadamard ASL is presumably more sensitive in WM due to a lower ATT-related bias. Therefore, lower WM BOLD-CVR is more likely caused by biophysical properties of the BOLD effect than lower WM CVR. For example, lower WM cerebral blood volume (CBV) has been discussed as a possible physiologic mechanism.<sup>13,14</sup>

In conclusion, our results indicate that BOLD and ASL-based CVR represent different aspects of the brain's physiological response to hypercapnia. Regarding ASL methods, our results support Hadamard ASL as the preferred method, which can be expected to offer additional benefits in patients with prolonged ATT, however offering less temporal resolution compared to pCASL.

**Acknowledgments / Funding Information:** We acknowledge the support by Ev. Studienwerk Villigst e.V (personal grant to GH) and the German research Foundation (DFG, grant PR 1039/6-3)

## References

1. Donahue, M.J., et al. Consensus statement on current and emerging methods for the diagnosis and evaluation of cerebrovascular disease. *J Cereb Blood Flow Metab* 38, 1391-1417 (2018).
2. Kaczmarz, S., et al. Hemodynamic impairments within individual watershed areas in asymptomatic carotid artery stenosis by multimodal MRI. *Journal of Cerebral Blood Flow & Metabolism* 41, 380-396 (2021).
3. Smeeing, D.P.J., Hendrikse, J., Petersen, E.T., Donahue, M.J. & de Vis, J.B. Arterial Spin Labeling and Blood Oxygen Level-Dependent MRI Cerebrovascular Reactivity in Cerebrovascular Disease: A Systematic Review and Meta-Analysis. *Cerebrovascular Diseases* 42, 288-307 (2016).
4. Zhao, M.Y., et al. Reproducibility of cerebrovascular reactivity measurements: A systematic review of neuroimaging techniques. *J Cereb Blood Flow Metab* 42, 700-717 (2022).
5. Donahue, M.J., et al. Bolus arrival time and cerebral blood flow responses to hypercapnia. *Journal of Cerebral Blood Flow and Metabolism* 34, 1243-1252 (2014).
6. van Osch, M.J., et al. Advances in arterial spin labelling MRI methods for measuring perfusion and collateral flow. *Journal of Cerebral Blood Flow and Metabolism* 38, 1461-1480 (2018).
7. Günther, M. Highly efficient accelerated acquisition of perfusion inflow series by cycled arterial spin labeling. in *Proceedings of the 15th Annual Meeting of ISMRM (Berlin, 2007)*.
8. Woolrich, M.W., et al. Bayesian analysis of neuroimaging data in FSL. *Neuroimage* 45, S173-S186 (2009).
9. Zhao, M.Y., et al. Cerebrovascular reactivity measurements using simultaneous (15)O-water PET and ASL MRI: Impacts of arterial transit time, labeling efficiency, and hematocrit. *Neuroimage* 233, 117955 (2021).
10. Zhao, M.Y., et al. Quantification of cerebral perfusion and cerebrovascular reserve using Turbo-QUASAR arterial spin labeling MRI. *Magnetic Resonance in Medicine* 83, 731-748 (2020).
11. Taneja, K., et al. Quantitative Cerebrovascular Reactivity in Normal Aging: Comparison Between Phase-Contrast and Arterial Spin Labeling MRI. *Frontiers in Neurology* 11(2020).
12. Richter, F., et al. Pseudo-continuous arterial spin labelling but not BOLD-fMRI yields homogenous cerebrovascular reactivity in grey and white matter. in *Annual Meeting of the European Society of Magnetic Resonance in Medicine and Biology (ESMRMB) (Basel, 2023)*.
13. Zhou, Y., Rodgers, Z.B. & Kuo, A.H. Cerebrovascular reactivity measured with arterial spin labeling and blood oxygen level dependent techniques. *Magn Reson Imaging* 33, 566-576 (2015).
14. Wang, H., et al. White matter BOLD signals at 7 Tesla reveal visual field maps in optic radiation and vertical occipital fasciculus. *NeuroImage* 269, 119916 (2023).

## Figures

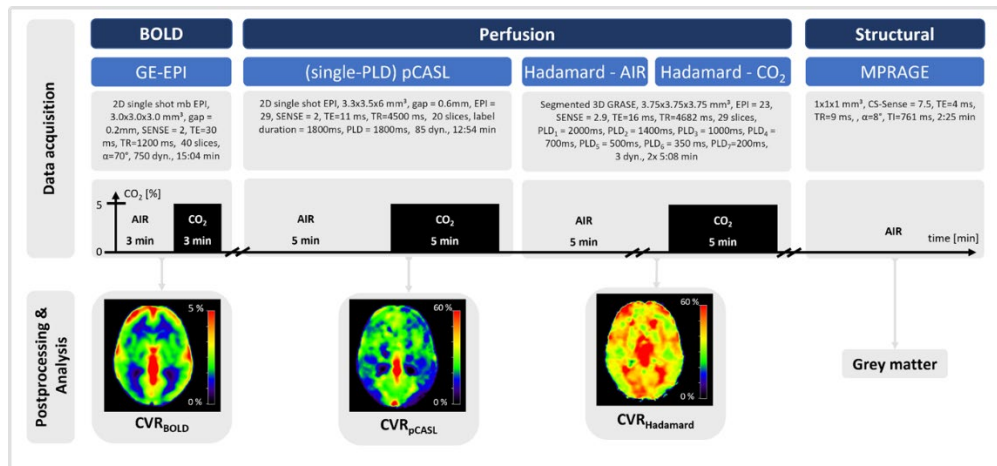


**Figure 1:** Overview of the imaging protocol and derived parameter maps. A block design of alternating air and hypercapnia (5% CO<sub>2</sub>) was used for cerebrovascular reactivity (CVR) assessment. Image acquisition was compared between BOLD-MRI and single post label delay (PLD) pseudo-continuous ASL (pCASL) as well as multi-PLD Hadamard ASL. Axial slices of group mean parameter maps are shown with the same scaling for both ASL methods, while BOLD-CVR scaling differs.

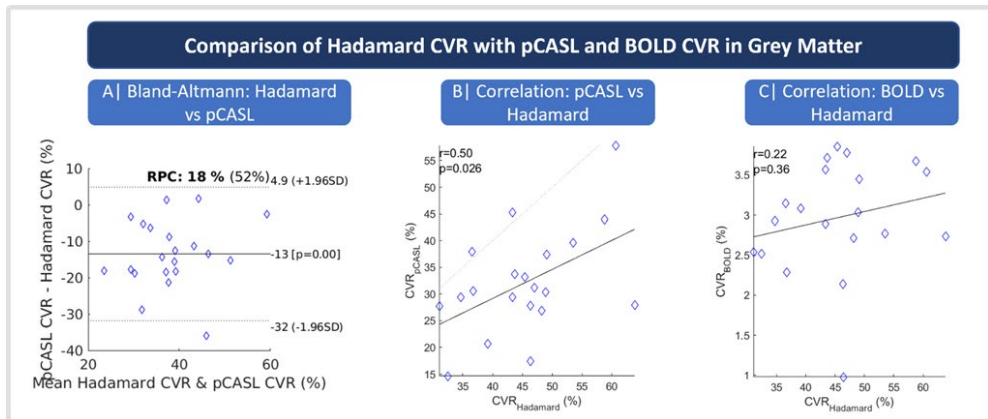


**Figure 2:** Comparing Hadamard pCASL with single PLD pCASL and BOLD-based CVR. Diamonds indicate GM averages of individual subjects. Bland Altman analysis indicates systematic underestimation of CVR by single-PLD vs. Hadamard pCASL (A). While a significant correlation was found between pCASL- and Hadamard-based CVR (B), correlation with BOLD (C) was rather weak.

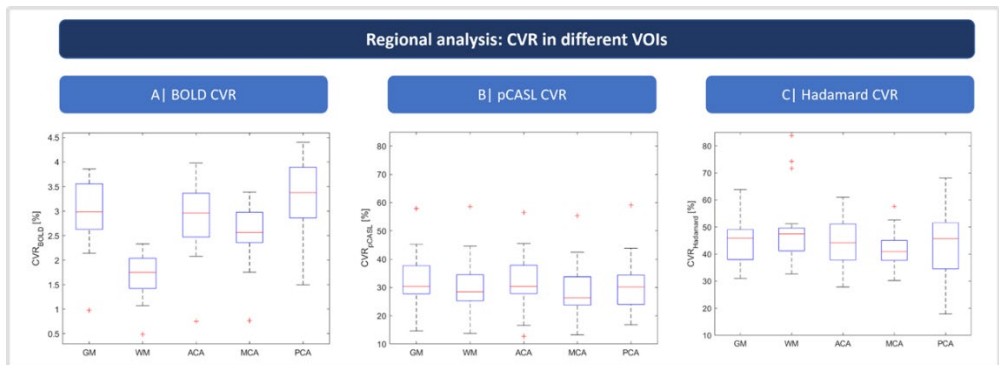


**Figure 3:** Regional analysis. BOLD-, pCASL- and Hadamard-based CVR were compared between volumes of interest (VOIs) of grey matter (GM), white matter (WM) and perfusion territories of the anterior, middle and posterior cerebral artery (ACA, MCA, PCA). CVR was elevated in GM compared to WM in BOLD-CVR and slightly elevated in the PCA territory, while both ASL techniques yielded similar CVR in all VOIs (note different y-axis scaling for BOLD CVR).

# Calibrated fMRI sequence with a background-suppressed pCASL/multi-echo BOLD dual-acquisition

I. Chavarría<sup>1</sup>, M. Vidorreta<sup>2</sup>, M. A. Fernández-Seara<sup>3,4</sup> & C. Caballero-Gaudes<sup>1</sup>

<sup>1</sup>Basque Center on Cognition, Brain and Language, Donostia-San Sebastián, Spain;

<sup>2</sup>Siemens Healthineers, Madrid, Spain;

<sup>3</sup>Radiology department, Clínica Universidad de Navarra, Pamplona, Spain;

<sup>4</sup>IdiSNA, Instituto de Investigación Sanitaria de Navarra, Pamplona, Spain.

## Synopsis and/or Summary of Main Findings

Calibrated fMRI enables the estimation of cerebral metabolic rate of oxygen (CMRO<sub>2</sub>) by measuring simultaneously cerebral blood flow (CBF) and BOLD. This work introduces a novel calibrated fMRI sequence that, using a dual acquisition approach, integrates a background-suppressed pseudo-continuous arterial spin labeling (pCASL) 3D GRASE for CBF and 2D multi-echo (ME) EPI for BOLD acquisition. Results in a healthy volunteer scanned during rest show tissue contrast and CBF values concordant with literature, and improved tSNR and functional connectivity maps in BOLD images due to the feasibility of applying optimal echo-combination and ME-based denoising. These results demonstrate that the proposed sequence is successfully optimizing both ASL and BOLD acquisitions, thus showing promise for advancing calibrated fMRI accuracy and quality by overcoming the limitations of previous ASL-BOLD calibrated fMRI sequences.

## Introduction:

Calibrated fMRI is a quantitative alternative to BOLD fMRI, enabling the estimation of cerebral metabolic rate of oxygen (CMRO<sub>2</sub>) by simultaneously measuring the cerebral blood flow (CBF), using arterial spin labeling (ASL), and BOLD [1,2]. To obtain these measurements, ASL sequences with dual-echo (DE) or multi-echo (ME) readouts are frequently employed [3,4]. Nevertheless, a dual-acquisition (DA) approach, which integrates a background suppressed (BS) pseudo-continuous ASL (pCASL) 3D GRASE and a standard BOLD 2D EPI module [5], enables to optimize both CBF and BOLD acquisition and can substantially enhance perfusion and BOLD data quality. The aim of this work is to improve this sequence by adding a 2D multi-echo (ME) EPI module for BOLD acquisition, enhancing BOLD sensitivity and allowing TE-dependent denoising [6,7].

## Methods:

We implemented a novel DA sequence (Figure 1) consisting on a BS pCASL single-shot 3D GRASE for CBF acquisition and 2D ME EPI for BOLD. Whole-brain acquisitions were performed on a healthy volunteer during resting state in a 3T Siemens PrismaFit scanner using a 64-channel receiver head coil with TR = 7 s, voxel resolution = 4x4x5.5 mm<sup>3</sup>, matrix size = 64x64, 16 slices and BW = 3004 Hz/Px. For pCASL, 72 label-control pairs were acquired with TE=31 ms, FA(exc/ref)=90°/160°, TF=12, slice oversampling=27.5%, slice Partial Fourier factor= 5/8, labeling duration=1.8 s, post-labeling delay=1.8 s and delay time = 1.3 s. For BOLD data, three TEs were collected at 17, 45 and 73 ms. Raw data was reconstructed offline using a MATLAB in-house code. Preprocessing (skull-stripping and volume registration) and computation of the CBF map (single-compartment model [8]) were performed using AFNI, and multi-echo combination and denoising with ME-ICA were done using TEDANA [7] and RICA [9]. Temporal SNR (tSNR) maps and seed-based functional connectivity maps were extracted from BOLD data.

## Results and Discussion:

Figure 2 shows representative M0, label and control images alongside the corresponding CBF maps. Average CBF values in whole-brain, gray and white matter were 44.75 ± 16.97, 51.20 ± 15.31 and 33.38 ± 12.33 ml/100g min, respectively. The CBF maps exhibit the anticipated quality and values concordant with literature [5, 10]. Figure 3 displays three example slices of each individual echo, the T<sub>2</sub>\*-weighted combination (usually known as optimally combined (OC), after ME-ICA denoising (OC denoised), the S<sub>0</sub> and T<sub>2</sub>\* maps. The tSNR maps in Fig. 3 illustrate increased values for OC compared to single echo and further heightened for OC denoised. The mean tSNR values in whole-brain, gray and white matter are respectively 73.03±38.76, 70.89±36.41 and 94.38±32.67 for TE<sub>2</sub>; 110.95±53.93, 104.02±49.09 and 149.84±47.75 for OC, and 129.01±60.93, 119.98±55.35 and 175.48±53.02 for OC denoised. Finally, the seed-based connectivity maps in Fig. 3 show the typical patterns observed for the Default Mode (DMN), Visual (VN) and Sensorimotor (SMN) networks. It is visible that connectivity strength and network size are increased with OC and ME-ICA denoising. In conclusion, these results show the potential of the proposed sequence for significantly enhancing the quality of calibrated fMRI with simultaneous ASL and BOLD data acquisition.

**Acknowledgments / Funding Information:** This study was supported by the Spanish Ministry of Economy and Competitiveness (Ramon y Cajal Fellowship, RYC-2017-21845), the Spanish State Research Agency (BCBL “Severo Ochoa” excellence accreditation CEX2020-001010/AEI/10.13039/501100011033) and the Basque Government (BERC 2022-2025). This research has been made possible through a Formación de Personal Investigador (FPI) contract for the completion of doctoral theses, granted by the Spanish Ministry of Economy and Competitiveness (PRE2019-090025), affiliated with the project (SEV-2015-0490-19-3).

## References:

- [1] Davis, T.L., et al. (1998) Proc Natl Acad Sci U S A, 95(4), 1834-1839. <https://doi.org/10.1073/pnas.95.4.1834>
- [2] Hoge, R.D., et al. (2012) Neuroimage, 62: 930-937. <https://doi.org/10.1016/j.neuroimage.2012.02.022>
- [3] Cohen, A.D., et al. (2017) PLoS One, 12(3):e0169253. <https://doi.org/10.1371/journal.pone.0169253>
- [4] Leontiev, O. & Buxton, R.B. (2007) NeuroImage, 35(1): 175-184. <https://doi.org/10.1016/j.neuroimage.2006.10.044>

- [5] Fernández-Seara, M., et al. (2016) *Neuroimage*, 142:474-482. <https://doi.org/10.1016/j.neuroimage.2016.08.007>
- [6] Posse S., et al. (1999) *Magn. Reson. Med.*, 42:87-97. [https://doi.org/10.1002/\(SICI\)1522-2594\(199907\)42:1<87::AID-MRM13>3.0.CO;2-O](https://doi.org/10.1002/(SICI)1522-2594(199907)42:1<87::AID-MRM13>3.0.CO;2-O)
- [7] DuPre, E., et al. (2021) *JOSS*, 6(66):3669. <https://doi.org/10.21105/joss.03669>
- [8] Wang, J., et al. (2005) *Radiology*, 235(1), 218-228. <https://doi.org/10.1148/radiol.2351031663>
- [9] Uruñuela, E. (2021). *Rica* (Version v1.0.17) [Computer software]. <https://doi.org/10.5281/zenodo.5788350>
- [10] Vidorreta M., et al. (2013) *Neuroimage*, 66:662-671. <https://doi.org/10.1016/j.neuroimage.2012.10.087>

## Figures

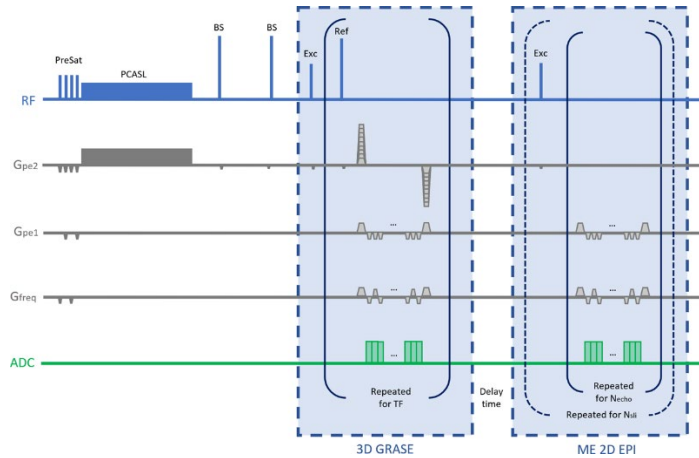


**Figure 1.** Sequence diagram of the proposed calibrated fMRI sequence showing presaturation (PreSat), background suppression (BS) and PCASL pulses, followed by a single-shot 3D GRASE, a delay time of 1.3 s, and the 2D ME EPI readout. The timing of the BS pulses has been optimized to null the 90% of static tissue signal at the start of the GRASE readout.

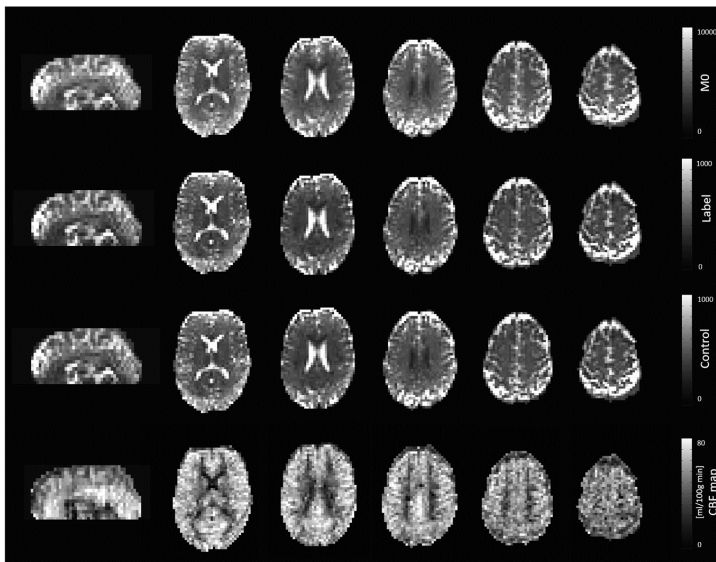


**Figure 2.** (From top to bottom row) Representative slices of M0, label, and control images, and the corresponding CBF map obtained with the proposed calibrated fMRI sequence in a healthy volunteer during rest.

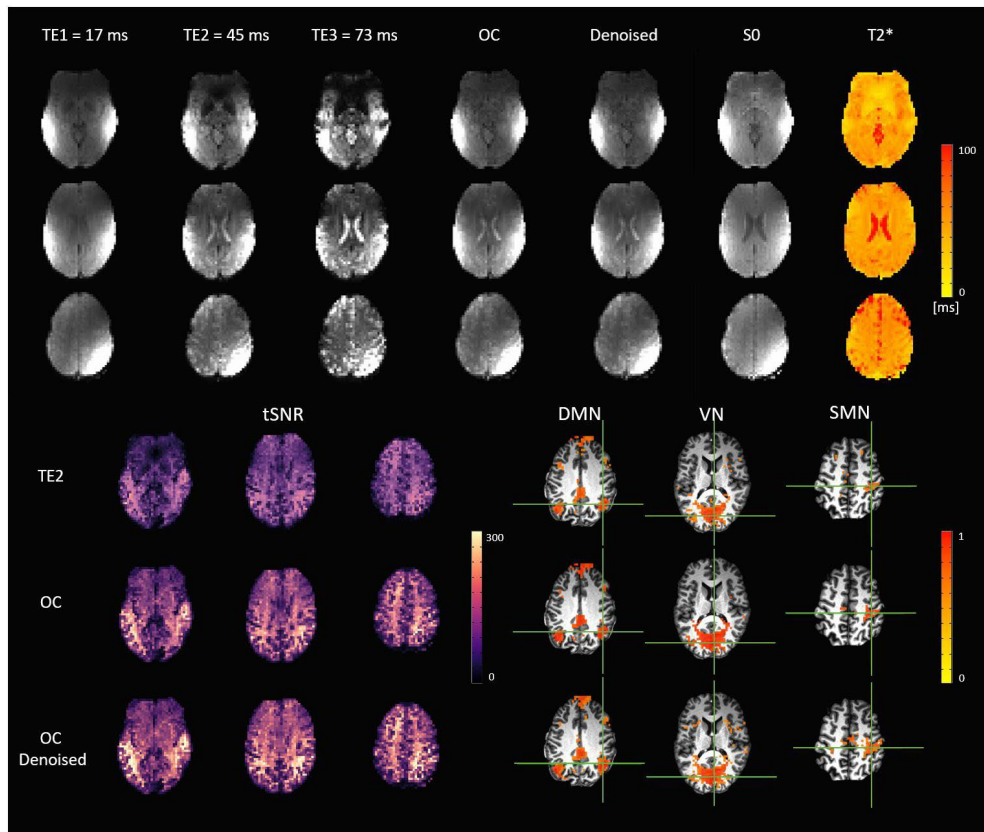


**Figure 3.** (top) Representative images for each individual echo, optimally combined (OC), optimally combined after denoising with TEDANA (OC denoised), S0 and T2\* maps. (bottom-left) tSNR maps for the second echo (TE2), OC and OC denoised. (bottom-right) Seed-correlation functional connectivity maps from seeds (see crosshairs) in left inferior parietal for the default mode network (DMN), extrastriate visual cortex for the primary visual network (VN) and left precentral gyrus (M1) for the sensorimotor network (SMN).

# Direct Imaging of Neuronal Activity (DIANA) in human somatosensory cortex at 3T: Artefact or should we care more about inhibition?

E. Zamboni<sup>1</sup>, I. Watson<sup>2</sup>, J. McStravick<sup>3</sup>, and A.J. Kennerley<sup>3</sup>

<sup>1</sup>School of Psychology, University of Nottingham, Nottingham, UK, NG7 2RD;

<sup>2</sup>School of Physics, Engineering, and Technology, University of York, York, UK, YO10 5DD;

<sup>3</sup>Institute of Sport, Department of Sports & Exercise Sciences, Manchester Metropolitan University, Manchester, UK, M15 6BH.

## Synopsis and/or Summary of Main Findings:

The possibility to measure direct neuronal activity noninvasively with Magnetic Resonance Imaging remains a key goal in the neuroimaging community. While standard functional neuroimaging methods provide information on brain physiology at relatively high spatiotemporal resolution (~1mm<sup>3</sup> and 1s respectively), they often remain pseudo measures of activity. The common Blood Oxygenation Level Dependent (BOLD) signal is a key example, the biophysics of which (including vascular weightings<sup>1</sup>) complicates interpretation. As such the push for novel acquisitions continues with movement away from hemodynamic surrogates<sup>2</sup> to more subtle measures of functional activity. Le Bihan (2006) used diffusion weighting<sup>3</sup> to investigate cellular swelling as a marker of neuronal activity. Recently Toi et al (2022) demonstrated the direct imaging of neuronal activity<sup>4</sup> using MRI at high field (9.4T) in animal models. MRI signal changes were found to correlate with evoked neuronal spiking in the somatosensory cortex 25ms after electrical stimulation of the whisker pad. However, the signal source of these approaches remains unknown and causes contention across the imaging community<sup>5,6,7,8</sup>. Here we implement the fast line scanning technique (with a functional time resolution of 5ms) used by Toi et al<sup>4</sup> and test it for non-invasive measures of somatosensory cortex in humans at 3T. We report our considerations following careful implementation of stimulation delivery/design, and optimisation of the pulse sequence to mitigate against neuronal inhibition.

## Introduction:

Noninvasive neuroimaging techniques allow exploration the functional organisation and processing of the cerebrum. Unfortunately, current standards in functional magnetic Resonance Imaging use Blood Oxygenation Level Dependent (BOLD) signals as a pseudo measure of neuronal activity based upon a complex interplay of cerebral hemodynamics (flow, volume and oxygenation). They are thus susceptible to confounds from the vascular physiology of the brain. Measures at high spatiotemporal resolution that directly capture neuronal activity would expand our understanding of the brain. A recent animal-based study by Toi et al.<sup>4</sup> proposed using fast MRI to measure evoked neuronal spiking. Coined direct imaging of neuronal activity (DIANA), their method coupled high field signal acquisition with fast switching gradients to sample at 5ms time resolutions with MRI. The study showed sequential propagation of neuronal activity through defined neural networks (thalamus-primary somatosensory cortex). This highlights the advantages and range of possible topics that could be addressed with this acquisition technique. Unfortunately, this method, like previous attempts using diffusion gradients to assess cell swelling, remains controversial<sup>5,6,7,8</sup>.

## Method:

Here we implement DIANA and test it in the human brain at 3T (SIEMENS MAGNETOM Vida). We used electrical stimulation of the sensorimotor pathways. To achieve the timing accuracy needed, we adopted a Digitimer solution (Figure 1) such that electrical stimulation across the thumb and ring fingers of participants was delivered ~50ms following the MR trigger pulse. Synchronisation of MR trigger & stimulation was handled and monitored by a MICRO1401 (CED) programmed with Spike. We achieved stimulus timing accuracies on the order of 1-5 $\mu$ s, minimising temporal blurring across the 2560 averages (~10min) acquisition period. Amplitude of stimulation was assessed before entering the scanner such that a 5Hz stimulation for 10min would result in perceived but not uncomfortable sensations. Standard BOLD fMRI measures (block design<sup>9</sup>) were also obtained to localise the DIANA acquisition plane (Figure 2).

## Results:

Our preliminary analysis shows reliable responses, following electrical stimulation of the fingers, in contralateral somatosensory cortex during standard BOLD acquisition (Figure 2). For DIANA we observe large non-localised signal peaks ~15-20ms & ~50-55ms post stimulus (Figure 3). While these delayed responses could reflect nerve conduction times<sup>10</sup>; the non-localised nature suggests an unknown artefactual origin. Closer examination of the signal in the contralateral somatosensory cortex does show underlying elevated signal amplitude around 20-50ms post stimulus. This could be reflective of the signals observed by Toi et al.<sup>4</sup>

## Conclusion:

The published DIANA sequence (Cartesian based) only measures the centre of k-space (where most of the DC signal change is measured) for 40/2560 repeats of the stimulus. We note that constant electrical stimulation can result in habituation of neural responses over time<sup>11,12</sup>. This has obvious repercussions for the DIANA signal: simply averaging across multiple repeats to obtain the '200ms time course' window of neuronal activity will not guarantee high sensitivity if inhibition is high during these 40/2560 repeats. We propose a radial based approach<sup>13,14</sup> which records the centre of k-space for every repeat. Using this approach effects of neuronal inhibition will be averaged out to improve the statistical power of DIANA.

**Acknowledgments / Funding Information:** We are grateful to all the volunteers that participated in this work and the Institute of Sport at Manchester Metropolitan University for investing in the development of cutting-edge imaging techniques and research.

**References:**

- [1] Kennerley AJ, et al. *Open Neuroimaging*. 2010; 4:1-8; [2] Huber L, et al. *NeuroImage*. 2019; 197:742-760; [3] Le Bihan D, et al. *PNAS*. 2006; 103(21):8263-8268; [4] Toi PT, et al. *Science*. 2022; 378:160-168; [5] Miller KL, et al. *PNAS*. 2007; 104(52):20967-20972; [6] Editorial Expression of Concern. *Science*. 2023; 381:1058-1058; [7] Choi SH, et al. *bioRxiv*. 2023; doi: 10.1101/2023.05.26.542419; [8] Hodono S, et al. *Imaging Neuroscience*. 2023; doi: 10.1162/imag\_a\_00013; [9] Sanchez-Panchuelo RM, et al. *Front Hum Neurosci*. 2018; doi: 0.3389/fnhum.2018.00235; [10] Chouhan S, *J Clin Diagn Res*. 2016; doi: 10.7860/JCDR/2016/14618.7037; [11] Thompson RF, et al. *Psychol Rev*. 1966; 73:16-43; [12] Kilngner CM, et al. *Human Brain Mapping*. 2012; 35(1):152-160; [13] Watson I, et al. *Proc Intl Soc Mag Recon Med*. 2023; [14] Kennerley AJ, et al. *British Journal of Oral and Maxillofacial Surgery*. 2022; 60(5):596-603

**Figures**

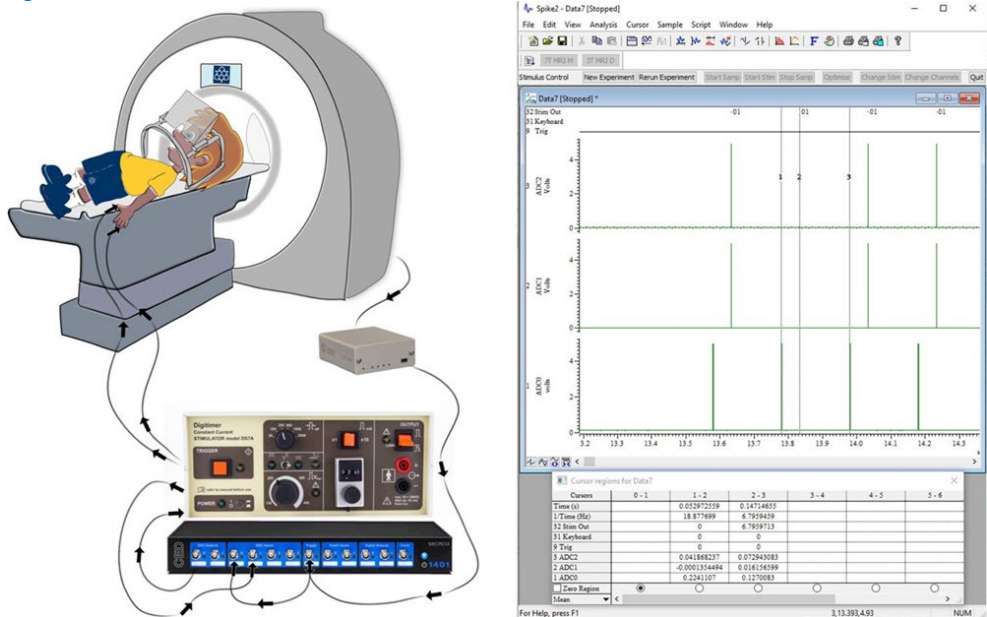


**Figure1:** Experimental setup – optical signal from MR trigger is converted to AD passing through CED as ADC0 input. DAC0 sends signal to Digitimer (also loops back into CED) to then start electrical stimulation of thumb and ring finger. Timing is recorded and saved via Spike2 (on the right).

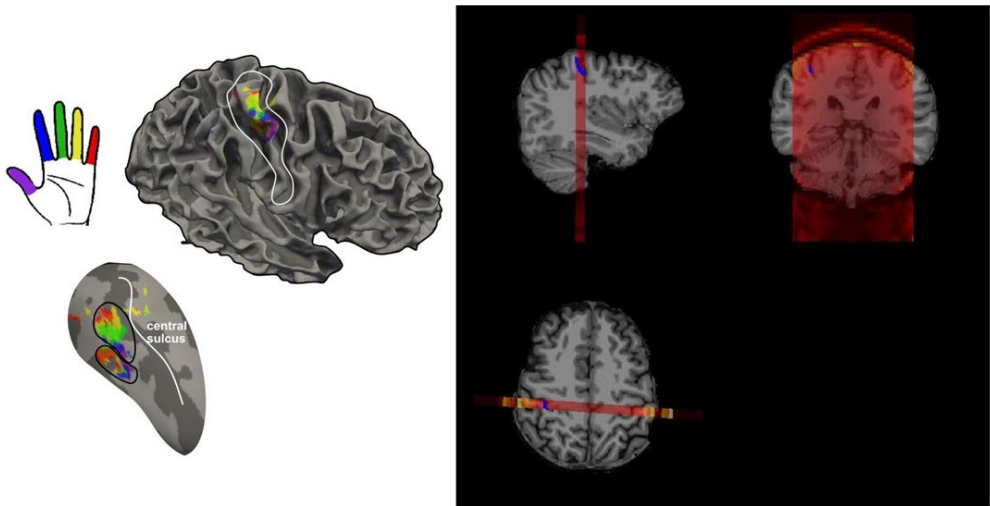


**Figure 2:** Somatotopic map of the left-hand digits acquired on a Siemens MAGNETOM Vida 3T system at the Institute of Sport, Manchester Metropolitan University. BOLD maps are displayed on inflated 3D model of the right hemisphere. The posterior bank of the central sulcus (white line) shows orderly representation of the digits. Insert at the bottom highlights the digit-topography. The right figure shows positioning of DIANA (red) overlaid on whole brain T1w MP2RAGE structural image and digits-ROI (blue).

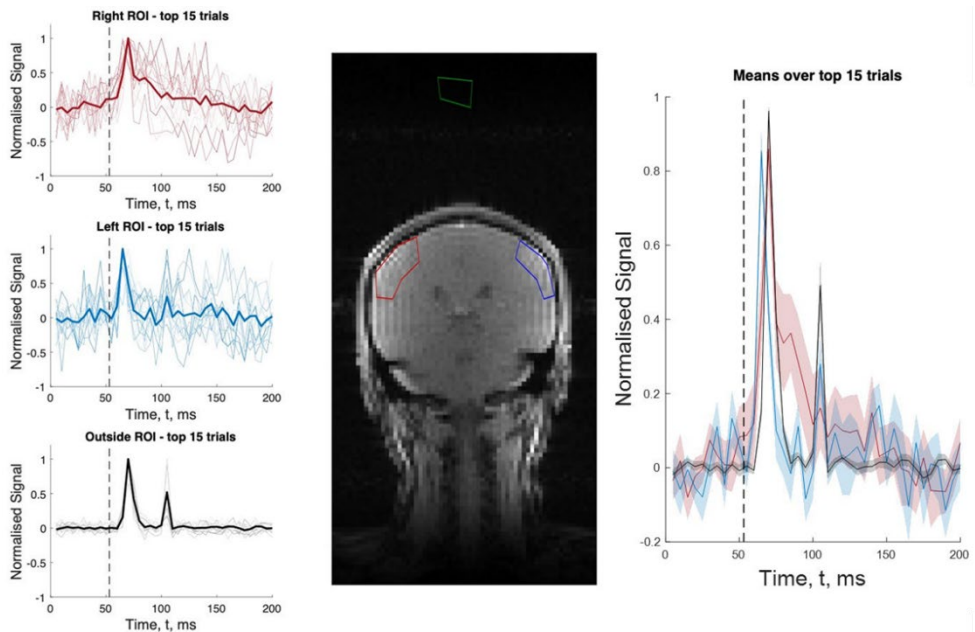


**Figure 3:** DIANA acquisition shows image artefact (black time course corresponding to green ROI) peaking at ~15ms post stimulus onset. Same peak is observed in DIANA signal from the right (red) and left (blue) ROIs. Interestingly, time course in the right hemisphere shows a second peak around ~30ms post stimulus onset, not present in the other ROIs. Thin lines (left panel) show individual trials, thick lines are means across trials.

# Physiopy: a community of physiological data users and Python suite for handling physiological data recorded in MRI settings

S. Moia<sup>1,2</sup>, R. G. Bayrak<sup>3</sup>, M. Miedema<sup>4</sup>, M.E. Picard<sup>5</sup>, D. Glen<sup>6</sup>, on behalf of the Physiopy Community<sup>7</sup>

<sup>1</sup>Neuro-X Institute, École polytechnique fédérale de Lausanne, Geneva, Switzerland;

<sup>2</sup>Department of Radiology and Medical Informatics (DRIM), Faculty of Medicine, University of Geneva, Geneva, Switzerland;

<sup>3</sup>School of Engineering, Vanderbilt University, Nashville, TN, USA;

<sup>4</sup>Department of Bioengineering, McGill University, Montreal, QC, Canada;

<sup>5</sup>Department of Psychology, Montreal University, Montreal, QC, Canada;

<sup>6</sup>SSCC, NIH/NIMH, Bethesda, MD, USA;

<sup>7</sup><https://physiopy.github.io/community/team>

## Synopsis

There is a growing interest in collecting complementary physiological data during neuroimaging data acquisition, either for physiological brain mapping [1] or physiological denoising [2]. However, substantial barriers still limit the widespread adoption of physiological data, e.g. the lack of open data, the limited amount of clear, accessible community guidelines, and isolated user communities. Born as a collaborative project, physiopy aims at removing these barriers with an open, community-based approach, welcoming all contributions of any kind. Physiopy leverages the Brain Imaging Data Structure (BIDS) protocol [3] and aims at building consensus on community practices among researchers in an open, transparent, and reproducible manner. The four pillars of the physiopy project are (i) a suite of easily usable software, (ii) clear documentation, (iii) community practices based on consensus, and (iv) a community of users, developers, and researchers interested in physiology.

The physiopy suite (Figure 1) is based on python and is currently composed of four toolboxes, all released under Apache-2.0 licenses, and at different stages of development: phys2bids [4] aids the registration, storage, and sharing of physiological data in BIDS format; peakdet [5] preprocesses and analyses physiological signals, and performs automatic and manual peak detection (Figure 2A); phys2denoise [6] models physiological signals for the purpose of denoising in functional neuroimaging studies; physioQC [7] helps quality assessment through automatic quality control metrics and visual reports. All toolboxes are developed to build reproducible workflows and are independent of each other—each fulfilling a specific task in the physiological signal preparation pipeline—to maximise interfacing with non-physiopy software. Figure 2B-C shows examples of outputs of the toolboxes.

Guiding software development and informed by its use, physiopy's community practices are compiled into easily available documentation based on bi-monthly open discussions and educational courses organized with the help of experts in the field of physiology. Documentation and videos are openly hosted on the community website (Figure 2D) under CC-BY-NC 4.0 licences.

Current development efforts are focused on (1) extending support to more proprietary formats and imaging modalities, (2) improving BIDS support and creating BIDS-Apps, (3) consolidating each workflow, improving and adding GUIs, and integrating a full (semi-)automated pipeline, (4) improving integration with other open toolboxes, (5) creating a common testing dataset across physiology-oriented developers, (5) reaching out to physiology-oriented communities to increase consensus on community practices, (6) improving community practices documentation and have it vetted by OHBM, (7) improving physioQC. Altogether, physiopy aims to become a complete toolkit and a guide for all tasks related to physiological data in a neuroimaging context. As an open and inclusive project, new contributions of any level of expertise are always welcome. We adopt the all-contributors acknowledgment system, which recognises all contributions of any kind (Fig. 3). To join the monthly meetings, ask questions, or provide suggestions, email to [physiopy.community@gmail.com](mailto:physiopy.community@gmail.com).



Figures

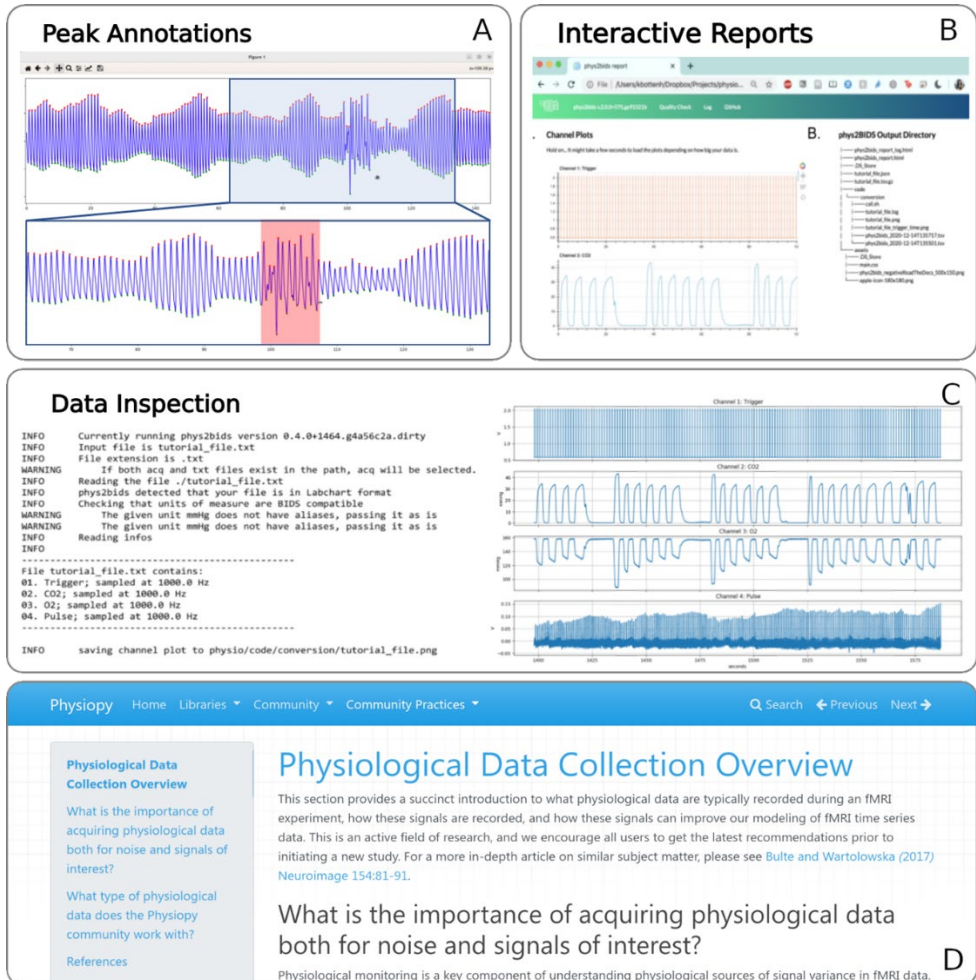


**Figure 1:** (A) Manual revision of automatic peak detection through peakdet's GUI; (B-C) Outputs examples of the physiopy suite; (D) Consensus-based community practices documentation

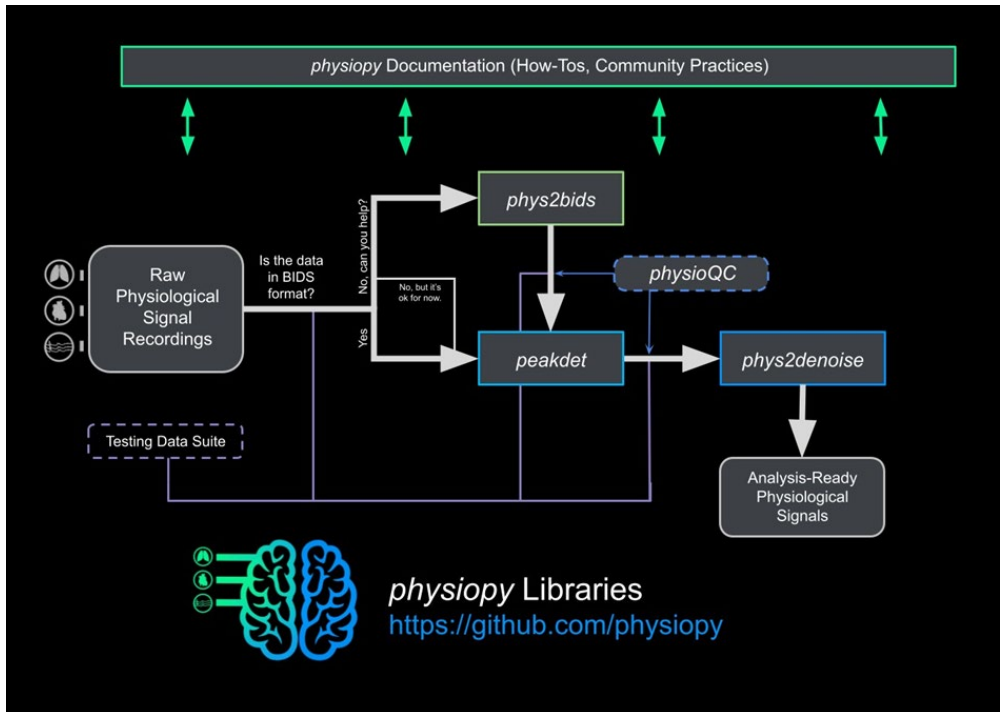


**Figure 2:** Physiopy suite, documentation, toolboxes, and pipeline. An important part of the suite is the software, based on community practices, that helps supporting and re-discussing such practices.

# Hemodynamic response function and an approximation of cerebrovascular reactivity in acute stroke patients

A. Cancino<sup>1,2</sup>, P. Muñoz<sup>3</sup>, P. Cox<sup>4</sup>, L. Acevedo<sup>4</sup>, S. Castillo<sup>4</sup>, A. Letelier<sup>4</sup>, A. Veloz<sup>5</sup>, M. Rodríguez-Fernandez<sup>2,6</sup>, S. Chabert<sup>2,5</sup>

<sup>1</sup> PhD Program in Sciences and Engineering for Health. Universidad de Valparaíso, Valparaíso, Chile,

<sup>2</sup>Millenium Institute for Intelligent Healthcare Engineering iHealth, Santiago, Chile,

<sup>3</sup>Center for Applied Neurological Sciences, Faculty of Medicine, Universidad de Valparaíso, Valparaíso, Chile,

<sup>4</sup>Hospital Carlos Van Buren, Valparaíso, Chile

<sup>5</sup>School of Biomedical Engineering, Universidad de Valparaíso, Valparaíso, Chile

<sup>6</sup>Institute for Biological and Medical Engineering, Pontificia Universidad Católica de Chile, Santiago, Chile.

## Synopsis and/or Summary of Main Findings

Hemodynamic function response (HRF) was described using an event related paradigm exploring the somatosensory cortex and describing qualitative the HRF and its relationship with an inflammatory marker. Also, an approximation of the cerebrovascular reactivity using the amplitude fluctuation of a functional MRI signal in the acute phase of brain ischemia. This work shows the different observations of onset HRF descriptors with CRP inflammation markers for the first time in the acute stage. The ALFF showed direct and Indirect Negative values related to the ischemic core. This opens a new use of fMRI signals to improve the understanding of CVR pathophysiology in a complex clinical condition.

## Abstract Body:

An ischemic stroke is the lack of blood flow in some part of the brain vasculature territory. This is the second leading cause of death. Neuroinflammation has shown a strong correlation between the severity and mortality rates of stroke patients<sup>1</sup>. Functional Magnetic Resonance Imaging (fMRI) is a valuable tool for monitoring changes in the brain. The interest in the changes in HRF at the acute stage and the impact of inflammation in the neuroimaging of stroke is unclear. This work incorporates the HRF as a quantitative marker and its relationship with inflammation and explores an approximation of cerebrovascular reactivity in a resting state signal approximation, during the first 48 hours of the stroke.

## Methods:

The Neurology Department of our local public hospital enrolled 23 volunteers diagnosed with an ischemic stroke. Indication of thrombolysis or thrombectomy was an exclusion criterion. This study received full approval from the local ethics committee. The severity of their symptoms using the National Institutes of Health Stroke Scale (NIHSS). Inflammation was characterized by quantifying C-reactive protein (CRP) and interleukin-6 (IL-6), which were determined directly in the immunoassay laboratory at admission. The fMRI was acquired in a 1.5 Tesla GE Signa EX. An event-related design with a passive motor paradigm was performed on the participants. fMRI preprocessing was performed using SPM12. The analyses were undertaken in Regions of Interest (ROI) from the hypoxic hemisphere "ischemic ROI" and the contralateral "non-ischemic ROI", localized in the postcentral gyrus in both hemispheres. We estimated the HRF parameters<sup>4</sup> by obtaining the height, latency, width, and onset of the curve using a MATLAB homemade code. We also estimated Cerebrovascular Reactivity (CVR) mapping with the amplitude frequency fluctuation (ALFF) of the signal<sup>3</sup>. The first step was obtaining the residual maps of the task-based trial to explore a signal similar to the resting state to estimate ALFF maps<sup>5</sup>

## Results

23 participants were included in the study. With an average age of 66.6 years and with a representation of 5 women. High variability in clinical compromise, hours elapsed from the last time seen well, and inflammatory markers. The clinical assessment was evaluated with NIHSS and ischemic volume (Table 1). The median and MAD values of the HRF characterization are shown in Table 1, the CRP and clinical measures of stroke correlate as previously reported, Except for IL6 and NIHSS (Figure 2). A wide spread of the data in the ischemic time to peak and the width were the main characteristics of the ischemic HRF. MAD differences between ischemic and non ischemic ROI were not statistically significant. The exploratory ALLF maps shown in the volumes available a Negative ALFF in the regions corresponding to the ischemic core (Figure 3)

## Conclusion:

There are still many questions to be answered about how this new physiological method can be applied to complex brain functioning in various clinical conditions. More research is needed to better understand its potential.

**Acknowledgments / Funding Information:** This work was funded by the National Agency of Research and Development (ANID-Chile) through Millennium Science Initiative Program – ICN2021\_004, FONDECYT 11201046 and 1231268). Ph.D. Scholarship Program /2023 - 21231977

## References

1. Hotter B, Hoffmann S, Ulm L, Meisel C, Fiebach JB, Meisel A. IL-6 Plasma Levels Correlate With Cerebral Perfusion Deficits and Infarct Sizes in Stroke Patients Without Associated Infections. *Front Neurol*. 2019.
2. Shan ZY, Wright MJ, Thompson PM, et al. Modeling of the hemodynamic responses in block design fMRI studies. *J Cereb Blood Flow Metab*. 2014.
3. Kannurpatti SS, Biswal BB. Detection and scaling of task-induced fMRI-BOLD response using resting state fluctuations. *Neuroimage*. 2008.
4. Fair DA, Schlaggar BL, Cohen AL, Miezin FM, Dosenbach NU, Wenger KK, Fox MD, Snyder AZ, Raichle ME,

Petersen SE. A method for using blocked and event-related fMRI data to study "resting state" functional connectivity. Neuroimage. 2007.  
 5. Liu P, Li Y, Pinho M, Park DC, Welch BG, Lu H. Cerebrovascular reactivity mapping without gas challenges. Neuroimage.

Tables and figures

Subjects Description	Age	Ischemic Volume (ml)	NIHSS	Hours elapsed	IL6 (pg/ml)	CRP (mg/ml)
Median	70	1.85	4	22	10.25	5.5
Range	[44 - 88]	[0.47 - 53.9]	[1 - 21]	[1 - 48]	[1.5 - 40]	[0.8 - 53.8]

HRF characterization ischemic and non ischemic hemisphere								
	H <sub>i</sub>	H <sub>ni</sub>	T <sub>i</sub> (s)	T <sub>ni</sub> (s)	W <sub>i</sub> (s)	W <sub>ni</sub> (s)	O <sub>i</sub> (s)	O <sub>ni</sub> (s)
Median	0,28	0,34	4,60	3,70	4,50	3,90	1,72	1,45
MAD	0,11	0,15	3,29	1,62	2,78	1,55	1,53	0,69

Height (H), the maximum signal change during the peri-stimulus time window (30 seconds was used in this study); time to peak (T), the time in seconds when signal change reached its maximum value; full width at half maximum of the HRF (W); the onset (O), the first time point following the stimulus at which signal intensity exceeded 10% of H.  
 i: Ischemic ni: Nonischemic  
 MAD: Median absolute deviation

Table 1: Subject Global Characterization and HRF characterization in the ischemic and non-ischemic hemisphere.

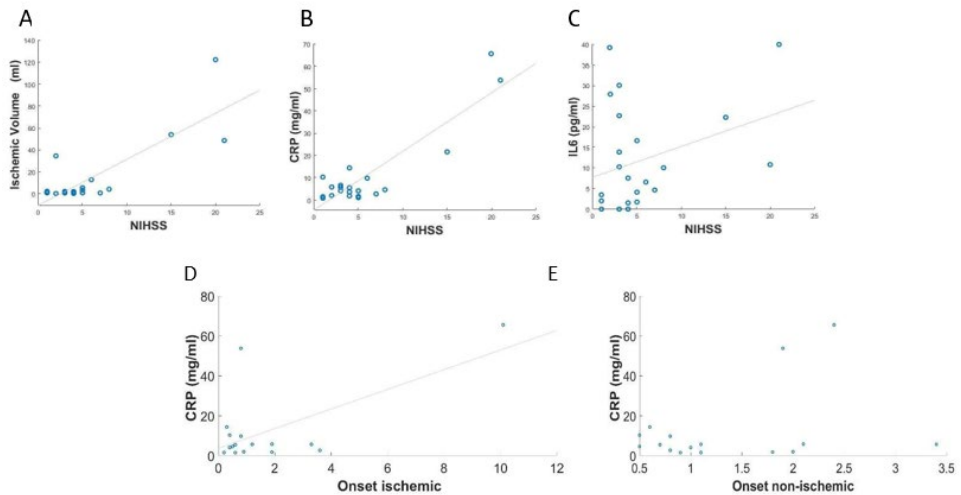
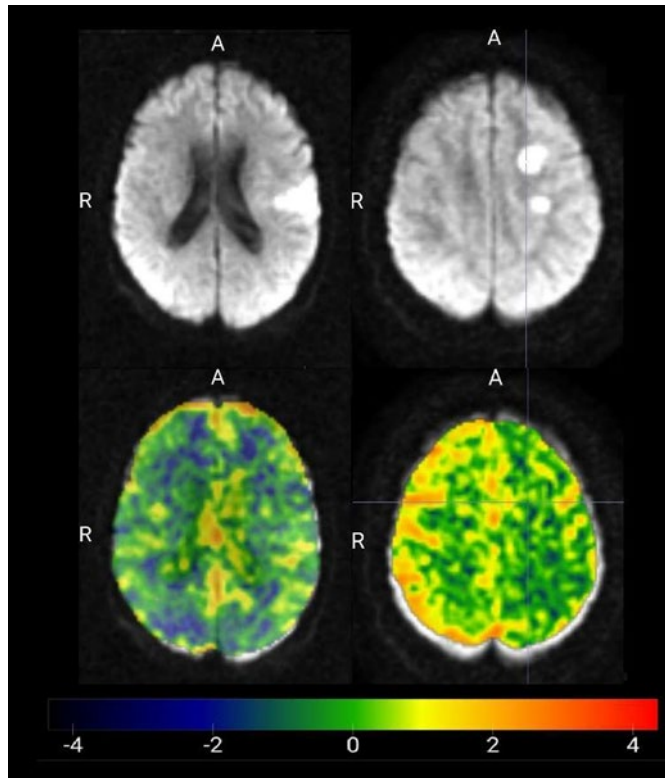


Figure 1. A) Ischemic volume and NIHSS correlation  $R=0.82$ ,  $p<0.001$  \*\*\* B) CRP at admission and NIHSS correlation  $R=0.89$  con  $p<0.001$  \*\*\* C) IL-6 at admission and ischemic volume  $R=0.26$ ,  $p<0.275$ . HRF parameter affected by inflammation. D) CRP at admission correlates with Onset at the ischemic hemisphere ( $R=0.634$   $p=0.008$ \*). E) Non-ischemic onset and CRP ( $R=0.360$ ,  $p=0.155$ ).



**Figure 2:** Diffusion-weighted images at  $b=1000$  for ischemic ROI definition and ALFF color maps as an approximation of CVR

# High CO<sub>2</sub> stimulus accuracy in ventilators using Additional CO<sub>2</sub> Facilitating CVR imaging in ventilated patients

G. Magnusson<sup>1</sup>, A. Tisell<sup>1,2</sup>, G. Cedersund<sup>1</sup>, C. Georgiopolus<sup>1</sup>, L. Tobieson<sup>1,2</sup>, M. Engström<sup>1</sup>

<sup>1</sup>HMV, Linköping University, Linköping, Sweden;

<sup>2</sup>Region Östergötland, Linköping, Sweden

## Synopsis and/or Summary of Main Findings:

We have developed a new method to administer CO<sub>2</sub>, Additional CO<sub>2</sub>, which enables high accuracy CO<sub>2</sub> stimulus in ventilators, facilitating future CVR imaging in ventilated patients.

## Background

Cerebrovascular Reactivity Imaging (CVR) is a novel method that has seen an increased interest the last years.1 However, the majority of studies are on free breathing patients, with very few studies done in ventilated patients.1,2 One reason is the lack of commercially available system to generate a CO<sub>2</sub> challenge, which is the most common choice of stimulus in CVR imaging.1

## Method

We set out to develop a new method for administering CO<sub>2</sub> which we call Additional CO<sub>2</sub>, to enable safe and reliable CO<sub>2</sub> stimulus in ventilated patients. Instead of providing the whole gas mixture for patients to breath, Additional CO<sub>2</sub> adds an additional flow of high concentration CO<sub>2</sub> in proportion to the main respiratory gas flow, targeting a specific CO<sub>2</sub> concentration in the inhaled gas. This enables a fast stimulus onset since no reservoir gas needs to be exchanged. We have tested our system using a ventilator and a test-lung. Additionally, we have recruited six healthy volunteers and compared our system with a traditional system for CO<sub>2</sub> administration, inspired by the system described by Tancredi et al.3, looking at target accuracy and generation of BOLD-based CVR maps.

## Result

Our system produces a reliable and accurate stimulus both in a ventilator and in healthy subjects. In the ventilator, the system seemed to undershoot the target value. However, the target accuracy was consistently better than 0.4 percentage units, CO<sub>2</sub> targets ranging from 0-5% in the inhaled gas. Further, in the healthy subjects, since no gas reservoir was being used, the system showed a fast stimulus onset and the target CO<sub>2</sub> level could be changed from one breath to the next.

## Conclusion

The Additional CO<sub>2</sub> method shows high CO<sub>2</sub> target accuracies in both ventilator and healthy subjects. The fast stimulus onset provides an additional benefit in that complicated target curves, such as ramp or sinusoidal, can be achieved. These findings provides a promising ground to facilitate CVR imaging in ventilated patients in the future.

## References

1. Sleight E, Stringer MS, Marshall I, Wardlaw JM, Thrippleton MJ. Cerebrovascular Reactivity Measurement Using Magnetic Resonance Imaging: A Systematic Review. *Front Physiol.* 2021 Feb 25;12:643468. doi: 10.3389/fphys.2021.643468. Erratum in: *Front Physiol.* 2022 Dec 09;13:1105285. PMID: 33716793; PMCID: PMC7947694.
2. Fierstra, J., Burkhardt, J.-K., van Niftrik, C.H.B., Piccirelli, M., Pangalu, A., Kocian, R., Neidert, M.C., Valavanis, A., Regli, L. and Bozinov, O. (2017), Blood oxygen-level dependent functional assessment of cerebrovascular reactivity: Feasibility for intraoperative 3 Tesla MRI. *Magn. Reson. Med.*, 77: 806-813. <https://doi.org/10.1002/mrm.26135>
3. Tancredi FB, Lajoie I, Hoge RD. A simple breathing circuit allowing precise control of inspiratory gases for experimental respiratory manipulations. *BMC Res Notes.* 2014 Apr 12;7:235. doi: 10.1186/1756-0500-7-235. PMID: 24725848; PMCID: PMC4005461.

Figures

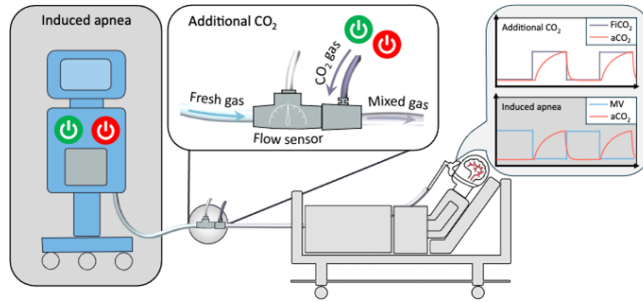


**Figure 1.** Schematic illustration of Induced apnea and Additional CO2, two methods for hypercapnic stimuli in ventilated patients. Induced apnea creates a hypercapnic stimulus by turning off and on the ventilator. For the Additional CO2 method, the ventilator is always on, and instead the addition of high concentration CO2 is turned on/off. Because the ventilator is always on, the patient's O2/CO2 levels is always monitored, offering extra safety.

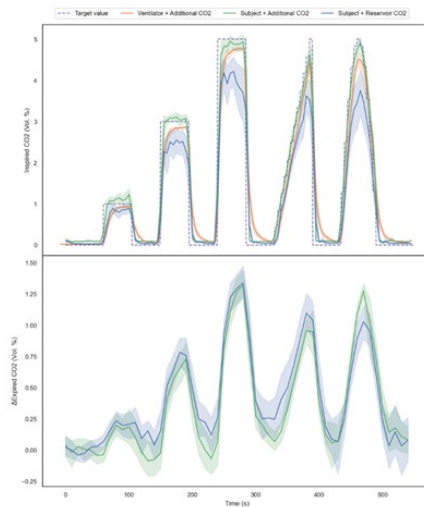


**Figure 2.** Showing the inspired CO2 (top part) and expired CO2 (bottom part) for the ventilator using the Additional CO2 method, healthy subjects using the Additional CO2 method and healthy subjects using the system inspired by Tancredi et al.3, here referred to as Reservoir CO2.

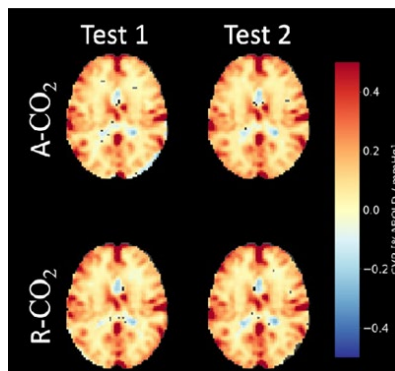


**Figure 3.** Example of BOLD-CVR maps from one subject who performed a test-rest experiment using both the Additional CO2 and Reservoir CO2 method (the later inspired by Tancredi et al.3). Qualitatively, we see that the two methods produce similar result. Imaging was done on Siemens 3T Prisma Scanner using a multi-echo BOLD sequence.

# Imaging-Based Analysis of Cerebrovascular Reactivity in Military Snipers Experiencing Repetitive Sub-concussive Impacts

K. Huynh<sup>1</sup>, C.C. Hambly<sup>1</sup>, G. Ramirez-Garcia<sup>2</sup>, N.S. Coverdale<sup>1</sup>, D.J. Cook<sup>1,3</sup>

<sup>1</sup>Centre for Neuroscience Studies, Queen's University, Kingston, ON, Canada

<sup>2</sup>Unidad Periférica de Neurociencias, Facultad de Medicina, Universidad Nacional Autónoma de México en Instituto Nacional de Neurología y Neurocirugía "Manuel Velasco Suarez", Ciudad de México, Mexico

<sup>3</sup>Department of Surgery, Queen's University, Kingston, ON, Canada

## Synopsis and/or Summary of Main Findings:

Here, we scanned 13 military snipers before and after a sniper training course where there is high exposure to repetitive subconcussive impacts from firing high caliber rifles. We investigated fluctuations in cerebrovascular reactivity (CVR) using blood oxygen level dependent (BOLD) data. A paired sample t-test was conducted to determine the effect of repeated subconcussive exposures on CVR; the subject's age and the number of days between MRI scans were included as covariates in the statistical model. There was a significant increase in CVR ( $P < 0.05$ ) in the anterior cingulate gyrus in the right cerebral cortex.

## Abstract Body:

Subconcussive impacts, a form of mild traumatic brain injury, has been shown to alter CVR following repetitive impact exposure in humans (Champagne et al., 2019a, Champagne et al., 2019b). However, prior work was limited by the recruitment of participants with variable head impact location, frequency, and magnitude. We have partnered with the Canadian Special Operations Forces Command (CANSOFCOM) to study subconcussive injury in their personnel. Military snipers are continually exposed to subconcussive impacts as the stock of their weapon impacts the shoulder and transfers recoil forces to the head. Overall, this allows for a highly reproducible model of occupational subconcussive exposure where the kinematics of the impact can be assessed. Anecdotally, some snipers report either constant neurological symptoms after an accumulation of high caliber rifle recoil forces throughout their careers or a decreased threshold for symptoms as their careers progress (Cardinal et al., 2018).

In the current study, 13 military snipers were recruited from the Canadian Special Operations Forces Command (CANSOFCOM) to assess changes in CVR following a sniper training course. All participants received an MRI scan before (PRE) and after (POST) a sniper training course. Although the exact number of days for sniper training are not reported, snipers were scanned as closely as possible both before and after their training (Table. 1.). Under hypercapnia, high-resolution T1-weighted anatomical images combined with BOLD were acquired. Initial processing of the BOLD data consisted of brain extraction (bet), motion correction (mcflirt), and segmentation (fast) using FSL (Jenkinson et al., 2012). BOLD-CVR data was calculated using the seeVR toolbox (Bhogal, 2021a, Bhogal, 2021b) then registered to MNI152. BOLD-CVR maps are filtered to show only grey matter (GM) regions (Fig. 1.) using FSL's fsmaths. It is hypothesized that CVR will increase following participation in the sniper training course.

A paired sample t-test was conducted to compare PRE and POST differences in individual GM BOLD-CVR maps using FSL's randomise. The subjects' age and number of days between MRI scans were included as covariates in the statistical model. Significant clusters were identified using a height threshold of  $P < 0.05$ , corrected for family-wise error from multiple comparisons based on the Monte Carlo permutation test (8192 permutations) in FSL's randomise. There was a significant increase in CVR in the anterior cingulate gyrus (ACG) in the right cerebral cortex (Fig. 2.). This supports the findings from a previous study consisting of six athletes diagnosed with sports-related concussion (SRC) (Militana et al., 2016). It was found that CVR increased in the ACG 3-6 days post-injury, compared to healthy controls (Militana et al., 2016). These findings suggest that repetitive subconcussive impacts may cause local increases in CVR, emphasizing the importance of incorporating additional cerebrovascular metrics when analyzing neurophysiological changes after subconcussive impacts.

## Figures and table

Days between scans
2
2
2
2
3
3
10
21
36
36
37
41
42

**Table. 1.** Number of days between PRE and POST MRI scans. The exact number of days for sniper training are not reported, but they were scanned as closely as possible both before and after their training (e.g., 1-3 days before and after sniper training).

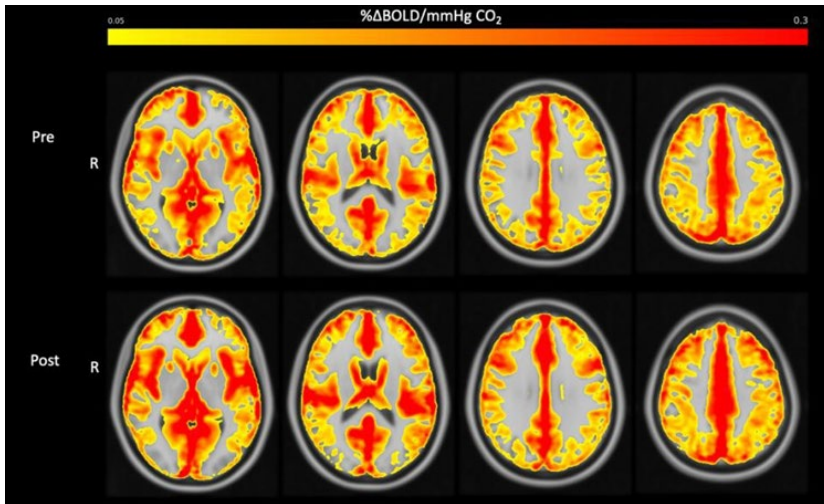


**Fig. 1.** Average lag-corrected CVR in grey matter for PRE and POST MRI scans in 13 snipers expressed in  $\% \Delta \text{BOLD} / \text{mmHg CO}_2$ . Images are in MNI standard space (2mm). BOLD = blood oxygen level dependent, CVR = cerebrovascular reactivity.

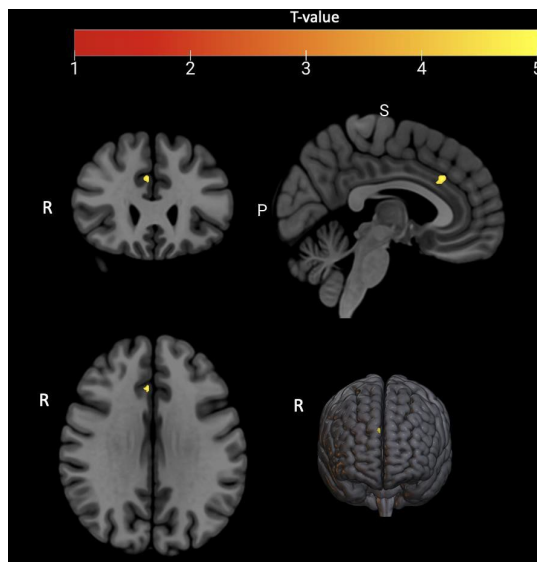
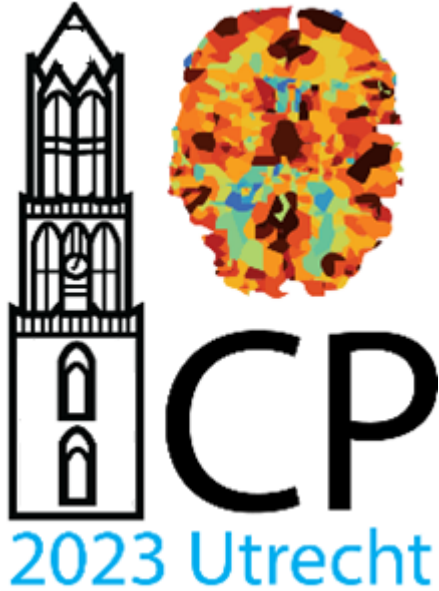


**Fig. 2.** POST > PRE CVR paired difference maps in grey matter for 13 snipers expressed in t-values (paired t-test;  $P < 0.05$ ; age and number of days between PRE and POST were included as covariates). Images are in MNI standard space (2mm). CVR = cerebrovascular reactivity.



# Acknowledgements

We thank our partners at Kalcio Healthcare, United Imaging and Ridderprint for supporting this great event.

